University of Alberta

Engineering and Characterization of Functionalized Solid Surfaces for Environmental and Health Applications

By

Jie Dong ©

A thesis submitted to the Faculty of Graduate Studies and Research in partial fulfillment of the requirements for the degree of

Doctor of Philosophy

in

Chemical Engineering

Department of Chemical and Materials Engineering

Edmonton, Alberta
Fall 2008

Library and
Archives Canada

Published Heritage
Branch

395 Wellington Street
Ottawa ON K1A 0N4
Canada

Bibliothèque et
Archives Canada

Direction du
Patrimoine de l'édition

395, rue Wellington
Ottawa ON K1A 0N4
Canada

Your file Votre référence
ISBN: 978-0-494-46308-6
Our file Notre référence
ISBN: 978-0-494-46308-6

NOTICE:
The author has granted a non-exclusive license allowing Library and Archives Canada to reproduce, publish, archive, preserve, conserve, communicate to the public by telecommunication or on the Internet, loan, distribute and sell theses worldwide, for commercial or non-commercial purposes, in microform, paper, electronic and/or any other formats.

The author retains copyright ownership and moral rights in this thesis. Neither the thesis nor substantial extracts from it may be printed or otherwise reproduced without the author's permission.

AVIS:
L'auteur a accordé une licence non exclusive permettant à la Bibliothèque et Archives Canada de reproduire, publier, archiver, sauvegarder, conserver, transmettre au public par télécommunication ou par l'Internet, prêter, distribuer et vendre des thèses partout dans le monde, à des fins commerciales ou autres, sur support microforme, papier, électronique et/ou autres formats.

L'auteur conserve la propriété du droit d'auteur et des droits moraux qui protège cette thèse. Ni la thèse ni des extraits substantiels de celle-ci ne doivent être imprimés ou autrement reproduits sans son autorisation.

In compliance with the Canadian Privacy Act some supporting forms may have been removed from this thesis.

While these forms may be included in the document page count, their removal does not represent any loss of content from the thesis.

Conformément à la loi canadienne sur la protection de la vie privée, quelques formulaires secondaires ont été enlevés de cette thèse.

Bien que ces formulaires aient inclus dans la pagination, il n'y aura aucun contenu manquant.

Canada

Dedicated to my parents Huiqun Dong and Guifen Xiao

and my husband Yimin Zeng

Abstract

Mesoporous silica coated magnetic nanocomposite particles were synthesized using self-assembled micelles as molecular templates, followed by sol-gel reaction of silica precursor, calcination to remove the organic templates and functionalization of the resultant mesoporous silica surface by silanation reaction. The functionalized composite can successfully remove mercury ions from aqueous solutions. The synthesis conditions were controlled to produce composites of large specific surface area, specific pore size, stable functionality and sufficient magnetization.

Magnetic zeolite composite with silver nanoparticles was synthesized by a simple, yet novel process of sintering magnetite particles with mineral zeolite. The composites feature both magnetic and molecular sieve properties. Following silver ion exchange and controlled thermal reduction, silver nanoparticles are formed on the surface of zeolite in the composites, resulting in a new class of magnetic, multi-functional materials with potential applications as recyclable catalysts, disinfectants and sorbents. In this study, the composites were characterized for the removal of elemental mercury vapor from flue gases. The sorbents can completely capture mercury up to 200°C. The capacity of sorbents is affected by the state, content and size of silver. Silver nanoparticles (<20 nm) have a strong mercury capture capability and large mercury capacity. The sorbent can be regenerated and recycled without performance degradation. Cumulative or extended thermal treatments at 400°C can improve the mercury capture capacity. The magnetic sorbent can be simply separated from fly ash by magnetic separation. In-plant test

confirms the feasibility of the sorbent to capture mercury from flue gases in a full-scale coal-fired power plant.

In an attempt to develop a biosensor, the adsorption of protein, Concanavalin A, on solid surfaces (polystyrene and germanium) from buffers at different pH values, was studied *in situ* by attenuated total reflection infrared spectroscopy (ATR-IR). The adsorbed protein layers were evaluated by the comparison of experimental spectra with simulated spectra of hypothetical surface layers using assumed parameters such as composition, thickness and structure of adsorbed layers. The focus of this study was to produce and understand a controlled and well-defined uniform layer of Con A for the next generation of biosensor applications.

Acknowledgements

I would like to express my sincerest gratitude and appreciation to my supervisor, Prof. Zhenghe Xu, for his patient guidance, continuous encouragement, and invaluable advice throughout the course of this research. I am impressed not only by his scientific knowledge, expertise and insight, but also by his good personality and his energy and optimism towards life.

I am also grateful to my co-supervisor, Prof. Steven M. Kuznicki for his support and guidance in doing this work. I never cease to be amazed by his enthusiasm, creativity, and quick perception of concepts.

I wish to thank Prof. Jerzy M. Mielczarski who supervised my research conducted in LEM, Nancy-Université, CNRS France, for further enriching my knowledge on the surface functionalization for biosensor application, and hand-on-hand instructions on experimental techniques and advanced infrared and XPS knowledge. I would also like to thank Mrs. Ela Mielczarski for her help on my research project and my living in France.

Thanks also go to Prof. Sieghard E. Wanke for serving as my committee member and his stimulating comments and discussion. His feedback greatly enhanced this dissertation. I also thank our research manager, Dr. David J.A. Kelly for his discussion and great help on experimental designs, Prof. Jacob Masliyah for sharing the instrument of AFM, FTIR and zetaphoremeter, Prof. Arthur Mar for providing the magnetization measurement and Dr. Yadollah Maham for introducing me the knowledge of TGA and mentoring me about professional teaching.

I am indebted to Dr. Jianjun Liu, Dr. Liyan Zhang, Dr. Haihong Li, Mr. Shiraz Merali, Ms. Andree Koenig, for training me on the operation of AFM, FTIR, zetaphoremeter, atomic absorption spectroscopy, XRD and thermal gravimetric analysis. I also wish to thank Dr. Feng Wang, Mr. George Braybrook, Ms. Tina Barker, Miss Carolyn Kenny and Dr. Alejandro Anson Casaos for the help with the characterization of TEM, SEM/EDX, BET surface area and pore volume. I would also like to thank Dr. Dimitre Karpuzov, Dr. Anqiang He and Dr. Shihong Xu from Alberta Centre for Surface Engineering and Science (ASCES) for the XPS characterization. I also thank Dr. K. Amy

Dambrowitz for valuable discussions in the paper preparation. Thanks also go to Mr. Jim Skwarok and Leanne Swekla for the lab and administrative management.

The main financial support from Natural Sciences and Engineering Research Council of Canada (NSERC)/EPCOR/AERI and the support from Canadian Foundation for Innovation of XPS facilities are acknowledged. The presented work is also in part financially supported by AMBIO and TASNANO European Commission (EC) projects, which is also acknowledged.

On the personal side, I am deeply indebted to my husband, Yimin Zeng for his continuous love, special support, encouragement, patience and advice. I am very lucky to have such an excellent husband and friend in my life. I would also like to thank my parents, who have been a lasting inspiring since I was a little girl. They support every decision I make to achieve great things in my life.

Finally, I would like to thank everyone who had given me a helping hand or encouraging words to finish my thesis.

Table of Contents

Chapter 1 Introduction..........1

1.1 General Background..........1

1.2 Objectives and Outline of the Thesis..........3

References..........6

Chapter 2 Synthesis, Characterization and Application of Magnetic Nanocomposites for the Removal of Heavy Metals from Industrial Effluents..........9

2.1 Background..........9

2.2 Existing Technology for Heavy Metal Removal..........10

2.2.1 Precipitation..........10

2.2.2 Adsorption..........10

2.2.3 Ion exchange..........11

2.2.4 Reverse osmosis..........11

2.2.5 Ion flotation..........12

2.3 Magnetic Composite Sorbents (MCS)..........13

References..........16

Chapter 3 Engineering and Characterization of Mesoporous Silica-Coated Magnetic Particles for Mercury Removal from Industrial Effluents..........19

3.1 Introduction..........19

3.2 Experimental..........21

3.2.1 Materials..........21

3.2.2 Synthesis Procedures..........21

3.2.3 Characterization..........23

3.2.4 Mercury Removal from Aqueous Solutions..........24

3.3. Results and Discussion..........25

3.3.1 Molecular Templating Studied by AFM..........25

3.3.2 Monitoring the Synthesis by Zeta Potential Measurement..........28

3.3.3 Surfactant Removal..........29

3.3.4 Characterization by Analytical TEM..........31

3.3.5 Magnetic Properties..........33

3.3.6 Functionalization and Mercury Loading..34
3.4 Conclusions..36
References...37
Chapter 4 Novel Synthesis of Magnetic Zeolite Composites with Surface-Supported Silver Nanoparticles for Mercury Removal from Flue Gases.............39
4.1 Introduction...39
4.2 Experimental 42
4.2.1 Materials...42
4.2.2 Preparation...42
4.2.3 Sorbent Characterization..43
4.2.4 Mercury Breakthrough Measurement..44
4.3 Results and Discussion...46
4.3.1 Synthesis of MagZ Composite...46
4.3.2 X-ray Photoelectron Spectroscopy (XPS) 47
4.3.3 Field Emission Scanning Electron Microscopy (FE-SEM) 50
4.3.4 Transmission Electron Miscroscopy (TEM) 51
4.3.5 Magnetization..52
4.3.6 Mercury Capture 53
4.4 Conclusions..55
References...55
Chapter 5 Characterization of Mercury Removal from Flue Gases by Novel Magnetic Zeolite Composites with Silver Nanoparticles.................................59
5. 1 Introduction..59
5.1.1 Background of Mercury Pollution...59
5.1.2 Existing Technology for Mercury Removal from Flue gases.........................59
5.1.3 Noble-metal-based Magnetic Zeolite Composite Sorbents...........................62
5.2 Experimental...63
5.2.1 Materials and Preparation..63
5.2.2 Characterization...64
5.3 Results..66
5.3.1 Mercury Breakthrough...66

    5.3.2 Mercury Capture Capacities..........67
    5.3.3 Sorbent Regeneration..........69
    5.3.4 Sorbent Recovery..........71
    5.3.5 Estimation of Sorbent Injection..........72
  5.4 Discussion..........73
    5.4.1 X-Ray Diffraction..........73
    5.4.2 Field Emission Scanning Electron Microscopy..........74
    5.4.3 Transmission Electron Microscopy..........76
  5.5 Mercury Capture in the Flue Gas of a Coal-fired Power Plant..........77
  5.6 Conclusions..........78
  References..........79

Chapter 6 Real Time Evaluation of the Composition and Structure of Concanavalin A Adsorbed on Polystyrene Surface..........81
  6.1 Introduction..........81
  6.2 Experimental..........83
  6.3 Results and Discussion..........84
    6.3.1 Optical Consideration of Adsorbed Layers..........84
    6.3.2 Polystyrene Contacted with Air or Aqueous Solution..........86
    6.3.3 Adsorption of Con A on Polystyrene..........87
    6.3.4 Adsorption Kinetics of Con A on Polystyrene..........92
    6.3.5 Nature and Structure of the Adsorbed Con A Layer..........93
    6.3.6 BSA Adsorption on Polystyrene Surface with Pre-adsorbed Con A..........98
    6.3.7 XPS Analysis..........99
  6.4 Conclusions..........102
  References..........104

Chapter 7 *In situ* Characterization of the Adsorbed Concanavalin A on Germanium Surface at Various pH..........109
  7.1 Introduction..........109
  7.2 Experimental..........112
    7.2.1 Materials..........112
    7.2.2 Surface Preparation..........112

7.2.3 Adsorption/ Desorption of Con A........113
7.2.4 Determination of Optical Constants........113
7.2.5 Infrared Spectroscopy........114
7.3 Results and Discussion........115
7.3.1 Optical Consideration........115
7.3.2 Adsorption Kinetics of Con A........117
7.3.3 Hydration of the Con A Adsorbed Layer........120
7.3.4 Desorption of Con A Layer........122
7.4 Conclusions........124
References........125
Chapter 8 General Discussion and Conclusions........131
8.1 Summary of the Obtained Results........131
8.2 Contributions to Original Knowledge........132
8.3 Future Directions........133
References........136
Appendix A Characterization Techniques........139
A.1 Introduction........139
A.2 Atomic Force Microscopy (AFM)........139
A.3 Fourier Transform Infrared Spectroscopy (FTIR)........141
A.4 Zeta Potential Measurement........144
A.5 X-ray Photoelectron Spectroscopy (XPS)........147
A.6 Scanning Electron Microscopy (SEM)........148
A.7 Transmission Electron Microscopy (TEM)........151
A.8 Particle Size Measurement........152
A.9 Thermal Gravimetric Analysis (TGA)........154
A.10 N_2 Adsorption-Desorption Isotherms........154
A.11 Magnetization Measurement........156
A.12 Atomic Absorption Spectroscopy (AAS)........157
A.13 Cold Vapor Atomic Fluorescence Spectroscopy (CVAFS)........158
A.14 Summary........158
References........159

Appendix B Continuation of Chapter 2..162
B.1 Methods for the Preparation of Magnetic Nanocomposites........................162
B.1.1 Molecular Self-assembly (SA) 162
B.1.2 Direct Silanation..165
B.1.3 A Novel Two-Step Silica-Coating..169
B.1.4 Mesoporous Silica Coating..173
B.1.5 Silanation on Mesoporous Silica Coated Magnetic Particles...............182
B.2 Practical Applications of MCS...185
B.2.1 SA Monolayer...185
B.2.2 Silanized Monolayers on Two-steps Silica-coated γ-Fe_2O_3.....................186
B.2.3 Poly(1-vinylimidazole)-grafting on Magnetic Nanoparticles................190
B.2.4 Functionalized Mesoporous Silica Coated Magnetic Particles.............193
B.3 Further Directions...197
B.4 Conclusions..198
References...199
Appendix C: Factorial Design to Study the So-gel Reaction in the Synthesis of Mesoporous Silica Coated Magnetite Particles...205
Appendix D: Sol-gel Reaction and Silanation...211
Appendix E: Theory of the Infrared Spectra Simulation...............................213
Appendix F: Supporting Information to Chapter 6..216
F.1 Experimental...216
F.2 Preparation of Thin film of Polystyrene for Con A Adsorption.....................217
F.3 Determination of Number of the Active Internal Reflections.......................218
F.4 Determination of Thickness and Structure of the Deposited PS Layer............218
References...221

List of Tables

Table 4.1 BET specific surface areas of materials……………………………………47

Table 5.1 The mercury species in flue gases of burning different types of coal……60

Table 5.2 Samples synthesis conditions and nomenclature…………………………64

Table 5.3 The important parameters and results from mercury capture capacity studies of various samples……………………………………………………………68

Table 5.4 The estimation of various sorbent injections for ≥80% mercury removal……………………………………………………………………………72

Table 6.1 Peak assignment of Con A reference spectrum……………………………89

Table 6.2 The positions of amide I and amide II absorbance bands observed for adsorbed layers at different conditions and obtained by spectral simulation………………………………………………………………………………98

Table 6.3 Surface atomic concentration of C, O, N, S determined for solid ConA and adsorbed layer at different conditions. Spectra recorded at different take off angles: at 0° -the largest penetration depth; at 60° and 75° , the penetration depth are ½ and ¼ of that at 0°, respectively…….100

Table B.1 Characteristics and stability of silica-coated γ-Fe_2O_3 by dense liquid, sol-gel, and two-step coating processes…………………………………………169

Table C.1 Conditions for 2^3 Factorial Design………………………………………206

Table C.2 Complete 2^3 Factorial Design: Factors and Levels…………………………206

Table C.3 Results of the 2^3 Factorial Design Experiments……………………………207

Table C.4 Summaries of Effects and Standard Errors for the 2^3 Factorial Design……………………………………………………………………………208

Table C.5 Optimization of the Experiment……………………………………………209

List of Figures

Figure 2.1 Illustration of magnetic separation technology in metal ions recovery from an industrial effluent..........14

Figure 2.2 Key-lock relation in potential applications of magnetic composites particles..........16

Figure 3.1 The flow chart of experimental procedure. I. dense liquid silica coating (DLSC); II. molecular templating; III. sol-gel reaction; IV. calcination; V. rehydration; VI. silanation..........22

Figure 3.2 Schematic diagram of a sol-gel silica coated DLSC-magnetite particle with templates..........23

Figure 3.3 A typical probing cycle in AFM interaction force measurement..........26

Figure 3.4 Interaction forces between a bare silica wafer and AFM tip in ethanol (solid circles) and CTAC ethanol solutions (open circles)..........27

Figure 3.5 Silica wafer in ethanol a) and in 5 mM CTAC ethanol solutions b) (circles represent voids to be filled by silica using sol-gel method)..........28

Figure 3.6 Zeta potential distributions of: a) bare magnetite (blank column) and DLS coated magnetite (slash shaded column); and b) templating on DLS coated-magnetite (cross shaded column) and sol-gel coated particles around the templates (dash shaded column)..........29

Figure 3.7 Thermal gravimetric analysis (TGA) of bare magnetite (the dotted line), sol-gel coated particles with templates (the solid line) and calcinated mesoporous magnetic particles (the dash line)..........30

Figure 3.8 Bright-field TEM micrograph of a mesoporous magnetic nanaocompostie particle. The separation of two particles by silica matrix is marked by arrows..........31

Figure 3.9 Energy Dispersive X-ray (EDX) emission spectra obtained on areas A and B..........32

Figure 3.10 Bright-field TEM image of the mesoporous silica layer with some of the pores highlighted by circles..........32

Figure 3.11 The spectrum of low-loss EELS of the silica layer..........33

Figure 3.12 Room temperature magnetization measurements of bare magnetite and mesoporous magnetic nanocomposite particles..34

Figure 3.13 Narrow-scan XPS spectra for sulfur and mercury on samples of functionalized mesoporous magnetic sorbents (dash line) and mercury loaded on the sorbents (solid line)..35

Figure 3.14 Mercury adsorption by functionalized magnetic sorbents at pH 2: a) isotherm curve; b) distribution coefficient curve..................................36

Figure 4.1 Schematic illustration of the synthesis process to produce a new class of magnetite-zeolite composite with surface-supported silver nanoparticles for the removal of mercury from a complex flue gas...............................41

Figure 4.2 Experimental set-up for the mercury breakthrough measurements..........45

Figure 4.3 N_2 adsorption/desorption isotherm curves of Zeolite and MagZ containing 30% zeolite...47

Figure 4.4 XPS narrow-scan spectra over the spectral region of (a) Si_{2p} (● the experimental data; ○ the calculated data; Δ Si_{2p} from zeolite; + Si_{2p} from silica), (b) Fe_{2p}, (c) Na_{1s} and (d) Ag_{3d} for various samples........................49

Figure 4.5 Backscattering SEM images of (a) MagZ composites particles and (b) MagZ-Ag^{o}. (c) EDX analysis (c) on areas 01, 02 and 03 of (b). (d) Magnified SEM image of area 01 in (b)..51

Figure 4.6 TEM image of MagZ-Ag^{o}...52

Figure 4.7 Magnetization characteristics of zeolite with SiO_2 (squares) and MagZ-Ag^{o} (triangles)..53

Figure 4.8 Mercury breakthrough as a function of temperature changes for the samples: (a) magnetite (star), (b) DLSC-Fe_3O_4 (open circle), (c) MagZ saturated with moisture (open square), (d) 120MagZ (filled circles) and (e) MagZ-Ag^{o} (filled triangles)..54

Figure 5.1 Schematics of application scheme of new magnetic zeolite sorbents with silver nanoparticles for mercury removal from flue gases.......................63

Figure 5.2 The experimental set-up for mercury capture capacity and sorbent regeneration tests...64

Figure 5.3 An illustration of the mercury capture capacity measurement.............65

Figure 5.4 Role of silver on various sorbents in mercury capture at varying temperatures..........67
Figure 5.5 The relationship of silver contens in samples and the mercury capacity..........68
Figure 5.6 Mercury capacities of MagZ-Ag° for ten cycles of capture/regeneration at ≥80% Hg° capture (dashed columns) and the capacity of MagZ-Ag° after 20 h continuous thermal treatment at 400°C (the blank column)..........69
Figure 5.7 The result of magnetic separation of sorbent from fly ash as a function of recycle numbers..........71
Figure 5.8 XRD analysis of (a) 2FeSi-Ag°, (b) 1/2 MagZ-Ag°, (c) MagZ-Ag°, (d) 2MagZ-Ag° and (e) Z-Ag°..........74
Figure 5.9 SEM images of (a) 2FeSi-Ag°; (b) 1/2MagZ-Ag°; (c) MagZ-Ag°; (d) 2MagZ-Ag° and (e) Z-Ag°..........75
Figure 5.10 TEM images of (a) Z-Ag°; (b) MagZ-Ag°; (c) 10-cycle regenerated MagZ-Ag°..........76
Figure 5.11 Mercury capture (ppb wt) by different sorbents over a 5-minute exposure in the flue gases of an operating Rankine Cycle coal-fired power plant..........77
Figure 6.1 Three considered models of experimental multilayers on Ge: A. stratified multilayer system with each phase homogeneous; B. multilayer system with mixed composition layers (Con A at different hydration level); C. multilayer system of Con A and BSA with patch-like structures..........84
Figure 6.2 Optical constants: refractive index n and absorption coefficient k as a function of wavenumber for: PS (thin solid line), Con A (thick solid line), BSA (dot line) and water (dashed line) used for spectral simulation of the systems under investigations..........85
Figure 6.3 Simulated reflection spectra for one reflection of 16 nm PS on Ge contacted with air and water for p- and s-polarizations. The thin solid line and dashed lines are for p- and s-polarizations in air, respectively; the

thick solid line and dot lines are for p- and s-polarizations in water, respectively..86

Figure 6.4 Ribbon representation of: A. dimer of Con A, 30 ×45 ×75 Å^3 dimension, B. tetramer of Con A, 60 ×70 × 70 Å^3 dimension (PDB, 1CES)............88

Figure 6.5 Reference spectra of solid samples of Con A and BSA recorded by ATR-IR at p-polarization. Notice different position of amide I bands which could be used to distinguish Con A with band at 1633 cm^{-1} characteristic for β-sheet structure from BSA with band at 1653 cm^{-1} characteristic for α-helix structure..88

Figure 6.6 Simulated spectra of 3 nm hypothetical Con A layer on PS where reflectivities are: R(Ge/16 nmPS/3nm Con A/water) and R_o(Ge/16 nm PS/water), calculated for p- (solid line) and s- (dashed line) polarizations with 12 reflections..90

Figure 6.7 Simulated spectra of 3 nm hypothetical Con A layer on PS where reflectivity are: R(Ge/16 nm PS/3nm Con A/air) and R_0(Ge/16nm PS/air), calculated for p- (solid line) and s- (dashed line) polarizations with 16 reflections..91

Figure 6.8 Kinetics of Con A adsorption on PS based on *in situ* recorded reflection spectra and determined from the intensity of amide I and amide II absorbance bands. Solid symbol lines are based on amide II. Empty symbol lines are based on amide I. Square symbols are for pH 7.4 and triangles are for pH 4.8. Con A layer thickness based on best fitting of experimental spectra by the simulated hypothetical surface layer with assumed thickness (model A)..93

Figure 6.9 *In situ* experimental spectra of Con A adsorbed on PS for p-polarization: A. pH 7.4, after 15min, 1h, 3h, 6h and 24h with monotonic increase in amide I absorbance band. B. pH 4.8 after 15min, 1h, 3h, 18h and 22h with monotonic increase in amide I absorbance band.............................94

Figure 6.10 Calculated optical constants: refractive index n and absorption coefficient k as a function of wavenumber for: dry Con A (solid line); Con A hydrated 30%, 0.7 : 0.3 = Con A : H_2O mixture phase (dot line) and hydrated 50% of Con A, 0.5 : 0.5 = Con A : H_2O mixture phase (dashed line)......95

Figure 6.11 *In situ* experimental spectra (solid line) recorded after 15 min of adsorption from pH 7.4 solution compared with the simulated spectra (dashed line). Reflectivity are following: R(Ge/16nm PS/3nm (0.7 Con A+0.3 H_2O)/H_2O and R_0(Ge/16nm PS/H_2O)......96

Figure 6.12 *In situ* experimental spectra (solid line) recorded after 24 h of adsorption from pH 7.4 solution compared with the simulated spectra (dashed line). Reflectivity are following: R(Ge/16nm PS/3nm (0.7 Con A+0.3 H_2O)/8nm (0.5 Con A + 0.5 H_2O)/H_2O and R_0(Ge/16nm PS/H_2O)......97

Figure 6.13 *Ex situ* experimental spectra recorded after 15 min adsorption of Con A from pH 4.8 solution (solid line) compared with the experimental spectra recorded after adsorption of BSA for 30 min on the surface with pre-adsorbed Con A (dot line) and the differential spectrum after and before BSA adsorption (dashed-dot line)......99

Figure 6.14 Schematic representation of nature and structure of experimentally documented steps of adsorption of Con A on polystyrene at pH 4.8 and 7.4 in quick and slow kinetic adsorption regions......103

Figure 7.1 Optical constants: refractive index n and absorption coefficient k as a function of wavenumber for Con A (the solid lines), water (the dotted lines) and Ge (the dashed lines) used for spectra simulation of the systems under investigations......114

Figure 7.2 Simulated spectra for 12 reflections of 3 nm Con A on Ge contacted with water for p-polarization (the solid line) and s-polarization (the dotted line)...... 116

Figure 7.3 Schematic illustration of the configuration used in simulation: (A). the reference system; (B). the sample system with Con A adsorbed layers......116

Figure 7.4 Kinetics of Con A adsorption on Ge based on *in situ* recorded reflection spectra of adsorbed Con A and determined from the intensity of amide I (the triangle symbols) and amide II (the circle symbols) absorbance bands.

The thickness of Con A layer is based on the best fitting of experimental spectra to the simulated hypothetical surface layer with assumed thickness……118

Figure 7.5 Schematic illustration of the surface coverage and orientation of Con A adsorbed at the Ge-water interface. For simplicity the hydration by water molecules is not shown……119

Figure 7.6 Ribbon diagrams of (A) the monomer of Con A, (B) the dimer of Con A and (C) the tetramer of Con A (Protein Data Bank: 2UU8 and 1CES)……120

Figure 7.7 The comparison of *in situ* experimental spectra (solid lines) with the simulated spectra (dashed lines). (A) 5 min at pH 4.8 (1) vs. 3 nm 30% hydrated Con A; (B) 21 h at 4.8 (1) vs. 7 nm 30% hydrated Con A; (C) 21 h at pH 7.4 vs. 10 nm 50% hydrated Con A and 7 nm 30% hydrated Con A……122

Figure 7.8 *In situ* experimental spectra of Con A after adsorption (21 h at pH 4.8 (2)) (the solid line), after 2 h water washing (the dashed line), 2 h NaCl (1 M) washing (the dotted line) and 20 h water washing (the dash-dot line)……123

Figure 7.9 *In situ* experimental spectra of Con A after adsorption (21h at pH 4.8(2)) (the solid line) and after SDS washing of the Con A adsorbed layer on Ge for 5min (the dashed line), 3h (the dotted line) and 20h (the dash-dot-dot line)……124

Figure A.1 Schematics of a typical atomic force microscope……140

Figure A.2 Optical schematic of an external reflection……143

Figure A.3 Typical setup of ATR-IR experiment……143

Figure A.4 Optical configuration of a DRIFTS cell……144

Figure A.5 Schematic representation of an electrical double layer around a particle……145

Figure A.6 Schematics of a typical electrophoresis cell of a zetaphoremeter……146

Figure A.7 The electron transition involved in the photoemission of a $2p_{3/2}$ electron from copper……148

Figure A.8 The structural illustration of SEM...149

Figure A.9 Electron specimen interaction and depth profile..............................150

Figure A.10 Schematic of an atomic-absorption experiment..............................157

Figure B.1 Infrared spectra in the high (A) and low-frequency (B) regions for (a) MHA in KBr, (b) MHA on γ-Fe_2O_3, and (c) γ-Fe_2O_3........................164

Figure B.2 Interactions involved in silanation..166

Figure B.3 Zeta-potentials of APTES-silanized magnetic particles from water before and after acid and base leaching...169

Figure B.4 Schematics of silica-coated magnetic nanocomposites by (a) sol-gel, (b) dense-liquid, and (c) two-step, i.e. (a) followed by (b), processes........170

Figure B.5 Illustration of the proposed synthesis process for the preparation of mesoporous magnetic nanocomposite particles: dense-liquid-silica coating (I), molecular templating (II), sol-gel process (III), calcination (IV), and functionalization (V)..175

Figure B.6 Interaction forces between a bare silica wafer and AFM tip in ethanol (solid squares) and CTAC ethanol solutions (open squares)..................177

Figure B.7 Silica wafer in ethanol a) and CTAC solutions b) (circles represent voids to be filled by silica using sol-gel method)..................................178

Figure B.8 Zeta potentials of different particles: (1) bare magnetite particles; (2) DLS coated magnetite particles; (3) templated DLS magnetite (4) sol-gel coated particles with templates; and (5) particles after calcination...179

Figure B.9 TEM images of untreated Fe_3O_4 particles (A) and Fe_3O_4 particles with template-assisted silica coatings (B). Micrograph (B) is a dark-field mage, obtained with tilt illumination...180

Figure B.10 Room temperature magnetization of bare magnetite and mesoporous magnetic nanocomposite particles..182

Figure B.11 (A) Schematic diagram for the synthesis of mesoporous-Fe_3O_4 silanized by 3-APTES. (B) DRIFTS spectra of mesoporous-Fe_3O_4 magnetic particles; after (a) calcination, (b) rehydroxylation, and (c) silanation by 3-APTES from toluene...184

Figure B.12 XPS spectra of narrow scans for the interested elements (a) γ-Fe_2O_3; (b) thiol-type magnetic sorbents; (c) after copper loading; and (d) after silver loading……………………………………………………………………186

Figure B.13 Copper loading on and removal from APTES silanized on silica-coated γ-Fe_2O_3 particles, in comparison to silica-coated γ-Fe_2O_3 particles at loading pH 5.3…………………………………………………………………….188

Figure B.14 The amount of copper detached vs. the amount of copper loaded………189

Figure B.15 Synthesis of poly(1-vinylimidazole) (A) and schematic illustration of polymer-grafted magnetic particles (B)……………………………………191

Figure B.16 Removal efficiency of Cu^{2+}, Ni^{2+} and Co^{2+} by, and loading capacity of Cu^{2+} on Mag-Im_{18}. Metal ion solution/Mag-Im_{18} = 10 mL/10 mg at initial solution pH 5.3……………………………………………………………192

Figure B.17 Removal efficiencies of Cu^{2+} and Co^{2+} by MagIm_{18} from a mixture of Cu^{2+}/Co^{2+} solution. Metal ion solution/Mag-Im_{18} = 10 mL/10 mg at initial $[Cu^{2+}]$ and $[Co^{2+}]$ concentration of 0.157 mmol/L and 0.170 mmol/L, respectively……………………………………………………………………193

Figure B.18 (A) Distribution and (B) adsorption isotherms of copper ions on different magnetic particles as a function of copper concentration: (a) Fe_3O_4 coated with silica without templating, (b) mesoporous-Fe_3O_4, (c) Fe_3O_4 coated with silica without templating but silanized by 3-APTES, and (d) mesoporous-Fe_3O_4 silanized with 3-APTES…………………………………194

Figure B.19 Loadings of transition metal ions on the amine-terminated mesoporous magnetic particles as a function of solution pH from (A) single-element solutions; and (B) a solution containing copper, nickel, and zinc, each at 0.5 mmol/L concentration………………………………………………………195

Figure B.20 Mercury adsorption by functionalized magnetic sorbents at pH 2: A) isotherm; and B) distribution…………………………………………………197

Figure C.1 Factorial Design Diagram for the Surface Area of the Sorbents ……….209

Figure D.1 Hydration and silanation process. (X: alkoxy or halide groups; Y: an organic functional group)……………………………………………………212

Figure E. 1 Schematic illustration of the interaction between infrared radiation and adsorbed layer..213

Figure F.1 (A) Schematic illustration of the assembled Teflon liquid cell with Ge reflection element for *in situ* adsorption studies by ATR-IR, (B) Directions of electric field components at Ge interface..............................217

Figure F.2 Simulated absorbance intensity of characteristic PS absorbance band at 1494 cm^{-1} versus thickness of hypothetical PS isotropic layer for p- (filled square line) and s- (open circle line) polarizations. Simulation was performed for system of R(Ge/PS/air) and R_0(Ge/air).....................219

Figure F.3 Experimental spectra (dashed lines) of deposited PS layer on Ge reflection element compared with simulated spectra (solid lines) of 16nm hypothetical isotropic PS layer for both polarizations................................220

List of Abbreviations

AA	Atomic Absorption
AAS	Atomic Absorption Spectroscopy
ACI	Activated Carbon Injection
AES	Auger Electron Spectroscopy
AFM	Atomic Force Microscopy
AFS	Atomic Fluorescence Spectroscopy
APTES	3-aminopropyl triethoxysilane
ARB	Aacid Red B
ARUPS	Angle-Resolved Ultraviolet Photoelectron Spectroscopy
ATR-IR	Attenuated Total Reflection Infrared Spectroscopy
BET	Brunauer-Emmett-Teller
BJH	Barrett-Joyner-Halenda
BSA	Bovine Serum Albumin
BT	Breakthrough
Con A	Concanavalin A
CTAC	Cetyl-trimethyl-ammonium Chloride
CVAFS	Cold Vapor Atomic Fluorescence Spectroscopy
DC	Direct Current
DI	Deionized
DLSC	Dense Liquid Silica Coating
DNA	Deoxyribonucleic Acid
DRIFTS	Diffuse Reflectance Infrared Fourier Transform Spectroscopy
DTA	ethylenediamine tetraacetate
DTDPA	3, 3'-dithiodipropionic acid
EDX	Energy Dispersive X-ray Analysis
EEC	Equivalent Exchange Capacity
EELS	Electron Energy Loss Spectroscopy
EPA	Environmental Protection Agency
ESP	Electrostatic Precipitators

EXAFS	Extended X-ray Absorption Fine Structure
FE-SEM	Field Emission Scanning Electron Microscopy
FGD	Flue Gas Desulfurization
FTIR	Fourier Transform Infrared Spectroscopy
GIXD	Grazing Incidence X-ray Diffraction
GT	Gold coated glass beads trap
HREELS	High Resolution Electron Energy Loss Spectroscopy
HRTEM	High Resolution Transmission Electron Microscopy
IEP	Isoelectric Point
IR	Infrared
LCM	Liquid-crystal Templating
LEED	Low-Energy Electron Diffraction
MagZ	Magnetite-Zeolite composites
MagZ-Ag$^+$	Silver ions exchanged MagZ
MagZ-Ag^0	Thermal reduced MagZ-Ag$^+$
MCS	Magnetic Composite Sorbents
MCT	Mercury Cadmium Telluride
MeHg+	methylmercury
MHA	16-mercaptohexadecanoic acid
MIP	Mercury Injection Port
MPTS	Mercapto-propyl-trimethoxy-silane
NETL	National Energy Technology Laboratory
NEXAFS	Near-edge X-ray Absorption Fine Structure
NMR	Nuclear Magnetic Resonance
PBS	Phosphate Buffered Saline
PCS	Photon Correlation Spectroscopy
PMOS	Periodic Mesoporous Organosilicas
PS	Polystyrene
pTSS	poly tris(trimethylsiloxy)silylstyrene
SA	Molecular Self-assembly
SAM	Self-assembled Monolayer

SANS	Small-Angle Neutron Scattering
SC	Scattering Coefficient
SCPM	Scattering Coefficient per Micron,
SCR	Selective Catalytic Reduction
SDS	Sodium Dodecyl Sulphate
SEM	Scanning Electron Microscopy
SFG	Sum Frequency Generation
STM	Scanning Tunneling Microscopy
TCA	Trichloroethane
TCE	Trichloroethene
TEM	Transmission Electron Microscopy
TEOS	Tetraethyl Orthosilicate
TGA	Thermal Gravimetric Analysis
TOF-SIMS	Time-of-Flight-Secondary Ion Mass Spectrometry
UPS	Ultraviolet Photoemission Spectroscopy
UV	Ultraviolet
XANES	X-ray Absorption Near Edge Spectroscopy
XPS	X-ray Photoelectron Spectroscopy
XRD	X-Ray Diffraction:
Z-Ag$^+$	Silver ions exchanged Zeolite
Z-Ag^0	Thermal reduced Z-Ag$^+$

List of Symbols

a	the particle diameter
abs	absorbance
C	a constant
c	the velocity of light
C_e	the equilibrium concentration
C_i	the initial concentration
C_{sca}	the scattering cross section
D	the diffusion coefficient
d_i	the film thickness
E	energy
e	the charge of electron
$E_{x,y,z}$	the components of electric field
H	the applied magnetic field
h	Planck's constant
I_o	the intensity of the zero-loss peak in EELS spectrum
I_t	the integral intensity of the total low-loss portion of the EELS spectrum
k	Boltzmann constant
K	the force constant of the bond between two atoms
K_d	the distribution coefficient
k_i	absorption index of optical constants
M	magnetic moment
m	mass
M_V	the molar volume of adsorbed gas
N	Avagadro number
n_i	refractive index of optical constants
P	the equilibrium pressure of adsorbates
P_0	the saturation pressure of adsorbates
Q_{sca}	dimensionless scattering efficiency parameter
r	the equivalent sphere's radius

R	the reflectivity of the reference layer
R_c	the universal gas constant
R_o	the reflectivity of the studied layer
S	specific surface area
s	the cross section area of adsorbed molecule
S_{total}	total surface area
T	temperature
t	time
U	the acceleration voltage
u_E	electrophoretic mobility
$V(t)$	induction voltage
V	the volume of the adsorbed gas
v	velocity
V_m	the volume of the monolayer adsorbed gas
α	the convergence semi-angle in TEM
Γ	the amount of mercury adsorbed per gram of sorbents
γ	the surface tension
ε	dielectric constant
ζ	zeta-potential
η	the solvent viscosity
θ	the incidence/scattering angle
κ	the reciprocal of the thickness of the double layer
λ	the wavelength
λ_i	the average mean free path
μ	the reduced mass
ρ	density
υ	the molecular vibrational frequency
$\bar{\upsilon}$	the wavenumber of absorption peak

Chapter 1 Introduction

1.1 General Background

With the industrial development and economic growth, the problems of environmental pollution, such as air pollution and waste discharge, are becoming increasingly a threat to human health. Considerable efforts have been devoted to developing fundamental understanding and viable technologies to reduce environmental consequences of industrial wastes. Researchers are dedicated to understanding and developing novel materials which can be applied in a more effective, economical and sustainable ways than the currently available materials for remediation of pollution. Meanwhile, the studies on biotechnology and biomaterials are also an important research area. The knowledge and understanding of the properties, interactions and interfacial phenomena between biomolecules and solid substance is essential in the field of enzymatic catalysis, biosensors, bio-implants, disease diagnostics, food quality control, marine adhesion and anti-fouling.

Surface functionalization/modification is a versatile technique and widely practiced in many fields. In general, some materials which have excellent bulk physical and chemical properties may not possess suitable surface properties required for specific applications. For this reason, surface functionalization/modification techniques that can transform these materials into valuable finished products became an important part of surface science and technology.

Generally, the surface-modification methods can be divided into two classes[1]: physical modifications and chemical modifications. The physical modification refers to surface treatment and coatings by physical methods, such as physical deposition of one material on the surface of a substrate, aiming at the desired surface property, such as hydrophobicity/hydrophilicity, super smooth or strong hardness. On the other hand, chemical modification utilizes the chemical reaction between a substrate and functional reagents to chemically bond functional groups on the surface of the substrate. The key advantage of this method is that the surface of the materials can be modified or tailored to acquire very distinctive properties through the choice of different functional groups, while maintaining the substrate properties. Because of the diversity of functional groups, there is a wide range of possibilities to functionalize a surface for different applications, such as heavy metal removal, biomolecular recognition, molecular separation or enzyme catalysis. Compared with the physical methods, the covalent attachment of a functional group onto a material surface provides long-term chemical stability of the introduced surface chemical properties.

Due to lack of chemical reactivity on most substrate surfaces, a surface activation process is often needed to create reactive sites that can generate further grafting processes. Practically, one can generate reactive groups through chemical reactions, UV irradiation, high-energy electron sputtering, γ-irradiation, plasma treatment, ozone exposure, etc..

Among the chemical surface-modification techniques, the formation of a self-assembled monolayer (SAM) has been intensively studied recently. SAM leads to a structure which is at, or close to, thermodynamic equilibrium, capable of self-healing/defect rejection, leading to a closely packed, well-ordered, and stable configuration on the surface.[2] Initially such monolayers have been generated mostly on metal surfaces, such as Au, Ag, and Cu, using thiol chemistry,[3,4] or alkylsiloxanes on hydroxyl-terminated surfaces, such as Si/SiO_2, Al/Al_2O_3, glass surfaces, using siloxy linkages.[5]

With the discovery of mesoporous materials,[6,7,8] a lot of attention has been directed to the modification and applications of this kind of materials, which possesses extremely high surface areas of easily accessible, uniformly distributed nano-pore structures and specific pore volume. These materials have seen applications in adsorption, separation, catalysis, biological sensing, medical usage, molecular engineering, and nanotechnology.

Zeolites are classical aluminosilicate microporous solids, known as "molecular sieve". They have unique structural, physical and chemical properties that make them valuable for many industrial, agricultural and environmental applications.[9, 10, 11] Natural zeolites are low cost and readily available materials of excellent cation exchange characteristics. They have been widely used as sorbents for the removal of heavy metal ions from aqueous industrial wastes.[12, 13, 14, 15, 16, 17, 18] The adsorption capacity of the zeolites originates from an open structure and a net negative charge in their framework, which can attract and hold cations. Various zeolites are reported to be incorporated with transition metal ions followed by calcination/reduction to act as excellent thermal catalysts[19, 20, 21] and photocatalysts.[22,23,24] In addition, zeolites are often used in the gas separation because of their nano-scale pore structures and unusual internal surface topology.[25, 26, 27, 28]

Magnetic separation is an easy, yet effective technique to separate target magnetic particles from complex multiphase systems. Tailoring the physical, chemical and surface properties of magnetic (composites) particles will enable selective or non-selective attachment of ions, molecules, macromolecules, cells, colloidal particles or liquid phases onto desired particles. Engineering magnetic composite particles is an interdisciplinary subject, which requires an integrated approach involving the manufacture and surface modification of appropriate composites with careful attention to the constraints imposed by end users. The properties of the composite particles are of critical importance to the successful application of the technology.[29]

1.2 Objectives and Outline of the Thesis

The major industries in Canada include mining, metallurgy, papermaking, petroleum refining, and agricultural industries. In the province of Alberta, the extraction and upgrading bitumen from oilsands and the use of coal in power plants are among the major industries. These industries are the major sources of air and water pollution. Therefore, considerable efforts have been made to reduce and minimize the negative effects from industries for sustainable utilization of resources while maintaining economic growth. The main objective of research for this thesis is to provide new materials and technology for the applications of pollution control (especially for the removal of heavy metals) and sensor development.

The thesis is in the paper format, and is organized as follows:

Chapter 1 provides a brief background of the motivation of this project and introduces the concepts and subjects to be studied. Specifically, it covers surface chemistry and modification relevant to mesoporous silica, zeolite and semi-conductor substrates for sorbent and sensor applications. Incorporating magnetic property into the sorbent materials is also a key feature of this study.

Chapter 2 provides an extensive review on "Synthesis, Characterization and Application of Magnetic Nanocomposites for the Removal of Heavy Metals from Industrial Effluents", which has been accepted for publication as a chapter of the book "*Emerging Environmental Technologies*" by Springer Publications 2008. This chapter includes an elaborated background of heavy metal pollution, the existing technology for heavy metal removal, and the development of magnetic composite sorbent. To make the thesis more concise, the details on the methods for the preparation of magnetic nanocomposites and their practical applications are presented in *Appendix B.*

Chapter 3 is a paper, "Engineering and Characterization of Mesoporous Silica-Coated Magnetic Particles for Mercury Removal from Industrial Effluents", published in *Applied Surface Science* 254 (2008) 3522-3530. This paper presents a novel synthesis procedure to produce mesoporous silica coated magnetic nanocomposite particles and provides the comprehensive characterization of each synthesis step. The molecular templating was studied by atomic force microscopy (AFM) in situ imaging. The critical role of each step in the synthesis was confirmed by zeta-potential measurements. The removal of surfactant and the thickness of the silica layer were determined by thermal gravimetric analysis (TGA) and transmission electron microscopy (TEM). The functionalization and mercury loading were determined by X-ray photoelectron spectroscopy (XPS) and atomic absorption spectroscopy (AAS). The resultant composite particles retain a high saturated magnetization and are easy to isolate by conventional magnetic separation. The major characterization techniques are reviewed in *Appendix A*.

Chapter 4 is a manuscript on "Novel Synthesis of Magnetic Zeolite Composites with Surface-Supported Silver Nanoparticles for Mercury Removal from Flue Gases", to be submitted. In this manuscript, a simple, yet novel synthesis of a magnetic composite sorbent by sintering silica-coated magnetite particles with the mineral zeolite was proposed and studied. Following silver ion exchange and controlled thermal reduction, silver nanoparticles are found to form on the surface of the zeolite in the composites. These multi-functional materials represent a new class of composites with potential applications as recyclable catalysts, disinfectants and sorbents. The composites feature both magnetic and molecular sieve properties, and could be collected from effluent streams by an external magnetic field. The novel magnetic zeolite composites are characterized by a suite of analytical techniques including XPS, SEM, TEM and N_2 adsorption/desorption isotherm. These multifunctional materials show the potential as sorbents for the removal of vapour-phase mercury from the flue gas of coal-fired power plants. Initial tests show a complete mercury capture by these novel sorbents at temperatures up to 200°C.

Chapter 5 is a manuscript on "Characterization of Mercury Removal from Flue Gases by Novel Magnetic Zeolite Composites with Silver Nanoparticles", to be submitted. This chapter firstly reviews the current techniques for mercury removal from flue gases, followed by the characterization of elemental mercury removal from flue gases by the novel magnetic zeolite composite sorbents proposed in Chapter 4. The mercury breakthrough temperature and mercury capacity were compared for sorbents of varied silver content. Selected sorbents were tested for magnetic recovery, regeneration and recyclability. The relationship between the content and size of silver in the sorbent and the mercury adsorption performance was examined. Finally, the novel sorbents were tested in situ by exposure to flue gases from a full-scale coal-fired power plant.

Chapter 6 is a paper on "Real Time Evaluation of the Composition and Structure of Concanavalin A Adsorbed on Polystyrene Surface", published in *Journal of Physical Chemistry B* 112 (2008), 5228-5237. It provides the fundamental understanding of surface modification by the adsorption of biomolecules, Concanavalin A (Con A) as an example of biosensor applications. In this study, *in situ* qualitative and quantitative evaluations of sub-monolayer and multilayer of adsorbed protein Con A on hydrophobic polystyrene surface were carried out by attenuated total reflection infrared spectroscopy (ATR-IR). The influence of pH and adsorption time on the composition and structure of the adsorbed protein layers was investigated by comparison of the experimental spectra with simulated spectra of hypothetical multilayer systems using assumed composition, thickness, and structure of adsorbed layer. The compositions, structure, kinetics of the adsorption of ConA and hydration level of the adsorbed layers were evaluated in great detail. Competitive adsorption of bovine serum albumin (BSA) on pre-adsorbed Con A layers was also investigated in order to characterize Con A surface distribution. Parallel studies using XPS support the conclusions drawn from IR investigations.

Chapter 7 is a paper on "In situ Characterization of the Adsorbed Cancanavalin A on Germanium Surface at Various pH", published in *Biotechnology Progress* 24 (2008), 972-980. It is an extension of the previous work (*Chapter 6)* with the use of more hydrophilic substrate germanium. The effect of pH history on the adsorption of Con A is investigated in pH cycles, starting at pH 4.8, followed by pH 7.4 and then returning to pH 4.8. It was found that adsorption was pH-dependent and irreversible to pH changes. The adsorption process is not solely electrostatically controlled. Protein-protein interaction by hydrogen bonding or hydrophobic interaction may dominate the adsorption process. The hydration of absorbed Con A layer at different pH was also evaluated. The washing experiments with water and various electrolyte solutions confirmed physisorption of Con A on germanium surface. The experimental methodology with the use of IR spectral simulation was proven to provide insights into the structure, composition and hydration level of the produced protein coatings.

Chapter 8 presents the overall discussion and conclusions of the study and recommendations for future work.

My role in these scientific papers is to design and perform the experiments, analyze the results, write the initial manuscripts and input the revision and correction from co-authors.

References

1 Ruckenstein, E.; Li, Z. F., *Adv. Colloid Interface Sci.* 2005, 113, 43-63.

2 Mrksich, M.; Whitesides, G. M. *Annu. Rev. Bioph. Biom.* 1996, 25, 55-78.

3 Ulman, A. *Chem. Rev.* 1996, 96, 1533-1554.

4 Bain, C. D.; Whitesides, G. M. *J. Am. Chem. Soc.* 1989, 111, 7164-7175.

5 Sagiv, J. *J Am Chem Soc* 1980, 102, 92-98.

6 Kresge, C. T.; Leonowicz, M. E.; Roth, W. J.; Vartuli, J. C.; Beck, J. S. *Nature* 1992, 359, 710-712.

7 Beck, J. S.; Vartuli, J. C.; Roth, W. J.; Leonowicz, M. E.; Kresge, C. T.; Schmitt, K. D.; Chu, C. T.-W.; Olson, D. H.; Sheppard, E. W.; McCullen, S. B.; Higgins, J. B.; Schlenker, J. L. *J. Am. Chem. Soc.* 1992, 114, 10834-10843.

8 Kresge, C. T.; Leonowicz, M. E.; Roth, W. J.; Vartuli, J. C. *U. S. Patent* 1992, 5,098,684.

9 Jeannette Scott. (Ed.) Zeolite technology and applications: recent advances, Park Ridge, N.J.: Noyes Data Corp., 1980.

10 Mohan, D.; Singh, K. P. *Water Res.* 2002, 36 (9), 2304-2318.

11 Auerbach, S. M.; Carrado, K. A.; Dutta, P. K. (Ed.) Handbook of Zeolite Science and Technology, New York: M. Dekker, c2003.

12 Ouki, S. K.; Cheeseman, C. R.; Perry, R. *J. Chem. Tech. Biotechnol* 1994, 59, 121-126.

13 Mohan, D.; Pittman, C. U. *J. Hazard. Mater.* 2007, 142(1-2), 1-53.

14 Ouki, S. K.; Kavannagh, M. *Water Sci. Tech.* 1999, 39 (10-11), 115-122.

15 Ouki, S. K.; Kavannagh, M. *Waste Manage. Res.* 1997, 15 (4): 383-394.

16 Curkovic, L.; CerjanStefanovic, S; Filipan, T. *Water Res.* 1997, 31 (6): 1379-1382.

17 Oter, O.; Akcay, H. *Water Environ. Res.* 2007, 79 (3): 329-335.

18 Berber-Mendoza, M. S.; Leyva-Ramos, R.; Alonso-Davila, P.; Mendoza-Barron, J. ; Diaz-Flores, P. E. *J. Chem. Technol. Biot.* 2006, 81 (6): 966-973.

19 Maxwell, I. E. *Adv. Catal.* 1982, 31, 1-76.

20 Yamashita, H.; Miura, Y.; Mori, K.; Shironita, S. ; Masui, Y. ; Mimura, N. ; Ohmichi, T. ; Sakata, T. ; Mori, H. *Pure Appl. Chem* 2007, 79(11), 2095-2100.

21 Sachtler, W. M. H.; Zhang, Z. C. *Adv. Catal.* 1993, 39, 129-220.

22 Matsuoka, M.; Iino, K.; Chen, H.; Anpo, M. *Res. Chem. Intermed* 2005, 31(1-3), 153-165.

23 Anpo, M.; Takeuchi, M.; Ikeue, K.; Dohshi, S. *Curr. Opin. Solid State Mater. Sci.* 2002, 6, 381-388.

24 Anpo, M.; Higashimoto, S.; Matsuoka, M.; Zhanpeisov, N. U.; Shioya, Y.; Dzwigaj, S.; Che, M. *Catal. Today* 2003, 78, 211-217.

25 Lai, Z. P.; Bonilla, G.; Diaz, I.; Nery, J. G.; Sujaoti, K.; Amat, M. A.; Kokkoli, E.; Terasaki, O.; Thompson, R. W.; Tsapatsis, M.; Vlachos, D. G. *Science* 2003, 300, 456-460.

26 Kusakabe, K.; Kuroda, T.; Murata, A.; Murata, A.; Morooka, S. *Ind. Eng. Chem. Res.* 1997, 36(3), 649-655.

27 Kusakabe, K; Kuroda, T.; Morooka, S. *J. Membrane Sc.* 1998, 148 (1): 13-23.

28 Jia, M. D. ; Chen, B. S. ; Noble, R. D. ; Falconer, J. L. *J. Membrane Sc.* 90 (1-2): 1-10, 1994.

29 Willians, R. A. (Ed.), (1992) Colloid and Surface Engineering: Application.c in the Process Industries, Butterworth Heinemann, Oxford, UK. Chapter 8.

Chapter 2 Synthesis, Characterization and Application of Magnetic Nanocomposites for the Removal of Heavy Metals from Industrial Effluents

Zhenghe Xu and Jie Dong, Chapter 6, pp. 105-148, in the book of *Emerging Environmental Technologies*, Springer Publications 2008

2.1 Background

The problem of disposing industrial wastes is as old as industry itself. Industrial wastes often cause serious water, air and soil pollution. Heavy metals are frequently found from chemical manufacturing, petroleum, fossil fuel combustion, painting and coating, mining, extractive metallurgy, nuclear and many other industries [1, 2]. The heavy metals most often implicated in accidental human poisoning are lead, mercury, arsenic and cadmium. Some heavy metals, such as zinc, copper, chromium, iron and manganese, are required by the body in trace amounts, but these same elements can be toxic to humans at higher concentrations. In addition to impairing fetuses development, poisoning of heavy metals generally can cause the damage of kidneys, brain, blood, liver, central nervous, digestive and skin systems. These toxicities have been well established in the scientific literature. Heavy metals can enter ground water and aquifers by direct industrial and consumer waste disposal or release from soils, and other industry solid wastes as a result of acid rain leaching.

The regulated levels of various heavy metal ions in drinking water are extremely low. For example, the world heath organization has set a maximum guideline concentration of 0.01 mg/L for As in drinking water [3] and the U.S. Environmental Protection Agency (EPA) has set a maximum limit of 0.005 mg/L for lead, 0.65 mg/L for copper and 0.002 mg/L for mercury in drinking water [4, 5]. It is a big challenge to remove these metal ions to such a low level from large volume, low concentration effluents in a cost effective manner. Discharge of metal ions to the environment not only causes serious health concerns but also is a waste of dwindling and valuable resources. Moreover, financial benefit could be gained by recovering these metals while detoxifying the water for recycling or soft disposal. Recovery of metals from effluent streams is thus in line with the principles of sustainable development.

Growing concerns about the environmental pollution, economic impact and the potential threat that these heavy metals pose to human being stimulated increasingly stringent control on the discharge of industrial wastes. Considerable efforts have been devoted to developing fundamental understandings and viable technologies to reduce environmental consequences of industrial wastes, aiming at cost effective and sustainable removal or selective recovery of heavy metals from industrial effluents [6, 7, 8, 9].

2.2 Existing Technology for Heavy Metal Removal

A number of approaches have been developed or suggested for the treatment of industrial effluents in order to meet mandatory discharge standards. The most commonly used techniques are precipitation, adsorption, ion exchange, reverse osmosis and ion flotation. A brief overview of these existing technologies is given below.

2.2.1 Precipitation

Precipitation is a well known process capable of removing heavy metals from aqueous solution [10]. For example, by the addition of sodium hydroxide or lime the solution pH is raised to a regime exceeding the solubility of metal hydroxides, causing the precipitation of metal hydroxides and lowering the concentration of metal ions in solution. This method is effective for the removal of large quantities of metals from contaminated water and is extensively used in industry because of its simplicity. The problems associated with precipitation process are slow solid-liquid separation, low density of solids and the ultimate disposal of the voluminous sludge which often contains a high content of water. The inappropriate disposal of unstable precipitates may cause secondary contamination of water because metal ions can be leached out from the sludge, returning to the aqueous environment. In addition, a polishing step is required for most precipitation processes in order to achieve low residual levels of metal ions in the processed water. Furthermore, precipitation is a costly method without the offset of producing secondary resources. There are only a few metals that can precipitate to form a valuable solid product, such as gypsum for the construction industry.

2.2.2 Adsorption

Adsorption process is based on the adsorption of soluble contaminants in solution onto a solid adsorbent. The widely used material of adsorption is activated carbon though sandstone, fly ash, clay and other surface reactive adsorbents are often used in waste water treatment. This method is capable of removing most toxic species, including Cu^{2+}, Cr^{4+}, Pb^{2+}, Hg^{2+} and Zn^{2+}. Since most adsorption processes are preformed in a column packed with adsorbents, a prefiltration step is needed for most industrial applications in order to remove finely-divided solids which may, otherwise, clog the channels available for transporting liquid. Regeneration of the adsorbent and the cost for carbon replacement are issues to be concerned with. In addition, the surface functionalization by solvent deposition and covalent attachment on ceramic supports as commonly used failed to demonstrate high ligand coverage and stability of the attached functional groups. These drawbacks can be overcome by applying the sol-gel processing method to form a silica network with functional ligands [11].

2.2.3 Ion exchange

The ion-exchange process relies on the exchange of certain undesirable cations or anions in wastewater with sodium, hydrogen, chloride, etc. in porous polymer resins of either a styrene or an acrylic matrix. The ion exchange process continues until the solution being treated exhausts the resin exchange capacity. The exhausted resin must be regenerated by other chemicals which replace the ions captured in the ion exchange operation, thus converting the resin back to its original composition for reuse in the next cycle. Many chelating resins have been reported but they do not show physical rigidity due to swelling of the polymeric skeleton, poor wettability, small surface area, poor selectivity, slow adsorption rate and challenge in regeneration [12, 13]. Clogging and regeneration of resins, similar to that encountered in the adsorption process by activated carbon, may also be experienced in this approach. In practice, wastewater to be treated by ion exchange is generally pre-filtered to remove suspended solids which could mechanically clog the resin bed.

2.2.4 Reverse osmosis

In industry, reverse osmosis removes minerals from boiler water at power plants. The water is boiled and condensed over and over again and must be as pure as possible to avoid fouling or corrosion of boilers. It is also used to clean effluent and brackish groundwater. The apparent limitations of this approach are concerns with membrane lifetime, loss in flux rate, relatively small amount of effluent that can be treated and limited types of materials that can be removed. Some solutions (strong oxidizing agents, solvents and other organic compounds) can cause dissolution of the membrane materials. Fouling of membranes by suspended solids in wastewater is another concern. Pre-treatment of effluents is thus necessary for reverse osmosis system.

2.2.5 Ion flotation

Ion flotation involves the removal of surface-inactive ions from aqueous solutions by the addition of surfactants capable of forming ion-surfactant pairs, and the subsequent passage of gas bubbles through the solutions. Due to the surface active nature of the surfactant, the ion-surfactant pairs are concentrated at the air/water interface of bubbles which float to the surface of the solution where they are removed as foams. In general, an ionic surfactant (known as collector in mineral processing) of opposite charge to the surface-inactive contaminants is used to induce an electrostatic force between them, thus forming ion-collector pairs. However, it is possible to use a non-ionic surfactant capable of forming coordination bonds with contaminants as a collector [14]. Ion flotation has been widely applied in base metal recovery, waste water treatment, removal of radioactive elements from water and the recovery of precious metals [15, 16]. The major advantage of ion flotation over activated carbon adsorption is that air bubbles are relatively inexpensive to produce and no desorption step is required. However, a stoichimometric ratio of surfactant molecules to ions to be removed is needed in ion flotation. Therefore, the process can be quite expensive and may only be used to float ions in solutions of low concentration.

In summary, each technique reviewed has its own limitations in industrial applications although they have been practiced to a varying degree. Low selectivity, complex to operate, high capital and energy costs and slow separation kinetics are the commonly inherent shortcomings. In addition, it is also inefficient in treating waste streams that contain low concentrations of contaminants and may fail when handling wastes of complex chemistry. Because the active materials are difficult to regenerate, these processes generate significant amounts of secondary waste.

2.3 Magnetic Composite Sorbents (MCS)

Magnetic composite sorbents (MCS) refers to the tailoring of physical, chemical and surface properties of magnetic composites to enable selective or non-selective attachment to the composites of ions, molecules, macromolecules, cells, colloidal particles or liquid phases from complex fluid systems [17]. In essence MCS is an interdisciplinary subject since it requires an integrated approach involving the manufacture and surface hybridization of appropriate composites with careful attention to the constraints imposed by end users. The properties of the composite particles are of critical importance to the successful application of the technology. The composite particles must fulfill a number of criteria relating to their shape, size, porosity, mechanical strength, chemical inertness, density, magnetic properties, wettability, surface charge, surface concentration of reactive groups, cost, ease of manufacture, sterilizability, aggregation properties and regeneration [17].

Some application examples of this technology are the use of magnetite particles to accelerate the coagulation of sewages [18], removal of radio nuclides from milk by functionalized polymers such as resin with embedded magnetite [19], the adsorption of organic dyes by poly(oxy-2,6-dimethyl-1,4-phenylene) [20], removal of an azo-dye, acid red B (ARB) from water by MnO-Fe_2O_3 composites as adsorbent-catalyst materials [21], oil spill remediation by polymer coated magnetic particles [22] and removal of heavy toxic metals and purification of the hazardous waste water by magnetic filtration/sorption technology [23, 24, 25]. In addition, magnetic nanoparticles with appropriate surface coatings have found various biomedical applications, as contrast agents in MRI (magnetic resonance imaging), colloidal mediators for cancer magnetic hyperthermia and active constituents of drug-delivery platforms, as well as for tissue repair, cell and tissue targeting and transfection [26, 27, 28, 29].

For selective recovery or removal of heavy metals from voluminous industrial effluents with suspended solids, the use of magnetic composite sorbents is of particular importance, as the technique combines the advantages of technical feasibility and flexibility with economic value and environmental acceptability. A schematic illustration of magnetic composite sorbents is shown in Figure 2.1 [30]. In this figure, magnetic composite particles are added to a hydrometallurgical processing suspension that contains precious metal ions and many other waste solid particulates. The precious metal ions selectively adsorb on the added magnetic composite particles through molecular recognition by surface functional groups. Along with the magnetic particles, the adsorbed metal ions are separated from the suspension by an external magnetic field. The metal ions loaded on the isolated magnetic particles can be stripped off by, for example, acid washing, and the particles can then be reused. Precious metals can, on the other hand, be produced from the concentrated ion solution by precipitation, crystallization, and/or electrowinning.

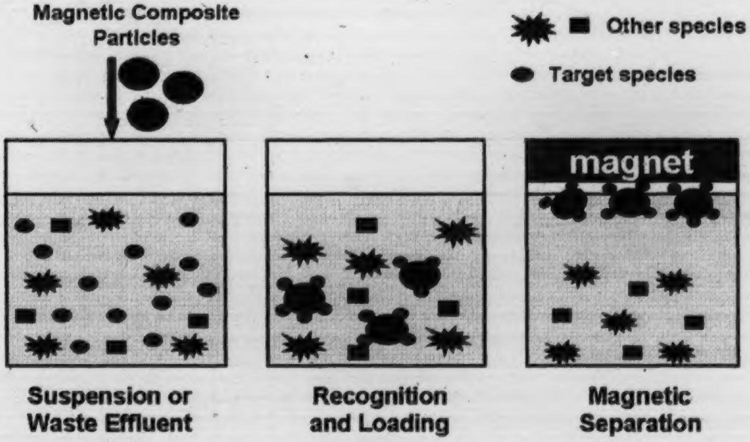

Figure 2.1 Illustration of magnetic separation technology in metal ions recovery from an industrial effluent. [29]

The methods used to prepare the magnetic particles can be divided into two general types [31]. The first method involves the coating of an existing magnetic material. Representative examples of this type are adsorption of proteins onto nickel microspheres [32], coupling of functionalized polymeric silane on magnetite [33, 34], adsorption of serum albumin onto aggregates of magnetite or other magnetic metal oxides during or immediately after ultrasonic disruption of the aggregates [35, 36], polymerization of monomers in the presence of magnetite [37, 38], encapsulation of iron oxide by emulsion polymerization [39, 40] and adsorption of Protein A to magnetite [41]. The second method involves the generation of the magnetic material in the presence of the coating material. Representative examples are precipitation of magnetite in the presence of dextran [42], serum albumin [43] and arabinogalactan [44]. A related method is the precipitation of magnetite in the pores or on the surface of an existing particle as magnetic tags [45].

In magnetic composite synthesis, magnetite is the most commonly used magnetic material since particles prepared from freshly precipitated magnetite are claimed to be superparamagnetic [46], a property which facilitates re-suspension of the particles after magnetic separation. Other magnetic materials, such as γ-Fe_2O_3, metallic iron, cobalt and nickel, are also used. In a recent review [47], Li et al. elaborated the synthesis, properties and environmental applications of nanoscale iron-based materials. Different physical and chemical methods used for synthesizing nano-iron based particles with desired size, structure and surface properties were reported. The applications of this kind of particles include degradation of chlorinated organic compounds (such as trichloroethane (TCA), trichloroethene (TCE), tetrachloroethene, or carbon tetrachloride), removal of metallic ions (such as arsenic (As), lead (Pb), mercury (Hg) and chromium (Cr)) and inorganic contaminants (such as selenium (Se), denitrification and reduction of carbon monoxide (CO)). A key mechanism of these applications is the oxidative nature of iron.

Lu et. al. [48], on the other hand, provided a detailed report on the special features, synthesis, protection/stabilization, functionalization and application of magnetic nanoparticles. Substantial progress in the size and shape control of magnetic nanoparticles has been made by developing methods such as co-precipitation, thermal decomposition and/or reduction, and molecular template or hydrothermal synthesis. Protection of magnetic particles against corrosion remains a major challenge. Therefore suitable protection strategies, for example, surfactant/polymer coating, silica coating and carbon coating of magnetic nanoparticles or embedment of nano magnetic particles in a matrix/support have been emphasized. Properly protected magnetic nanoparticles can be used as building blocks for the fabrication of various functional systems, and applied to catalysis and biotechnology.

It is evident that the application of magnetic nanocomposite particles to separation science and technology offers great flexibility. A key-and-lock relationship shown in Figure 2.2 [49] can be developed to describe various applications of magnetic nanocomposites. The lock varies from metals or toxic species as in environmental applications, to antigen or streptavidin as in biological applications, while the key could be a specific ligand, antibody or biotin. The approaches on the preparation of magnetic nanocomposites particles, such as molecular self-assembly, direct silanation, two-step silica coating and mesoporous silica coating, and their practical applications as sorbent for industry effluent management will be reviewed in Appendix B.

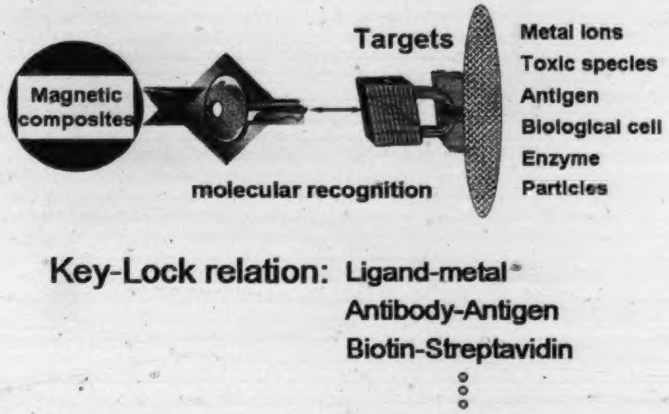
Targets
Magnetic composites
molecular recognition
Metal Ions
Toxic species
Antigen
Biological cell
Enzyme
Particles
Key-Lock relation:
Ligand-metal
Antibody-Antigen
Biotin-Streptavidin

Figure 2.2 Key-lock relation in potential applications of magnetic composites particles. [48]

References

[1] Alloway, B.J. (Ed.) (1995) Heavy Metals in Soils. Chapman and Hall, Glasgow, UK. Chapters 6, 8, 9 and 11.

[2] McDonald, D. G.; Grandt, A. F. (1981) Limestone- Lime Treatment of Acid Mine Drainage-Full Scale. *EPA Project Summary*. EPA-600/S7-81-033.

[3] Yamamura, S. (2000) Drinking Water Guidelines and Standards, World Health Organization, Geneva, Switzerland, http://www.who.int/water_sanitation_health/dwq/arsenicun5.pdf

[4] Maximum Contaminant Level Goals and National Primary Drinking Water Regulation for Lead and Copper; Proposed Rule (1996), http://www.epa.gov/EPA-WATER/1996/April/Day-12/pr-20958DIR/pr-20958.txt.html

[5] National Primary Drinking Water Regulations: Public Notification Rule (2000), http://www.epa.gov/EPA-WATER/2000/May/Day-04/w9534.htm

[6] Nuñez, L.; Kaminski, M. D. (1998) *Chem. Technol.* 9, 41.

[7] Xu, Z.; Liu, Q.; Finch, J. A. (1997) *Appl. Surf. Sci.* 120, 269.

[8] Shiraishi, Y.; Nishimura, G.; Hirai, T.; Komasawa, I. (2002) *Ind. Eng. Chem. Res.* 41, 5065.

[9] Lee, B.; Kim, Y.; Lee, H.; Yi, J. (2001) *Microporous Mesoporous Mater.* 50, 77.

[10] Stumm, W.; Morgan, J. J. (1995) Aquatic Chemistry, Jon Wiley & Sons, Inc., New York, 804.

[11] Lee, J. S.; Gomes-Salazar, S.; Tavlarides, L. L. (2001) *React. Funct. Polym.* 49, 159.

[12] Yu, M.; Tian, W.; Sun, D.; Shen, W.; Wang, G.; Xu, N. (2001) *Anal. Chim. Acta.* 428, 209.

[13] Nam, K. H.; Tavlarides, L. L. (2003) *Solvent Extr. Ion Exc.*, 21, 899.

[14] Pinfold, T. A. (1972) Ion Flotation, in Robert Lemlich (Ed.), Adsorptive Bubble Separation Techniques, Academic Press, New York.

[15] Nicol, S. K.; Galvin, K. P. and Engel, M. D. (1992) *Miner. Eng.* 5, 1259.

[16] Berg, E. W.; Downey, D. M. (1980) *Anal. Chim. Acta* 120, 273.

[17] R. A. Willians (Ed.), (1992) Colloid and Surface Engineering: Application.c in the Process Industries, Butterworth Heinemann, Oxford, UK. Chapter 8.

[18] Booker, N. A.; Keir, D.; Priestley, A.; Rithchie, C. D.; Sudarmana, D. L.; Woods, M. A. (1991) *Water Sci. Technol.* 123, 1703.

[19] Sing, K. S. (1994) *Technol. Profile* 21, 60.

[20] Safarik, I.; Safarikova, M.; Buricova, V. (1995) *Collect. Czech. Chem. Commun.* 60, 1448.

[21] Wu, R.; Qu, J.; Chen, Y. (2005) *Water Res.* 39, 630.

[22] Orbell, J. D.; Godhino, L.; Bigger, S. W.; Nguyen, T. M.; Ngeh, L. N. (1997) *J. Chem. Edu.* 74, 1446.

[23] Borai, E. H.; El-Sofany, E. A.; Morocos, T. N. (2007) *Adsorption* 13, 95.

[24]Feng, D.; Aldrich, C.; Tan, H. (2000) Hydrometallurgy, 56, 359.

[25] Denizli, A.; Özkan, G.; Arica, M. Y. (2000) *J. Appl. Polym. Sci.* 78, 81.

[26] Duguet, E; Vasseur, S; Mornet, S; Devoisselle, J. M. (2006) *Nanomedicine*, 1, 257.

[27] Gupta, A. K.; Naregalkar, R. R.; Vaidya, V. D.; Gupta, M. (2007) *Nanomedicin*, 2, 23.

[28] Gao, X.; Yu, K. M. K.; Tam, K. Y.; Tsang, S. C. (2003) Chem. Commun. 24, 2998.

[29] Rudge, S. R.; Kurtz, T. L.; Vessely, C. R.; Catterall, L. G.; Williamson, D. L. (2000) *Biomaterials* 21, 1411.

[30] Wu, P.; Xu, Z. (2005) *Ind. Eng. Chem. Res.* 44, 816.

[31] Skold, C. N. (2007) U.S. Patent 7,169,618.

[32] Giaever, I. (1976) U.S. Patent 3,970,518.

[33] Whitehead, R. A. ; Chagnon, M. S.; Groman, E. V.; Josephson, L. (1985) U.S. Patent 4,554,088.

[34] Phanapavudhikul, P.; Waters, J. A.; Perez de Oritiz, E. S. (2003) *J. Environ. Sci. Heal A* 38, 2277.

[35] Liberti, P. A.; Piccoli, S. P. (1996) U.S. Patent 5,512,332.

[36] Liberti, P. A.; Pino, M. A. (1997) U.S. Patent 5,597,531

[37] Yen, S.-P. S.; Rembaum, A.; Molday, R. S. (1979) U.S. Patent 4,157,323.

[38] Daniel, J.-C.; Schuppiser, J.-L.; Tricot, M. (1982) U.S. Patent 4,358,388.

[39] Liu, X.; Guan, Y.; Ma, Z.; Liu, H. (2004) *Langmuir* 20, 10278-10282.

[40] Pich, A.; Bhattacharya, S.; Ghosh, A.; Adler, H.-J.P. (2005) *Polymer* 46, 4596.

[41] Senyei, A. E.; Widder, K. J. (1980) U.S. Patent 4,230,685.

[42] Molday, R. S. (1984) U.S. Patent 4,452,773.

[43] Owen, C. S.; Silvia, J. C.; D'Angelo, L.; Liberti, P. A. (1989) U.S. Patent. 4,795,698.

[44] Palmacci, S.; Josephson, L. (1993) U.S. Patent 5,262,176.

[45] Ugelstad, J.; Ellingsen, T.; Berge, A.; Helgee, O. B. (1987) U.S. Patent 4,654,267.

[46] Groman, E. V.; Josephson, L.; Lewis, J. M. (1989) U.S. Patent 4,827,945.

[47] Li, L.; Fan, M.; Brown, R. C.; Leeuwen, J. V.; Wang, J.; Wang, W.; Song, Y.;Zhang, P. (2006) *Crit. Rev. Env. Sci. Tec.* 36, 405.

[48] Lu, A. H.; Salabas, E. L.; Schuth, F. (2007) *Angew. Chem. Int. Edit.* 46, 1222.

[49] Liu, Q. (1996) An innovative approach in magnetic carrier technology, PhD. Thesis, McGill University, Montreal.

Chapter 3 Engineering and Characterization of Mesoporous Silica-Coated Magnetic Particles for Mercury Removal from Industrial Effluents

Jie Dong, Zhenghe Xu and Feng Wang, *Appl. Surf. Sci.* 254 (2008) 3522-3530

3.1 Introduction

Industrial wastes often cause serious water, air, and soil pollution. Heavy metals are frequently found in wastewaters originating from chemical manufacturing, painting and coating, mining, extractive metallurgy, nuclear, and other industries. Growing concerns about the environmental pollution, economic impact and the dangers that these heavy metals pose to human being have stimulated increasingly stringent control of industrial effluent discharge. Considerable efforts have been devoted to developing fundamental understanding and viable technologies to reduce environmental consequences of industrial wastes, aiming at cost effective and sustainable removal or selective recovery of heavy metals from industrial effluents [1].

Mercury is generally considered to be one of the most toxic metals in the wastewaters. Wastewaters constitute a large volume but contain relatively low concentration of mercury. The removal of Hg ions from aqueous solutions depends on the nature of the water and the concentration of mercury. A number of approaches, such as reduction, precipitation, ion exchange, reverse osmosis, adsorption and coagulation, have been suggested for the removal of mercury from industry effluents. Among these methods, selective adsorption deserves particular attention, because the sorbent materials can be made highly efficient and easy to handle, and in some cases they can be regenerated. Activated carbons are found to be very effective for the removal of mercury [2, 3, 4, 5]. However, despite its effectiveness, activated carbon is quite expensive. The recovery of the spent sorbents for regeneration or safe discharge is relative complex and costly if it is not impossible [6].

Mesoporous materials with regular geometries have been attracting worldwide interest due to their potential applications in adsorption, separation, catalysis, biological sensing, medical usage, molecular engineering, and nanotechnology [7, 8, 9, 10, 11, 12, 13, 14, 15]. These materials have large uniform nano-pore structures, high specific surface area and specific pore volume. These unique features of the materials are quite desirable for many designated environmental cleanup applications. Utilizing the materials to remove heavy metals from aqueous wastes could be achieved by surface functionalization which endows the mesoporous silica a strong and specific affinity with targeted metal ions.

Silanation has been identified as a most promising avenue for introducing specific surface functional groups on mesoporous silica surfaces [16,17, 18, 19, 20, 21, 22]. The functionalized materials have a high adsorption capacity for mercury and other heavy metals. The nanometer-scale pore structure of open frame network provides an uninhibited access of the metal ions to every ligand site in the structure, which is the most important advantage of these types of adsorbent. However, the functionalized mesoporous silica itself has inherent limitations in industrial applications. One noticeable challenge is to separate the loaded fine particles from a complex multiphase system for safe disposal or recovery of the adsorbed metal ions and recycle of the sorbents.

Magnetic separation provides a convenient method for separation of solid particles in a multiphase suspension. With magnetic separation, spent sorbents of magnetic property can be effectively isolated from the main effluent stream for safe disposal or regeneration. Several prior studies have been carried out to fabricate a novel sorbent material, which combines the advantages of mesoporous silica and magnetic separation [23, 24]. Among these investigations, the coating of tiny inexpensive magnetic particles with functional ligands to fabricate inorganic and organic hybrid particles [25, 26, 27, 28] is now considered to be the most versatile and the easiest to be adopted. The sorbents prepared by this method can provide sufficient magnetization by choosing the proper size of core magnetic particles for the subsequent magnetic separation.

However, the synthesized mesoporous magnetic particles on prior studies show several application limitations. Depending on preparation methods of magnetic sorbents, either the strength of magnetization of the mesoporous composite became too weak, or the sorbent was not properly protected for applications in harsh working environments, such as strong acidic effluents. In terms of film thickness, film uniformity, specific surface areas, pore volume and pore size, the quality of the synthesized silica coatings on magnetic particles is extremely sensitive to synthesis conditions, such as reaction time, synthesis temperature, reactant concentration, type and amount of catalyst, quality of solvent, etc. Up to date, there is no clear quantification as to how these conditions affect the quality of the synthesized mesoporous silica films.

In this chapter, it is aimed at understanding the fundamentals of synthesis processes. The modern analytical techniques such as atomic force miscroscopy (AFM), transmission electron microscopy (TEM), electron energy loss spectroscopy (EELS) and X-ray photoelectron spectroscopy (XPS), coupled with the classical electrokinetic measurement, are used to provide direct information on the formation and properties of the resultant products in various synthesis stages. The mercury loading capacity on the functionalized mesoporous magnetic nanocomposites is determined by atomic absorption spectroscopy (AAS).

3.2 Experimental

3.2.1 Materials

Magnetite particles of <5 μm sizes (98% Fe_3O_4) from Aldrich Canada were used as received. Sodium silicate ($Na_2SiO_3 \cdot 5H_2O$), cetyl-trimethyl-ammonium chloride (CTAC, 25 wt% in water), tetraethyl orthosilicate (TEOS, 98%) and mercapto-propyl-trimethoxy-silane (MPTS, 95%) from Aldrich were used in dense liquid silica coating, molecular templating, sol-gel reaction and functionalization, respectively. Ammonium hydroxide (29.4 wt%) purchased from Fisher Scientific was used as catalyst. Absolute ethanol, Millipore de-ionized water (Millipore, Canada) and HPLC grade toluene (>99%, Aldrich) were used whenever needed. A mercury atomic absorption standard solution (1000 ppm Hg in 10% HNO_3) from Fisher Scientific was diluted to different concentrations as needed for mercury adsorption tests.

3.2.2 Synthesis Procedures

A typical procedure [29, 30, 31] for the preparation of mesoporous magnetic sorbents is summarized in Figure 3.1. Adopted in this study were the optimal synthesis conditions for the sol-gel reaction, identified in a previous factorial design study (see *Appendix C*) [31]. After the generation of mesoporous silica on magnetite core, procedures for functionalization were modified from previous experiment. To optimize the silanation reaction, 2 g of the particles were hydrolyzed by steaming for 3 h. The objective of steam pre-treatment of the silica-coated particles is to increase hydroxyl group density on mesoporous silica surfaces and hence improve silane coupling reactions with MPTS. After steam-treatment, the particles were dried in a vacuum oven at room temperature for 3 h to remove free water. The dried sample was dispersed well in 300 mL of toluene by vigorous stirring under a nitrogen atmosphere. After addition of 4 mL MPTS, the reaction was allowed to proceed at room temperature for 24 h. The resulting product was separated by a hand magnet, washed with toluene and dried overnight under vacuum at room temperature. The functionalization of particles with this scheme led to a higher Hg loading capacity than that using previous procedure [31].

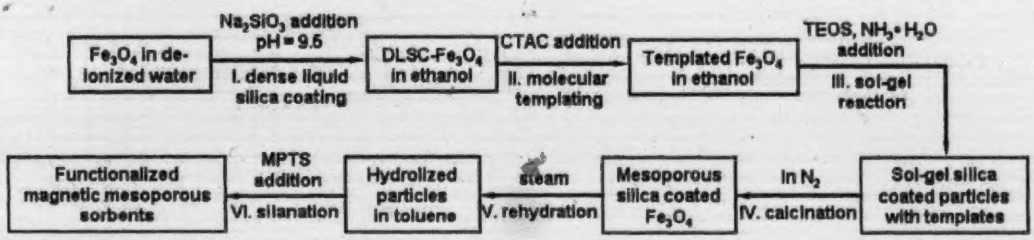
Fe_3O_4 in de-ionized water
Na_2SiO_3 addition pH = 9.5
I. dense liquid silica coating
DLSC-Fe_3O_4 in ethanol
CTAC addition
II. molecular templating
Templated Fe_3O_4 in ethanol
TEOS, $NH_3 \cdot H_2O$ addition
III. sol-gel reaction
Sol-gel silica coated particles with templates
In N_2
IV. calcination
Mesoporous silica coated Fe_3O_4
steam
V. rehydration
Hydrolized particles in toluene
MPTS addition
VI. silanation
Functionalized magnetic mesoporous sorbents

Figure 3.1 The flow chart of experimental procedure. I. dense liquid silica coating (DLSC); II. molecular templating; III. sol-gel reaction; IV. calcination; V. rehydration; VI. silanation.

Figure 3.2 shows a schematic diagram of the composite particles. The dense liquid silica (DLS) coating forms a dense layer of SiO_2 on magnetite, which protects the magnetite core from being leached in excessive acidic industrial effluents. The negatively charged silica surface also facilitates the assembly of cationic surfactant micelles on the surface, allowing effective molecular templating. During sol-gel reaction, the positive nature of molecular templates promotes the formation of silica precipitates within the voids among the templates, resulting in a three dimensional continuous silica network. After calcination, the templates are removed from the structure, leading to the formation of magnetic mesoporous nanocomposite particles.

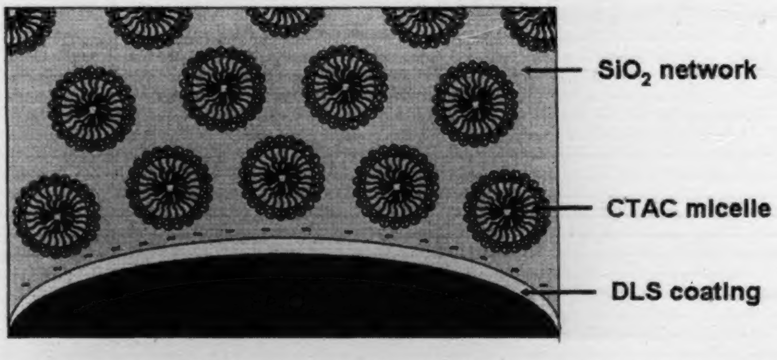

Figure 3.2 Schematic diagram of a sol-gel silica coated DLSC-magnetite particle with templates.

3.2.3 Characterization

Atomic force microscopy (AFM): Imaging of templates and surface force measurement in ethanol and surfactant-in-ethanol solutions were carried out with a Nanoscope® E AFM (Digital Instrument, Santa Barbara, CA). It consists of a piezoelectric translation stage, a cantilever substrate, a laser beam system, a split photodiode and a fluid cell. Cleaned hydrophilic silica wafer was used as the substrate to mimic dense liquid silica-coated magnetite surfaces used in the synthesis of magnetic mesoporous nanocomposite particles. *In situ* imaging and force measurement was performed in CTAC micelle ethanol solutions. The micelle ethanol solutions were injected into the fluid cell slowly and the system was allowed to incubate for 1 h before measurements.

Zeta potential measurement: Zeta potential distribution measurement was carried out using a Zetaphoremeter III (SEPHY/CAD). The detailed experimental procedures and principles of the instrument have been described elsewhere [32]. In these tests, particles collected at different synthesis stages were washed by DI water and then placed in 1 mM KCl aqueous solutions. The prepared suspension was dispersed by ultrasonic bath for about 15 min prior to each measurement.

Transmission electron microscope (TEM): The particles were dispersed in acetone by sonication and then transferred to a thin carbon film supported on TEM copper grids. The morphology of the synthesized mesoporous magnetic nanocomposite particles was examined by a JEOL 2010 TEM equipped with a Gatan 666 parallel-EELS spectrometer.

TEM images were obtained using the bright-field imaging mode at 200 kV acceleration voltage. The low-loss electron energy loss spectra were collected in TEM diffraction mode (image-coupled spectrometer) with a collection semi-angle of 1.5 mrad and energy dispersion of 0.2 eV/channel. The thickness of the silica layer was estimated from the spectra of low-loss EELS [33].

X-ray photoelectron spectroscopy (XPS): XPS spectra were obtained on a Physical Electronics PHI 5400 X-ray photoelectron spectrometer (Perkin-Elmer) with a Mg Kα anode as x-ray source (15 kV, 400 W) at a takeoff angle of 45°. The source X-ray was not filtered, and the instrument was calibrated against the C1s band at 285 eV. The spectra were recorded at a constant pass energy of 35.75 eV. The spectra were taken under a background pressure of ca. 1×10^{-9} Torr.

Other techniques were also used to characterize the products, providing complementary information, such as the removal of surfactant templates by thermal gravimetric analysis (TGA); the specific surface areas by AutoChem II 2920 analyzer, and magnetization by Quantum Design 9T-PPMS dc magnetometer (San Diego, CA, USA).

3.2.4 Mercury Removal from Aqueous Solutions

Mercury atomic absorption standard solution (1000 ppm Hg in 10% HNO_3) was purchased from Fisher Scientific. The loading capacity of mercury on the prepared magnetic sorbents was determined by analyzing the mercury concentrations in aqueous solutions before and after contact with the sorbents. In a typical loading test, 25 mg of the sorbents was mixed with 10 mL of mercury aqueous solutions of varying initial mercury concentration from 10 to 60 ppm. The suspension was stirred and shaken on a horizontal automatic shaker for 1 h. After removing the sorbents by a hand magnet, the mercury concentration in the remaining supernatant was determined by an atomic absorption spectroscopy (AAS), VARIAN 220FS.

The amount of mercury adsorbed per gram of sorbents, Γ (in mg/g), is determined by equation below,

$$\Gamma = \frac{(C_i - C_e) \times V_s}{1000 \times m} \tag{3.1}$$

where C_i is the initial mercury ion concentration (before contact) and C_e is the equilibrium mercury ion concentration (after contact) (both in ppm), V_s is the volume of the aqueous solution (in milliliters), and m is the mass of adsorbents (in grams).

To evaluate the selectivity, the distribution coefficient (K_d in mL/g) of mercury on the surface in comparison to that in solution is defined by the following equation

$$K_d = \frac{C_i - C_e}{C_e} \times \frac{V_s}{m} \tag{3.2}$$

The distribution coefficient represents the affinity of an ion exchanger for a particular ion and is an indicator of the selectivity of the ion exchanger to the particular ion in the presence of a complex matrix of interfering ions. For a successful separation process, K_d must have a value greater than 100 mL/g.

3.3. Results and Discussion

3.3.1 Molecular Templating Studied by AFM

Figure 3.3 shows a typical probing cycle in an interaction force measurement between an AFM probing tip and a solid sample surface using AFM. At large separation (position a), interaction forces between the tip and sample surface are negligible as such that the spring cantilever remains at an undeflected state. As the sample approaches the tip (right to left from position a to position b on the force curve), the interaction force between the tip and sample surface at a certain separation causes the deflection of the spring cantilever upward or downward, depending on the nature of the force. With further approaching to each other, the force increases in magnitude until the cantilever irreversibly jumps into contact with the sample surface. From this point onward, the cantilever and sample move together (constant compliance regime above position c) until reaching its set upward limit. The sample then retracts back. If there is an adhesion force between the tip and the sample, the sample will pull the tip downward as it retracts until the restoring force of the cantilever spring exceeds the adhesion force (position d), where the cantilever jumps back to its normal position. One force probing cycle is completed.

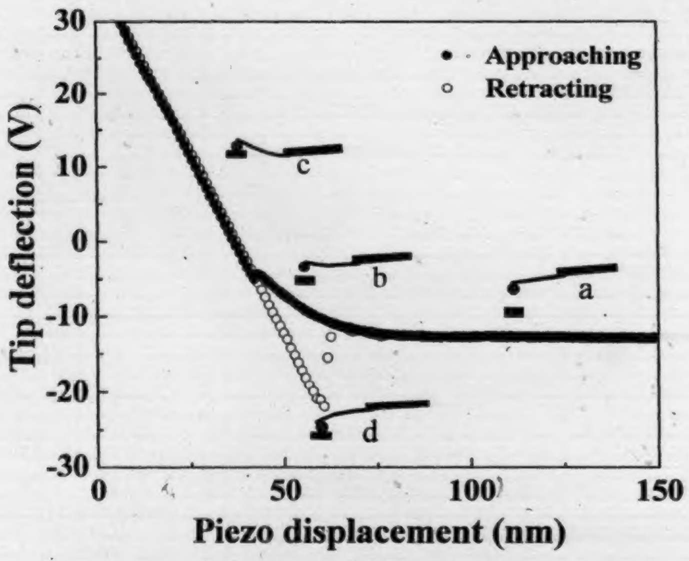

Figure 3.3 A typical probing cycle in AFM interaction force measurement.

Figure 3.4 (solid circles) shows the interaction forces between a cantilever tip and bare silica wafer in pure ethanol. There is a measurable attraction between the two at the separation distance below 10 nm. This attractive force is attributed to van der Waals forces. After replacing the ethanol by 5 mM CTAC in ethanol solution and incubation for one hour, a repulsive force between the tip and the sample during approaching is evident, starting at 20 nm as shown in Figure 3.4 by open circles. This long-range repulsion is attributed to the overlap of electric double layers around two positively charged surfaces. It appears that the cationic CTAC surfactant adsorbs on both AFM tip and silica surfaces, rending them both positively charged (as illustrated in the schematic insert of Figure 3.4). At a separation distance around 9 nm, a maximum repulsive force barrier is observed and the tip jumps inward by a distance of 5.7 nm. After this jump-in, a continuous increase in repulsive force is observed as the sample pushed upward against the AFM tip by about 4 nm. This type of force profiles over such a short separation distance suggests a surface of compressible nature, in great contrast to the case measured in pure ethanol, indicating a soft silica surface in CTAC ethanol solutions. Considering all the details in this force profile, the observed jump-in can be interpreted as the removal of a single layer of micelles from the gap between the tip and sample under the applied force of AFM tip. It is therefore reasonable to conclude that the silica surface is covered by CTAC micelles, and the size (diameter) of micelles or thickness of micelles on silica is in the range of around 5.7 nm. The size measured here is in excellent agreement with the reported value by Ducker [34].

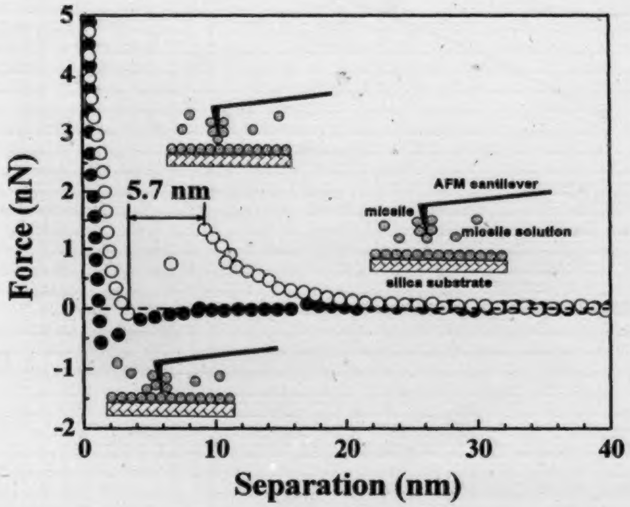

Figure 3.4 Interaction forces between a bare silica wafer and AFM tip in ethanol (solid circles) and CTAC ethanol solutions (open circles).

The AFM images of silica in ethanol and 5 mM CTAC ethanol solution are shown in Figure 3.5 a) and b), respectively. The silica wafer in ethanol exhibits a smooth, featureless topography (Figure 3.5 a). The image of silica wafer obtained in CTAC ethanol solution (Figure 3.5 b), on the contrary, shows well defined features. It is interesting to note that the size of high spots is about 6 nm, a value very close to the jump-in distance observed on the force profile. It appears that CTAC at 5 mM concentration in ethanol forms pseudo-spherical micelles. These micelles are assembled on silica surface with well-defined voids of 10-nm diameter. For better view, the magnified image of the marked area is shown on the left corner with circles to highlight the voids. By filling in these voids with desired materials and removing the micelles, one can obtain mesoporous surfaces of desired materials. Clearly these assembled micelles can serve as templates for synthesis of mesoporous silica coatings on silica coated magnetic particles.

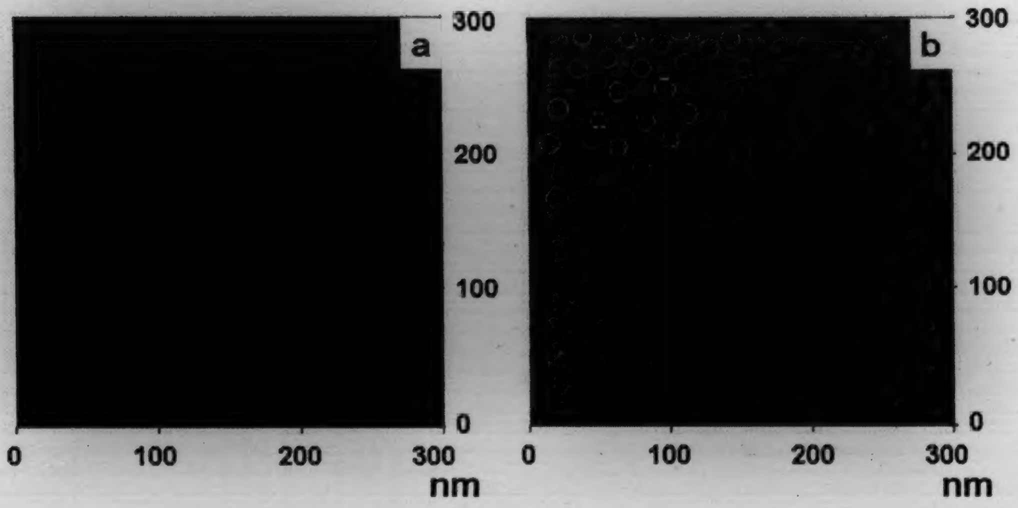

Figure 3.5 Silica wafer in ethanol a) and in 5 mM CTAC ethanol solutions b) (circles represent voids to be filled by silica using sol-gel method).

3.3.2 Monitoring the Synthesis by Zeta Potential Measurement

To confirm the role of each step in the proposed synthesis, the zeta potential distributions of bare magnetite, DLS coated magnetite, templated DLSC magnetite, sol-gel coated particles around templates, and the particles after calcination were measured over a wide pH range. The zeta potential distributions of particles collected at various stages of synthesis measured in 1 mM KCl aqueous solutions of pH 5.3 are compared in Figure 3.6. Figure 3.6a) shows that the bare magnetite at this pH is positively charged with a zeta potential distribution peaked at 18 mV. This finding is consistent with the reported iso-electric point of magnetite at pH around 7. After DLS coating, the particles become negatively charged with a zeta potential distribution peaked at -25 mV. This zeta potential value corresponds closely to the reported values of silica particles at this pH, confirming that magnetite particles are fully covered by silica films. This silica coating acts as a protective layer to avoid direct contact of the magnetite core with the liquid to be treated. The negative charge of the silica-coated surface, on the other hand, facilitates the assembly of cation surfactant micelles arisen from electrostatic attraction.

After CTAC templating, the particles become strongly positively charged with a zeta potential profile peaked at 38 mV, as shown in Figure 3.6b). Such a big shift in zeta potential value is a direct evidence of the assembly of positively charged CTAC micelles on negatively charged, DLS-coated magnetite particles. After sol-gel reaction to fill the voids observed in the AFM images (Figure 3.5b), the particles become negatively charged again, although its peak is located at -16 mV which is less negative than the values for DLS coated magnetite particles. This observation suggests that the trapped CTAC template partially balances the negative charge of silica in the templates voids. After calcination at 540 °C, the zeta potential distribution returns to about -25 mV (not shown), identical to DLS coated magnetite particles. This finding strongly suggests a complete removal of the templates by calcination, leaving behind the silica network on the magnetite surface.

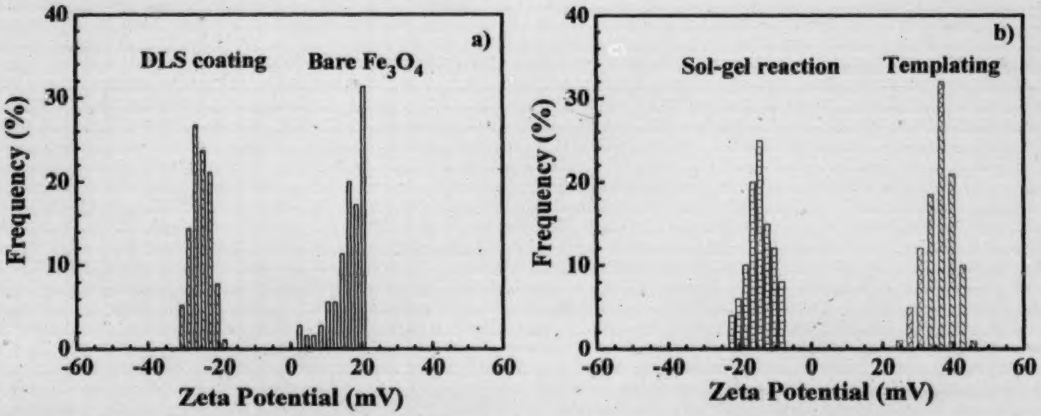

Figure 3.6 Zeta potential distributions of: a) bare magnetite (blank column) and DLS coated magnetite (slash shaded column); and b) templating on DLS coated-magnetite (cross shaded column) and sol-gel coated particles around the templates (dash shaded column).

3.3.3 Surfactant Removal

Since most metal oxides decompose at a higher temperature than organic components, a convenient method to remove organic molecules from solid surfaces is calcination. Thermal gravimetric analysis (TGA) can dynamically track the weight changes of particles. Therefore, a net weight loss in the temperature range where metal oxides remain stable can be attributed to the decomposition or evacuation of the organic substances, monitoring the departure of surfactants. To confirm the successful templating and templates removal, bare magnetite, sol-gel silica coated particles with templates and calcinated particles were analyzed using TGA in a nitrogen atmosphere. The nitrogen atmosphere is used to prevent the oxidization of magnetite during TGA analysis. The results of TGA analysis are shown in Figure 3.7. As anticipated, there is no weight loss for bare magnetite over the temperature range studied. For sol-gel silica coated particles with templates, a significant weight loss is observed at temperature between 220°C and 400°C. Since the physisorbed water has been removed during preheating of the samples at 120°C, the observed weight loss (~ 3.14%) is attributed to the removal of CTAC templates, confirming the assembly of CTAC micelles on DLS coated magnetite. These micelles remained on particle surfaces during sol-gel process, a phenomenon observed in zeta potential distribution measurement (Figure 3.6b). Above 540°C, the particle weight remains constant, indicating the completion of templates removal. It is interesting to note that the weight loss of calcinated magnetic composite particles at 540°C is negligible, suggesting that a calcination temperature of 540°C is sufficient to remove the CTAC templates in the synthesis process. This is also confirmed by the results of zeta potential distribution measurement in Figure 3.6b).

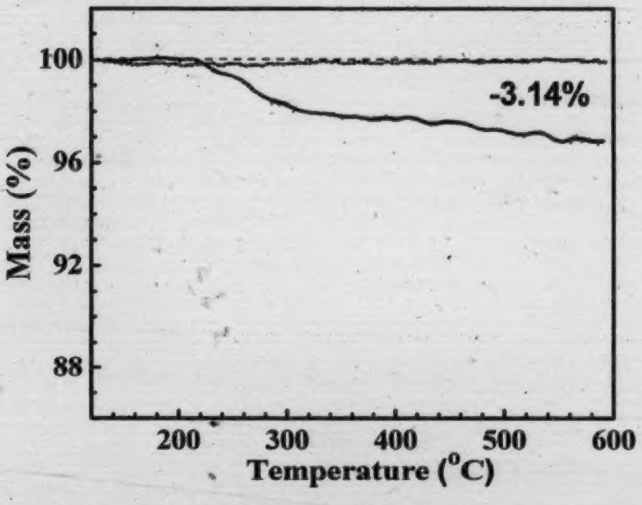

Figure 3.7 Thermal gravimetric analysis (TGA) of bare magnetite (the dotted line), sol-gel coated particles with templates (the solid line) and calcinated mesoporous magnetic particles (the dash line).

3.3.4 Characterization by Analytical TEM

A typical bright-field TEM image taken for the final products is shown in Figure 3.8. A uniform silica layer of about 80-90 nm thick (the grey edge of area A) is seen to cover magnetite cores (the black area B). There is more than one particle being separated from each other in the TEM image, as marked by the arrows in the grey transition area between particles. However, there is only one single core included in each composite particle, indicating the minimized aggregation of primary particles during synthesis. The composition of areas A and B was determined by the energy dispersive X-ray spectroscopy (EDX). The spectra for areas A and B are shown in Figure 3.9. In area A (Figure 3.9 A), a strong Si-*K* peak, but weak Fe-*K* peaks were observed, indicating the coating of silica on magnetite. However, in area B (Figure 3.9B), the peak intensities corresponding to the two elements are reversed, suggesting the magnetite core of the nanocomposite. It should be noted that the strong copper peaks arise from the TEM grid material.

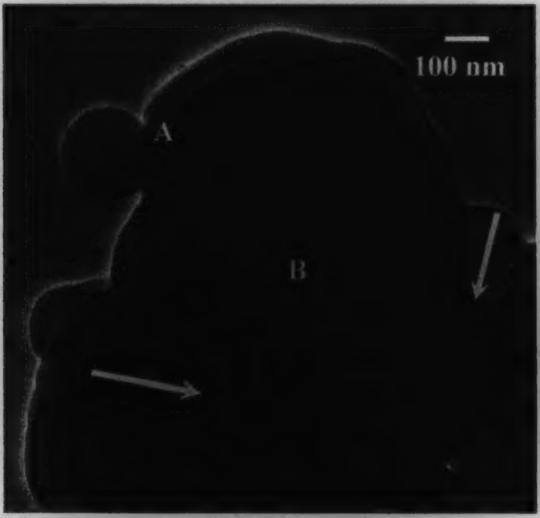

Figure 3.8 Bright-field TEM micrograph of a mesoporous magnetic nanaocompostie particle. The separation of two particles by silica matrix is marked by arrows.

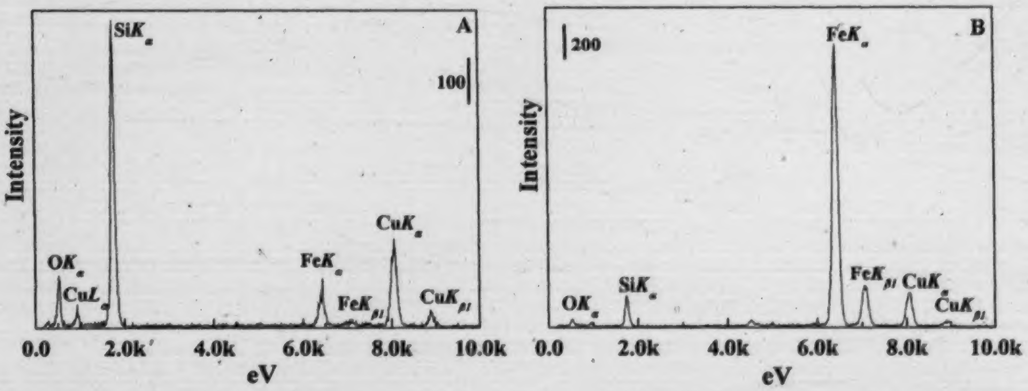

Figure 3.9 Energy Dispersive X-ray (EDX) emission spectra obtained on areas A and B.

Bight-field TEM image of higher resolution reveals the expected honeycomb porous structure of the silica layer (Figure 3.10). For easy viewing, some of the voids are highlighted by circles. The pore size is estimated to be around 6~7 nm. This value is in excellent agreement with the size of the templates assembled on silica wafer, studied by *in situ* atomic force microscopy as shown in Figures 3.4 and 3.5.

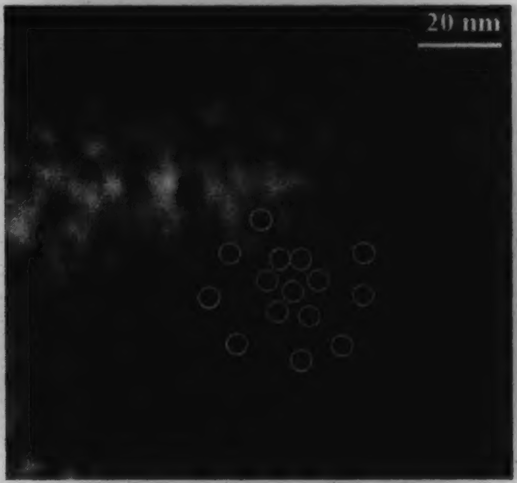

Figure 3.10 Bright-field TEM image of the mesoporous silica layer with some of the pores highlighted by circles.

The thickness of silica coatings can be measured from the low loss EELS spectrum, using the formula,

$$d_i = \lambda_i \ln\frac{I_t}{I_o} \tag{3.3}$$

where d_i is the film thickness, I_t is the integral intensity of the total low-loss portion of the spectrum, I_o is the intensity of the zero-loss peak, λ_i is the average mean free path [33]. The measured spectrum of the silica layer, by using a selected area aperture, is presented in Figure 3.11. The values of $\ln\frac{I_t}{I_o}$ and the mean free path for silica coatings are calculated to be 0.73 and 115 nm, respectively. From these two values, the film thickness is estimated to be about 83.6 nm, which is in excellent agreement with the value visually observed from the TEM image (Figure 3. 8).

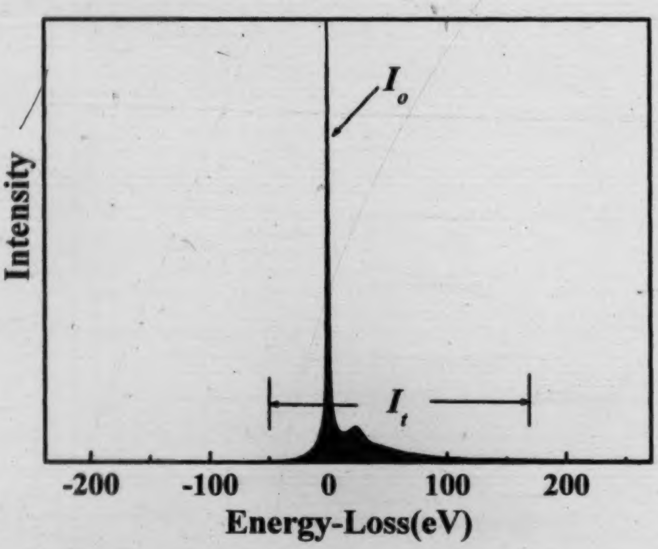

Figure 3.11 The spectrum of low-loss EELS of the silica layer.

3.3.5 Magnetic Properties

The magnetization characteristics of synthesized particles is a major concern for potential industrial applications. A strong magnetization is required for the collection by magnet from a complex multiphase system. As shown in Figure 3.12 the room temperature saturatation magnetization of bare magnetite is 85.5 emu/g, which reflects the properties of Fe_3O_4 without any oxidation. For the final mesoporous magnetic nanocomposite particles the saturation magnetization remains strong at 73.0 emu/g. The observed decrease of 15% in saturation magnetization is attributed to the coating of diamagnetic silica. Such a reduction does not hinder the subsequent magnetic separation after the resultant mesoporous magnetic particles are loaded with mercury. More importantly, magnetite particles coated with mesoporous silica remain fairly paramagnetic as shown by minimal coercivity and hysteresis on the magnetization curves (insert of Figure 3.12). This magnetization characteristic ensures that the magnetite particles do not become permanently magnetized after exposure to an external magnetic field, which in turn permits the particles to be re-dispersed without significant aggregation when the magnetic field is removed. It is clear that the magnetic sorbents prepared as such can be recycled in practice by magnetic separation, and the high specific surface area (150 m^2/g) makes it an ideal candidate for functionalization to possess high loading capacity.

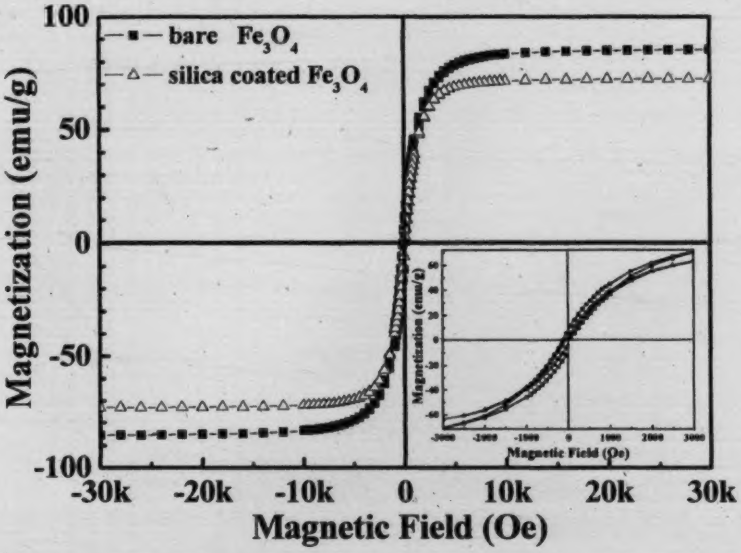

Figure 3.12 Room temperature magnetization measurements of bare magnetite and mesoporous magnetic nanocomposite particles.

3.3.6 Functionalization and Mercury Loading

X-ray photoelectron spectroscopy (XPS) is a surface sensitive analytical technique. It is used to provide the evidence of functionalization of thiol group on synthesized mesoporous silica surfaces and mercury loading. The narrow-scan spectra of sulfur and mercury are shown in Figure 3.13. The S_{2p} band appeared on the functionalized mesoporous magnetic sorbent. After mercury loading on the functionalized sorbent, the intensity of S_{2p} peak remained. Before the sorbent being exposed to Hg^{2+} solutions, no mercury was detected on the sample. After contacting the sorbent with mercury-containing aqueous solutions, Hg_{4d} bands around 359 and 379 eV appeared, indicating up-take of mercury, most likely through the binding with sulfur on the sorbent. It is shown that the role of thiol functionalization is to provide the chance of ion exchange of H^+ in –SH group with Hg^{2+} in the solution because of the strong affinity of mercury and sulfur to achieve the goal of mercury removal from solutions. It was found that the mercury adsorption was negligible by mesoporous silica-coated magnetite particles without functionalization. Since the position of Hg_{4f} overlaps with that of Si_{2p}, the signal of Hg_{4d} was collected to indicate the uptake of mercury, although at a relatively low intensity.

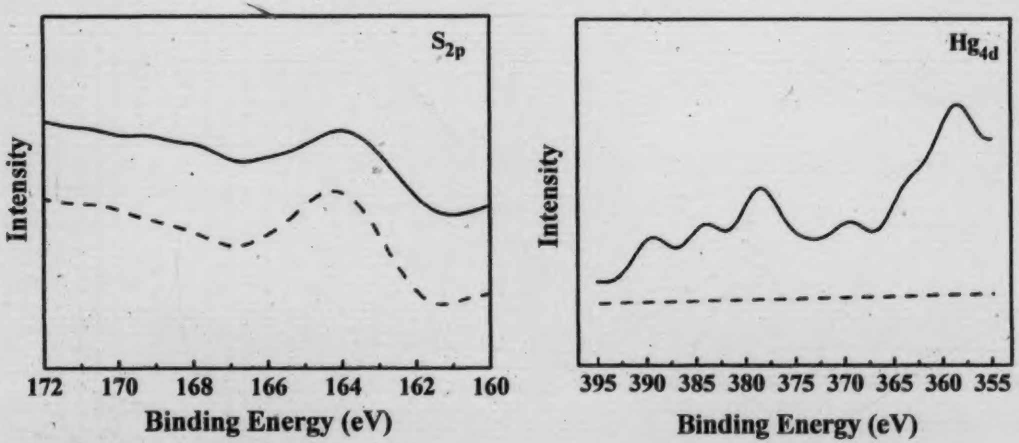

Figure 3.13 Narrow-scan XPS spectra for sulfur and mercury on samples of functionalized mesoporous magnetic sorbents (dash line) and mercury loaded on the sorbents (solid line).

To quantify mercury uptake by the prepared magnetic sorbents, the loading capacity is determined using the procedures described in experimental section 3.2.4. After functionalization, mesoporous magnetic sorbents show a strong affinity for mercury in aqueous solutions. The adsorption isotherm in Figure 3.14a indicates monolayer chemisorption of mercury on functionalized mesoporous magnetite surfaces. The maximum loading of mercury at pH 2 is 14 mg/g, which is about five times higher than previous capacity test at the same pH [31]. It should be noted that the functionalization conditions were not optimized in the current study. However, it is worth to optimize functionalization conditions to obtain the highest mercury loading capacity. As shown in Figure 3.14b, the mercury loading distribution coefficient (K_d) is well above 100 at pH 2, demonstrating the applicability of this kind of mesoporous magnetic particles for mercury removal from industrial effluents.

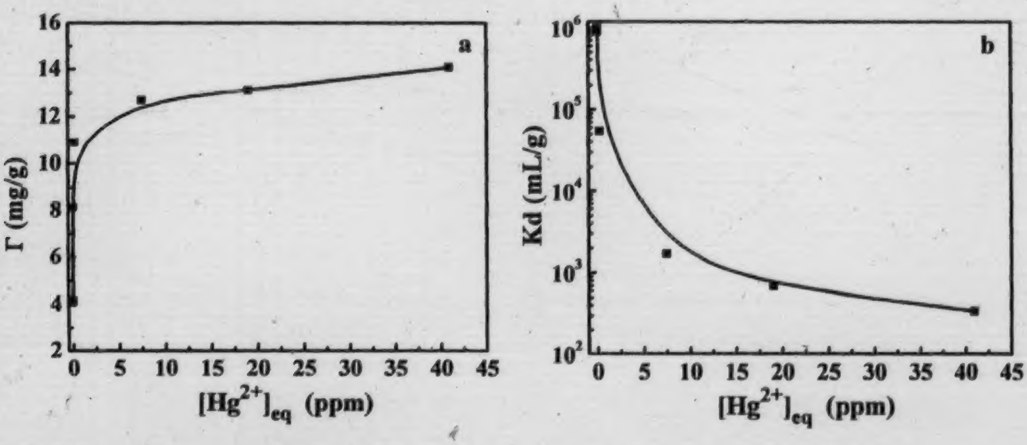

Figure 3.14 Mercury adsorption by functionalized magnetic sorbents at pH 2, (a) isotherm curve; (b) distribution coefficient curve.

3.4 Conclusions

Under the optimal synthesis conditions, the specific surface area of the resultant mesoporous magnetic sorbents as high as 150 m^2/g was obtained, in comparison to 0.07 m^2/g for bare magnetite. The molecular templating was confirmed by AFM in situ imaging. The micelle size determined by AFM imaging is in the range of 6 nm with the well-defined voids of 10 nm among the micelles for silica filling. Zeta-potential measurements confirmed the important role of each step in the synthesis of mesoporous silica-coated layer on magnetite. TGA proved the removal of surfactant by calcination without damage of magnetite core and silica layers. TEM micrographs showed the thickness of the silica layer to be about 80~90 nm and the pore size around 6~7 nm. XPS analysis confirmed functionalization and mercury loading on mesoporous magnetic sorbents. The mercury loading capacity as high as 14 mg/g was obtained at aqueous solution pH around 2. The resultant composite particles were determined to be paramagnetic with a specific saturation magnetization of 73 emu/g. Such particles could be easily separated for regeneration and recycle by conventional magnetic separation.

References

[1] J. Barron-Zambrano, S. Laborie, Ph. Viers, M. Rakib, G. Durand, J. of Membrane Sci., 229(2004), 179.

[2] G. McKay, M.J. Bino, Environ. Pollut. 66 (1990) 33.

[3] G. McKay, M.J. Bino, A.R. Altamemi, Water Res. 19 (1985) 491.

[4] X. Ma, K.S. Subramanian, C.L. Chakrabarti, R. Guo, J. Cheng, Y. Lu, W.F. Pickering, J. Environ. Sci. Health A27 (6) (1982) 1389.

[5] C.P. Huang, D.W. Blankenship, Water Res. 18 (1984) 37.

[6] D. Mohan, V. K. Gupta, S.K. Srivastava, S. Chander, Colloid Surface A 177 (2001) 169.

[7] K. Ariga, J. Nanosci. Nanotech. 4 (2004) 23.

[8] K. Ariga, Chem. Rec. 3 (2004) 297.

[9] J. L. Shi, Z. L. Hua, L. X. Zhang, J. Mater. Chem. 14 (2004) 795.

[10] A. Stein, Adv. Mate. 15 (2003) 763.

[11] C. Sanchez, B. Lebeau, F. Chaput, J. P. Boilot, Adv. Mater. 15 (2003) 1969.

[12] M. E. Davis, Nature 417 (2002) 813.

[13] D. E. de Vos, M. Dams, B. E. Sels, P. A. Jacobs, Chem. Rev. 102 (2002) 3615.

[14] F. Schüth, W. Schmidt, Adv. Mater. 14 (2002) 629.

[15] D. J. Cardin, Adv. Mater. 14 (2002) 553.

[16] X. Feng, G. E. Fryxell, L.-Q.Wang, A.Y. Kim, J. Liu, K. M. Kemner, Science 276 (1997) 923.

[17] L. Mercier, T. J. Pinnavaia, Microporous Mesoporous Mat. 20 (1998) 101.

[18] L. Mercier, T. J. Pinnavaia, Environ. Sci. Technol. 32 (1998) 2749.

[19] M.H. Lim, , C.F. Blanford, A.Stein, Chem. Mater. 10 (1998) 467.

[20] J. Brown, L. Mercier, T. J. Pinnavaia, Chem. Commun. 1 (1999) 69-70.

[21] J. Brown, R. Richer, L. Mercier, Microporous Mesoporous Mat. 37 (2000) 41.

[22] V. Antochshuk, M Jaroniec, Chem. Commun. 3 (2002) 258.

[23] A. Nourlinos, A. Simopoulos, D. Petridis, H. Okumura, G. Hadjipanayis, Adv. Mater. 13 (2001) 289.

[24] D. Feng, C. Aldrich, H. Tan, Hydrometallugy 56 (2000) 359.

[25] F. Caruso, Adv. Mater., 13 (2000) 11.

[26] F. Caruso, A.S. Susha, M. Giersig, H. Mohwald, Adv. Mater., 11 (1999) 950.

[27] M. Ohmori, E. Matijevic, J. Colloid Interface Sci., 160 (1993) 288.

[28] Z. Xu, Q. Liu, J.A. Finch, Appl. Surf. Sci., 120 (1997) 269.

[29] Q. Liu, Z. Xu, J. A. Finch, R. Egerton, Chem. Mater., 12 (1998) 3936.

[30] P. Wu, J. Zhu, Z. Xu, Adv. Funct. Mater., 14 (2004) 345.

[31] J. Dong, Z. Xu, 2006, in Proceedings: Functional Fillers and Nanoscale Minerals, ed. by J.J. Kellar, SME, Inc., Littleton, CO, pp. 241-252.

[32] Z. Xu, J. Liu, J. W. Choung, Z. Zhou, Int. J. Miner. Process. 68 (2003) 183.

[33] R. F. Egerton, Electron Energy-Loss Spectroscopy In The Electron Microscope, Plenum Press (1996) 2nd version.

[34] J.-F. Liu, G. Min, W. A. Ducker, Langmuir, 8 (1992) 1831.

Chapter 4 Novel Synthesis of Magnetic Zeolite Composites with Surface-Supported Silver Nanoparticles for Mercury Removal from Flue Gases

Jie Dong, Zhenghe Xu and Steven M. Kuznicki, to be submitted

4.1 Introduction

Zeolites are members of the family of aluminosilicate microporous solids known as molecular sieves. [1] The unique structural, physical and chemical properties of zeolites make them valuable for many industrial, agricultural and environmental applications.[2,3,4] Natural zeolites are low cost, readily available materials with excellent cation exchange characteristics which have been widely explored as sorbents for the removal of heavy metal ions from aqueous industrial wastes. [5,6,7,8,9,10,11] The adsorption capacity of zeolites originates from an open structure and a net negative charge in their framework, which can attract and hold cations. Transition metal ions can be incorporated into zeolites and, after calcination, form nano sized particles with excellent thermal- and photo-catalytic properties. [12,13,14,15,16,17,18,19] Zeolites are also frequently applied to gas separations because of their nano-scale pore structures and unique internal surface topology. [20,21,22,23,24,25]

The zeolites commonly used to remove heavy metal ions from industrial effluent are in the form of fine powders and must be recovered by solid-liquid separation subsequent to the purification process. Although these separations are possible for single-phase liquid or gas detoxification processes, the practical application of fine zeolite powders to complex multiphase systems (such as flue gases containing fly ash or industrial effluents containing finely divided particulates) is rather limited. A new technology to separate the spent sorbent powders from treated streams could extend the applications of zeolites to a much wider range of systems. If a zeolite composite were magnetic, for example, it could be readily separated and recovered from complex multiphase systems by the application of an external magnetic field, opening the door for sorbent regeneration, safe disposal of the waste and/or recovery of loaded valuable species.

Research efforts to render zeolites magnetic have been limited. Transition metal ions such as Fe^{2+}, Co^{2+} and Ni^{2+} have been introduced into zeolites by ion exchange. Thermal decomposition of $Fe(CO)_5$ in the Faujasite-type zeolite NaX has been reported.[26] The cations are converted to their metallic state by thermal reduction, which results in zeolites with magnetic properties. Reduction in a hydrogen atmosphere at temperatures as high as 400-600°C is not uncommon. [27,28] Other reducing agents such as NH_3 or CO have been frequently used at more moderate temperatures (300°C), particularly in the case of nickel reduction.[29] Reductions in solution by solvated electrons and Na^{-1} anions in an ether solvent[30,31] or by sodium borohydride[32,33] at ambient temperature have also been reported.

The existing methods for preparing magnetic zeolites do not produce materials that meet the requirements of industrial applications, as the reduced metal clusters are not protected and are readily oxidized. In a laboratory setting, unstable magnetic zeolites can be handled in glove-boxes, but, in industrial applications, rapid oxidation of the metal clusters will shorten the life cycle of the materials. In addition, the saturation magnetization of the magnetic zeolites prepared by the existing protocols is too low to be practical for magnetic separation in real-life applications. Further, the complete reduction of metal ions stabilized by framework coordination within zeolites requires high temperature calcination and concomitant high energy consumption, increasing the cost of sorbent preparation.[34] A stable and protected, readily synthesized magnetic material with sufficient saturation magnetization is required if magnetic zeolites are to be used as industrial sorbents.

In this chapter, a novel, simple and robust method is proposed to synthesize a new class of magnetic zeolite composite suited to environmental and industrial applications. In this process (Figure 4.1), a silica thin film is condensed on micron-sized magnetite (Fe_3O_4) particles. The dense liquid silica (DLS) coating isolates the magnetite particles from contact with the surrounding environment, thereby protecting the magnetite particles from corrosion and oxidation in harsh application environments. At the same time, the coating acts as a bridge to bind the DLS-coated magnetite to fine zeolite molecular sieve particles. During high temperature sintering, the dense liquid silica undergoes polycondensation and dehydration on both magnetite and zeolite particles, leading to the formation of magnetite-zeolite composites (MagZ). Sintering is achieved with a minimal amount of silica coating, which envelops the magnetite but not sufficient to coat the zeolite surface except for particle-particle contacts. Under such a controlled manner, the exposed surfaces of the zeolite remain available for ion exchange and molecular sieve functions. These mechanically stable MagZ composites feature both magnetite and zeolite properties which can be fully developed and exploited for adsorption, separation and catalysis.

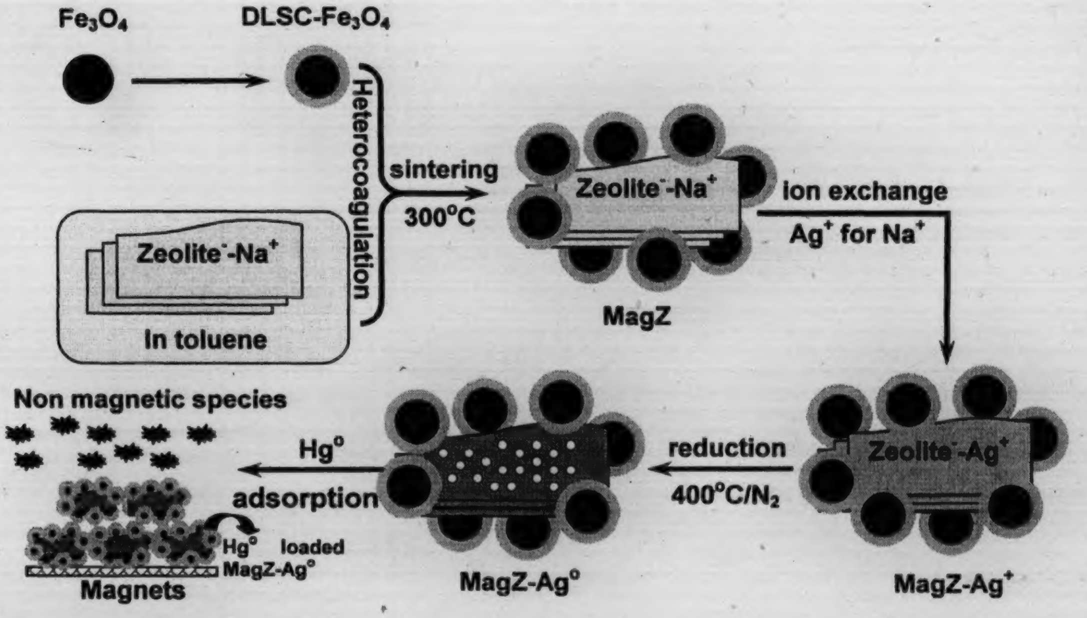
Fe_3O_4
DLSC-Fe_3O_4
Heterocoagulation
sintering
300°C
Zeolite⁻-Na⁺
In toluene
Zeolite⁻-Na⁺
MagZ
ion exchange
Ag⁺ for Na⁺
Zeolite⁻-Ag⁺
MagZ-Ag⁺
reduction
400°C/N_2
MagZ-Ag°
Hg°
adsorption
Non magnetic species
Hg° loaded
MagZ-Ag°
Magnets

Figure 4.1 Schematic illustration of the synthesis process to produce a new class of magnetite-zeolite composite with surface-supported silver nanoparticles for the removal of mercury from complex flue gases.

The proven properties of silver make it an excellent candidate metal to incorporate into MagZ composite materials. [35,36,37,38,39,40] Silver exchanged zeolites are exceptional adsorbents for noble gases, [41,42] while silver nanoparticles have proven antimicrobial activity, [43,44] and silver zeolite can be used as photocatalyst. [45,46] In addition, silver can amalgamate with mercury at elevated temperatures but, at temperatures above 227°C, the silver-mercury amalgam decomposes to release the mercury.[47] As shown in Figure 4.1, silver ions are incorporated into the zeolite component of MagZ by ion exchange, generating MagZ-Ag^+. After thermal reduction of the exchanged silver ions at 400°C, silver nanoparticles are formed on the zeolite surfaces in composites designated as MagZ-Ag°.

The synthesis described in Figure 4.1 produces a new class of functional materials that combine the ion exchange capacity of natural zeolites with the properties of metallic silver and the convenience of magnetic separation. The magnetic composites can be easily isolated from complex, multiphase systems for recycle and regeneration. The produced MagZ-Ag° is of potential applications as catalysts, bacterial disinfectants for municipal water, or sorbents for the removal of elemental mercury from the flue gases of coal-fired power plants, a pressing environmental concern. In this study, the synthesis of a promising new composite, MagZ-Ag°, is verified and characterized by X-ray Photoelectron Spectroscopy (XPS), Scanning Electron Microscopy (SEM), Transmission Electron Microscopy (TEM), electrokinetics, N_2 adsorption/desorption isotherm and magnetization measurements. In addition, Hg° capture by the new sorbent is demonstrated by measuring the mercury breakthrough temperature using Cold Vapour Atomic Fluorescence Spectrometry (CVAFS).

4.2 Experimental

4.2.1 Materials

Raw mineral zeolite from the deposit at Bowie, Arizona (chabazite with erionite and clinoptilolite contaminants) was obtained from GSA Resources of Tucson, Arizona, USA,[44] and pulverized to a fine powder (<200 mesh). Silver nitrate for ion exchange was purchased from Fisher Scientific. Sodium silicate ($Na_2SiO_3 \cdot 5H_2O$) and colloidal silica (Ludox, 40%), both used in the dense liquid silica coating, and magnetite (98% Fe_3O_4, $< 5\ \mu m$) were purchased from Aldrich. Millipore de-ionized water (Millipore, Canada) was used whenever needed.

4.2.2 Preparation

Magnetite particles (1 g) were mixed with deionized water (90 mL) by vigorous mechanical agitation. The suspension was heated to 90°C, a sodium silicate (1 M) solution with colloidal silica was added into the suspension, and hydrochloric acid (0.1 M) was added dropwise to maintain the pH at 9.5 ± 0.2. The silica coating reaction continued for 1 hour, after which the suspension was cooled to room temperature. The coated particles were separated from the solution with a hand magnet, rinsed twice with deionized water and collected by hand magnet. Silica coating of Fe_3O_4 was confirmed by zeta potential measurement and TEM imaging. Zeolite was dispersed in toluene by sonication and the DSLC-Fe_3O_4 particles were added into the suspension. After a short period of sonication and mixing, the composite particles were allowed to settle out of solution, the supernant was decanted, and the residual toluene was removed under vacuum. The solids were heated at 300°C in N_2 for 1 hour. The dried composite cake was crushed in a mortar and the powder was screened to obtain <100-mesh particles, designated as MagZ. Total exchange of Na^+ for Ag^+ in MagZ was performed in an aqueous silver nitrate solution containing silver (approximately 2.5 mEq of zeolite exchange capacity as determined by ICP[44]) at 80°C overnight. The ion-exchanged MagZ was thoroughly washed with de-ionized water to remove any unexchanged silver ions and dried overnight at 80°C. To convert the silver ions to metallic silver particles, the ion-exchanged composite was reduced at 400°C in a nitrogen environment for 1 hour. The final magnetic composite with surface-supported silver nanoparticles is designated as MagZ-Ag^o.

4.2.3 Sorbent Characterization

The spectra of X-ray Photoelectron Spectroscopy (XPS) were obtained on a Physical Electronics PHI 5400 x-ray photoelectron spectrometer (Perkin-Elmer) with an Mg K_α anode (15 kV, 400 W) at a takeoff angle of 45°. The source X-ray was not filtered, and the instrument was calibrated against the C_{1s} band at 285 eV. Spectra were recorded at a constant pass energy of 35.75 eV under a background pressure of approximately 1×10^{-9} Torr.

Field Emission Scanning Electron Microscopy (FE-SEM) imaging was performed on a JSM6301FXV SEM (JEOL), operating in backscatter mode at the accelerating voltage of 20 kV. Energy Dispersive X-ray Analysis (EDX) was performed with a PGT (Princeton Gamma Tech) IMIX x-ray analyzer. Samples were coated with Cr for electron conduction.

Transmission Electron Microscopy (TEM) imaging was performed on a JEOL-2010 TEM. The particles were dispersed in toluene and then transferred to a thin carbon film supported on TEM copper grids. The micrographs of synthesized particles were obtained in bright-field imaging mode at 200 kV acceleration voltage.

Zeta potential distribution measurement was carried out using a Zetaphoremeter III (SEPHY/CAD). Detailed experimental procedures and principles of the instrument have been described elsewhere.[48] For these tests, particles were suspended in 1 mM KCl solutions by sonication for 15 minutes prior to each measurement.

Specific surface areas were determined from N_2 adsorption/desorption isotherms measured at liquid nitrogen temperatures in a Quantachrome Autosorb-1 unit, using a modified multi-point BET technique.

Saturation magnetization was determined with a Quantum Design (San Diego, CA, USA) 9T-PPMS DC magnetometer. The susceptibility was corrected for contributions from the diamagnetism of the sample holder and the underlying sample.

4.2.4 Mercury Breakthrough Measurement

Elemental mercury (Hg°) breakthrough studies were conducted by injecting standard Hg° vapour (50 μL) into a 3 mm ID borosilicate glass chromatographic column containing 50 mg of the test sorbent. Any mercury breaking through the sorbent continued downstream and was captured by a gold-coated glass bead trap (GT). The Hg° captured on the GT was thermally desorbed by rapid heating to 450°C and the mercury signal was analyzed by cold vapour atomic fluorescence spectroscopy (CVAFS) on a Tekran Model 2500 CVAFS detector. The chromatographic column and its contents were maintained at the test temperature for the duration of the experiment. Ultra-high purity argon flowing at 40 mL/min was used as the carrier gas and the sorbent was held in place with muffled quartz glass wool, which does not adsorb mercury. After each test, the sorbent was heated to 400°C for 20-30 min to release the captured mercury and regenerate the sorbent for the next breakthrough test.

To determine the amount of mercury breakthrough, the GT-CVAFS set-up (Figure 4.2) was calibrated prior to sorbent breakthrough tests by injecting a known amount of mercury. After heating the GT, all of the injected mercury was released and detected at the CVAFS as a sharp peak. The area underneath the peak was integrated as (A_{cal}) and the corresponding area for one picogram of mercury (*CAL, also known as calibration constant*), is determined by the equation

$$CAL = \frac{A_{cal}}{V \times \rho_{cal}}$$

where V is the volume of Hg° injected (50μL), ρ_{cal} (pg/μL) is the concentration of mercury at the temperature when mercury is sampled for calibration.

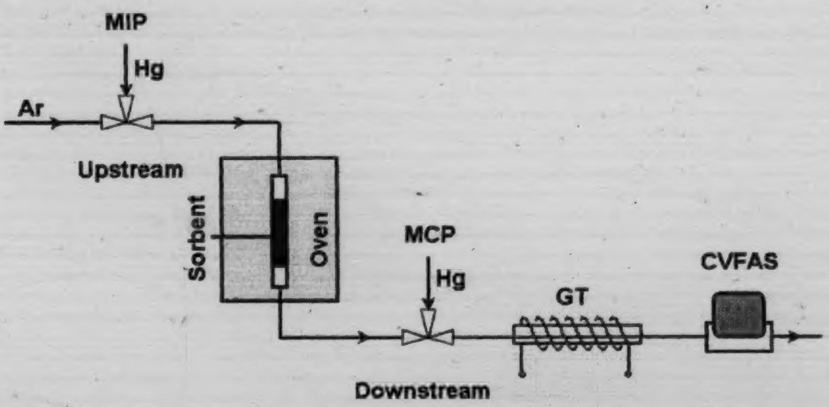

Figure 4.2 Experimental set-up for the mercury breakthrough measurements. (MIP: mercury injection port; MCP: mercury calibration port; GT: a gold coated glass beads trap)

During breakthrough tests, any Hg° that broke through the sorbent was collected for 20 mins by the GT. The mercury retained on the GT was released by rapid heating of the GT and determined by the CVAFS. From the area underneath the peak (A_{BT}) and the calibration constant, the amount of mercury breaking through the sorbent could be readily calculated. If the same volume of mercury is injected in the breakthrough tests as in calibration, the percentage of mercury breakthrough (BT%) can then be calculated by

$$BT\% = \frac{A_{BT}\,\rho_{CAL}}{A_{CAL}\,\rho_{SMP}} \times 100\%$$

where ρ_{SMP} (pg/μL) is the concentration of mercury at the temperature when mercury is taken for the breakthrough test. Because the concentration of Hg° is very sensitive to temperature, the concentration correction is extremely important to calculate accurate amount of mercury injected. The mass balance (the amount of Hg° breakthrough + Hg° captured = total injected amount) in the tests was found within 96% and 103%.

4.3 Results and Discussion

4.3.1 Synthesis of MagZ Composite

The successful coating of Fe_3O_4 with silica was directly confirmed by electrokinetics. The isoelectric point (IEP) of bare magnetite measured in this study is pH 6.8, close to the reported value for mineral magnetite. After DLS coating, the IEP of the coated particles was found to be at pH 2.0, the same as the IEP of mineral or fused silica, indicating that the magnetite particles were well protected by a silica layer.

The use of an organic solvent (toluene), rather than an aqueous solution to disperse zeolite, but heterocoagulate zeolite and DLSC-Fe_3O_4, is critical to this synthesis. In an aqueous solution, the dense liquid silica on magnetite would dissolve into the solution and migrate to zeolite. This process would reduce the strength of the sinter between magnetite and zeolite, unless excess silica was used in the synthesis. More importantly, the silica transferred from DLSC-magnetite could block the pores of zeolite, which are required for ion exchange. Since silica is insoluble in toluene, the use of toluene as a solvent ensures that the silica coating remains on magnetite with negligible transfer to zeolite, avoiding blockage of zeolite pores, while ensuring the binding by silica coating on magnetite with zeolite.

The accessibility of the zeolite pores in the MagZ composite was confirmed by nitrogen adsorption/desorption measurements, as shown in Figure 4.3. The isotherms indicate the presence of microporous and mesoporous structures in both zeolite and MagZ. The specific surface areas of the materials were calculated using the Brunauer-Emmett-Teller (BET) adsorption equation and are summarized in Table 4.1. The zeolite used in this study has large specific surface area of 472 m^2/g, mainly due to its nanoporous structure, which results in a high interior surface area (410 m^2/g). The exterior surface area of the zeolite (62 m^2/g) will support the silver nanoparticles after thermal reduction and migration to the zeolite surface. Magnetite, a non-porous, crystalline dense material, has an extremely low specific surface area (< 0.07 m^2/g), [49] and does not contribute significantly to the specific surface area of the composite. The synthesized composite has a specific BET surface area of 164 m^2/g, which is close to one-third of the measured surface area of zeolite and consistent with the input ratio of approximately 30% zeolite into the MagZ composite. These results indicate that the novel protocol of synthesis effectively minimizes the blockage of zeolite pore in the MagZ composite.

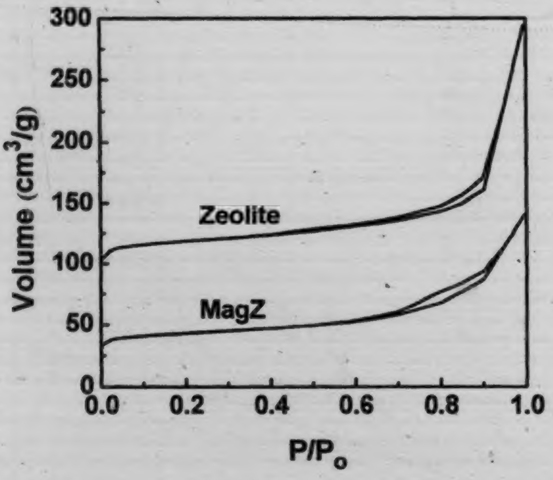

Figure 4.3 N_2 adsorption/desorption isotherms of Zeolite and MagZ containing 30% zeolite.

Table 4.1 BET specific surface areas of materials

Materials	Total surface area (m^2/g)	External surface area (m^2/g)	Internal surface area (m^2/g)
Zeolite	472	62	410
MagZ	164	46	118

4.3.2 X-ray Photoelectron Spectroscopy (XPS)

Figure 4.4 (a) shows the narrow-scan XPS spectra of silicon for samples of unbound zeolite and the composites MagZ, MagZ-Ag^+ and MagZ-Ag°. The Si_{2p} band of zeolite peaks at 102.3 eV, in the range of binding energy for aluminosilicate (102 ~ 103 eV). In the MagZ composite, the silicon peak shifts to 102.9 eV. Considering the Si_{2p} peak of SiO_2 between 103.2 eV and 103.8 eV, the shift of Si_{2p} after the formation of MagZ indicates successful surface polycondensation of DLS coating on Fe_3O_4 and zeolite particles. The experimental profile can be fitted by two separate Si_{2p} peaks, one from silicon in zeolite (102.3 eV) and the other from silica (103.6 eV). The presence of Si_{2p} of 102.3 eV confirms that the binding of DLSC-Fe_3O_4 on zeolite did not block the zeolite surface. In the silver-exchanged and thermally reduced composites, MagZ-Ag^+ and MagZ-Ag°, the Si_{2p} peak remains the same as that observed for MagZ, indicating that the ion-exchange and thermal treatments do not impact the surface characteristics of the composite or the framework of zeolite.

A low-intensity Fe_{2p} band is detected in the untreated zeolite (Figure 4.4 (b)), indicating the presence of iron impurities in the naturally occurring mineral zeolite used in this study. In MagZ and the silver treated composites, the Fe_{2p} peak remains weak. This is surprising, as enhanced Fe_{2p} band would be expected after iron-containing magnetite is bound to zeolite in the magnetic composites. However, the protective layer of DLS coating shielded magnetite particles as confirmed by the absence of Fe_{2p} band on XPS spectrum of DLSC-Fe_3O_4. As a result, within the effective penetration depth of x-ray, only the Si signal from the SiO_2 coating was collected and contributes to the overall spectra (Figure 4.4 (a)). The consistent intensity of Fe_{2p} bands in the composites (MagZ, MagZ-Ag^+ and MagZ-Ag°) and zeolite samples indicates that the original zeolite remains accessible to x-rays and resultant ejection of photoelectrons to be detected by XPS. This finding support that the zeolite in the composites retains its original characteristics.

Successful exchange of sodium by silver ions in MagZ is confirmed by narrow scan XPS spectra of the samples. Figure 4.4 (c) shows the disappearance of the sodium band at 1067 eV in silver-exchanged MagZ-Ag^+ and MagZ-Ag°, accompanied by the appearance of silver bands (Ag_{3d}) at 368.4 and 374.3 eV in Figure 4.4 (d). No substantial differences between the spectra of MagZ-Ag^+ and MagZ-Ag° are observed, even though the silver in MagZ-Ag° has been reduced to metallic silver. It is possible that partial reduction of Ag^+ occurs during MagZ-Ag^+ sample preparation, which includes incubation and dehydration at 80°C. Similar observations have been reported for other silver zeolite materials.[50] It is well documented that the XPS band of $Ag_{3d5/2}$ in metallic form at 368.0 ~ 368.3 eV overlaps with that of Ag_2O, and exhibits only a marginal shift to lower binding energy at 367.3 ~ 367.9 eV for the extreme case of AgO. [51] It is therefore reasonable to observe an $Ag_{3d5/2}$ XPS band for exchanged monovalent Ag^+ at 368.4 eV. A small but reproducible shift of $Ag_{3d5/2}$ band towards higher binding energy in the MagZ-

Ag° sample as indicated in Figure 4.4 (d) confirms the reduction of Ag^+ after thermal treatment.

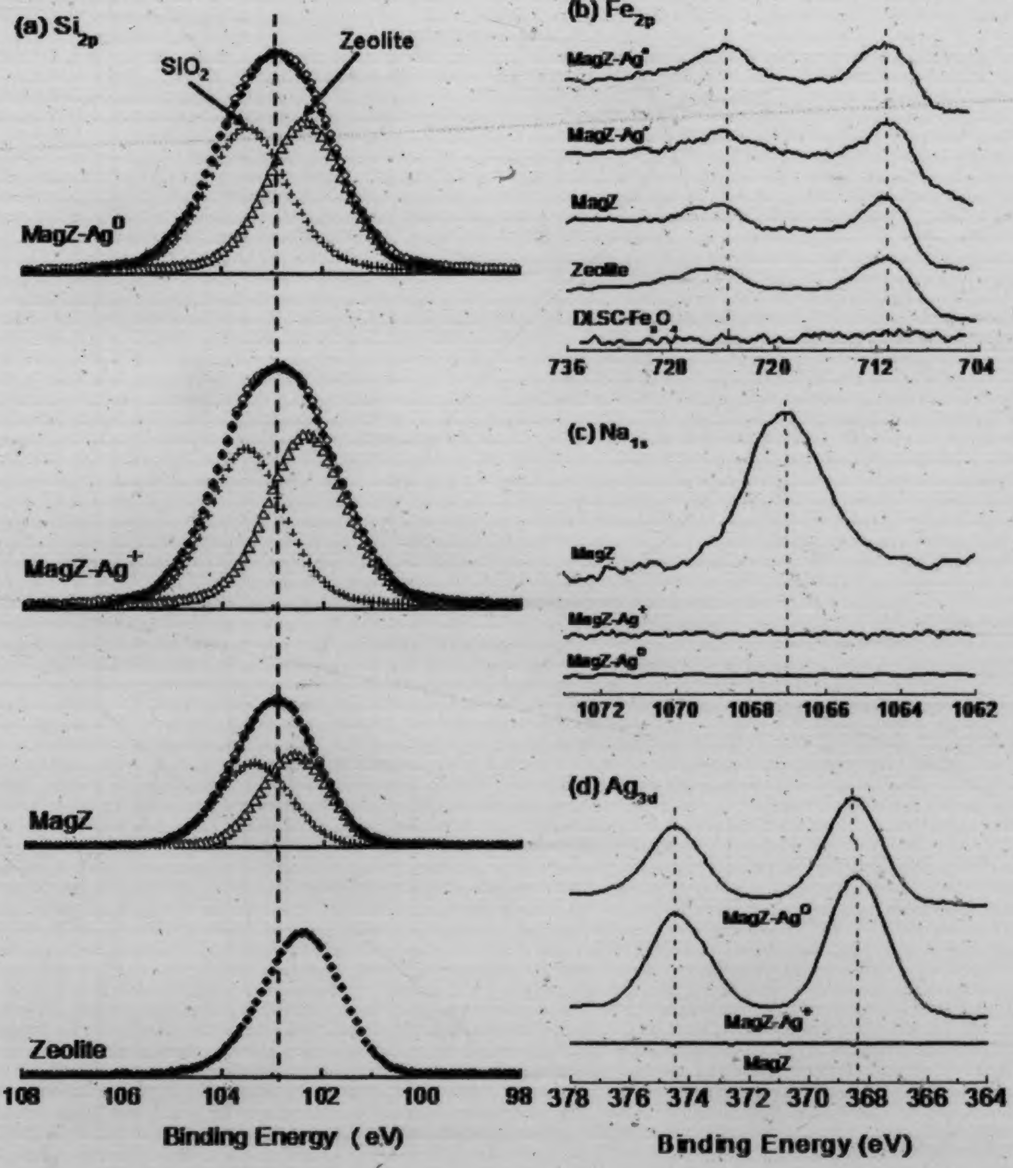

Figure 4.4 XPS narrow-scan spectra over the spectral region of (a) Si_{2p} (● the experimental data; ○ the calculated data; Δ Si_{2p} from zeolite; + Si_{2p} from silica), (b) Fe_{2p}, (c) Na_{1s} and (d) Ag_{3d} for various samples.

4.3.3 Field Emission Scanning Electron Microscopy (FE-SEM)

Micrographs of the MagZ composites taken in backscattering mode are shown in Figure 4.5. In this mode the electron intensity is proportional to the atomic number of the element. For the composite samples, magnetite appears brighter than zeolite, as the iron in magnetite has higher atomic number than the silicon and aluminum in zeolite. The image of MagZ under low magnification (Figure 4.5 (a)) shows that magnetite and zeolite composite particles are well separated from each other. The final functional composite, MagZ-Ag°, is shown at large magnefication in Figure 4.5 (b). The zeolite particles in this micrograph are grey and the brighter Fe_3O_4 particles are tightly attached to zeolite particles.

Energy dispersive x-ray analysis (EDX) (Figure 4.5 (c)) on selected regions of MagZ-Ag° confirms the composition of the composite. The spectra of particles 01 and 02 exhibit the x-ray characteristics of Si, Al and Ag, with a negligible x-ray count for Fe, indicative of zeolite containing silver. The spectrum for the brighter smaller particle (03) is dominated by the iron signal, with small silicon peaks and no aluminum or silver signals, confirming not only that the particles are magnetite with a thin layer of silica, but also that the silver remains localized on zeolite and does not migrate onto silica-coated magnetite. In MagZ-Ag°, the coated magnetite particles are stably bound with zeolite in a composite that can endure washing, stirring and heating.

The magnified image of a silver zeolite region of MagZ-Ag° clearly shows a number of shiny spots distributed on the surface of the zeolite (Figure 4.5 (d)), along with some wires and larger pools of metal. The spots are silver, as determined by separate EDX analysis, with an apparent size of approximately 30 nm. Finer silver particles cannot be resolved by SEM.

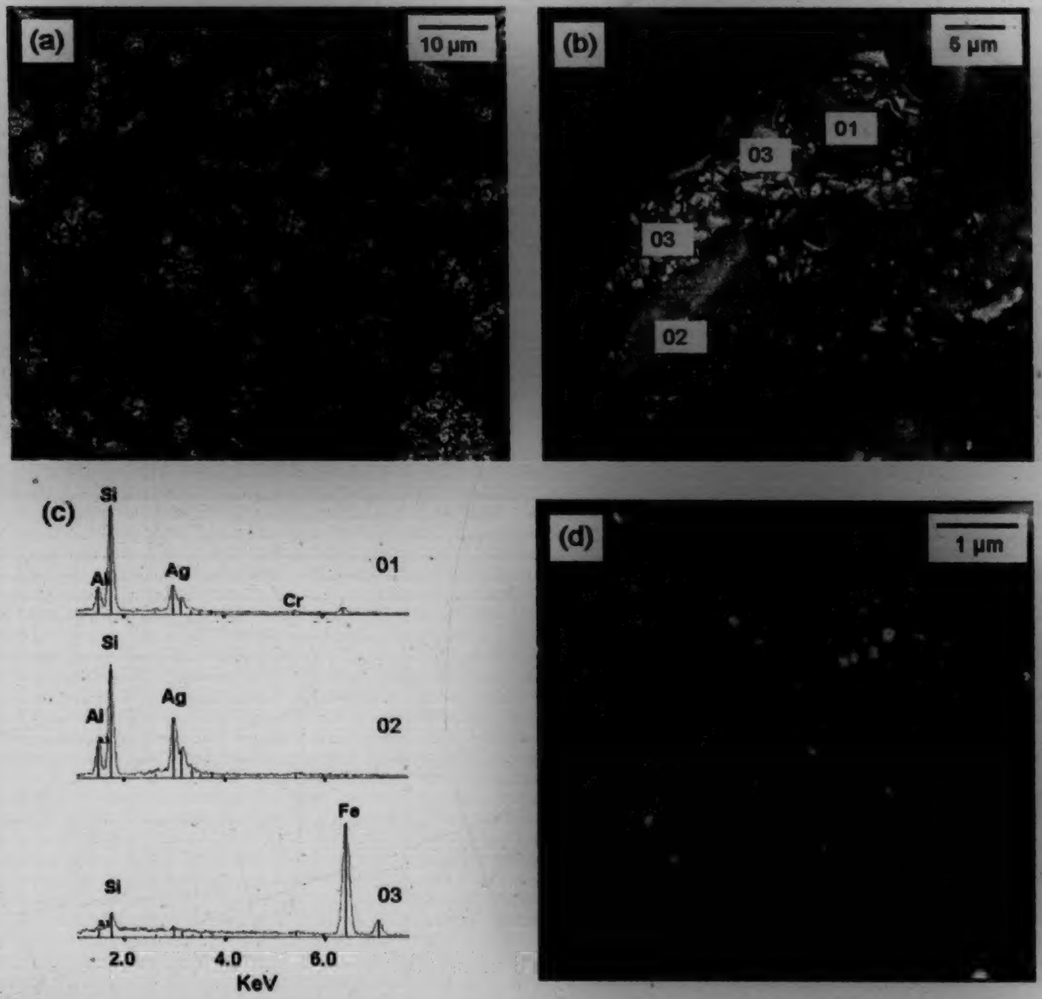

Figure 4.5 Backscattering SEM images of (a) MagZ composites particles and (b) MagZ-Ag°. (c) EDX analysis on areas 01, 02 and 03 of (b). (d) Magnified SEM image of area 01 in (b).

4.3.4 Transmission Electron Microscopy (TEM)

TEM imaging reveals more detailed morphological information about the silver particles distributed on the surface of the mineral zeolite in MagZ-Ag° (Figure 4.6). The majority of silver nanoparticles are in the range of 1-7 nm in diameter, and the larger particles are aggregates of two or more small silver nanoparticles. The relatively large silver particles observed in the SEM micrograph are aggregate silver nanoparticles at the defects of the zeolite. The dark region in the left part of Figure 4.6 is identified as magnetite by EDX analysis. A thin layer of the DLSC that bridges magnetite and zeolite after high temperature sintering is visible at the edge of the magnetite particles.

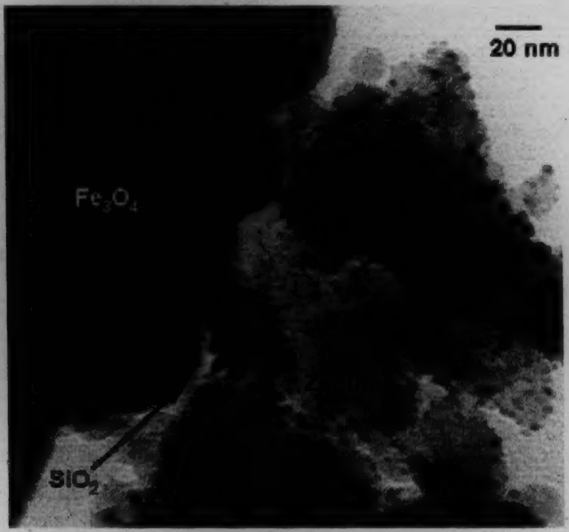

Figure 4.6 TEM image of MagZ-Ag°.

4.3.5 Magnetization

A key feature of the novel composite MagZ-Ag° is its magnetic properties, which make it simple to separate and regenerate, whether it is used as a sorbent, catalyst or disinfectant. DLC-silica and zeolite are diamagnetic materials, and must be combined with magnetite (Fe_3O_4) to make a magnetic composite. The synthesized composite MagZ-Ag° exhibits a saturation magnetization of approximately 40 emu/g, with minimized coercivity and negligible magnetization hysteresis (Figure 4.7). These magnetization characteristics ensure that the DLS-coated magnetite attached to zeolite does not become permanently magnetized after exposure to an external magnetic field, which in turn permits the composite particles to be re-dispersed without aggregation when the magnetic field is removed. Combining the DLS-coated magnetite with zeolite reduces the value of its saturation magnetization from 85 emu/g for raw magnetite. However, at the current portion of magnetite in MagZ-Ag°, the composite remains sufficiently magnetic to be attracted by normal magnets for isolation and/or separation.

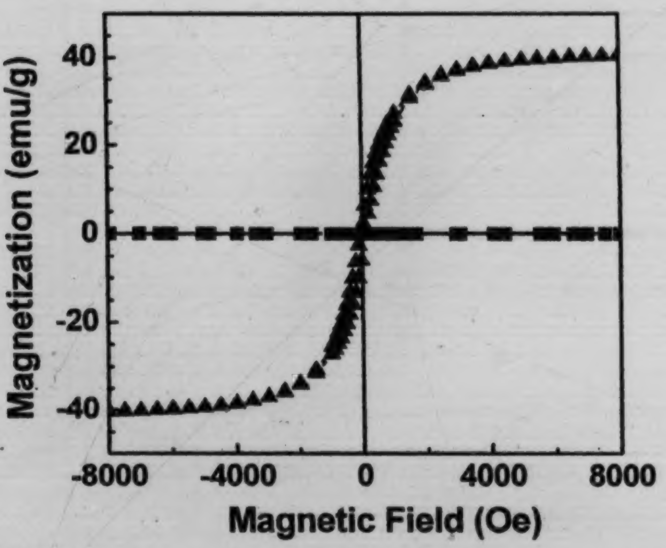

Figure 4.7 Magnetization characteristics of zeolite with SiO_2 (squares) and MagZ-Ag° (triangles).

4.3.6 Mercury Capture

The Hg° breakthrough characteristics of a sorbent over a given temperature range will determine suitable temperature range of potential applications for that sorbent and provide insights into Hg° capture mechanisms. Figure 4.8 shows the percent of mercury breakthrough as a function of temperature for composites collected at various stage of synthesis. As anticipated, raw magnetite does not adsorb mercury at all, exhibiting a Hg° breakthrough above 95%, even at room temperature. After the silica coating is applied to Fe_3O_4 to form DLSC-Fe_3O_4, the mercury breakthrough remains as high as 90% at room temperature, indicating that the silica layer does not adsorb Hg°.

Zeolites are known for their extraordinary adsorptive capability because of their high surface areas and porous internal structure. However, Hg° breakthrough for MagZ at room temperature is 95%. In contrast, MagZ samples pre-heated slowly up to and kept at 120°C for 1 hour (designated as 120MagZ) show complete mercury capture at room temperature. Up to 100°C, 120MagZ captures 90% of Hg° in the gas stream. However, when the test temperature is increased to 150°C, 53% of Hg° in the feed gas stream breaks through, and at 200°C, the Hg° breakthrough reaches 98%.

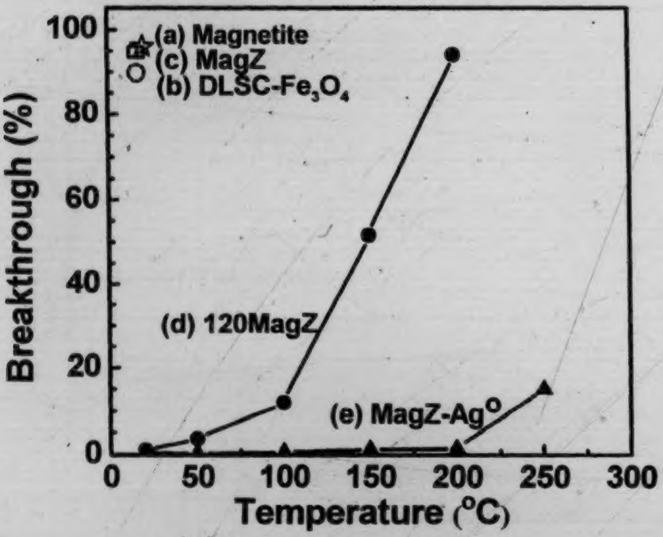

Figure 4.8 Mercury breakthrough as a function of temperature changes for the samples: (a) magnetite (star), (b) DLSC-Fe_3O_4 (open circle), (c) MagZ saturated with moisture (open square), (d) 120MagZ (filled circles) and (e) MagZ-Ag° (filled triangles).

These observations suggest that the zeolite component in MagZ is naturally saturated with moisture during storage. The moisture occupies the internal surface and volume as such that Hg° molecules cannot enter the system to be adsorbed. After preheating to remove the moisture, the advantages of the high specific surface area and large pore volume of zeolite come into effect. Mercury can adsorb on the zeolite in 120MagZ by physical adsorption/condensation. However, the physisorption of mercury on 120MagZ is not sustainable at higher temperatures. The increase of thermal energy of mercury with increasing temperature exceeds the interaction force of physisorption between mercury and the zeolite surface. Therefore, mercury can not adsorb stably on the sorbent. Since the temperature of flue gases from typical Rankine cycle coal-fired plants approaches 150°C, 120MagZ is not a suitable sorbent for mercury removal from these flue gases.

MagZ-Ag° demonstrates complete mercury capture below 200°C (Figure 4.8). The silver nanoparticles on the surface of MagZ-Ag° significantly improve mercury capture by the amalgamation of Hg° with silver. With an increase in temperature to 250°C, approximately 20% of the mercury breaks through the sorbents and mercury breakthrough reaches 100% when capture temperature increased to 400°C. Dramatically improved mercury capture by MagZ-Ag° at higher temperatures demonstrates the importance of silver nanoparticles in mercury capture. The amalgamation of Hg° with Ag° leads to a more stable sorption than the physisorption. Since MagZ-Ag° is unable to capture Hg° at 400°C, it is anticipated that spent MagZ-Ag° isolated by magnetic separation can be regenerated by thermal treatment at 400°C. The detailed results of regeneration and in situ flue gas tests will be continued in the next chapter.

4.4 Conclusions

In this communication, a novel and simple method is proposed to synthesize a new class of magnetic zeolite composites with surface-supported silver nanoparticles as sorbents for mercury removal. Surface characterization by XPS confirms the synthesis, including the formation of the MagZ composite, ion exchange of Ag^+ in MagZ, and thermal reduction of Ag^+ to Ag° nanoparticles. SEM and TEM micrographs show tight binding of magnetite on zeolite in the composite, with silver particles (1-7 nm in diameter) arrayed on the surface of the zeolite. Silver particles of approximately 30 nm are also observed. MagZ-Ag° composites are magnetic, with a satisfactory saturation magnetization of 40 emu/g for magnetic separation. The composite can adsorb Hg° up to 200°C, which is higher than the temperature of physisorption and suitable for the mercury removal from flue gases of typical Rankine cycle coal-fired plants.

References

[1] D.W. Breck, in: Zeolites Molecular Sieves: Structure, Chemistry and Uses, J. Wiley, New York, US **1974**.

[2] J. Scott. (Ed.) *Zeolite Technology and Applications: Recent Advances*, Park Ridge, N.J., Noyes Data Corp. **1980**.

[3] D. Mohan, K. P. Singh, *Water Res.* **2002**, *36* (9), 2304-2318.

[4] S. M. Auerbach, K. A. Carrado, P. K. Dutta (Ed.) *Handbook of Zeolite of Science and Technology*, New York, M. Dekker, **2003**.

[5] S. K. Ouki, C. R. Cheeseman, R. Perry, *J. Chem. Tech. Biotechnol* **1994**, *59*, 121-126.

[6] D. Mohan, C. U. Pittman, *J. Hazard. Mater.* **2007**, *142*(1-2), 1-53.

[7] S. K. Ouki, M. Kavannagh, *Wat. Sci. Tech.* **1999**, *39*(10-11), 115-122.

[8] S. K. Ouki, Kavannagh, M. *Waste Manage. Res.* **1997**, *15* (4), 383-394.

[9] L. Curkovic, S. Cerjan-Stefanovic, T. Filipan, *Water Res.* **1997**, *31*(6), 1379-1382.

[10] O. Oter, H. Akcay, *Water Environ. Res.* **2007**, *79*(3), 329-335.

[11] M. S. Berber-Mendoza, R. Leyva-Ramos, P. Alonso-Davila, J. Mendoza-Barron, P. E. Diaz-Flores, *J. Chem. Technol. Biotechnol.* **2006**, *81*(6), 966-973.

[12] I. E. Maxwell, *Adv. Catal.* **1982**, *31*, 1-76.

[13] T. Jüstel, D. U. Wiechert, C. Lau, D. Sendor, U. Kynast, *Adv. Func. Mater.* **2001**, *11*(2), 105-110.

[14] H. Yamashita, Y. Miura, K. Mori, S. Shironita, Y. Masui, N. Mimura, T. Ohmichi, T. Sakata, H. Mori, *Pure Appl. Chem.* **2007**, *79*(11), 2095-2100.

[15] W. M. H. Sachtler, Z. C. Zhang, *Adv. Catal.* **1993**, *39*, 129-220.

[16] A. Dong, N. Ren, W. Yang, Y. Wang, Y. Zhang, D. Wang, J. Hu, Z. Gao, Y. Tang, *Adv. Func. Mater.* **2003**, *13*(12), 943-948.

[17] M. Matsuoka, K. Iino, H. Chen, M. Anpo, *Res. Chem. Intermed.* **2005**, *31*(1-3), 153-165.

[18] M. Anpo, M. Takeuchi, K. Ikeue, S. Dohshi, *Curr. Opin. Solid State Mater. Sci.* **2002**, *6*(5), 381-388.

[19] M. Anpo, S. Higashimoto, M. Matsuoka, N. U. Zhanpeisov, Y. Shioya, S. Dzwigaj, M. Che, *Catal. Today* **2003**, *78*(1-4), 211-217.

[20] L. I. Devriese, L. Cools, A. Aerts, J. A. Martens, G. V. Baron, J. F. M. Denayer, *Adv. Func. Mater.* **2007**, *17*(18), 3911-3917.

[21] Z. P Lai, G. Bonilla, I. Diaz, J. G. Nery, K. Sujaoti, M. A. Amat, E. Kokkoli, O. Terasaki, R. W. Thompson, M. Tsapatsis, D. G. Vlachos, *Science* **2003**, *300*(5618), 456-460.

[22] S.P.B. Kremer, C.E.A. Kirschhock, M. Tielen, F. Collignon, P.J. Grobet, P.A. Jacobs, J.A. Martens, *Adv. Func. Mater.* **2002**, *12*(4), 286-292.

[23] K. Kusakabe, T. Kuroda, A. Murata, A. Murata, S. Morooka, *Ind. Eng. Chem. Res.* **1997**, *36*(3), 649-655.

[24] K. Kusakabe, T. Kuroda, S. Morooka, *J. Membrane Sci.* **1998**, *148* (1), 13-23.

[25] M. D. Jia, B. S. Chen, R. D. Noble, J. L. Falconer, *J. Membrane Sci.* **1994**, *90*(1-2), 1-10.

[26] F. J. Lázaro, J. L. García, V. Schünemann, Ch. Butzlaff, A. Larrea, M. A. Zaluska-Kotur, *Phys. Rev. B* **1996**, *53*(20), 13934 - 13941.

[27] P. Braunstein, R. Devenish, P. Gallezot, B. T. Heaton, C. J. Humphreys, J. Kervennal, S. Mulley, M. Ries, *Angew. Chem. Int. Edit.* **1988**, *27*(7), 927-929.

[28] B. Coughlan, M. A. Keane, *J. Catal.* **1990**, *123*(2), 364-374.

[29] M. Che, M. Richard, D. Olivier, *J. Chem. Soc., Faraday Trans.* **1980**, *76*, 1526-1534.

[30] J. A. Cowen, K. L. Tsai, J. L. Dye, *J. Appl. Phys.* **1994**, *76*(10), 6567-6569.

[31] K. L. Tsai, J. L. Dye, *Chem. Mater.* **1993**, *5*, 540-546.

[32] L. Zhang, A. Manthiram, *J. Mater. Chem.* **1996**, *6*, 999-1004.

[33] I. Hussain, I. Gameson, P. A. Anderson, M. Slaski, P. P. Edwards, A. Dyer, *J. Chem. Soc., Dalton Trans.* **1996**, *5*, 775-781.

[34] T. Schmauke, M. Menzel, E. Roduner, *J. Mol. Catal. A-Chem.* **2003**, *194*, 211-225.

[35] Y. Shen, Y. H. Lin, C. W. Nan, *Adv. Func. Mater.* **2007**, *17*(14), 2405-2410.

[36] S. Z. Zhang, W. H. Ni, X. S. Kou, M. H. Yeung, L. D. Sun, J. F. Wnag, C. H. Yan, *Adv. Func. Mater.* **2007**, *17*(16), 3258-3266.

[37] H. L. Wang, L. M. Qi, *Adv. Func. Mater.* **2008**, *18*(8), 1249-1256.

[38] D. S. Koktysh, X. R. Liang, B. G. Yun, I. Pastoriza-Santos, R. L. Matts, M. Giersig, C. Serra-Rodriguez, L. M. Liz-Marzan, N. A. Kotov, *Adv. Func. Mater.* **2002**, *12*(4), 255-265.

[39] J. H. Zhang, J. B. Liu, S. Z. Wang, P. Zhan, Z. L. Wang, N. B. Ming, *Adv. Func. Mater.* **2004**, *14*(11), 1089-1096.

[40] V. Bastys, O. Pastoriza-Santos, B. Rodriguez-Gonzalez, L. M. Liz-Marzan, *Adv. Func. Mater.* **2006**, *16*(6), 766-773.

[41] S. M. Kuznicki, A. Ansón, A. Koenig, T. M. Kuznicki, T. Haastrup, E. M. Eyring, D. Hunter, *J. Phys. Chem. C* **2007**, *111* (4), 1560-1562.

[42] A. Ansón, S. M. Kuznicki, T. Kuznicki, T. Haastrup, Y. Wang, C. C. H. Lin, J. A. Sawada, E. M. Eyring, D. Hunter, *Micropor. Mesopor. Mater.* **2008**, 109(1-3), 577-580.

[43] Y. M. Wang, G. J. Du, H. Liu, D. Liu, S. B. Qin, N. Wang, C. G. Hu, X. T. Tao, J. Jiao, J. Y. Wang, Z. L. Wang, *Adv. Func. Mater*, **2008**, *18*(7), 1131-1137.

[44] S. M. Kuznicki, D. J. A. Kelly, J. Bian, C. C. H. Lin, Y. Liu, J. Chen, D. Mitlin, Z. Xu, *Micropor. Mesopor. Mater.* **2007**, *103*(1-3), 309-315.

[45] X. B. Cao, L. Gu, L. Zhuge, W. J. Gao, W. C. Wang, S. F. Wu, *Adv. Func. Mater.* **2006**, *16*(7), 896-902.

[46] V. R. Reddy, A. Currao, G. C. Calzaferri, *J. Mater. Chem.* **2007**, *17*, 3603-3609.

[47] R. Nowakowski, J. Pielaszek, R. Dus, *Appl. Surf. Sci.* **2002**, *199*, 40-51.

[48] Xu, J. Liu, J. W. Choung, Z. Zhou, *Int. J. Miner. Process.* **2003**, *68*(1-4), 183-196.

[49] P. Wu, J. Zhu, Z. Xu, *Adv. Func. Mater.* **2004**, *14*(4), 345-351.

[50] G. E. Pavlovskaya, C. F. Horton-Garcia, C. Dybowski, D. R. Corbin, T. Meersmannt, *J. Phys. Chem. B* **2004**, *108*(5), 1584-1589.

[51] C. D. Wagner, A. V. Naumkin, A. Kraut-Vass, J. W. Allison, C. J. Powell, J. R. Rumble Jr., (Compiled and Evaluated), *NIST X-ray Photoelectron Spectroscopy Database*, NIST Standard Reference Database 20, Version 3.4 (Web Version).

Chapter 5 Characterization of Mercury Removal from Flue Gases by Novel Magnetic Zeolite Composites with Silver Nanoparticles

Jie Dong, Zhenghe Xu and Steven M. Kuznicki, to be submitted

5. 1 Introduction

5.1.1 Background of Mercury Pollution

Coal-fired power plants, which contributes to major anthropogenic mercury emissions, will continue to be a major source of world energy production in the foreseeable future. Most of the mercury in the atmosphere is believed to be elemental mercury vapor that can circulate for several months to several years. Once mercury deposits on soils or in water, mercury may accumulate within living organisms through food chains and ultimately transform into a highly toxic organic form of methylmercury $[MeHg]^+$ by biological processes. Human exposure to $[MeHg]^+$ by eating contaminated fish and seafood will lead to adverse health consequences related to neurological and developmental damage, such as loss of sensory or cognitive ability, tremors, handicaps, convulsions or even death, depending on the $[MeHg]^+$ concentration in the ingested food.[1]

Even though mercury is a trace element in coal with relatively low contents varying with coal rank (0.01-3.3 mg/kg),[2] its emission into the environment can be substantial due to the large number and scale of operating coal-fired power plants distributed golbally. In flue gas streams of coal combustion, the concentration of mercury (both elemental and oxidized) typically ranges from 1 to 35 $\mu g/m^3$.[3,4] In general, oxidised mercury can be removed from the flue gas through wet scrubbing or dry sorbent injection for SO_x and NO_x emission control. However, only a small amount of vapour phase mercury can be removed along with the fly ash by particulate control devices, e.g. electrostatic precipitators (ESP) or baghouses, with the rest being emitted to the atmosphere as a hazard air pollutant. U.S. coal-fired power plants were estimated to emit 44.2 ton of mercury into the air in 2004.[5] The U.S. Environmental Protection Agency (EPA) has determined that the mercury emitted from utility power plants should be controlled and proposed regulations on mercury emissions.

5.1.2 Existing Technology for Mercury Removal from Flue gases

Mercury in coal is probably associated with the sulfide minerals such as pyrite (FeS_2) and cinnabar (HgS) in solid solutions. Some mercury may be organically bound to coal macerals.[6] These mercury compounds are not thermally stable. During coal utilization, all forms of mercury transform into elemental mercury which is emitted with combustion flue gas into the air. With decreasing gas temperatures, elemental mercury in the flue gas is able to react with other flue gas components. Some of the elemental mercury is converted to oxidized forms (primarily mercuric chloride) and some is affiliated with particulate matters leaving the system. Mercury is present in the flue gas in varying percentages of three basic chemical forms: particulate-bound, oxidized, and elemental mercury. The US National Energy Technology Laboratory (NETL) reported the mercury speciation in flue gas derived from different types of coal[7] (see Table 5.1). The elemental mercury is determined to be the hardest to remove because of its low melting point (-38.87 °C), low equilibrium vapour pressure (0.25 Pa at 25 °C) and low solubility in water (60 mg/l at 25 °C).[8]

Table 5.1 The mercury species in flue gases of burning different types of coal[7]

Type of Coals	Elemental mercury (%)	Oxidized mercury (%)	Particulate-bound mercury (%)
Bituminous coals	20	35	45
Sub-bituminous coals	65	20	15
Lignite coals	85	10	5

Current mercury cleanup technologies under investigation include activated carbon injection, non-activated carbon-based sorbent injection, catalyst- or chemical additive- promoted oxidation of elemental mercury coupled with sulfur control systems.

Sorbents based strategies

Injecting a sorbent such as powdered activated carbon into the flue gas represents one of the simplest and most tested approaches to controlling mercury emissions from coal-fired boilers. The mercury vapor in the flue gas contacts the sorbent and attaches to its surface. The sorbent with captured mercury is then collected by the existing particulate control device, either an electrostatic precipitator or fabric filter. Activated carbon and chemically modified activated carbons have been extensively tested.[9, 10] The chemical modification of activated carbons includes impregnation with chlorine, sulphur, bromide or iodine to improve mercury capture. The effectiveness of activated carbon as an adsorbent is attributed to its unique properties, including large specific surface area, high degree of surface reactivity, unselective adsorption and favourable pore sizes. Activated carbon can be manufactured from a variety of sources such as lignite, peat, coal, wood, petroleum coke, etc.. The features of these activated carbons have been reviewed in a large number of publications.[5]

However, the application of activated carbon injection (ACI) for mercury capture at coal-fired utility boilers is still in its early stages. The effectiveness of ACI for mercury capture under varied flue gas conditions (e.g., fuel properties, flue-gas temperature, and trace-gas constituents such as chlorine, sulfur, NOx, and calcium) is still being investigated. DOE (U.S. Department of Energy) estimated a cost for this control technology (at 90% mercury removal) between $50,000 and $70,000 per pound of mercury removal. This technology could cost the coal-fired utility industry $2.6 billion to $7.3 billion dollars per year.[11] Furthermore, the effect of long-term use of ACI (or any other injected sorbent or additive) on plant operations has yet to be determined. It is likely that some degradation in the performance of downstream equipment, primarily particulate collection devices, may occur. In addition, for utilities that sell their fly ash for cement manufacture, increase in carbon content (or the addition of other chemical compounds) may negatively affect their ability to market the product, and incur additional disposal costs. Full-scale testing of activated carbon at one site resulted in unacceptable carbon levels in ash that the sale of the fly ash was not possible during the test period.

Additives- and Catalysts- Promoted Mercury Oxidation

Oxidized mercury can be effectively captured in coal-fired power plants equipped with wet flue gas desulfurization (FGD) systems. Therefore, a method to convert the elemental mercury to oxidized mercury in the flue gas would enhance overall mercury capture without sorbent injection. Mercury oxidation technologies being investigated include additive of catalysts, use of chemical additives and co-firing of materials. Based on the hypothesis that a sulfide-donating species could assist in capturing Hg^{2+}, the H_2S gas was first selected as a potential additive.[12, 13] Addition of oxidants such as chlorine-containing salts added to the lignite can promote the conversion of elemental mercury to more reactive oxidized forms. For an actual selective catalytic reduction (SCR) unit, some Ti/V-based SCR catalysts as well as Al_2O_3, TiO_2 and V_2O_5 are capable of oxidizing a certain amount of elemental mercury in flue gas. WO_3, on the other hand, can strongly promote elemental mercury oxidization.

The catalytic oxidation process of mercury, which remains under development, uses catalyst materials on honeycomb substrates to promote the oxidation of elemental mercury in the flue gas from coal-fired power plants.[14] Investigations showed that the carbon-based and fly-ash-based materials can be successfully combined with alumina, extruded and fired to produce a reactive honeycomb monolith. The activities of these two catalyst materials for mercury oxidation are about equal to that of the commercially available SCR catalyst. In addition, noble metal-impregnated catalysts have shown high potential to oxidize elemental mercury.[15]

5.1.3 Noble-metal-based (Ag) Magnetic Zeolite Composite Sorbents

One alternative to ACI might be the use of noble metal-based mercury sorbents. The noble metals, including gold and silver, will form reversible amalgams with mercury. Noble metals (mostly gold films) coated on silica, alumina, glass beads or other materials have been used to pre-concentrate gaseous metallic mercury.[16, 17, 18] However, the high cost and instability of the gold film coated on different substrates make it unfeasible in practical applications.[17, 19, 20] To effectively and economically collect trace amounts of mercury from the flue gases of coal-fired power plants, a noble metal-based sorbent should be stable, with high affinity for the targets, which can be readily engineered for effective separation from complex, multiphase systems and regenerated repeatedly.

In *Chapter 4*, a novel, yet simple method is proposed to synthesize magnetic zeolite composites with silver nanoparticles. This material is an excellent candidate sorbent for elemental mercury removal from the flue gases of coal-fired power plants. In the proposed application, mercury vapor in flue gas is captured by the sorbent, and the mercury-loaded sorbent is then collected by an existing particulate control device and separated from the fly ash by magnetic separation. After mild heat treatment to release captured mercury, the sorbent is regenerated for the next cycle of mercury capture. The application of the new sorbents in the mercury removal from flue gases is illustrated in Figure 5.1.

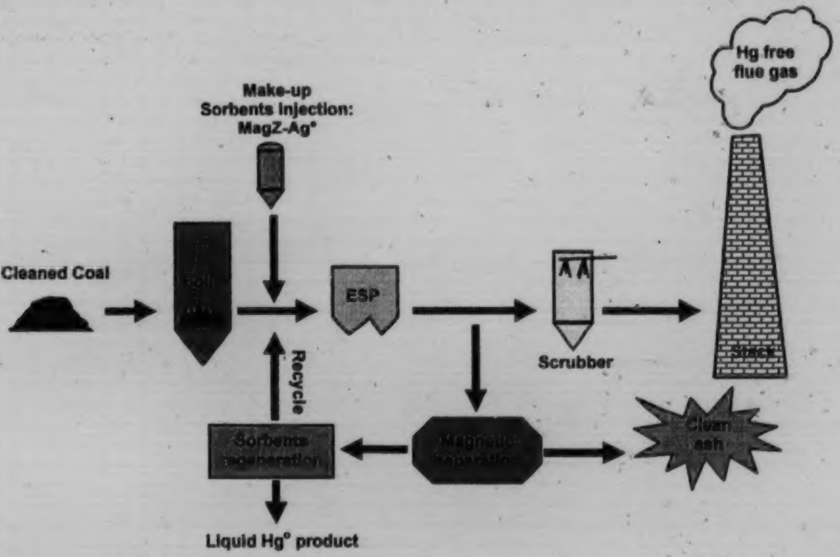
Hg free flue gas
Make-up Sorbents Injection: MagZ-Ag°
Cleaned Coal
ESP
Scrubber
Stack
Recycle
Sorbents regeneration
Magnetic separation
Clean ash
Liquid Hg° product

Figure 5.1 Application schemes of new magnetic zeolite sorbents with silver nanoparticles for mercury removal from flue gases.

This chapter focuses on the evaluation of the suitability of this novel magnetic zeolite composites with silver nanoparticles as sorbents for the removal of elemental mercury vapor. The mercury breakthrough temperature and mercury capacity were compared for sorbents of varied silver content. Selected sorbents were tested for magnetic recovery, regeneration and recyclability. The relationship between the content and size of silver in the sorbent and the mercury adsorption performance was examined. Finally, the novel sorbents were tested in situ by exposure to flue gases from a full-scale coal-fired power plant.

5.2 Experimental

5.2.1 Materials and Preparation

The materials and experimental procedures for the preparation of magnetic zeolite composite (MagZ) are the same as described in Chapter 4. For this study, MagZ-Ag° samples of varied silver content were prepared by ion exchange with different amounts of

$AgNO_3$, followed by thermal reduction. The samples and synthesis conditions are summarized in Table 5.2. DLSC-Fe_3O_4 and zeolite were prepared following the same procedures.

Table 5.2 Samples synthesis conditions and nomenclature

Source Sample	$AgNO_3$ Concentration	Post-Ion Exchange Nomenclature	Post-Reduction Nomenclature
MagZ	EEC*	MagZ-Ag^+	**MagZ-Ag°**
MagZ	1/2EEC	1/2MagZ-Ag^+	**1/2MagZ-Ag°**
MagZ	2EEC	2MagZ-Ag^+	**2MagZ-Ag°**
DLSC-Fe_3O_4	2EEC	2FeSi-Ag^+	**2FeSi-Ag°**
Zeolite	EEC	Z-Ag^+	**Z-Ag°**

* EEC: equivalent exchange capacity of zeolite (2.5 meq/g).

5.2.2 Characterization

The mercury breakthrough measurement was the same as the described in Chapter 4.2.4. The Hg° adsorption capacities of sorbents were estimated by continuous mercury breakthrough monitoring, which provides a real-time or near-real-time response for Hg^0 measurements over a long period. The experimental set-up is shown in Figure 5.2. A Dynacalibrator with a built-in permeation tube (with a mercury emission rate of 42.5 ng/min at 50°C and flow rate of 137 mL/min) was used as the mercury source for the continuous mercury monitoring tests.

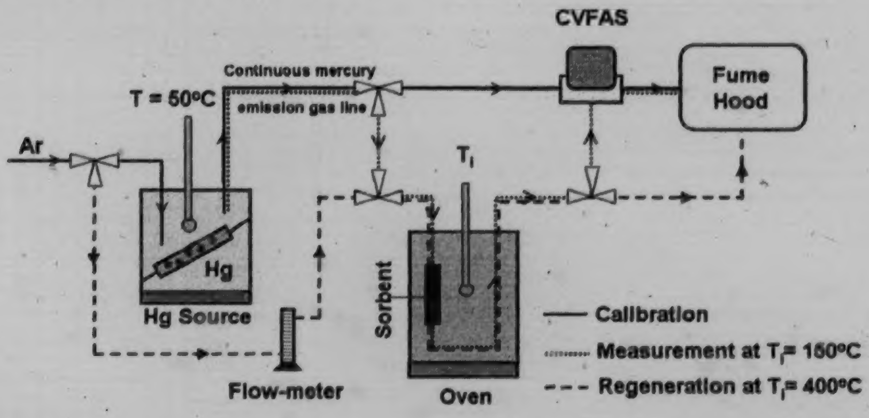
CVFAS
Fume Hood
Continuous mercury emission gas line
T = 50°C
Ar
T_i
Hg
Hg Source
Sorbent
Flow-meter
Oven
Calibration
Measurement at T_i= 150°C
Regeneration at T_i= 400°C

Figure 5.2 The experimental set-up for mercury capture capacity and sorbent regeneration tests.

Mercury inlet concentration and background signal were recorded by the CVAFS detector. The area between the inlet mercury concentration line and the background baseline was used to calculate the total mercury passing through the system, while the area between the inlet mercury concentration line and the mercury breakthrough curve (real time effluent mercury concentration curve) was used to determine the mercury captured by the sorbent. The specific amount of mercury captured by the sorbent was determined in terms of "µg Hg adsorbed/g sorbent". From the practical application point of view, the mercury capture capacity of the sorbent is integrated to the time when mercury breakthrough reaches a threshold value of 20%, i.e. ≥ 80% of mercury removed from the stream. The capacities of sorbents were determined at 150°C which reflects the practical flue gas temperature. An illustration of the capacity measurement is shown in Figure 5.3.

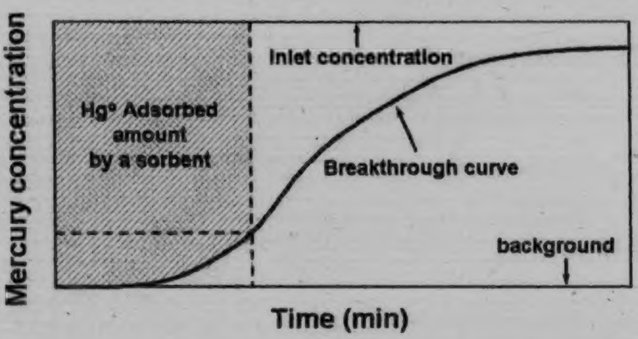

Figure 5.3 An illustration of the mercury capture capacity measurement.

After each mercury capacity measurement, sorbents were removed from the continuous mercury emission gas line and regenerated by heating to 400°C and flushing with argon carrier gas for 2 hrs. The temperature was then decreased to 150°C and the sorbent was placed back into the continuous mercury emission gas line to initiate another capacity measurement cycle.

The sorbents were characterized by X-ray diffraction (XRD) analysis using a RIGAKU Rotating Anode XRD System with an RU-200B generator. Wide angle x-ray diffraction patterns of powers were collected from 10° to 120° at 40kV and 160 mA using cobalt as the anode. SEM imaging was performed on a JSM6301FXV SEM (JEOL), operating in backscatter mode at 20kV accelerating voltage. Energy dispersive x-ray analysis (EDX) was performed with a PGT (Princeton Gamma Tech) IMIX x-ray analyzer. Samples were coated with Cr for electron conduction. TEM imaging was performed on a JEOL-2010 Transmission Electron Microscopy. Particles were dispersed in toluene and transferred to a thin carbon film supported on a TEM copper grid. The micrographs of synthesized particles were obtained in bright-field imaging mode at 200 kV acceleration voltage.

5.3 Results

5.3.1 Mercury Breakthrough

The increase in Hg° breakthrough temperature by silver nanoparticles in MagZ-Ag° has been previously demonstrated in Chapter 4. The amalgamation of Hg° with Ag° leads to a more stable sorption than the physisorption. In this study, three MagZ-Ag° species containing different levels of surface-supported silver particles, 1/2MagZ-Ag°, MagZ-Ag° and 2MagZ-Ag°, were prepared to investigate whether the amount of silver loading on MagZ plays a role in enhancing mercury capture. Silver zeolite (Z-Ag°), which contains no magnetite, was compared with MagZ-Ag° to assess the possible impact of Fe_3O_4 incorporation on the formation of silver particles and subsequent Hg° capture. 2FeSi-Ag°, which contains no zeolite, was prepared to determine whether mercury can be captured by silver deposited (but not ion exchanged) on the surface of DLS-coated Fe_3O_4.

The results in Figure 5.4 show that 2FeSi-Ag° could capture almost all the mercury in carrier gas at low temperature (< 100°C). Since DLSC-Fe_3O_4 has been proven to adsorb negligible Hg° at the same temperature (Chapter 4), the observed capture of mercury by 2FeSi-Ag° is attributed to silver deposited on DLSC-Fe_3O_4. However, at temperatures higher than 150°C, mercury broke through 2FeSi-Ag° quickly. At 250°C, mercury breakthrough reached 100%. The mercury capture characteristics of 2FeSi-Ag° was substantially different from the samples of the 1/2MagZ-Ag°, MagZ-Ag° and 2MagZ-Ag°, which showed little mercury breakthrough at temperatures below 200°C. At 250°, a noticeable mercury breakthrough was observed, increasing to 20% as silver content decreases to 1/2EEC in 1/2MagZ-Ag°. This observation indicates that the silver nanoparticles formed on the samples of 1/2MagZ-Ag°, MagZ-Ag° and 2MagZ-Ag°

exhibit superior performance of mercury capture at high temperatures as compared with silver deposited on 2FeSi-Ag°. Z-Ag° performed the best, showing negligible mercury breakthrough even at 250°C. Compared to Z-Ag°, the presence of magnetite in MagZ-Ag° reduces mercury capture capability at 250°C, possibly by affecting the silver nanoparticles. The reasons will be addressed in the discussion.

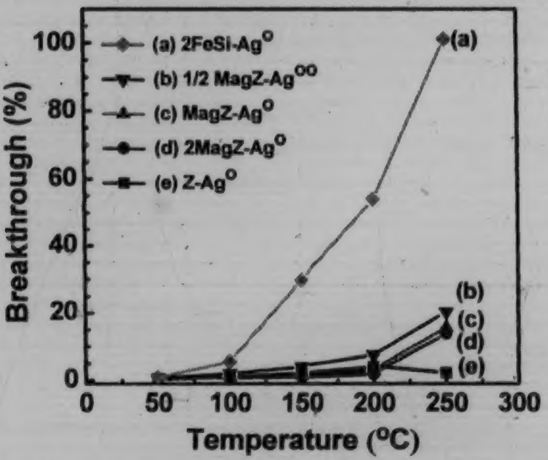

Figure 5.4 Role of silver on various sorbents in mercury capture at varying temperatures.

5.3.2 Mercury Capture Capacities

The mercury capture capacities of various sorbents were calculated from the individual continuous mercury breakthrough curves, and the steps were the same as described in section 5.2.2. The important results were summarized in Table 5.3. As expected, the performance is closely related to the silver contents in the samples. The relationship of silver contents in the samples and the mercury capacity is plotted in Figure 5.5. For a given sample size, e.g. 50 mg, 2FeSi-Ag° shows a negligible mercury capacity, but Z-Ag° shows the largest capacity and longest using time, due to its highest silver contents among the samples.

The amount of silver in 2MagZ-Ag° is 9.1 wt%, which is higher than the silver content in MagZ-Ag°. The additional silver may come from the excess silver ions in the solution adsorbing on MagZ of large specific surface area. After complete adsorption, no more silver could be brought into the MagZ, so that the amount of silver on MagZ is less than silver added. Furthermore, the washing would also remove some weakly attached silver ions from the surface of MagZ. As a result, the silver content in 2MagZ-Ag° is less than the twice of that in MagZ-Ag° even though twice as much of silver is available in solution.

Table 5.3 The important parameters and results from mercury capture capacity studies of various samples

Sample Name	Amounts (mg)	Time* (min)	Capacity** (µg Hg°/g Total)	(µg Hg°/g Zeolite)	Wt% of Ag
2FeSi-Ag°	52	<1	0.79	-	1.1
1/2MagZ-Ag°	51	10	8.0	27	3.4
MagZ-Ag°	51	18	13.3	44	7.0
2MagZ-Ag°	49	56	43.9	146	9.1
Z-Ag°	48	586	502.5	502.5	27.6

* For the listed amount of samples, the time of a sorbent can be used to reach ≥ 80% mercury captured.

** The capacity is calculated to reach ≥ 80% mercury captured.

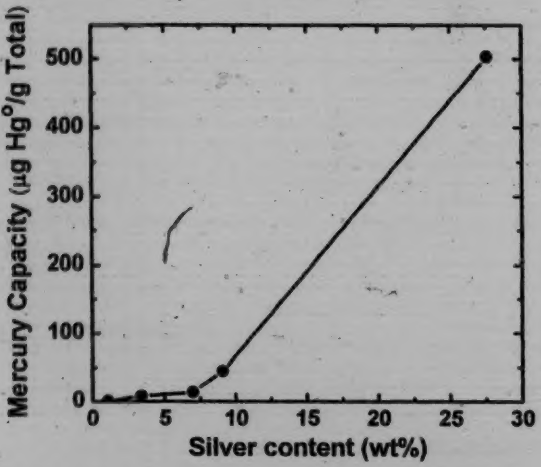

Figure 5.5 The relationship of silver contents in samples and the mercury capacity.

Although the silver content (27.6 wt%) in Z-Ag° was only about three times of the silver in MagZ-Ag°, depending on the content of zeolite in MagZ, the capacity of Z-Ag° was thirty times of the capacity of MagZ-Ag°. Similarly, even for Mag-Ag° and

2Mag-Ag°, the mercury capacity does not correlate with the amount of Ag° in the sorbent. All of these observations indicate that other factors, such as size of the silver particles and state of silver, also impact the mercury capacity, which will be discussed later in this chapter.

5.3.3 Sorbent Regeneration

In this study, regeneration of spent sorbent was accomplished by thermally treating the spent sorbent at 400°C for two hours. This temperature was identified as the lowest temperature at which a negligible amount of mercury was captured by MagZ-Ag°. A thorough release of the captured mercury by decomposition of Ag°-Hg° amalgam at this temperature is anticipated. A higher temperature was supposed to accelerate mercury release kinetics, but may change the morphology of silver in the sorbent and magnetic properties of magnetite component. The capacities were estimated for ≥80% Hg° capture and the results are shown in Figure 5.6.

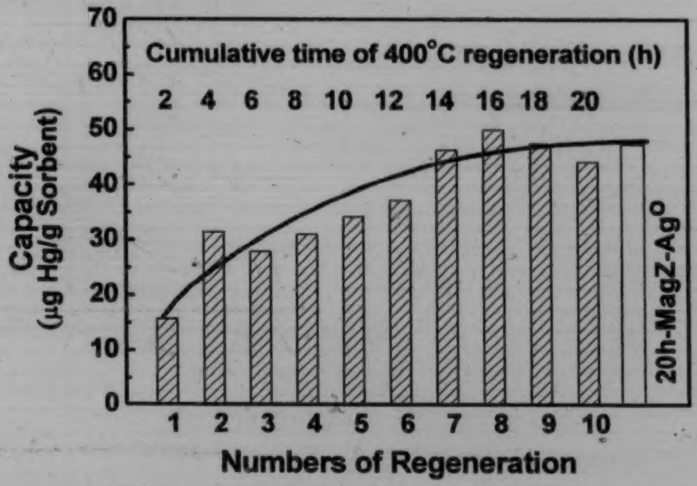

Figure 5.6 Mercury capacities of MagZ-Ag° for ten cycles of capture/regeneration at ≥80% Hg° capture (dashed columns) and the capacity of MagZ-Ag° after 20 h continuous thermal treatment at 400°C (the blank column).

It was very interesting to observe that the capacity of MagZ-Ag° increased with more capture/regeneration cycles. The capacity of the first cycle for 80% Hg° capture was 15.7 μg/g, within the range of experimental error of 10-15%. The capacity of the second utilization reached 31.4 μg/g, representing a 50% increase in mercury capture capacity of the first utilization. The capacity increased steadily with more cycles of applications. At the tenth cycle, the capacity (44.2 μg/g) was almost three times that of the first cycle.

The increase in the Hg° adsorption capacity of MagZ-Ag° following regeneration at 400°C likely indicates increases in the Ag° available for Hg° capture. As shown in Figure 5.6, the effect of the 400°C thermal treatments is cumulative and the Hg° adsorption capacity increases with further regeneration cycles. It is possible that the regeneration, essentially a thermal reduction performed in an inert gas atmosphere, results in partial transformation of Ag^+ to Ag°. Alternately, extended thermal treatment may result in the migration of reduced Ag° from the cages of the zeolite framework to the surface, where the surface-supported silver nanoparticles are most accessible for effective Hg°capture.

A support experiment was performed to prove the effect of thermal treatment time. One $MagZ\text{-}Ag^+$ sample was continuously heated to and kept at 400°C for 20 hours. The mercury capture capacity was then measured in the same way as the cycle experiments. The capacities were also shown in Figure 5.6 (the blank column). It is extremely interesting to note that the capacity of MagZ-Ag° after 20 hr thermal treatment at 400°C was very close to that of tenth cycled MagZ-Ag° with a cumulative of 20 h heat treatment. Thus, it is proved that longer treatment do improve the mercury capacity of MagZ-Ag°. However, in practical application, two hours of thermal treatment is sufficient to trigger the initial mercury capture capability. With more mercury capture/regeneration cycles, the performance of the sorbent will be steadily improved rather than degraded, which is a very attractive feature of this sorbent.

Another important fact worth to discuss is that the mechanism of amalgamation between Ag° and Hg° is a surface sensitive adsorption process. The diffusion of mercury atoms into the silver particles is extremely slow and may be considered negligible. Thermodynamically, Ag° and Hg° can form amalgam over wide ratios. The theoretical capacity of MagZ-Ag° should be 130 mg Hg/g, calculated based on a 1:1 Ag° and Hg°

ratio. However, the obtained maximum capacity of the tenth cycle of MagZ-Ag° is 44.2 μg/g, only 0.034% of the theoretical capacity. Therefore, if the 20 h thermal treatment converts most of the Ag^+ to Ag°, it appears that the surface area of Ag° is a limiting factor. For the same amount of Ag°, the particles with much smaller size will have much larger surface areas and hence higher mercury capture capacities. The different size of silver particles in various samples could partially accounts for the observed variation of the mercury capacity with silver contents.

5.3.4 Sorbent Recovery

One of the most important features of the magnetic composite sorbent is the magnetic property, which enables the magnetic separation of the spent sorbent from complex multi-phases. The magnetic sorbents with adsorbed mercury and fly ash are collected by electrostatic precipitator (ESP). The magnetic sorbents can be recovered from fly ash by magnetic separation for regeneration and recycle. In experiments, raw fly ash was well mixed with the sorbent to a certain ratio by shaking in a container. A hand magnet was then attached to the bottom of the container, so the magnetic sorbent was collected to the bottom by magnetic force, while non-magnetic fly ash mainly aluminum silicate, is discarded to achieve the separation of magnetic sorbent.

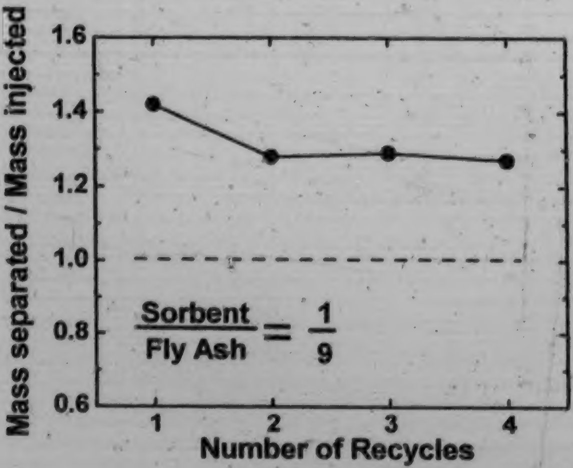

Figure 5.7 The result of magnetic separation of sorbent from fly ash as a function of recycle numbers.

Figure 5.7 shows the result of separating one part of magnetic sorbent from nine parts of fly ash. The ratio of the mass separated to the mass of sorbent injected is about 1.4 after the first use. The increase in the mass separated is attributed to the attachment of very fine ash to the surface of MagZ-Ag°. The recovered sorbent was mixed with fly ash and separated for another three cycles. This ratio is maintained at about 1.3, without further accumulation of ash on the surface. Since the magnetic sorbent is black color and fly ash is light grey, visually no black particles were found in the rejected fly ash, indication a complete recovery of the spent sorbent. As a result, the rejected fly ash is sorbent free, which is favourable for cement manufacture.

5.3.5 Estimation of Sorbent Injection

From the calculated capacities (Table 5.3 and Figure 5.6), the quantitative estimation of the amount of sorbent injection (mg/m^3) is provided here. The parameters used for flue gas are as following: mercury concentration in flue gas is 35 $\mu g/m^3$; volume flow rate of flue gas is 1000 m^3/h; residence time is 10 s. Base on these parameters, the required amount of various sorbents to reach ≥ 80% of mercury removal is summarized in Table 5.4.

Table 5.4 The estimation of various sorbent injections for ≥80% mercury removal

sorbent	capacity (μg/g)	injection amount (kg/h)
2FeSi-Ag°	0.79	44.42
1/2MagZ-Ag°	8.00	4.38
2MagZ-Ag°	43.90	0.80
MagZ-Ag° -1	15.70	2.23
MagZ-Ag° -2	31.42	1.11
MagZ-Ag° -3	27.86	1.26
MagZ-Ag° -4	31.02	1.13
MagZ-Ag° -5	34.15	1.02
MagZ-Ag° -6	37.12	0.94
MagZ-Ag° -7	46.24	0.76
MagZ-Ag° -8	49.98	0.70
MagZ-Ago -9	47.49	0.74
MagZ-Ag° -10	44.16	0.79
20h MagZ-Ag°	46.84	0.75
Z-Ag°	502.54	0.07

These results represent the amount of sorbents required for only one injection and they reach the removal limit and are collected for regeneration. The current activated carbon injection (ACI) from EPCOR is 61 kg/h.[21] Except 2FeSi-Ag°, all the other samples performed much better than ACI. Since Z-Ag° can not be effectively separated from fly ash, it is not suitable for direct injection, but may be good for developing mercury cartridge.

5.4 Discussion

5.4.1 X-Ray Diffraction

XRD is used to characterize and identify of polycrystalline phases. In the XRD pattern, the characteristic peak of polycrystalline silver for (111) face is located at $2\theta = 44.7°$ and for (200) face at $2\theta = 51.8°$. In Figure 5.8 these two peaks are clearly visible for the samples of 2FeSi-Ag°, 1/2MagZ-Ag°, MagZ-Ag° and 2MagZ-Ag°. The peak at 50.9° is from magnetite. The intensity of these peaks is in the order of 2MagZ-Ag° ≈ MagZ-Ag° > 1/2MagZ-Ag° > 2FeSi-Ag. The intensity of these peaks reflects the amount of silver in the sample. Thus, this observation is consistent with x-ray composition analysis shown in Table 5.3.

However, Z-Ag° has the highest silver content in x-ray composition analysis, but does not show any peaks of silver in the XRD pattern (Figure 5.8). Two possible reasons may explain this observation. First, the Ag° in Z-Ag° may be very small in size and less well defined in crystallinity, leading to insufficient elastic scattering of x-ray to give the characteristic peaks. Alternatively, the transformation of Ag^+ to Ag° may only occur partially, and Ag^+ did not have characteristic peaks in XRD. Since Z-Ag° has the large of mercury capacity, indicating the presence of Ag°, the second reason appears unlikely the case. Characterization of SEM and TEM will provide more insights on those sorbents.

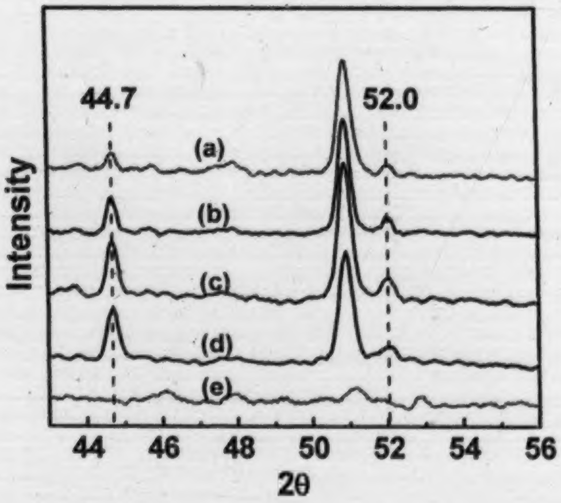

Figure 5.8 XRD analysis of (a) 2FeSi-Ag°, (b) 1/2 MagZ-Ag°, (c) MagZ-Ag°, (d) 2MagZ-Ag° and (e) Z-Ag°.

5.4.2 Field Emission Scanning Electron Microscopy

Figure 5.9 (a) shows the randomly deposited silver on the surface of 2FeSi-Ag°. They were large pieces and only occasionally observed due to the small amount of silver (1.1 wt%). The visible silver peaks found on XRD diffractions of 2FeSi-Ag° come from these polycrystalline Ag° pieces even though the atomic concentration of silver in 2FeSi-Ag° is not high. In the micrographs of 1/2MagZ-Ag° and MagZ-Ag° (Figure 5.9 (b, c)), clear silver particles are observed. The size of silver particles ranges from 100 to 200 nm. The surface prevalence of Ag° for 1/2MagZ-Ag° (Figure 5.9(b) was lower than that for MagZ-Ag° (Figure 5.9(c)). Figure 5.9 (d) shows the distribution of Ag° on the surface of 2MagZ-Ag°. Some larger Ag° aggregates were observed. It appears that the overdose of $AgNO_3$ at 2EEC concentration during the ion exchange caused sintering of small Ag° due to increased concentration and reduced inter-particle distances. These silver particles in Figure 5.9 (b, c, and d) produced characteristic Ag° peaks in XRD. However, in the image of Z-Ag° (Figure 5.9 (e)) large Ag° particles were not observed. Only scattered tiny shiny spots were visible, showing that the size of silver particles in Z-Ag° was much smaller than those in 1/2MagZ-Ag°, MagZ-Ag° and 2MagZ-Ag° samples. Silver particles of extremely small sizes in Z-Ag° do not lead to Ag° diffraction peaks in XRD as shown in Figure 5.8 (e).

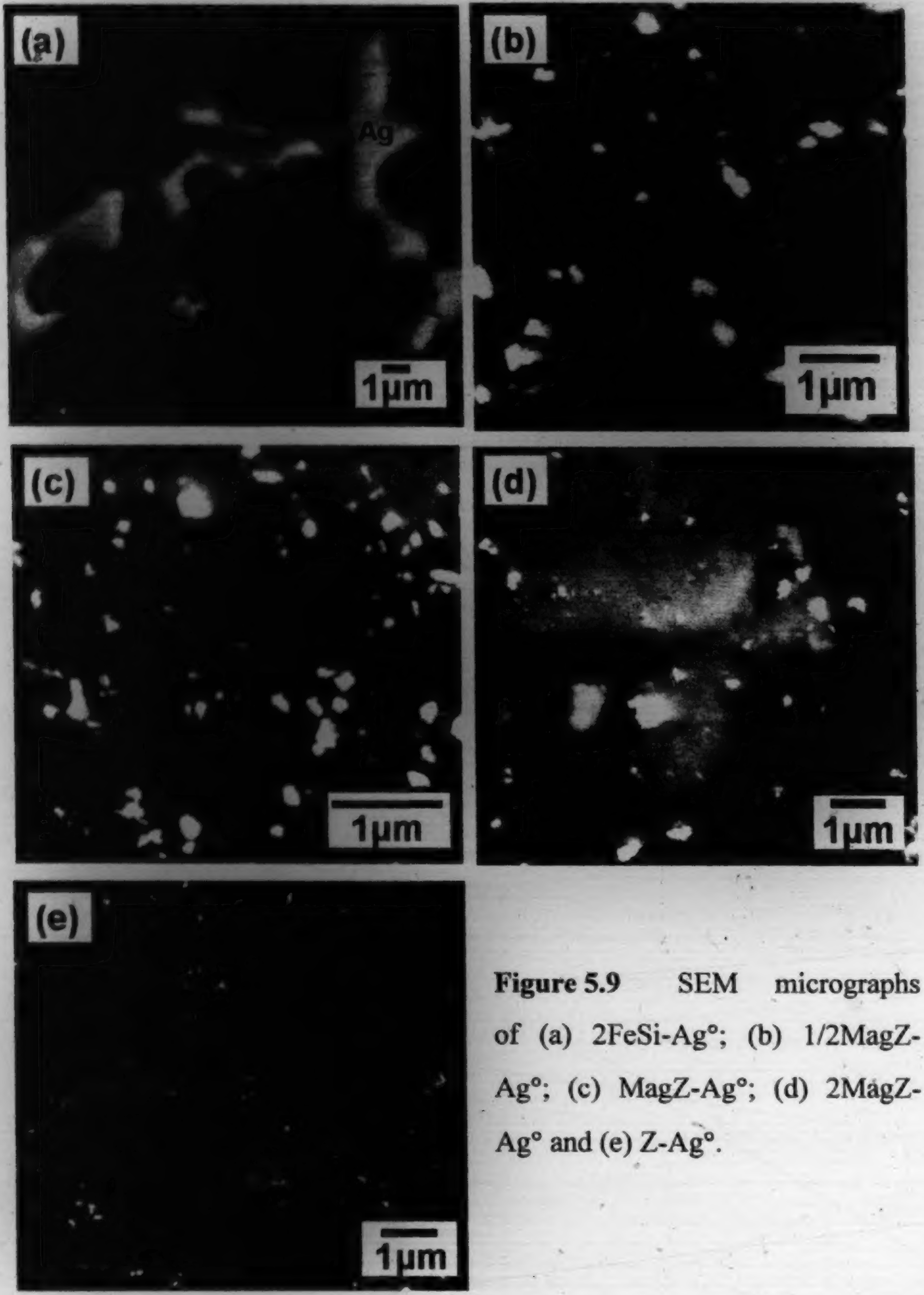
(a)
Ag
1µm
(b)
1µm
(c)
1µm
(d)
1µm
(e)
1µm

Figure 5.9 SEM micrographs of (a) 2FeSi-Ag°; (b) 1/2MagZ-Ag°; (c) MagZ-Ag°; (d) 2MagZ-Ag° and (e) Z-Ag°.

5.4.3 Transmission Electron Microscopy

Under TEM, silver nanoparticles of sizes between 5~10 nm are observed on the surface of zeolite in both Z-Ag° and MagZ-Ag° samples, as shown in Figures 5.10 (a) and (b). This observation indicates the similar origin of these silver nanoparticles from the zeolite framework. A few big particles with the sizes around 20 nm were also observed in Z-Ag°, which may come from the aggregation of small silver nanoparticles.

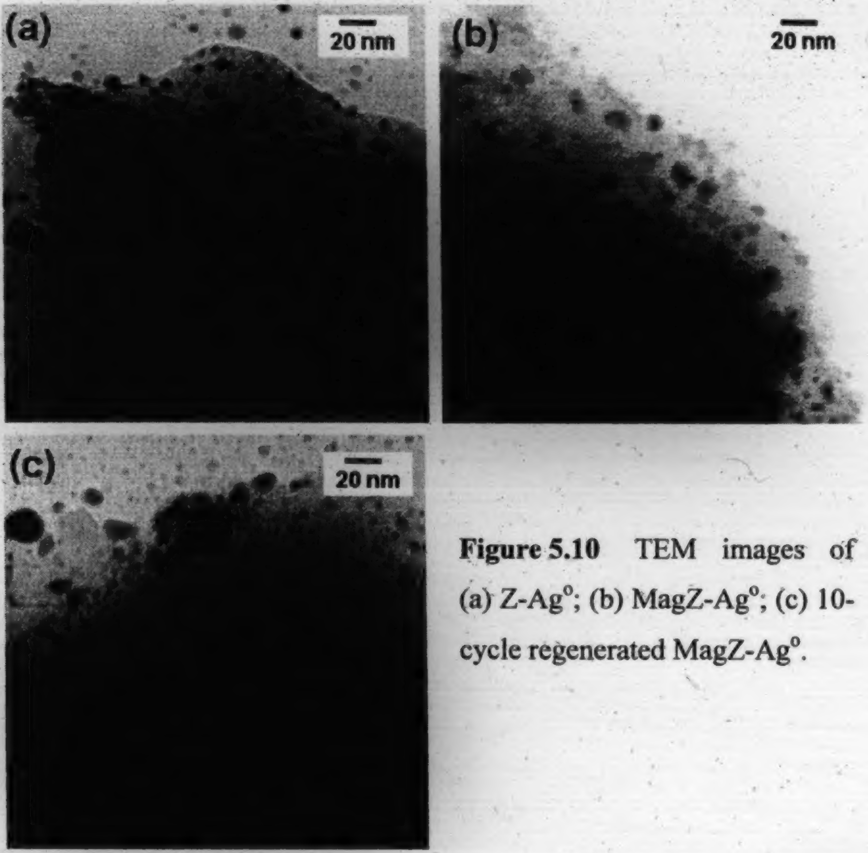

Figure 5.10 TEM images of (a) Z-Ag°; (b) MagZ-Ag°; (c) 10-cycle regenerated MagZ-Ag°.

Although silver particles around 20 nm were not observed on the MagZ-Ag° sample under TEM, the larger size silver aggregates (~150 nm) are visible in SEM micrograph of Figure 5.9 (c). Overall, Z-Ag° and MagZ-Ag° samples share the same feature of silver nanoparticle (5~10 nm), but MagZ-Ag° has more large aggregates than Z-Ag°. Therefore, the differences of the mercury capacities of MagZ-Ag° and Z-Ag°, calculated as "mg Hg/g equivalent zeolite", appear to come from the effect of particle size. The prevalence of silver nanoparticles in Z-Ag° provides large surface area and high surface activity of silver, and thus the large mercury capacity.

The TEM image of MagZ-Ag° after 10 times Hg° adsorption and regeneration was shown in Figure 5.10(c). It was found that the size of Ag° nanoparticle did not change dramatically, but the number of silver nanoparticles increased upon Hg° adsorption/regeneration (Figure 5.10(c)). Therefore, it is believed that the silver nanoparticles are stablized on the surface of zeolite with enhanced concentration of silver nanoparticles during multiple adsorption and desorption, translating to enhanced mercury capture capacity, as demonstrated in the multiple recycle test.

5.5 Mercury Capture in the Flue Gas of a Coal-fired Power Plant

Three of the samples were exposed to the flue gases of a Rankine Cycle coal-fired power plant at EPCOR Genesee station to evaluate the mercury capture in a practical environment. The components of flue gas include $H_2O(v)$, CO_2, SO_x, NO_x, O_2, CO, HCl/HF and fly ash, which could be detrimental to mercury capture. In these tests, various sorbents were exposed to the flue gas for 5 minuets. The mercury adsorbed on each sample is shown in Figure 5.11. These results give an indication on the capability and robustness of the sorbent for mercury capture in a practical application environment.

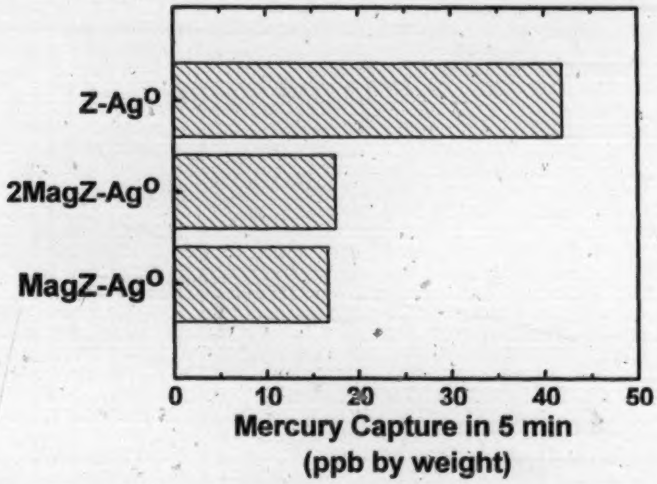

Figure 5.11 Mercury capture (ppb wt) by different sorbents over a 5-minute exposure in the flue gases of an operating Rankine Cycle coal-fired power plant.

MagZ-Ag° and 2MagZ-Ag° captured a similar amount of mercury, much less than the amount (40%) captured by Z-Ag°. However, on the basis of zeolite, MagZ-Ag° and Z-Ag° captured about same amount of mercury after 5-minute exposure. One the other hand, even though the silver content in 2MagZ-Ag° is higher than that in MagZ-Ag°, 2MagZ-Ag° did not capture any more mercury than MagZ-Ag° within the same exposure time. The additional silver of large size in 2MagZ-Ag° does not provide extra adsorption of mercury. Although magnetic zeolite sorbents do not capture as much mercury as Z-Ag°, the easy separation and recycle of the spent magnetic zeolite sorbents will compensate the decrease of mercury adsorption by multi-application, while Z-Ag° will be lost in the fly ash.

5.6 Conclusions

In this chapter, three MagZ-Ag° species containing different levels of surface-supported silver particles, 1/2MagZ-Ag°, MagZ-Ag° and 2MagZ-Ag°, were prepared to investigate whether the amount of silver loading on MagZ plays a role in enhancing mercury capture. Silver zeolite (Z-Ag°) was compared with MagZ-Ag° to assess the possible impact of Fe_3O_4 incorporation on silver particles formation and subsequent Hg° capture. 2FeSi-Ag° was prepared to determine whether mercury can be captured by silver deposited (but not ion exchanged) on the surface of DLS-coated Fe_3O_4.

1/2MagZ-Ag°, MagZ-Ag° and 2MagZ-Ag° showed a complete capture of mercury up to 200°C, which was higher than that of 2FeSi-Ag° (100°C), but lower than that of Z-Ag° (250°C). The mercury capture capacities of these samples for a single use are in the increasing order of 2FeSi-Ag°, 1/2MagZ-Ag°, MagZ-Ag°, 2MagZ-Ag°, and Z-Ag°. XRD, SEM and TEM studies show that the breakthrough temperature and capacities of these samples were related to the amount of silver loading and the size distribution of silver (nano)particles. The 2FeSi-Ag° contains only low content, large size silver pieces; 1/2MagZ-Ag°, MagZ-Ag° and 2MagZ-Ag° contain both large silver aggregates (~150 nm) and silver nanoparticles (5~10 nm); and Z-Ag° contains only silver nanoparticles (<20nm). The presence of magnetite may be the reason of large silver aggregates. The silver nanoparticles with the size below 20 nm are the most effective and efficient component to capture mercury.

MagZ-Ag° was selected to test sorbent regeneration and recyclability for totally 10 cycles. The calculated capacities were found to increase with more cycles of application. The cumulative thermal treatments at 400°C during mercury desorption/sorbent regeneration process may promote the further transformation of Ag^+ to Ag° and the migration of Ag° from the cages of zeolite framework to the zeolite surface. Independent experiment of MagZ-Ag° after 20h continuous thermal treatment shows the close mercury capacity as that of MagZ-Ag° after 10 cycles of application and regeneration. It demonstrates that extended treatment at 400°C can improve the mercury capacity of MagZ-Ag°.

The magnetic sorbents can be separated successfully by a hand magnet from fly ash. Although some fine ash particles attached to the sorbent, the fly ash did not accumulate on the surface during multi-cycle application and separation. The amount of sorbent injection was estimated to range from 2.23 kg/h to 0.79 kg/h, for the first and tenth cycle of application, which is less than the current amount of activated carbon injection.

Mercury capture from the flue gases of a full-scale coal-fired power plant demonstrated the capability of the sorbents to capture mercury in the presence of H_2O(v), CO_2, SO_x, NO_x, O_2, CO, HCl/HF and fly ash, and showed the robustness of the sorbents. It is clear that the MagZ-Ag° has great potential in providing a viable solution to control mercury emission from coal-fired power plants.

References

1 Mishima, A. *Bitter Sea: The Human Cost of MInamata Disease*. Kosei Publishing Co., Tokyo, Japan, 1992.

2 His, H.; Chen, S.; Rostam-Abadi, M.; Rood, M. J.; Richardson, C. F.; Carey, T. R.; Chang, R. *Energy Fuel* 1998, 12, 1061-1070.

3 Serre, S. D. ; Silcox, G. D. *Ind. Eng. Chem. Res.* 2000, 39, 1723.

4 Wu, B.; Peterson, T. W.; Shadman, F. *Fuel Process. Technol.* 2000, 63, 93–107.

5 Yang, H.; Xu, Z.; Bland, A. E.; Judkins, R. R. *J. Hazard. Mater.* 2007, 146,1-11.

6 Pavlish, J. H.; Sondreal, E. A.; Mann, M. D. *Fuel Process. Technol.* 2003, 82, 89–165.

7 Pavlish, J. H. ; Holmes, M. J.; Benson, S.A. *Fuel Process. Technol.* 2004, 85,563–576.

8 Lopez-Anton, M. A.; Tascon, J. M. D.; Martinez-Tarazona, M. R. *Fuel Process. Technol.* 2002, 77, 353.

9 Krishnan, S. V., Gullett, B. K., Jozewicz, W., *Environ. Sci. Technol.* 1994, 28, 1506–1512.

10 Sinha, R. K., Walker, P. L. *Carbon* 1972, 10, 754.

11 DOE-Fossil Energy: Mercury Emission Control R&D, http://www.fossil.energy.gov/programs/powersystems/pollutioncontrols/overview_mercurycontrols.html

12 Audeh, C. A.; Hoffma, B. E., 1991, U. S. Patent 4, 981, 577.

13 Degnan, T. F.; LeCours, S. M., 2002, U. S. Patent 6, 350, 372.

14 Presto, A. A.; Granite, E. J.; Karash, A.; Hargis, R. A.; O'Dowd, W. J.; Pennline, H. W. *Energy Fuel* 2006, 20(5), 1941-1945.

15 Cao, Y.; Chen, B.; Wu, J.; Cui, H.; Smith, J.; Chen, C. K.; Chu, P.; Pan, W. P. *Energy Fuel* 2006, 21(1), 145-156.

16 Nowakowski, R.; Kobiela, T.; Wolfram, Z.; Dus, R. *Appl. Surf. Sci.* 1997, 115, 217-231.

17 Kobiela, T.; Nowakowski, B.; Dus, R. *Appl. Surf. Sci.* 2003, 206,78-89

18 Morris, T.; Kloepper, K.; Wilson, S.; Szulczewskil, G. *J. Colloid Interf. Sci.* 2002, 254 ,49–55

19 Nowakowski, R.; Pielaszek, J.; Dus, R. *Appl. Surf. Sci.* 199 (2002) 40-51

20 Kobiela, T.; Wolfram, Z.; Dus, R. *Appl. Surf. Sci.* 1997, 115 ,217-231

21 EPCOR Genesee 1&2 Mercury Control, prepared by D. Whitten, February 2002, modified by R. Alexander, November 2003.

Chapter 6 Real Time Evaluation of the Composition and Structure of Concanavalin A Adsorbed on Polystyrene Surface

Jerzy A. Mielczarski, Jie Dong and Ela Mielczarski, *Journal of Physical Chemistry B* 112 (2008), 5228-5237

6.1 Introduction

The interaction of proteins with surfaces is an important topic, which is involved in a wide range of phenomena and applications. Protein adsorption can contribute to bacterial fouling of marine equipment,[1] blockage of filtration membranes in bioseparation processes,[2] and the deposition of plasma proteins onto implants or other biomaterials and subsequently triggering blood-clotting activity and modification of the biological responses.[3,4,5] The fabrication of biosensors and immunoassay methods also is dependent on the immobilization of proteins.[6] The growing demand for a biologically active, well-organized, stable protein layer is urgently required to address these problems.

Factors that govern protein-surface interactions, are determined by the physicochemical state of the substrate, the protein surface active groups and the solution environment. Factors including bound ions, surface charge, surface roughness, surface elemental composition, surface energetics, etc., all have to be considered in defining the role of the solid-solution interface.[7] The interactions that exist between protein and solid surfaces involve a complex interplay of van der Waals forces, hydrogen bonding, and electrostatic and hydrophobic forces.[8,9] Previous studies of protein adsorption on solid surfaces show that both hydrophobic and electrostatic interactions determine the amount of protein adsorbed[10] and that the effect of electrostatic interactions becomes more important when the adsorption is performed at low ionic strength where the screening effect of added salts is weakened.[11,12] The topography and properties of substrates are also very important, because only when the surface is well-defined can the conformational changes of the adsorbed protein molecules be investigated and understood. Mica,[13,14] graphite,[15] silicon wafer[16,17,18] and polymers[19,20,21,22] are typical smooth substrates used to study the properties of adsorbed proteins. Despite an increased understanding of many aspects of protein adsorption in recent years, the characterization of the adsorbed protein layer, such as its composition, conformation, orientation and denaturation, remains a crucial issue. Better understanding of these characteristics would greatly aid in the development of biomedical devices and many other protein-based technologies.

Concanavalin A (Con A) is a lectin obtained from jack beans (*Canavalia ensiformis*)[23], which has well–defined molecular dimensions in its native state and good stability characteristics that prevent complete unfolding at the protein-surface interface. Con A demonstrates a specific interaction with carbohydrates that occurs in most microorganisms and viruses. It plays a prominent role in cell adhesion and recognition of pathogens and is one of the useful probes in studying cell carbohydrates.[24, 25]

Various techniques have been applied to study the molecular adsorption at the air/liquid, liquid/liquid, and solid/liquid interfaces. The commonly used methods can be classified in different categories. The first represents a large group that includes: optical and spectroscopic techniques such as ellipsometry,[26, 27] infrared (IR) spectroscopy,[28, 29, 30] Raman spectroscopy,[31] vibration sum frequency spectroscopy,[32, 33, 34, 35, 36] total internal reflection fluorescence (TIFR),[37] and surface plasmon resonance.[38] The second group is led by atomic force microscopy (AFM),[39, 40] a method primarily involved in imaging characterization. The third group includes radiation-emission methods, such as X-ray photoelectron spectroscopy (XPS),[41] time-of-flight-secondary ion mass spectrometry (ToF-SIMS),[42, 43, 44] and neutron reflection spectroscopy.[45] The other techniques, such as streaming potential,[46] electrochemical impedance spectroscopy,[47] and radioactive labeling,[48] are also commonly used.

Among all of these techniques, Fourier transform infrared spectroscopy (FTIR) is one of the most well-suited methods to study protein states. It has a sufficient sensitivity to examine the structure of proteins in solution[49, 50] and even after adsorption on surfaces.[51, 52] One particular advantage of the FTIR method is its apparent ease and rapidity of acquiring good-quality spectra of the adsorbed proteins in a variety of environments. *In situ* characterization in aqueous solutions could provide the original direct information about protein adsorption at surfaces.

This chapter focuses on *in situ* investigation and understanding the adsorption of Con A on polystyrene (PS) surfaces obtained under varying conditions of pH by the use of attenuated total reflection infrared spectroscopy (ATR-IR). This spectroscopic technique combined with the spectral simulation of hypothetical adsorbed Con A layers, provides new and in-depth insight into experimental spectra interpretation. This approach aims to prevent the misinterpretation of spectral changes caused by optical effects as those resulting from physicochemical modifications of the adsorbed protein molecules on the surface. Comprehensive quantitative and qualitative structural evaluations, including XPS characterization, of the adsorbed layer are provided. The long-term goal of this work is to establish correlations between the adsorption conditions, the composition, and the structure of adsorbed protein layers, and their biological activity for various applications.

6.2 Experimental

Adsorption of Con A on Polystyrene

Con A was adsorbed from a solution containing 1mg/mL Con A in PBS buffered solutions at pH 4.8 and 7.4. The adsorption time varied from a period of a few minutes to 24 h. In situ monitoring of Con A adsorption by IR spectroscopy was performed with the use of a Teflon liquid cell. The ATR germanium reflection element covered with a 16 nm PS layer was positioned between two parts of the Teflon cell that creates PS-aqueous solution interfaces on both sides of the germanium crystal. A freshly prepared aqueous solution was introduced into the cell on one side of the ATR crystal and subsequently flowed through a continuous path within the cell before exiting the cell at the other end. The number of active reflections when the IR beam monitored the PS-aqueous solution interface was equal to 12. This number was calculated based on the experimentally observed absorbance bands of water with the aid of spectral simulation.The used experimental setup ensures a spectral sensitivity at the 0.1 nm level of the Con A layer (or 1/40 of the 3 nm monolayer of Con A).

Following adsorption, the composition and structure of the surface were characterized ex situ by ATR and XPS. After incubation, the samples were removed from the Con A solution, washed with water, dried quickly with nitrogen, and immediately analyzed. The number of active reflections for ATR *ex situ* measurements of the PS-adsorbed layer interface was equal to 16.

6.3 Results and Discussion

6.3.1 Optical Consideration of Adsorbed Layers

The system under investigation was characteristically multicomponent and multilayer. During *in situ* spectroscopic studies, the interaction of IR reflected beam with the multiphase system was complex, giving rise to different optical effects. The recorded reflection spectrum is a function of the optical constants of the component of each layer, the thickness of each deposited or adsorbed layer, their three-dimensional distribution (ordering, uniform, or patch-like structures), and the degree of hydration. Three models of surface layers considered in this study are presented in Figure 6.1.

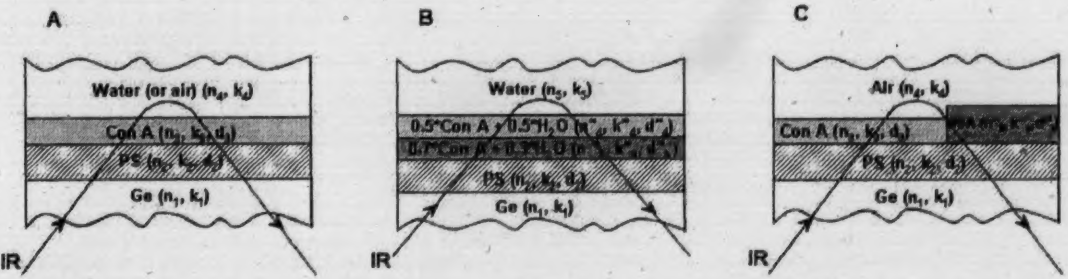
A
B
C
Water (or air) (n_4, k_4)
Con A (n_3, k_3, d_3)
PS (n_2, k_2, d_2)
Ge (n_1, k_1)
IR
Water (n_5, k_5)
0.5*Con A + 0.5*H$_2$O (n''_4, k''_4, d''_4)
0.7*Con A + 0.3*H$_2$O (n''_3, k''_3, d''_3)
PS (n_2, k_2, d_2)
Ge (n_1, k_1)
IR
Air (n_4, k_4)
Con A (n_3, k_3, d_3)
PS (n_2, k_2, d_2)
Ge (n_1, k_1)
IR

Figure 6.1 Three considered models of experimental multilayers on Ge: A. stratified multilayer system with each phase homogeneous; B. multilayer system with mixed composition layers (Con A at different hydration level); C, multilayer system of Con A and BSA with patch-like structures.

Model A is a classical uniformly distributed multilayer system where Con A forms a compact uniform layer as observed in the solid structure. For model B, protein hydration is considered, which results in the modification of optical constants (*n* and *k*) that correlate with the degree of hydration. This model shows examples of 30% and 50% hydrated hypothetical layers. Using these amounts the spectra of Con A were calculated by applying the new optical constants for the first adsorbed layer: n_3''(=$0.7\times n_{\text{Con A}}+0.3\times n_{H_2O}$), and k_3''(=$0.7\times k_{\text{Con A}}+0.3\times k_{H_2O}$), and for multilayer Con A adsorption: n_4'' (=$0.5\times n_{\text{Con A}}+0.5\times n_{H_2O}$), k_4'' (=$0.5\times k_{\text{Con A}}+0.5\times k_{H_2O}$). In model C, BSA is adsorbed on the bare PS surface remaining after Con A adsorption. In this case, each component retained its optical properties, and the overall simulated spectra from the protein layer are the summation of Con A and BSA spectra in varying concentrations.

Considering reflection spectra of multilayer systems, the position and shape of absorbance bands and their relative intensities could be modified significantly with respect to corresponding transmission spectra of the same free-standing samples. These changes result from optical effects and should be evaluated before a final analysis of the data is performed prior to drawing any conclusion relating to the chemical modification taking place during adsorption. Even more sensitive to optical effects is the intensity of observed absorbance bands that also change as a function of frequency of the reflected beam.[53] The qualitative and quantitative interpretation of reflection spectra improves tremendously by the use of spectral simulation.[54,55,56,57,58,59,60,61,62] Without the theoretical optical consideration of the system under investigation, conclusive interpretation of spectroscopic reflection data is impossible or very limited at best.

The spectral simulations were made for p- and s-polarizations with the use of exact equations based on Hansen's formulas[63] for a stratified system of isotropic phases with parallel interface boundaries. The calculations were performed using up to five phase models of surface product distributions (Figure 6.1) and optical constants of each phase. Other details of the spectral simulation were reported previously[55,56,57].

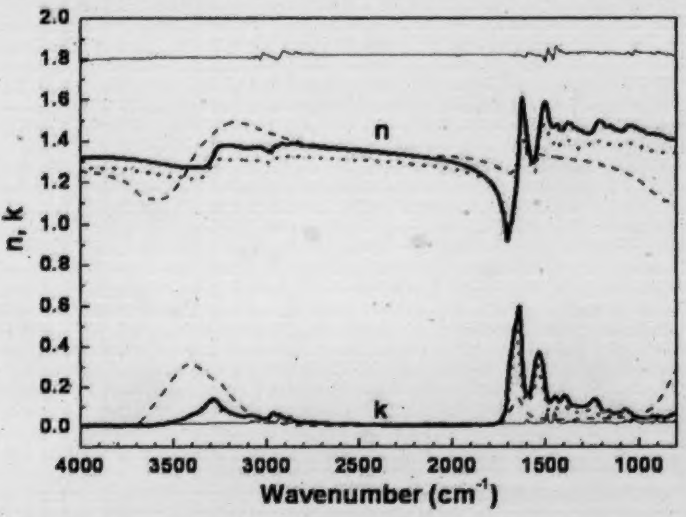

Figure 6.2 Optical constants: refractive index n and absorption coefficient k as a function of wavenumber for: PS (thin solid line), Con A (thick solid line), BSA (dot line) and water (dashed line) used for spectral simulation of the systems under investigations.

The optical constants n and k for Ge and water were obtained from a reference book[64] and reference paper,[65] respectively. The optical constants of air are $n=1$ and $k=0$. The optical constants of other components of the deposited PS or adsorbed layers of Con A and BSA were determined in a similar way to that reported recently[66] by the IR external reflection method. The optical constants used for simulated spectra of hypothetical layers of PS, Con A, and BSA together with those of water are presented in Figure 6.2. It was assumed that optical constants of the deposited PS layer and the adsorbed Con A or BSA layers were very similar to those of their bulk phases. This could be a crude assumption. A discussion of this issue is presented in the following sections.

6.3.2 Polystyrene Contacted with Air or Aqueous Solution

Simulated reflection spectra for one reflection of 16 nm PS on Ge in contact with air and with water, respectively, are presented in Figure 6.3. While the spectra of PS simulated in air show only positive absorbance bands, the simulated spectra with the presence of water are more complex. There are positive and negative bands with strong changes in the position and shape depending on the use of polarizations.

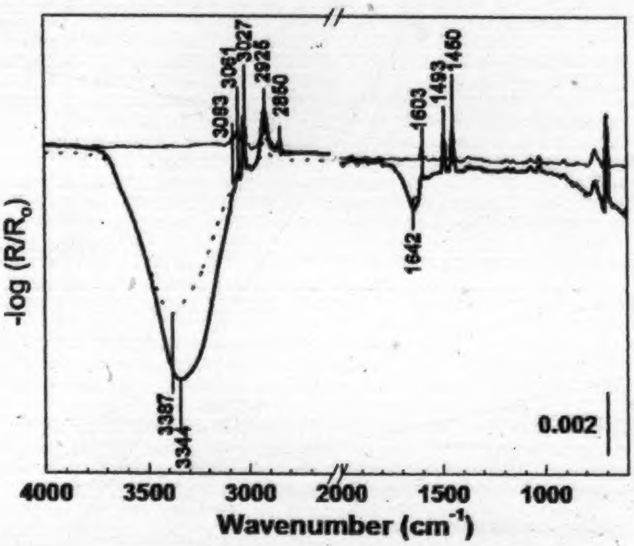

Figure 6.3 Simulated reflection spectra for one reflection of 16 nm PS on Ge contacted with air and water for p- and s-polarizations. (The thin solid line and dashed lines are for p- and s-polarizations in air, respectively; the thick solid line and dot lines are for p- and s-polarizations in water, respectively.)

By definition, an absorbance is described in this system as

$$Abs = -\log \frac{R(Ge/16nmPS/H_2O)}{R_0(Ge/H_2O)}$$

Hence, in the reference configuration, the water is in direct contact with the Ge element, while in the presence of the PS layer, water is moved away from the Ge interface by 16 nm, making the water absorbance lower. This interpretation explains the occurrence of negative bands presented in Figure 6.3: the bands around 3360 and 1642 cm^{-1} and the drop in baseline to a negative absorbance in the region below 1000 cm^{-1}, all of which are characteristic for water absorbance. Moreover, striking differences are observed in the spectra calculated for the p- and s-polarizations. The stretching vibration of the OH group is shifted from 3344 to 3387 cm^{-1}, and the corresponding shape is changed. Furthermore, the intensity ratio of the bands are deviated from 2 : 1 as would be expected for p- and s-polarized spectra of thick water layers.[53] All these changes predicted by simulation in ATR spectra resulted from the deposition of a 16 nm PS layer on Ge in the presence of water. It is emphasized that all predicted changes of water absorbance bands result from optical effects and do not indicate any changes in chemistry or any specific water structure formation at the PS-H_2O interface.

The complex interaction of a reflected beam with a multiphase system could be investigated in detail by considering changes in the electric field components in three dimensions passing two interfaces in a similar way to that reported.[56,57] However, this consideration is out of the scope of this study.

6.3.3 Adsorption of Con A on Polystyrene

Con A has a well-defined structure in solution at low pH values (<5) forming a canonical dimer, and at a neutral or higher pH values (>7), two such dimers associate with their back sheets[67, 68] to form a tetramer. It is proposed that the forces driving the formation of the tetramer are van der Waals and hydrogen-bonding interactions.[69] Con A is composed of two or four identical subunits, each with molecular weight of 25,500 Da.[70,71] The structures with their dimensions are shown in Figure 6.4[72]. It is important to note that the center of the tetramer forms a large water-filled cavity of about 25 Å ×25 Å × 8 Å.[68] The Con A is a dynamic structure in solution. The two dimers may rotate several degrees relative to each other and may even show a small translation, leading to a different hydrogen-bonding scheme at the dimer-dimer interface.[73]

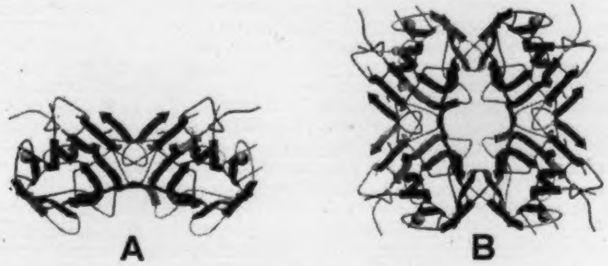

Figure 6.4 Ribbon representation of: A. dimer of Con A, 30 ×45 ×75 Å^3 dimension, B. tetramer of Con A, 60 ×70 × 70 Å^3 dimension (PDB, 1CES).

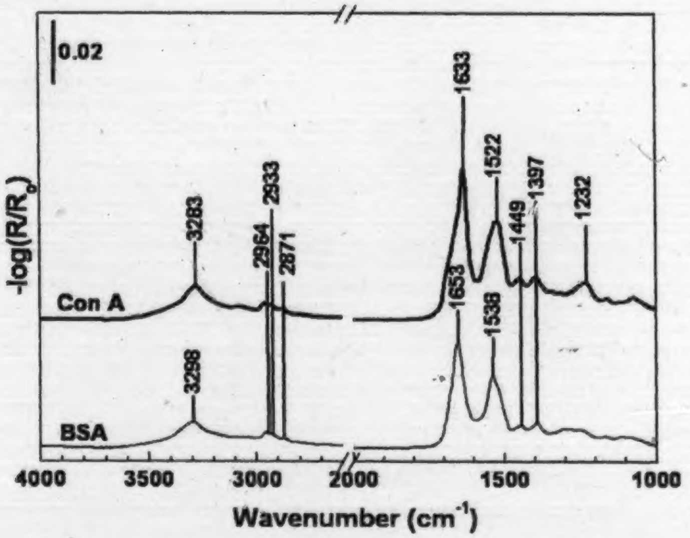

Figure 6.5 Reference spectra of solid samples of Con A and BSA recorded by ATR-IR at p-polarization. Notice different position of amide I bands which could be used to distinguish Con A with band at 1633 cm^{-1} characteristic for β-sheet structure from BSA with band at 1653 cm^{-1} characteristic for α-helix structure.

The reference spectrum of Con A recorded by the ATR technique is shown in Figure 6.5. The spectrum exhibits characteristic bands that result primarily from vibrations in the peptide linkages. The peak assignments are shown in Table 6.1.

Table 6.1 Peak assignment of Con A reference spectrum[74, 75, 76]

Position (cm^{-1})	Assignment
~3283	Stretching NH 'amide A' band
2964	Asymmetric stretching of $-CH_3$
2933	Fermi resonance of $-CH_3$
2870	Symmetrical stretching of $-CH_3$
1633	Amide I of β-sheet
1522	Amide II of C-N stretching
1449	CH_2 deformation
1397	Deprotonated acidic COO^- groups
1232	Amide III

The Con A spatial structure presented (Figure 6.4A) indicates a well-packed hypothetical monolayer of Con A. The dimer could produce at least a 3 nm thick adsorption layer with molecules lying at the most flat position on the surface. Therefore, the first optical consideration of the expected reflection spectra was carried out with an assumption of a 3 nm hypothetical adsorbed layer of Con A for which simulation results in water are presented in Figure 6.6. The absorbance spectrum of Con A is defined as

$$Abs = -\log\left(\frac{R(Ge/16nmPS/3nmConA/H_2O}{R_o(Ge/16nmPS/H_2O}\right)$$

From close analysis of the simulated spectra (Figure 6.6) for p- and s-polarizations, the following observations can be made: the negative band of water around 3386 cm^{-1} results from moving the interface water layer away from Ge by 19 nm as compared to 16 nm as is in the reference configuration R_o. This relatively small negative intensity water band is clearly visible and will cause only a small distortion of the amide I band at around 1640 cm^{-1}, which is in fact a combination band of the positive amide I band of the 3 nm layer of Con A and the negative band of water at the 1642 cm^{-1} (also see Figure 6.3 where the negative water band at 1642 cm^{-1} component is clearly visible). This indicates that quantitative evaluation of the adsorbed amount of Con A from *in situ* spectra is more accurate when it is carried out based on the intensity of the amide II band than that of amide I band in the case of both polarizations. It was observed later that the intensity of the amide I band always is lower than expected. It is also important to emphasize that the negative water band at around 3300 cm^{-1} is in fact a combination band of the positive component of the N-H vibrational band known as amide A. This is documented by observation of the positive absorbance band at 3278 cm^{-1}.

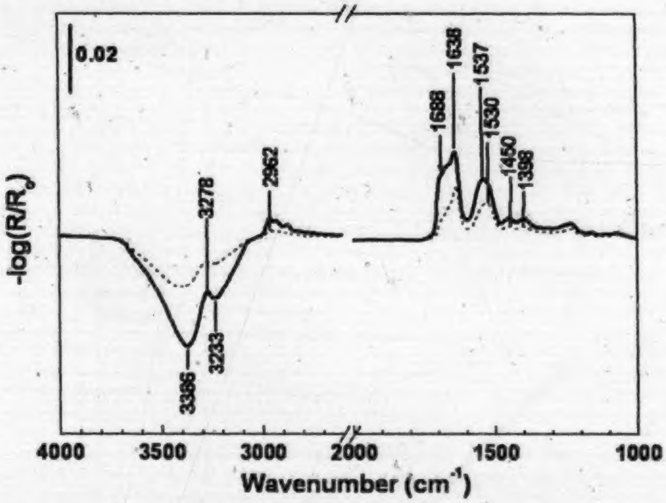

Figure 6.6 Simulated spectra of 3 nm hypothetical Con A layer on PS where reflectivities are: R(Ge/16 nmPS/3nm Con A/water) and R$_o$(Ge/16 nm PS/water), calculated for p- (solid line) and s- (dashed line) polarizations with 12 reflections.

There is also a very significant difference between spectra predicted for p- and s-polarizations. Much stronger intensities of amide I and amide II absorbance bands were predicted for p-polarization than for s-polarization. There is also a considerable difference in the shape of the amide I bands between these two polarizations. For s-polarization the spectrum of the amide I band at 1638 cm^{-1} (Figure 6.6) could be interpreted as an indication of a β-sheet structure, while the p-polarization spectrum can be assigned to mixture of β-sheet (band at 1638 cm^{-1}) and α-helix structures (shoulder at 1688 cm^{-1}) . Obviously, this interpretation is misleading because the simulated spectra represent an isotropic β-sheet structure of Con A. This difference could, at least partly, result from a larger subtraction of the water component for p-polarization than for s-polarization. However, the major reason is a special optical effect that is related to the observation that Con A in the region of the amide I band shows an exceptionally low refractive index, below 1.0 (Figure 6.2). As was reported and explained recently,[61, 62] for a spectral region where one phase shows a refractive index below 1.0, there are strong optical effects including the appearance of a new "absorbance" band.

Strange modifications (blue shifts) of the amide I band were also observed in the IR reflection spectra of adsorbed proteins on metallic surfaces.[77, 78] This clearly shows the importance of the developing a rigorous spectral interpretation methodology to avoid misinterpretation of all reflection spectra that are susceptible to optical effects.

It is emphasized that the interpretation of the *in situ* spectra is much more difficult for multilayer systems where numerous optical effects could take place. For example, it is expected that the ATR spectra of the isotropic ultrathin layer recorded for p- and s-polarizations are identical based on previous reports.[53] As documented in this work, this is not the case for the multilayer system (Figure 6.6), even if each phase is considered to be an isotropic ultrathin film below 20 nm.

A somewhat simpler case is for *ex situ* measurements, where samples were investigated after drying and the absorbance was defined as

$$Abs = -\log \frac{R(Ge/16nmPS/3nmConA/air)}{R_o(Ge/16nmPS/air)}$$

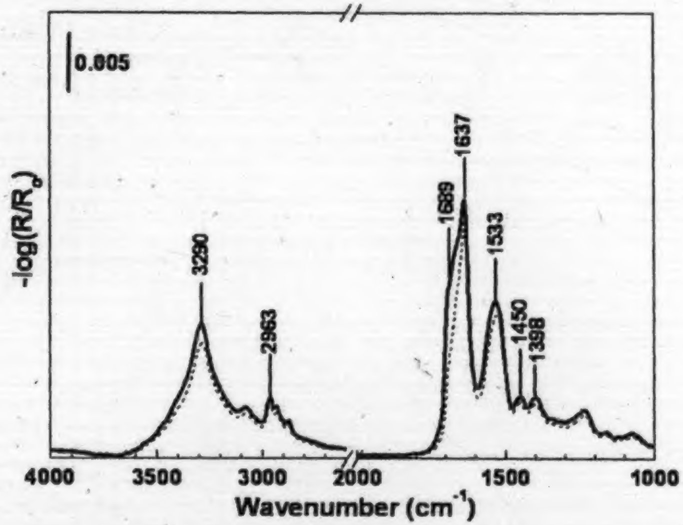

Figure 6.7 Simulated spectra of 3 nm hypothetical Con A layer on PS where reflectivity are: R(Ge/16 nm PS/3nm Con A/air) and R_0(Ge/16nm PS/air), calculated for p- (solid line) and s- (dashed line) polarizations with 16 reflections.

The simulation results are presented in Figure 6.7. There is a lack of negative bands from water, and all observed absorbance bands are characteristic for Con A as was deduced from comparison with the reference ATR spectrum (Figure 6.5) of solid Con A. However, even in this case, there are some differences predicted in the shape of the amide I band between p- and s-polarizations. As was already explained, the most probable reason is the optical effect caused by an exceptionally low refractive index, below 1.0, in this spectral region for Con A.

The presented optical considerations show many optical effects that may modify the spectrum of adsorbed Con A molecules on PS in the system under investigation. The difficulties were clearly demonstrated to perform the conclusive and proper judgment of spectroscopic data without misleading interpretations. The essential role of spectral simulation as a vital tool in data analysis was emphasized.

6.3.4 Adsorption Kinetics of Con A on Polystyrene

On the basis of the observed changes in the intensity of the amide I and amide II bands, the kinetics of Con A adsorption is shown in Figure 6.8 for pH 7.4 and 4.8. Two different adsorption regions can be distinguished: (i) initially, a rapid adsorption takes place followed by (ii) a much slower adsorption process.

At pH 7.4, the first step of adsorption is reached quickly. The coverage is around 2.5 nm, which is close to the value considered to be the possible thinnest hypothetical monolayer (3 nm) of Con A. This suggests that the first adsorbed layer is attributed to the adsorption of the Con A dimer. After this point, the adsorption continues at slow kinetics, reaching an ~8 nm thick layer after 24 h. The estimated thickness of the adsorbed layer based on the intensity of amide II was larger and more accurate than that from the amide I absorbance band for reasons explained in the previous section.

At pH 4.8, following a rapid adsorption region, the formation of an ~1.5 nm layer was observed. This represents half of the possible thinnest hypothetical monolayers. An extension of adsorption time to 22 h resulted in an increase to around 2.7 nm, which is very close to that predicted for the thinnest hypothetical monolayer. Under acidic pH conditions, the adsorption process is restricted, and Con A is prevented from further adsorption on the surface. The observed low coverage suggests that the adsorbed Con A undergoes conformational changes and that denaturation takes place or, in contrast, the adsorbed Con A molecules are distributed on the surface and exist as well-separated individual entities surrounded by water molecules available to interact with other biological molecules. The kinetic data presented show clearly that the adsorption of Con A at pH 7.4 occurs differently from that observed at pH 4.8. In the following section, more information will be provided to further support the adsorption model.

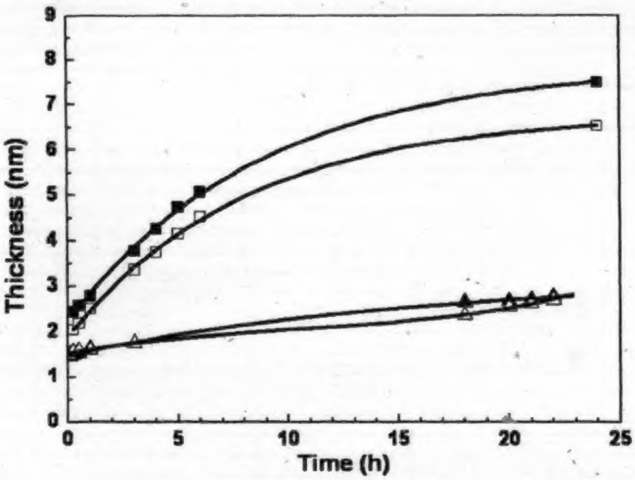

Figure 6.8 Kinetics of Con A adsorption on PS based on *in situ* recorded reflection spectra and determined from the intensity of amide I and amide II absorbance bands. Solid symbol lines are based on amide II. Empty symbol lines are based on amide I. Square symbols are for pH 7.4 and triangles are for pH 4.8. Con A layer thickness based on best fitting of experimental spectra by the simulated hypothetical surface layer with assumed thickness (model A).

6.3.5 Nature and Structure of the Adsorbed Con A Layer

The experimental spectra of Con A adsorbed at different time intervals on PS at pH 7.4 recorded *in situ* for p-polarization (Figure 6.9A) show striking differences when compared to the simulated spectra of isotropic hypothetical Con A monolayers (Figure 6.6). These are: (i) a different shape of the amide I bands, devoid of a shoulder at 1688 cm^{-1} in the recorded spectra, and (ii) a very intriguing experimental observation that the water negative bands around 3350 cm^{-1} remain at low intensities (almost constant) with an increase of adsorption time, whereas the adsorbed amount of Con A increases from 2.5 to 8 nm (see Section 6.3.4 Adsorption Kinetics of Con A on PS). The performed simulation indicates that for the 8 nm layer of the adsorbed Con A, the water bands at around 3350 cm^{-1} should display a negative intensity of around 0.08 absorbance units, which is 3 times higher than the value of 0.027 observed experimentally.

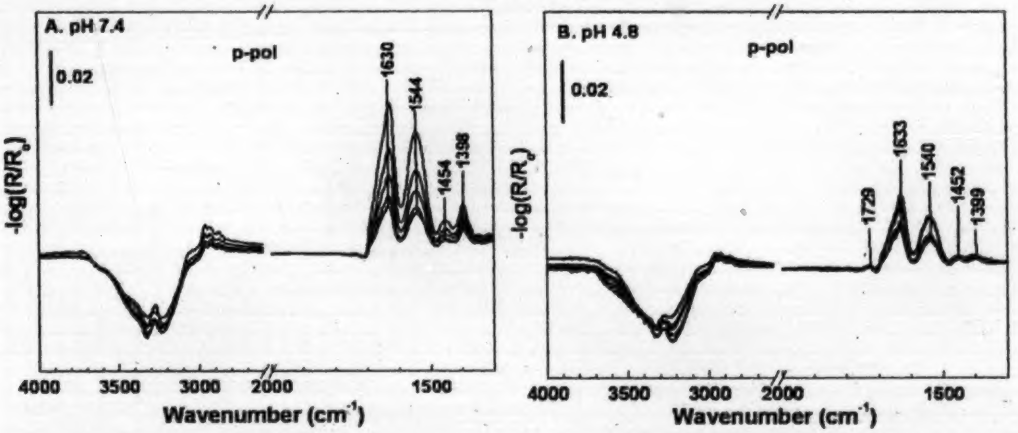

Figure 6.9 *In situ* experimental spectra of Con A adsorbed on PS for p-polarization: A. pH 7.4, after 15min, 1h, 3h, 6h and 24h with monotonic increase in amide I absorbance band. B. pH 4.8 after 15min, 1h, 3h, 18h and 22h with monotonic increase in amide I absorbance band.

The growing intensity of the amide I and amide II bands was observed simultaneously. These together indicate that the water remains in the vicinity of the PS interface in the range of 8 nm that is in contrast to the assumption of the stratified model of adsorbed layers (Figure 6.1A). Hence, the experimental data suggest that a large amount of water is included in the Con A adsorbed layer and that the content of water (hydration) increases with the thickness of this mixed Con A-water layer as presented in Figure 6.1B.

This finding has another important consequence in that the hydrated Con A has different optical constants than dry Con A. The stratified model of well-separated phases should be replaced by a model that also includes the possibility of the presence of a mixed phase where two components such as Con A and water form one phase with optical properties related to the content of each component (Figure 6.1B). It is very important to notice that the refractive index of the hydrated Con A does not correspond to a value below 1.0 as it is observed for the dry Con A phase (Figure 6.10). This has a very important consequence because the simulated spectrum of adsorbed hydrated Con A does not exhibit a strong shoulder at 1688 cm^{-1} (Figure 6.11) as compared to the non-hydrated layer of Con A (Figure 6.6). The use of a mixed phase model for simulation of the absorbance bands of amide I for p-polarization fits more closely to the experimental results, supporting the concept of the strong hydration of the Con A adsorbed layer in contact with aqueous solution. The experimental spectra of the best-fit (Figure 6.11) data corresponded to an adsorbed Con A submonolayer when 30% of hydration of Con A was assumed at pH 7.4. After 24 h of adsorption when multilayer coverage was observed (Figure 6.12), the best-fit data corresponded to an assumption of 30% hydration of Con A for the first adsorbed layer that was in direct contact with PS and 50% of hydration of Con A in the multilayer structure. It could be suggested that Con A molecules adsorbed on top of the first dimer layer are in a tetrameric structure. It was previously documented that the tetramer has the ability to absorb water in its cavity.[68] Hydration of protein molecules was already postulated.[79,80,81,82]

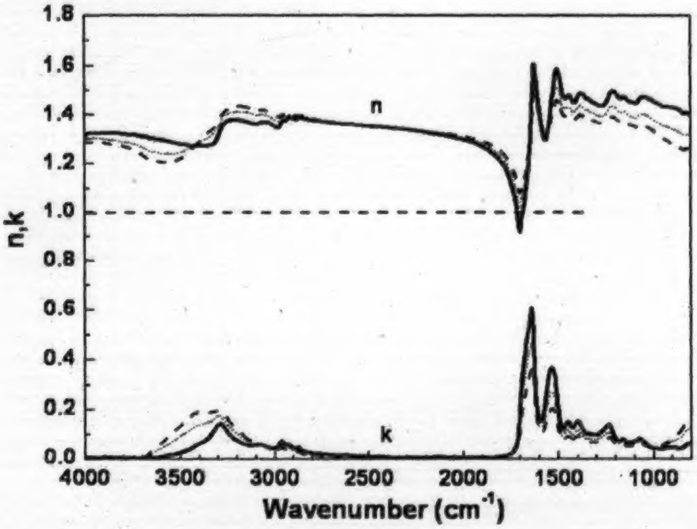

Figure 6.10 Calculated optical constants: refractive index n and absorption coefficient k as a function of wavenumber for: dry Con A (solid line); Con A hydrated 30%, 0.7: 0.3 = Con A : H_2O mixture phase (dot line) and hydrated 50% of Con A, 0.5 : 0.5 = Con A : H_2O mixture phase (dashed line).

At pH 4.8 when the highest coverage does not exceed the 3 nm layer (Figure 6.8) the model of the surface structure with the hydrated phase of Con A also fits better to the experimental data than the dry Con A phase model (Figure 6.1A). In this case, hydration of around 30% was determined. In summary, the model of the adsorbed layer with mixed component phases (hydrated Con A) better describes the experimental spectroscopic data recorded for p-polarization. Similar conclusions also can be drawn from close analysis of *in situ* spectra recorded for s-polarization (Figures 6.11 and 6.12).

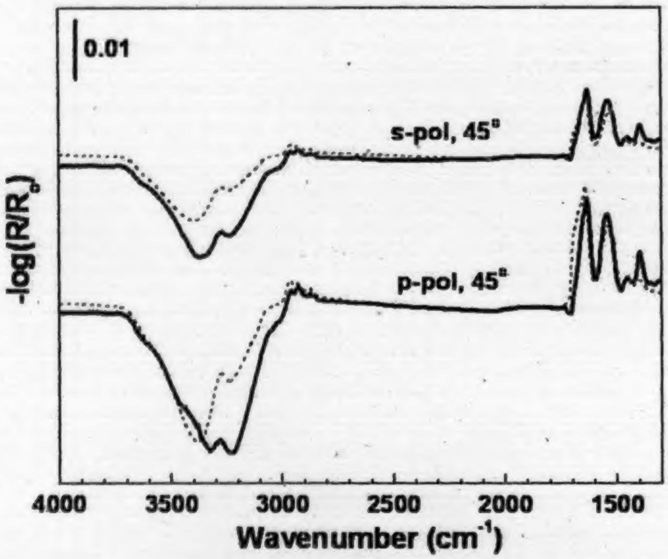

Figure 6.11 *In situ* experimental spectra (solid line) recorded after 15 min of adsorption from pH 7.4 solution compared with the simulated spectra (dashed line). Reflectivity are following: R(Ge/16nm PS/3nm (0.7 Con A+0.3 H_2O)/H_2O and R_0(Ge/16nm PS/H_2O).

Another interesting observation refers to chemical changes between adsorption layers of Con A under conditions of pH 4.8 and 7.4. At lower pH values at both polarizations, an absorbance band is observed at 1729 cm^{-1}, which is due to acidic COOH groups (Figure 6.9B). This band is absent at pH 7.4, while the higher intensity band at 1398 cm^{-1} appears (Figure 6.9A). The latter band indicates deprotonation and the formation of the COO- groups in the Con A adsorbed layer. The protonation/deprotonation reaction of carboxylic groups could be one of the factors of the observed differences in the Con A adsorption at different pH values.

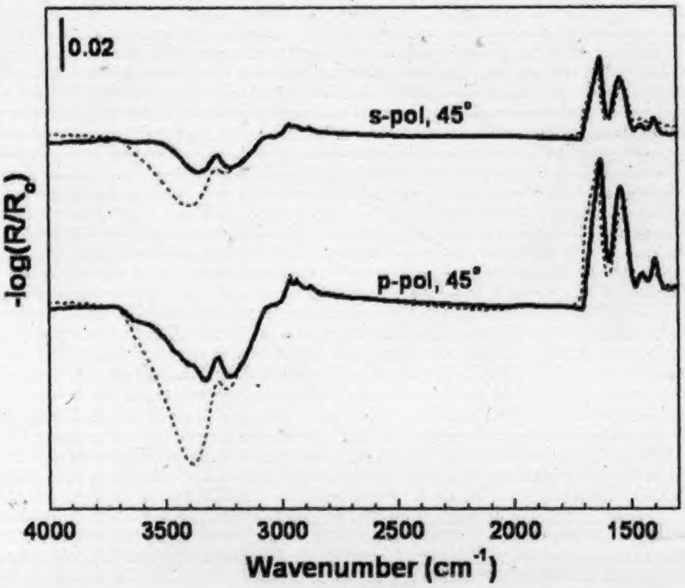

Figure 6.12 *In situ* experimental spectra (solid line) recorded after 24 h of adsorption from pH 7.4 solution compared with the simulated spectra (dashed line). Reflectivity are following: R(Ge/16nm PS/3nm (0.7 Con A+0.3 H_2O)/8nm (0.5 Con A + 0.5 H_2O)/H_2O and R_0(Ge/16nm PS/H_2O).

The shape and intensity of negative water bands observed for p- and s-polarized spectra are very different from those simulated for the hypothetical Con A layer. At submonolayer coverage (Figure 6.11) in the spectral region of the asymmetric vibration of water molecules (around 3400 cm^{-1}), the fitting is much better than in the region of the symmetric vibration. A reverse observation was made for multilayer. These observations are in good agreement with two types of postulated hydration of adsorbed Con A. It could be suggested that water molecules surrounding and interacting with Con A molecules undergo organization. This issue requires more study to be conclusive.

In Table 6.2, absorbance band positions of amide I and amide II are summarized. Close analysis indicates that some shifts in the band positions observed between p- and s-polarized spectra are, at least partly, caused by optical effects. This is clearly documented by simulation results when an isotropic structure was assumed. Therefore, the observed changes in the band positions cannot be simply interpreted as evidence of changes in conformation or molecular orientation. Nevertheless, the significantly lower position of the amide I band for the adsorbed multilayer (pH 7.4 and 24 hours) at 1627 cm^{-1} could imply the formation of a strongly hydrated tetramer structure. The band at position 1631-1633 cm^{-1} could be assigned to the adsorbed low hydrated Con A dimer form. The non-hydrated Con A layer shows a band position at 1639 cm^{-1} as was indicated by simulation.

Table 6.2 The positions of amide I and amide II absorbance bands observed for adsorbed layers at different conditions and obtained by spectral simulation.

Con A on PS	Amide I		Amide II	
	p-pol (cm^{-1})	s-pol (cm^{-1})	p-pol (cm^{-1})	s-pol (cm^{-1})
pH 7.4, 15min	1633	1631	1544	1538
pH 7.4, 24h	1627	1627	1544	1542
pH 4.8, 5min	1633	1633	1539	1535
pH 4.8, 22h	1631	1629	1544	1540
simulation	1639	1635	1537	1530

There is also an interesting observation regarding the amide II band at lower positions of 1539 and 1535 cm^{-1} for the sample with the lowest (around half a monolayer) coverage. These positions may suggest a strong interaction of the Con A molecule with the substrate and a weak intermolecular interaction.

6.3.6 BSA Adsorption on PS Surface with Pre-adsorbed Con A

BSA is a strong adsorbed protein that can be used as a blocking reagent of other protein adsorption.[83,84,85] As was already determined (Figure 6.8) at pH 4.8 and 15 min of incubation time, the adsorbed amount of Con A was equal to a 1.5 nm layer, which is an equivalent to half of a close-packed monolayer of the adsorbed Con A molecules. This estimation implies that there still exists around half of the PS surface that could be occupied by strongly adsorbed molecules such as BSA. Comparison of the recorded spectrum after Con A adsorption to that after an additional exposure to BSA solution (Figure 6.13) demonstrated a very low co-adsorption of BSA and a very low desorption of Con A (see differential spectrum).

The adsorbed amount of BSA is identified by the positive low intensity band at 1657 cm^{-1} characteristic of the α-helix structure, whereas desorption of Con A is indicated by the negative low intensity band at 1635 cm^{-1} characteristic of the β-sheet structure. The comparison of experimental spectra (Figure 6.13) with those simulated for the patch–like structure model of the surface layer (Figure 6.1C) indicates that BSA co-adsorption is limited to around 8% of PS surfaces. In a separate experiment of BSA adsorption on bare PS, a strong adsorption takes place (data not shown). A 3.5 nm thick layer of BSA was observed after 30 min of adsorption. These observations together suggest that at the submonolayer coverage of Con A, the dimer molecules are well and uniformly distributed with an intermolecular distance somewhat smaller than the size of BSA molecules (40 Å x 40 Å x 140 Å). This uniform surface structure of Con A (no patches) prevents BSA from adsorbing on PS.

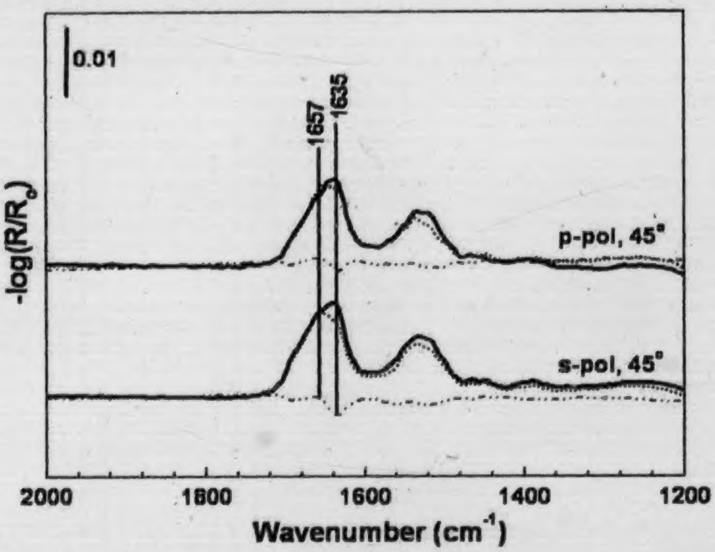

Figure 6.13 *Ex situ* experimental spectra recorded after 15 min adsorption of Con A from pH 4.8 solution (solid line) compared with the experimental spectra recorded after adsorption of BSA for 30 min on the surface with pre-adsorbed Con A (dot line) and the differential spectrum after and before BSA adsorption (dashed-dot line).

Another considered explanation necessitates the dramatic changes in the Con A conformation involving almost a 2 times higher surface occupation by the adsorbed Con A molecules on PS. There is, however, no experimental evidence to support such an explanation.

6.3.7 XPS Analysis

Angle resolved XPS is a well-established surface sensitive technique that gives elemental surface composition information from a sample depth of not more than a few

(3-5nm) nanometers (effective information depth at angles of 75 and 60° are around one-quarter and one-half of that at 0°, respectively), and therefore, the distribution and structure of the adsorbed protein layer can be studied by following a combination of observed signals: (i) an increase of the signal from the adsorbed layer, N 1s line, and (ii) the attenuation of the signal from the PS substrate, carbon π bond, shake-up satellite line. A summary of the qualitative and quantitative results of Con A adsorbed layers on polystyrene are presented in Table 6.3.

Table 6.3 Surface atomic concentration of C, O, N, S determined for solid Con A and adsorbed layer at different conditions. Spectra recorded at different take off angles: at 0° -the largest penetration depth; at 60° and 75° , the penetration depth are ½ and ¼ of that at 0°, respectively.

Samples	C 1s	O 1s	N 1s	S 2p
Con A powder	69.83	16.60	13.30	0.27
Con A, 22 h, pH 4.8				
0°	84.61	7.59	7.15	—[a]
60°	81.24	9.28	9.29	—
75°	80.68	9.07	10.12	—
Con A, 15 min, pH 4.8				
0°	85.34	8.01	6.34	—
60°	85.48	6.70	7.69	—
75°	83.27	7.91	8.64	—
Con A, 24 h, pH 7.4				
0°	70.45	15.77	13.63	0.02
60°	72.33	13.48	14.19	—
75°	73.29	12.59	14.12	—
Con A, 15 min, pH 7.4				
0°	77.56	12.12	9.65	—
60°	76.38	12.07	11.39	—
75°	75.52	11.59	12.74	—

[a] "—, too low to be measured"

The 16 nm deposited PS layer forms a continuous film (very small signal from the substrate) that is very pure (only 0.4% of oxygen in from OH groups). There is also a clear C1s line at 291.3 eV characteristic for the π bond of the shake-up satellite of PS. Adsorption of Con A is clearly visible by the observation of higher intensity N 1s, O 1s, and C 1s lines of the characteristic carbon groups COO^-, C=O, C—O, and C—N. Moreover, attenuation of the PS signal of the π bond of the shake-up satellite of C 1s indicates the Con A layer formation.

At take-off angles of zero, it was observed that the surface atomic concentration after 24 h of adsorption at pH 7.4 was identical to that found for the reference spectrum of solid Con A and that the signal from PS completely disappeared. This indicates that the produced 8 nm thick adsorbed layer (Figure 6.8) is uniformly distributed over the PS surface. Another interesting observation is a small increase of the N 1s signal and a strong decrease of the O 1s signal with a decreasing depth of analysis (or increasing take-off angle). This suggests that Con A oxygen containing groups such as OH and COOH are located closer to the PS/Con A interface, implying their importance in the adsorption of the protein on the substrate.

At pH 7.4 with a lower coverage than the monolayer (Figure 6.8, 15 min of incubation), the surface concentration of nitrogen is lower than that for the powder form of Con A, whereas the signal of the π bond of the shake-up satellite of C 1s of polystyrene is relatively high. An observed significant signal from the PS substrate is in good agreement with IR observation of the formation of submonolayer coverage under these conditions. The interesting observation is a significant increase of surface nitrogen concentration accompanied by a nearly complete disappearance of the signal from PS with an increasing take-off angle to 75°. There exists only one surface structure that could explain these observations. Con A is uniformly distributed over the PS surface with similar distances between Con A molecules attached directly to the surface. Any surface Con A structures such as patch-like or close-packed are excluded.

Since at pH 7.4 Con A exists in solution as a tetramer[72], it would be interesting to consider the possibility of the first monolayer made of tetramers. If it is assumed that a quick adsorption (Figure 6.8, 15 min) provides less than half of the monolayer of tetramers (6.5 nm assumed for tetramer and 2.6 nm observed experimentally), more than half of the PS surface would be free of Con A tetramer molecules, and as a consequence, the signal from the PS substrate should be easy to see. This is not supported by XPS results, which clearly indicate a strong attenuation effect on PS by the adsorbed Con A molecules. This indicates that Con A molecules cover all PS surfaces evenly by smaller molecules than tetramers. Therefore, the dimer monolayer formed is proposed at pH 7.4 after 15 min adsorption.

Con A adsorbed from the pH 4.8 solution forms only submonolayer coverage. After 15 min of adsorption, the surface concentration of nitrogen is around half (6.34%) of the value expected for the completed coverage of the PS substrate (13.3%). This is in good agreement with IR findings and supports the explanation of the uniform surface distribution of adsorbed Con A molecules. After 22 h of adsorption, the amount of Con A is higher but still below a monolayer. However, at the same time, the signals from the PS substrate are very similar to those obtained after 15 min of adsorption. This striking observation supports the conclusion that a change in orientation of the adsorbed Con A molecules took place. It is postulated that at first the dimer of Con A adsorbs with the most flat position at the PS surface. After a long incubation period, the already and newly adsorbed molecules change position to a more vertical to surface. This ensures a higher surface concentration of Con A as well as maintaining an intermolecular distance between the adsorbed dimer molecules, which explains the observed constant signal from PS.

6.4 Conclusions

A schematic representation of the experimentally documented steps of the adsorption of Con A on PS at pH 4.8 and 7.4 is presented in Figure 6.14.

At pH 4.8, Con A could be adsorbed only directly on the PS surface. Multilayer adsorption from acidic solution was not observed. Con A – Con A interaction is limited to the formation of a Con A dimer that adsorbs on PS. Initially, the rapid step of the adsorption of the Con A dimer covers only around 50% of the PS surface. The dimers are uniformly distributed with similar intermolecular distances of 3-4 nm. During the second slow adsorption step more dimer molecules were found on the PS surface. The change in orientation occured from generally flat to a more vertical position. This preserves the intermolecular distance between adsorbed dimers at higher surface concentrations. The adsorbed dimer molecules are hydrated. There is around 30% of water in the Con A layer.

At pH 7.4, the adsorption kinetics of Con A is faster, and multilayer coverage can be achieved. During the initial phase, a very fast step of the adsorption, a close-packed Con A dimer monolayer was produced with a thickness of around 3 nm. This layer contains around 30% of water. After 24 h of incubation additional Con A molecules were adsorbed on the top of the first layer. They were strongly hydrated, and the content of water was about 50%. It was proposed that on top of the first dimer, a compact layer of the adsorbed Con A is in the form of tetramer.

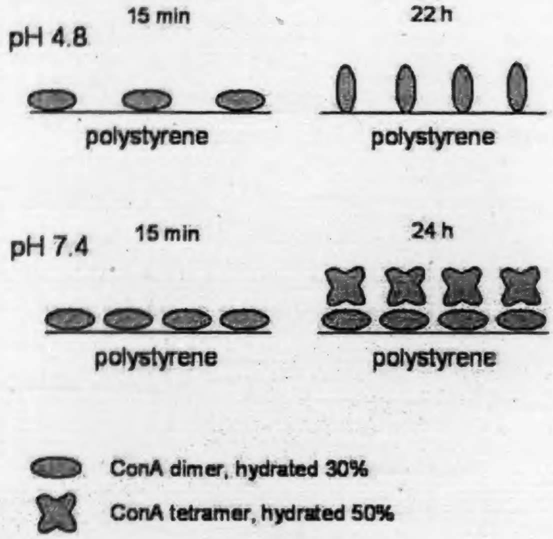

Figure 6.14 Schematic representation of nature and structure of experimentally documented steps of adsorption of Con A on polystyrene at pH 4.8 and 7.4 in quick and slow kinetic adsorption regions.

This work demonstrates the advantage of the combination of *in situ* IR spectroscopy with *ex-situ* XPS spectroscopy supported by spectral simulation techniques to deduce the Con A nature, structure, and orientation at the interface. The applied methodology allows us to distinguish the observed spectral changes due to pure optical effects, associated with the passing of an incident beam through the multilayer system, from the chemical and structural changes caused by physicochemical interactions of protein with the polymer surface. This reduces significantly the possibility of misinterpretation of the recorded spectra of the protein layer and is rewarded by a deeper insight into the structure and composition of the sample. Similarly, this methodology can be applied to probe and to deduce interface phenomena of numerous protein and other biologically active molecules at solid surfaces.

Supporting Information is available in Appendix F, concerning experiments, preparation, and characterization of uniform PS films and spectral simulation of PS layer.

References

[1] Costerton, J. W.; Cheng, K.-J.; Geesey, G. G.; Ladd, T. I.; Nickel, J. C.; Dasgupta, M.; Marrie, T. J. *Annu. Rev. Microbiol.* **1987**, *41*, 435-464.

[2] Birk, H. W.; Kistner, A.; Wizemann,V.; Schutterle, G. *Artif. Organs* **1995**, *19*, 411-415.

[3] Albelda, S. M.; Buck, C. A. *FASEB J.* **1990**, *4*, 2868-2880.

[4] Gluszko, P.; Rucinski, B. J.; Musia, J.; Wenger, R. K.; Schmaier, A. H.; Colman, R. W.; Edmunds, L. H., Jr.; Niewiarowski, S. *Am. J. Physiol. Heart Circ. Physiol.* **1987**, *252*, 615-621.

[5] Feng, M.; Morales, A. B.; Beugeling, T.; Bantjes, A.; Vanderwerf, K.; Gosselink, G.; Degrooth, B.; Greve, J. *J. Colloid Interface Sci.* **1996**, *177*, 364-371.

[6] Benmakroha, Y.; Zhang, S.; Rolfe, P. *Med. Biol. Eng. Comput.* **1995**, *33*, 811-821.

[7] Israelachvili, J. *Intermolecular and Surface Forces,* 2nd edition; Academic Press: London, 1992.

[8] Norde, W. *Macromol. Symp.* **1996**, *103*, 5-18.

[9] Elwing, H.; Welin, S.; Askendal, A.; Nilsson, U. R.; Lindström, I., *J. Colloid Interface Sci.* **1987**, *119*, 203-210.

[10] Norde, W. *Adv. Colloid Interface Sci.* **1986**, *25*, 267-340.

[11] Lubarsky, G. V.; Browne, M. M.; Mitchell, S. A.; Davidson, M. R.; Bradley, R. H. *Colloid Surf. B: Biointerfaces*, **2005**, *44*, 56-63.

[12] Ortega-Vinuesa, J. L.; Gálvez-R[illegible]iz, M. J.; Hidalgo-Álvarez, R. *Langmuir* **1996**, *12*, 3211-3220.

[13] Waner, M. J.; Gilchrist, M.; Schindler, M.; Dantus, M. *J. Phys. Chem. B* **1998**, *102*, 1649-1657.

[14] Kim, D. T.; Blanch, H. W.; Radke, C. J. *Langmuir* **2002**, *18*, 5841-5850.

[15] Marchin, K. L.; Berrie, C. L. *Langmuir* **2003**, *19*, 9883-9888.

[16] Giacomelli, C. E.; Norde, W. *J. Colloid Interface Sci.* **2001** *233*, 234-240.

[17] Giacomelli C. E., Bremer M. G. E. G., Norde W. *Macromol. Symp.* **1999**, *145*, 125-136.

[18] Daly, S. M.; Przybycien, T. M.; Tilton, R. D. *Langmuir* **2003**, *19*, 3848-3857.

[19] Maste, M. C. L.; Pap, E. H. W.; van Hoek, A; Norde, W.; Visser, A. J. W. G. *J. Colloid Interface Sci.* **1996**, *180,* 632-633.

[20] Browne, M. M.; Lubarsky, G. V.; Davidson, M. R.; Bradley, R. H. *Surf. Sci.* **2004**, *553,* 155-167.

[21] Chen, C.; Wang, J.; Woodcock, S. E.; Chen, Z. *Langmuir* **2002**, *18*, 1302-1309.

[22] Briggman, K. A.; Stephenson, J. C.; Wallace, W. E.; Richter, L. J. *J. Phys.Chem. B* **2001**, *105*, 2785-2791.

[23] Sharon, N.; Lis, H. *Science* **1972**, *177*, 949-959.

[24] Revel, D. J.; Knight, J. R.; Blyth, D. J.; Haines, A. H.; Russel, D. A. *Langmuir* **1998**, *14,* 4517-4524.

[25] Gestwicki, J. E.; Strong, L. E.; Cairo, C. W.; Bohem, F. J.; Kiessling, L. L. *Chem. Biol.* **2002,** *9*, 163-169.

[26] Nygren, H.; Arwin, H.; Welinklintstrom, S. *Colloids Surf., A* **1993**, *76*, 87-93.

[27] Malmsten, M. *Colloids Surf. B* **1995**, *3*, 371-381.

[28] Bieri, M.; Burgi, T. *J. Phys. Chem B* **2005**, *109*, 22476-22485.

[29] Müller, M.; Werner, C.; Grundke, K.; Eichhorn, K. J.; Jacobasch, H. J. *Microcim. Acta Suppl.* **1997**, *14*, 671-674.

[30] Lenk, J. T.; Horbett, T. A.; Ratner, B. D.; Chittur, K. K. *Langmuir* **1991**, *7*, 1755-1764.

[31] Strehle, M. A.; Roesch, P.; Petry, P.; Hauck, A.; Thull, R.; Kiefer, W.; Popp, J. *Phys. Chem. Chem. Phys.* **2004**, *6*, 5232-5236.

[32] Chen, X.; Clarke, M. L.; Wang, J.; Chen, Z. *Int. J. Mod. Phys. B* **2005**, *19*, 691-713.

[33] Kim, G.; Gurau, M.; Kim, J.; Cremer, P. S. *Langmuir* **2001**, *18*, 2807-2811.

[34] Chen, X.; Clarke, M. L.; Wang, J.; Chen, Z. *Int. J. Modern Phys. B*; **2005**, *19*, 691-713.

[35] Wang, J.; Chen, X.; Clarke, M. L.; Chen, Z. *J. Phys. Chem. B* **2006**, *110*, 5017-5024.

[36] Clarke, M. L.; Wang, J.; Chen, Z. *J. Phys. Chem. B* **2005**, *109*, 22027-22035.

[37] Hlady, V. *Appl. Spectrosc.* **1991**, *45*, 246-252.

[38] Mrksich, M.; Sigal, G. B.; Whitesides, G. M. *Langmuir* **1995**, *11*, 4383-4385.

[39] Balashev, K.; Jensen, T. R.; Kjaer, K.; Bjornholm, T. *Biochimie.* **2001**, *83*, 387-397.

[40] Galli, C.; Collaud Coen, M.; Hauert, R.; Katanaev, V. L.; Wymann, M. P.; Gröning, P.; Schlapbach, L. *Surf. Sci.* **2001**, *474*, L180-L184.

[41] McArthur, S. L. *Surf. Interface Anal*. **2006**, *38*, 1380-1385.

[42] Xia, N.; May, C.J.; McArthur, S.L.; Castner, D. G. *Langmuir* **2002**, *18*, 4090-4097.

[43] Wagner, M. S.; Castner, D. G. *Applied Surface Science* **2004**, *231*, 366-376.

[44] Tidwell, C. D.; Castner, D. G.; Golledge, S. L.; Ratner, B. D.; Meyer, K.; Hagenhoff, B.; Benninghoven, A. *Surf. Interface Anal.* **2001**, *31*, 724-733.

[45] Armstrong, J.; Salacinski, H. J.; Mu, Q.; Seifalian, A. M.; Peel, L.; Freeman, N.; Holt, C. M.; Lu, J. R. *J. Phys. Condens. Matter.* **2004**, *16*, 2483-2492.

[46] Ethève, J.; Déjardin, P. *Langmuir* **2002**, *18*, 1777-1785.

[47] Diniz, F. B.; Ueta, R. R. *Electrochim. Acta* **2004**, *49*, 4281-4286.

[48] Chinn, J. A.; Posso, S. E.; Horbett, T. A.; Ratner, B. D. *J. Biom. Mater. Res.* **1992**, *26*, 757-778.

[49] Sarver, R. W., Jr.; Krueger, W. C. *Anal. Biochem.* **1991**, *194*, 89-100.

[50] Dong, A.; Caughey, W. S.; Du Clos, T. W. *J. Biol. Chem.* **1994**, *269*, 6424-6430.

[51] Buijs, J.; Norde, W.; Lichtenbelt, J. W. Th. *Langmuir* **1996**, *12*, 1605-1613.

[52] Chen, S. S.; Chittur, K. K.; Sukenik, C. N.; Culp, L. A.; Lewandowska, K. *J. Colloid Interface Sci.* **1994**, *162*, 135-143.

[53] Harrick, N. J. *Internal reflection spectroscopy*, Harrick Scientific Corporation, Ossining, New York, 3rd printing 1987.

[54] Mielczarski, J. A.; Yoon, R. H., *J. Phys. Chem.,* **1989**, *93*, 2034-2038.

[55] Mielczarski, J. A.; Yoon, R. H. *Langmuir*, **1991**, 7, 101-108.

[56] Mielczarski, J. A. *J. Phys. Chem.*, **1993**, *97*, 2649-2663.

[57] Mielczarski, J. A.; Mielczarski, E. *J. Phys. Chem.*, **1995,** *99*, 3206-3217.

[58] Mielczarski, J. A.; Mielczarski, E.; Zachwieja, J.; Cases, J. M. *Langmuir* **1995**, *11*, 2787-2799.

[59] Mielczarski, E.; Mielczarski, J. A.; Cases, J. M. *Langmuir* **1998,** *14*, 1739-47.

[60] Mielczarski, J. A.; Mielczarski, E.; Cases, J. M. *Langmuir* **1999**, *15*, 500- 508.

[61] Mielczarski, J. A.; Mielczarski, E. *J. Phys. Chem.* **1999**, *103*, 5852-5859.

[62] Mielczarski, E.; Duval, Y.; Mielczarski, J. A. *J. Phys. Chem. B* **2002**, *106* (46), 11985-11992.

[63] Hansen, W. N. *J. Opt.Soc. Am.* **1968**, *58*, 380.

[64] Palik, E. D. *Handbook of Optical Constants of Solids*, Naval Research Laboratory, Washington, D. C., Academic Press Inc. **1985**.

[65] Downing, H. D.; Williams, D. J. *J. Geophys. Res.* **1975**, *80*, 1656.

[66] Mielczarski, J. A.; Milosevic, M.; Berets, S. L. *Appl. Spectrosc.* **1992**, *46*, 1040-1044.

[67] McCubbin, W. D.; Kay, C. M. *Biochem. Biophys. Res. Commun.* **1971**, *44*, 101–111.

[68] Bouckaert, J.; Loris, R.; Poortmans, F.; Wyns, L. *Proteins. Struct. Funct. Genet.* **1995**, *23*, 510–524.

[69] Bouckaert, J.; Loris, R.; Poortmans, F.; Wyns, L. *Proteins: Struct., Funct., Genet.* **1995**, *23*, 510–524.

[70] Wang, J. L.; Cunningham, B. A; Edelman, G. M. *Pro. Nat. Acad. Sci. U.S.A.* **1971**, *68*, 1130-1134.

[71] Edmundson, A. B.; Ely, K. R.; Sly, D. A.; Westholm, F. A.; Powers, D. A.; Liener, I. E. *Biochemistry.* **1971**, *10*, 3554-3559.

[72] Shoham, M.; Yonath, A.; Sussman, J. L.; Moult, J.; Traub, W.; Kalb, A. J. *J. Mol. Biol.* **1979,** *131*, 137-155.

[73] Naismith, J. H.; Habash, J.; Harrop, S.; Helliwell, J. R.; Hunter, W. N.; Wan, T. C. M.; Weisgerber, S.; Kalb Gilboa , A. J.; Yariv, J. *Acta Crystallogr.* **1993,** *D49,* 561–571.

[74] Bieri, M.; Bürgi, T. *Phys. Chem. Chem. Phys.* **2006,** *8*, 513-520.

[75] Steiner, G.; Tunc, S.; Maitz, M.; and Salzer, R. *Anal. Chem.* **2007**, *79*, 1311-1316.

[76] Ernst-Bonberg, M. L.; Worsham, L. M. S.; Williams, S. G., *Biochim. Biophys. Acta*, **1993**, *1164*, 273-282.

[77] Liedberg, B.; Ivarsson, B.; Hegg, P.-O.; Lundström, I. *J. Colloid Interface Sci.* **1986**, *114*, 386-397.

[78] Ihs, A.; Liedberg, B.; Uvdal, K.; Törnkvist, C.; Bodö, P.; Lundström, I. *J. Colloid Interface Sci.* **1990**, *140*, 192-206.

[79] Lubarsky, G. V.; Davidson, M. R.; Bradley, R. H. *Biosens. Bioelectron.* **2007**, *22*, 1275-1281.

[80] de Jongh, H. H.; Goormaghtigh, E.; Ruysschaert, J. M. *Anal. Biochem.* **1996**, *242*, 95-103.

[81] Careri, G.; Giansanti, E. G. *Biopolymer,* **1979**, *18*, 1187-1203.

[82] Poole, P. L.; Finney, J. L. *Biopolymers* **1984**, *23*, 1647-1666.

[83] Coen, M. C.; Lehmann, R.; Gröning, P.; Bielmann, M.; Galli, C.; Schlapbach, L. *J. Colloid Interface Sci* **2001**, *233*, 180-189.

[84] Chen, S.; Liu, L.; Zhou, J.; Jian, S. *Langmuir* **2003**, *19*, 2859-2864.

[85] Howell, S.W.; Inerowicz, H.D.; Regnier, F.E.; Reifenberger, R. *Langmuir* **2003**, *19,* 436-439.

Chapter 7 *In situ* Characterization of the Adsorbed Concanavalin A on Germanium Surface at Various pH

Jie Dong, Jerzy A. Mielczarski, Ela Mielczarski and Zhenghe Xu, *Biotechnology Progress* 24 (2008), 972-980

7.1 Introduction

The adsorption of proteins from solution onto solid surfaces has attracted much attention due to its scientific importance and a wide range of applications.[1, 2, 3] In medical and food industries, for example, it is essential to remove adsorbed proteins since even a small amount of deposited proteins may give rise to the subsequent adsorption of fibrous proteins, leading to adverse biological consequences.[4, 5, 6] Protein adsorption can also contribute to blood clotting and heart disease.[7] In addition, the controlled adsorption of proteins is essential in the fields of enzymatic catalysis, biosensors, and disease diagnostics.[8, 9] The immobilization of proteins is crucial because of the potential to improve the stability of enzymes under extreme conditions.[10]

Recently, much effort has been made to investigate the interaction of proteins with different solid substrates. Although many studies have shown that the amount of protein adsorbed on a solid substrate is strongly influenced by the nature and strength of interactions between the surface and proteins, the level of adsorption can also be easily altered by a shift in the balance of the interactions involved, i.e., electrostatic forces, van der Waals forces, conformational entropy changes, and hydrophobic interactions. Thus, surface adsorption can be increased by the gain of conformational entropy from (partially) unfolding at the surface, the shift of pH close to the isoelectric point, or specific ion bindings.[11] Hydrophobic and ionic interactions are often regarded as the most important driving forces for surface adsorption, but the relative significance of these interactions in a given system depends on the details of the protein structure and the properties of the particular surface involved. The varieties of the interactions and the differences in size, shape, and flexibility of protein molecules have made it difficult to rationalize the behaviour of proteins at interfaces.

Ball and Jones[12] used ATR-IR spectroscopy to observe the adsorption of the globular protein lysozyme from D_2O solutions onto a silicon ATR crystal. They determined the amount adsorbed with time by ATR and studied the effect of changing pD and/or heating on the structure of protein in the adsorbed layer. The authors found the same spectral changes in adsorbed proteins as those occurring in the heat-set gelation of concentrated solutions of globular proteins at lower temperatures. Such spectral changes were believed to be due to the presence of the surface which promoted molecular and structural rearrangements. Using ATR-IR spectroscopy, Ishiguro et al.,[13] recently studied the adsorption of hen egg white lysozyme and bovine serum albumin (BSA) on a solid poly tris(trimethylsiloxy)silylstyrene (pTSS) surface in D_2O solution. From the area and shape of the amide I band of each spectrum, the amount of adsorption and the secondary structure of adsorbed lysozyme were determined simultaneously, as a function of adsorption time. The authors found that lysozyme molecules formed discrete assemblies (domains) on the surface, and the assemblies grew over several hours to have a definite architecture independent of the amount adsorbed. As for BSA, the extent of the conformational change was solely determined by the adsorption amount, regardless of the bulk concentration and the adsorption time. These differences in the adsorption properties of lysozyme and BSA may result from their different conformational stabilities.

Con A is a lectin obtained from jack bean (*Canavalia ensiformis*).[14] It has been proven to be an interesting and useful lectin. Con A is a robust type III protein[15] with well known properties and affinity interactions, which is characterized by good stability to be prevented from complete unfolding at the protein-solid interface. The usefulness of ConA lies in its specific binding action with certain carbohydrate-containing receptors. It is used in biology and biochemistry to characterize glycoproteins and other sugar-containing entities. It is also used in lectin affinity chromatography, cell adhesion/sorting and recognition of pathogens.[16, 17] It agglutinates red blood cells, complexes with blood group substances,[18] immunoglobulin glycopeptides[19] and carcinoembryonic antigens,[20, 21] and interacts with human plasma low density lipoprotein.[22] It has also been reported that Con A can react with E. coli[23] and interacts with lipopolysaccharide.[24] ConA often causes cancer cells to aggregate, but not normal cells.[25, 26] Con A conjugate of antitumor drugs has also been used in drug delivery systems of cultured cells.[27]

Despite the successes of modern pharmacology and surgery, an appropriate and correct diagnosis is still necessary to conquer a disease. Fast, easy, qualitative and inexpensive analytical methods are highly desirable if not necessary for a wide spectrum of applications. Therefore, it is very much necessary to carry out several bioassays in parallel, and meanwhile there is a clear demand for integrity and miniaturization of biosensors. Both of the above requirements have led to sparked interest in the fabrication of biomolecular patterns. In the last decade, significant achievements have been reported in the development of biomolecular microarrays and polymers used in biosensor production.[28]

The immobilization of biological molecules on a sensor's surface is extremely crucial for biosensor design. Many methods have been developed to solve this problem. There are many different ways of immobilizing proteins on hard substrates (usually glass, mica, silicon or gold surfaces). However, the protein immobilization remains a major problem since the functionality of protein depends on the mode of protein attaching to a substrate.[29] In the current study, it is intend to correlate biological activity of proteins with the adsorption conditions, the compositions, and the structure of adsorbed protein layers on different substrate for the biosensor applications. The methodology of comparing in situ FTIR spectra with the spectra of hypothetical multilayer systems simulated with assumed parameters such as composition, thickness and structure, developed in previous study, is very effective to obtain the information on the adsorption of protein.

In the previous study of Con A adsorption on a hydrophobic polystyrene (PS) surface[30] (Chapter 6), the effect of pH was examined for different adsorption time. This study is an extension of the previous work with the use of more hydrophilic substrate. For several protein systems,[31] it was well-established that the amount of protein adsorbed is not only sensitive to pH, but also to the history of pH that the interface is exposed, i.e. the path used to establish the final pH. Thus, in this work, the effect of pH history on the adsorption of Con A is investigated in a pH cycle, starting at pH 4.8, followed by pH 7.4 and then returning to 4.8. The reason of choosing pH 4.8 and 7.4 to perform this study is that Con A exists in two different structures in solutions at these two typical pH values. It is well documented that when pH is less than 5, Con A is present as a canonical dimer with dimension of 30 Å × 45 Å × 75 Å[32]. At neutral or higher pH (> 7) two such dimers were associated with their back sheets[33, 34] to form tetramer of dimensions around 60 × 70 × 70 (Å^3).[32] As mentioned earlier, the surface adsorption of a protein on a solid substrate is also influenced by the structure and properties of the protein. Therefore, these two characteristic pH values are ideal for studying the influence of different conformations of Con A on its adsorption.

The adsorption of Con A at the solid-water interface was characterized by attenuated total reflection infrared (ATR-IR) spectroscopy. With the help of spectral simulation, the surface assembling models of Con A on germanium substrate covered by native oxide at different time and pH are proposed. An explanation based on the property of Con A at different pH values is put forward to understand the adsorption mechanism, and the hydration of adsorbed layers is estimated. Subsequently, desorption of the adsorbed Con A layer in different aqueous solutions is examined.

7.2 Experimental

7.2.1 Materials

Con A was purchased from Sigma-Aldrich (C2010, essentially carbonate and salt free) and used directly without further purification. Phosphate buffered saline (PBS) buffer solution was prepared from KH_2PO_4 (1.47 mM), Na_2HPO_4 (6.46 mM), KCl (2.68 mM) and NaCl (0.137 M). NaOH or HCl was separately added to adjust the pH of solutions. 1 M NaCl and 0.035 M sodium dodecyl sulphate (SDS) solutions were used to study desorption of Con A. All reagents used were of analytical grade. Ultra-pure water from the Millipore (Milli-Q system) was used throughout the experiments. The solutions used in the experiments were freshly prepared.

7.2.2 Surface Preparation

Germanium ATR reflection element with dimension of 50 × 20 × 3 mm^3 and reflection angle of 45° was polished with alumina powder (< 0.05 μm), rinsed with water and toluene. The characteristics of the Ge surface were similar to that of the silicon wafer[35], with a thin native oxidized layer. The surface containing hydroxide and oxide surface species was slightly hydrophilic with a contact angle around 40°. The prepared Ge reflection element was assembled with a Teflon® liquid cell as described before[30]. The number of active internal reflections for *in situ* monitoring of protein adsorption/ desorption was calibrated to be 12 by the bands of water at 1643 and 3408 cm^{-1}.

7.2.3 Adsorption/ Desorption of Con A

Adsorption of Con A on germanium was carried out from 1 mg/ml Con A in PBS buffered solutions at various pH values (4.8 - 7.4 - 4.8). The aqueous solution was pumped (12.5 mL/min) into the cell on one side of ATR crystal, flowing through the connecting tubes and the cell on the other side of the ATR crystal, and finally returning to the bulk solution. Spectra were collected at p- and s-polarizations as a function of time and the total adsorption time at each pH was 21 h. For desorption, different washing solutions, such as: H_2O, NaCl and SDS, were used. They flowed through the cell over designed period of time, and the corresponding reflection spectra of the adsorbed layer were recorded *in situ*.

7.2.4 Determination of Optical Constants

The system under investigation is stratified into multilayer component. During *in situ* spectroscopic studies, the interaction of the infrared reflected beam with the multi-phase system is complex, giving rise to different optical effects. The recorded reflection spectrum is a function of the optical constants (n_i, k_i) of each multi-layer component, the thickness of surface layer, the three dimensional distribution of orientation, uniform or patch-like structures on the surface and the degree of hydration of adsorbed protein.

All the optical constants used for simulation of infrared spectra of hypothetical Con A layer on Ge at the presence of water are shown in Figure 7.1. Optical constants (n, k) of Ge and water were taken from the reference book[36] and published report[37], respectively. The optical constants of air were set at $n = 1$ and $k = 0$. The optical constants of adsorbed Con A were determined in a similar way to the previously described by infrared external reflection method[38]. It is assumed that optical constants of the adsorbed Con A layer are very similar to those of its bulk phases. This may be a crude assumption, since the effect of hydration causes changes in the optical property of adsorbed proteins, making them different from their dry state. This issue is to be discussed in detail in the next section.

The spectral simulations were made for p- and s-polarizations with the use of exact equations based on Hansen's formulas[39] for stratified system of isotropic phases with parallel interface boundaries.

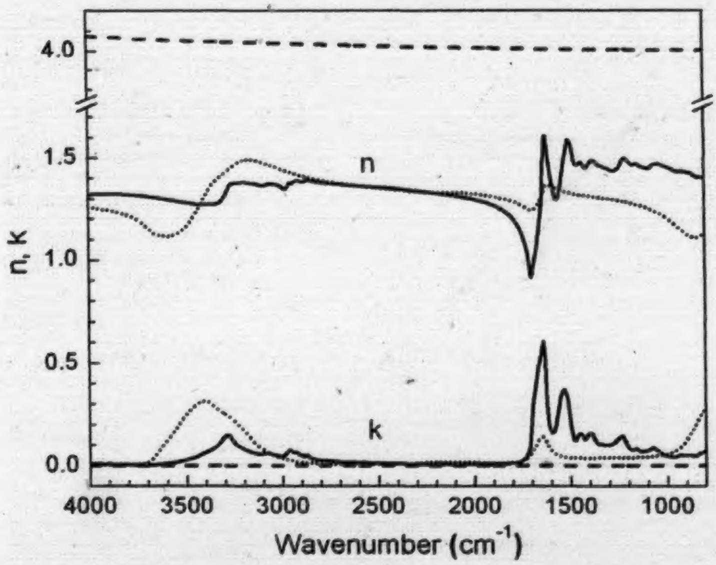

Figure 7.1 Optical constants: refractive index n and absorption coefficient *k* as a function of wavenumber for Con A (the solid lines), water (the dotted lines) and Ge (the dashed lines) used for spectra simulation of the systems under investigations.

7.2.5 Infrared Spectroscopy

Infrared spectra were recorded on a Fourier transform infrared (FTIR) spectrometer (Bruker IFS55) equipped with a mercury cadmium telluride (MCT) detector and an attenuated total reflection (ATR) attachment. A wire-grid polarizer was placed before the sample, providing p- or s-polarized incident light. These accessories were from Harrick Scientific Co. The reflection spectra of the adsorbed layers were obtained by the use of polarized light at the incidence angle of 45°. The spectrometer was purged with dry air (Balston filter) to minimize the disturbance of water vapor and carbon dioxide to the recorded spectra. The unit of intensity was defined as $-\log(\frac{R}{R_0})$, where R_0 and R are the reflectivities of the system without and with adsorbed Con A layers, respectively. For both reference and sample spectra 200 scans were collected. The resolution was set at 4 cm^{-1} (zero-filled = 2) with Blackman–Harris, three-term apodization.

7.3 Results and Discussion

7.3.1 Optical Consideration

For reflection spectra of adsorbed layer of Con A in stratified systems, the position and shape of characteristic absorbance bands of Con A and their relative intensities can be modified significantly with respect to corresponding transmission spectra of the same free standing sample[40]. The experience shows that the qualitative and quantitative interpretation of reflection spectra provides tremendous insights into molecular assembly and orientation by the use of spectral simulation.[41,42,43,44,45,46,47,48,49] Without the theoretical optical consideration of the system under investigation, the conclusive interpretation of spectroscopic reflection data is impossible or very limited at the best. Therefore, prior to drawing any conclusion relating to the chemical modification taking place during Con A adsorption, the changes resulting from optical effects must be evaluated before performing a final analysis of the data.

Close analysis of optical properties of Con A and water (Figure 7.1) reveals that there is overlapping of absorbance bands of water at around 3400 and 1640 cm^{-1} with that of Con A at 3280 cm^{-1} (due to N-H stretching vibration) and amide I band at around 1620 cm^{-1}, which complicates spectra interpretation. However, a positive finding is that the absorption coefficient of water in the region of amide I band is below 1/4 of the value for Con A characteristic band. The spectral feature in this region provides precise interpretation of protein amide I band.

The simulated spectra of 12 reflections for 3 nm Con A in the system of Ge/Con A/H_2O are presented in Figure 7.2. The 3 nm adsorbed layer represents the thickness of hypothetical Con A layer in the most flat position of adsorbed dimmers.[32] The simulated spectra of Con A layer in the presence of water are complex. There are positive and negative bands with strong changes in the intensity, depending on the use of polarizations. The simulated absorbance is defined as:

$$Abs = -\log \frac{R_{(Ge/3nmConA/H_2O)}}{R_{o(Ge/H_2O)}} \qquad (1)$$

where R is the reflectivity of the sample system, and R_o is the reflectivity of the reference system. The studied system is specified by the subscripts.

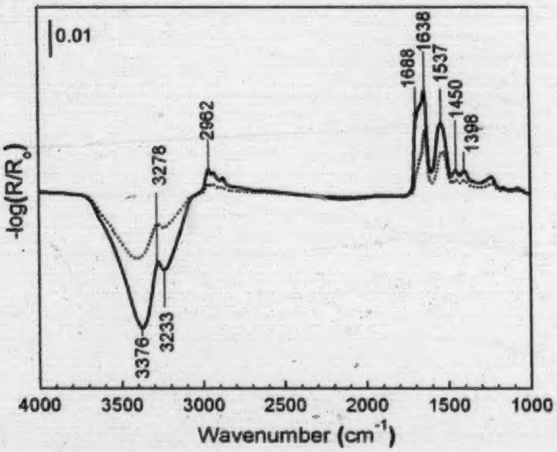

Figure 7.2 Simulated spectra for 12 reflections of 3 nm Con A on Ge contacted with water for p-polarization (the solid line) and s-polarization (the dotted line).

In the reference system, the water is in direct contact with Ge element while for the sample system in the presence of the Con A layer, the water is moved away from Ge surface by 3 nm Con A, as schematically shown in Figure 7.3. In the latter case, the absorbance by water is relatively lower. This spectral feature leads to an overall spectrum of negative absorbance of characteristic bands for water and positive absorbance of characteristic bands for Con A. The intensity of positive bands for Con A at 3278 cm^{-1} (due to N-H stretching vibration) is relatively weak. In contrast, the intensity of broad negative bands for water around 3350 cm^{-1} (owing to OH stretching vibration) is much stronger.

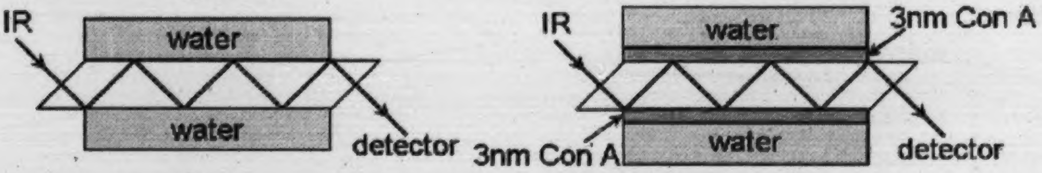

Figure 7.3 Schematic illustration of the configuration used in simulation: (A). the reference system; (B). the sample system with Con A adsorbed layers.

On the other hand, the intensity of negative "water" band is two times stronger for p- polarization than for s-polarization since the depth of penetration of evanescent wave outside of reflection element is two times larger for p-polarization. This spectral feature is pure optical effect which does not involve any changes in chemistry or any specific water conformation at Ge/Con A/H_2O interface. Similarly, the negative water band subtracted from positive amide I at 1640 cm^{-1} makes the intensity of the band somewhat lower than that of the original should be for the adsorbed Con A. By applying spectral simulation the real adsorbed amount of Con A can be determined precisely from reflection infrared spectra. More interestingly, any significant changes in conformation of adsorbed Con A can be investigated and distinguished, for example, from hydration effect of the adsorbed proteins. There is also another important optical effect which can modify shape of amide I band (the shoulder at 1688 cm^{-1} in Figure 7.2). This effect is caused by the strong dispersion of refractive index of Con A with exceptional value below 1.0 (see Figure 7.1). Details and discussion of these optical phenomena can be found in a previous paper.[30]

7.3.2 Adsorption Kinetics of Con A

Figure 7.4 shows kinetics of Con A adsorption on Ge through the pH cycle of 4.8 - 7.4 - 4.8. Three different regions of the adsorption can be distinguished. In the beginning of region I (pH 4.8) a quick adsorption of Con A on Ge surface is observed, with the formation of a layer around 3 nm thick, which is close to a monolayer coverage with the assumption of the most flat orientation of Con A molecules at the interface. As Con A adsorption progresses, remarkably slower kinetics is observed, reaching a thickness of 5 nm after 21 h.

The 5 nm thick layer could be achieved by simple co-adsorption of Con A in the second layer. The other possibility is a rearrangement of the adsorbed Con A molecules in the first layer to more vertical orientations. In addition to the thinnest hypothetical monolayer (3 nm) of Con A dimer, there are 4.5 nm intermediate monolayer and 7.5 nm thick layer with vertical orientation of Con A adsorbed on germanium crystal (see Figure 7.5). Hence, with changing orientation from flat to intermediate and even vertical orientation, the 5 nm thick monolayer of Con A molecules can also be achieved. This 5 nm close-packed monolayer is the maximum amount that is observed on germanium at pH 4.8. In the same solution half thinner adsorbed layer of Con A on polystyrene (1.5 nm after 30 min and 2.5 nm after 21 h) was reported [30]. This finding indicates that hydrophilic Ge is a more favourable substrate for Con A adsorption than hydrophobic polystyrene. Based on the observation and conclusions from the previous studies of Con A adsorption on hydrophobic polystyrene[30] (Chapter 6), an adsorption model of Con A on Ge surface is proposed. The schematic diagram of the adsorption process at pH 4.8 is shown in Figure 7.5 A/B, showing a transition of some adsorbed molecules from a flat configuration (A) to vertical orientation (B) as adsorption progresses.

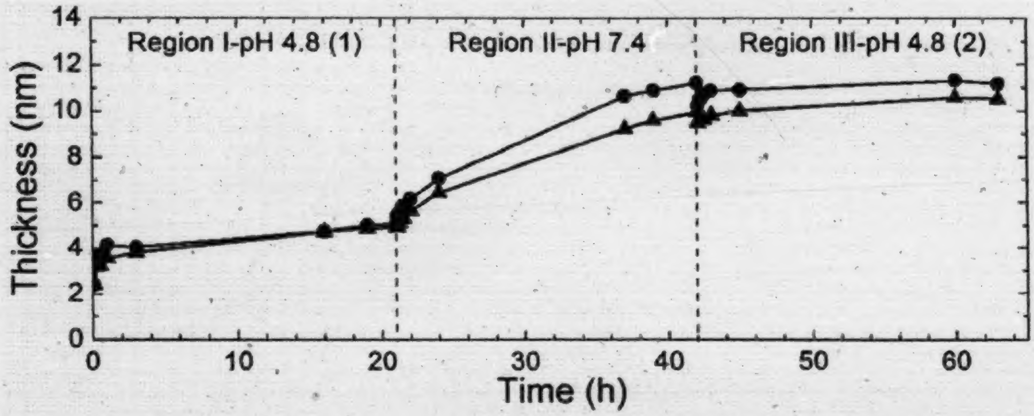

Figure 7.4 Kinetics of Con A adsorption on Ge based on *in situ* recorded reflection spectra of adsorbed Con A and determined from the intensity of amide I (the triangles) and amide II (the circles) absorbance bands. The thickness of Con A layer is based on the best fitting of experimental spectra to the simulated hypothetical surface layer with assumed thickness.

Electrostatic interaction and surface hydrophilicity are often considered to be the dominant driving force for protein adsorption. The amount of adsorption is determined by a combination of the interactions between the protein molecules in the adsorbed layer and between the protein and solid substrate. In this case, it was found that Con A and Ge surfaces have strong interaction to build up the first layer in a short period (also see desorption section). After the initial adsorption, the lateral electrostatic repulsion between Con A molecules plays a role. Since pH 4.8 is close to the isoelectric point of Con A (pH 4.5 ~ 5.5),[50] the repulsive force is not sufficient to drive molecules away from the surface. However, the reorganization of the adsorbed Con A molecules reduces the repulsion, allowing the surface to accommodate more molecules and leading to the formation of a close-packed monolayer.

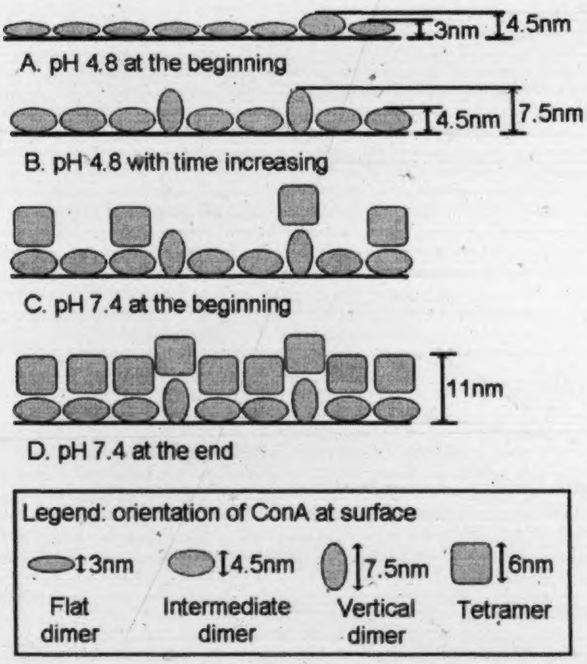
A. pH 4.8 at the beginning

B. pH 4.8 with time increasing

C. pH 7.4 at the beginning

D. pH 7.4 at the end

Figure 7.5 Schematic illustration of the surface coverage and orientation of Con A adsorbed at the Ge-water interface. For simplicity the hydration by water molecules is not shown.

When the pH was increased to 7.4 (region II in Figure 7.4), Con A molecules start to adsorb on the previously adsorbed Con A monolayer. With increasing time, Con A continuously adsorbs at a faster rate than that over the first period at pH 4.8. Up to another 21 h, an additional 6 nm thick Con A layer is deposited on previously adsorbed Con A monolayer. It is known that Con A molecules exist as tetramer in aqueous solution at pH 7.4. The further adsorption of Con A is therefore in the form of Con A tetramer formed in the solution. The corresponding adsorption model is shown in Figure 7.5 C/D.

It is known that the monomer of Con A constitutes of three β-sheets (Figure 7.6 (A)): the 6-stranded back sheet, the 7-stranded front sheet and a smaller 5-stranded S-sheet which plays a major role in holding the two large sheets together. At pH below 6, the strand in back sheet (nearest the X axis) is hydrogen bonded to its symmetry-related mate in the typical anti-parallel manner, forming the canonical dimer of Con A (Figure

7.6 (B)). Around pH 7, association of the dimer around the Y and Z axes to another dimer produces the tetramer of four identical subunits (Figure 7.6 (C)) [51, 52]. Several charged and ionisable side chains are buried upon tetramer formation, while in the dimer the side chains are on the surface, accessible to solvent. Hydrogen bonding has a major influence on the formation of dimer or tetramer.[53] The additional adsorption at pH 7.4 is believed to result from strong hydrogen bonding formed between the adsorbed dimer layer and the forthcoming tetramer.

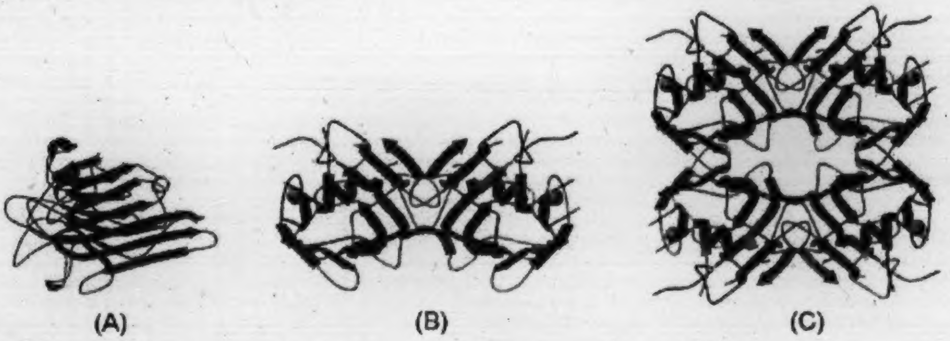

Figure 7.6 Ribbon diagrams of (A) the monomer of Con A, (B) the dimer of Con A and (C) the tetramer of Con A (Protein Data Bank: 2UU8 and 1CES).

When the pH of the flowing solution returns to 4.8 (2) (region III in Figure 7.4), a sudden small decrease in the thickness was observed, followed by a gradual recovery to the level before pH change within one hour. There is no further change in the thickness of adsorbed Con A, indicating that a stable state is reached after 1h.

The observed irreversibility of adsorption indicates that the adsorption process is not controlled solely by electrostatic forces as a change in pH back to 4.8 would change electrostatic interaction and hence Con A adsorption. As shown in Figure 7.4, such a change was not observed. It appears that hydrogen bonding or hydrophobic interaction dominates the protein-protein interactions and hence their overall adsorption process. These interactions are sufficiently strong to ensure that Con A remains attached to the substrate while changing pH.

7.3.3 Hydration of the Con A Adsorbed Layer

Figure 7.4 shows clearly that the estimated amount of adsorption from amide I and amide II is almost the same for the first 21 h at pH 4.8. However, for the consecutive adsorption at higher pH, the amounts estimated from amide I are always lower than that from amide II. Because the water level inside of Con A can influence the intensity of amide I band as discussed above, the differences of the thickness estimation on amide I and amide II could come from the different water levels inside the protein at each adsorption stage.

For the estimation of hydration level of adsorbed Con A layer the methodology is used based on the assumptions of the formation of mixed phase where both Con A and water components form one phase with optical properties related to the content of each component, as proposed before.[30] Figure 7.7 (A) shows the experimental spectra for 5 min adsorption at pH 4.8 and the simulation results with the assumption of 30% hydration of Con A. The simulated spectra of 3 nm thick adsorbed layer have the best fit with those experimentally observed in the spectral range of amide and water characteristic bands. After 21h adsorption at pH 4.8, the best agreement between simulated and experimental results led to a layer thickness of 7 nm with 30% hydration (Figure 7.7 (B)). Towards the end of subsequent 21 h adsorption at pH 7.4, an additional 10 nm layer with 50% hydration is estimated to fit the simulated spectra with those measured as shown in Figure 7.7 (C). It should be noted that the thickness discussed here is for the hydrated Con A layers, which is thicker than that estimated from the crystalline Con A used in previous simulation (Figure 7.4). For example, when a crystalline structure of Con A is assumed for hypothetical layer, the best fit limited to amide I and amide II absorbance bands indicates a 5-nm thick layer of Con A after 21 h of adsorption at pH 4.8 as shown in Figure 7.4. However, when the hydration of the Con A adsorbed layer is taken into consideration, the best fit of simulated spectra with those measured leads to a real thickness of surface layer around 7 nm, including a hydration level of 30% water (Figure 7.7 (B)).

In general, for the water bands around 3200 - 3400 cm^{-1} (Figure 7.7), with intensities being used for hydration determination, the simulated spectra of s-polarization fit experimental data better than that of p-polarization. The difference between p- and s-polarizations is that for s-polarization an electric field vector has only one component parallel to the interface plane, whereas for p-polarization two components, one parallel and the other vertical are present. The larger discrepancy between the experimental and simulated spectra is observed for p-polarization for all adsorption layers (Figure 7.7) over water asymmetric vibration region around 3380 cm^{-1}. This finding clearly indicates that water molecules have a preferential organization in the Con A adsorbed layer.

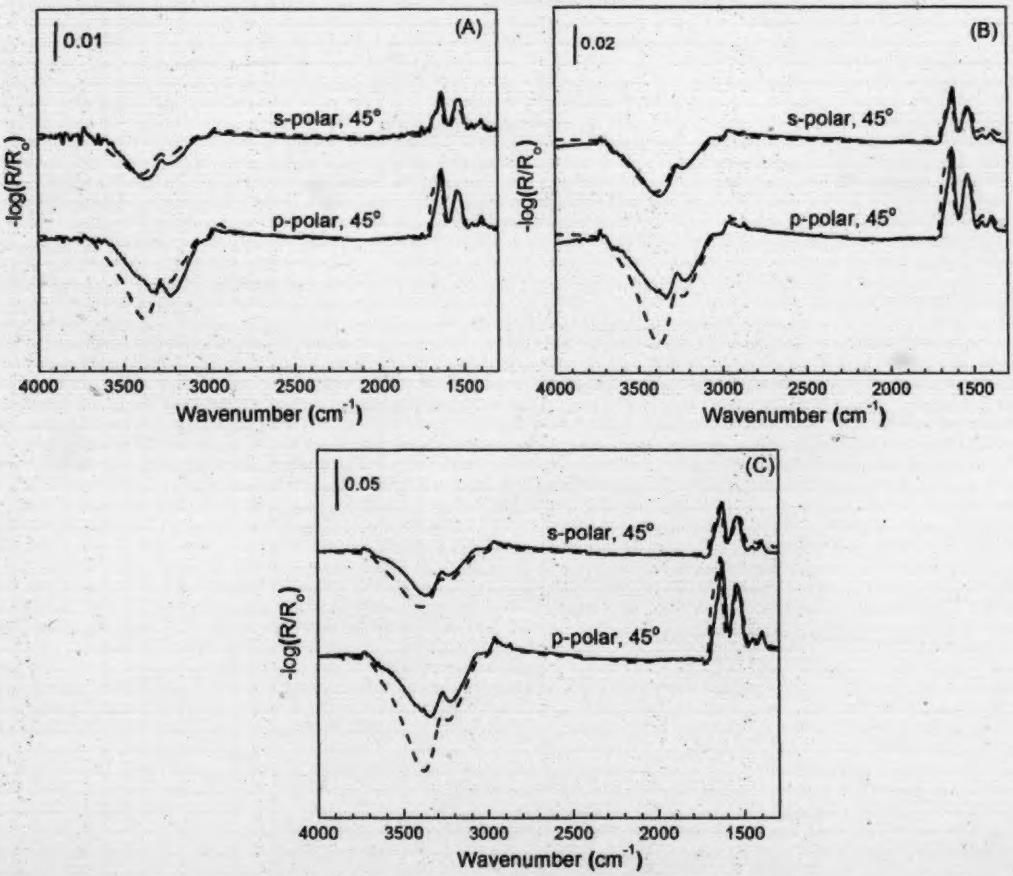

Figure 7.7 The comparison of *in situ* experimental spectra (solid lines) with the simulated spectra (dashed lines). (A) 5 min at pH 4.8 (1) vs. 3 nm 30% hydrated Con A; (B) 21 h at 4.8 (1) vs. 7 nm 30% hydrated Con A; (C) 21 h at pH 7.4 vs. 10 nm 50% hydrated Con A and 7 nm 30% hydrated Con A.

7.3.4 Desorption of Con A Layer

After the pH cycles of adsorption, the Con A solution was replaced by different aqueous solutions to study the stability of Con A layers on Ge surfaces. Ultra-pure water, 1 M NaCl solution and ultra-pure water again were subsequently pumped through the cell for a desired period of time. The spectra collected *in situ* at the end of each washing are shown in Figure 7.8. No noticeable difference was observed between spectra before and after washing with water, indicating a good stability of the adsorbed Con A layer in water. However, it is interesting to note that the spectrum after NaCl washing shows abnormal increases in the absolute values of bands (amide I and water). These observations suggest that the hydration of the adsorbed Con A layer, i.e. the entrapment of water in the adsorbed Con A layer, become decreased in 1M NaCl. Con A molecules in "drier" layer are situated closer to Ge surface, leading to higher reflection intensity[40]. Similarly, removing of water from the Con A adsorbed layer leads to more negative water band at around 3300 cm^{-1}. It is interesting to note that the hydration/dehydration process is reversible as reflected by the spectrum collected after subsequent water washing, returning to the case before contact with NaCl. These results clearly show that the adsorbed Con A layer is very stable in water and even in strong electrolyte solution containing 1 M NaCl. The hydration level of Con A layer could be modified by the change of electrolyte concentration. However, the overall conformation and distribution of the adsorbed Con A do not appear to be affected.

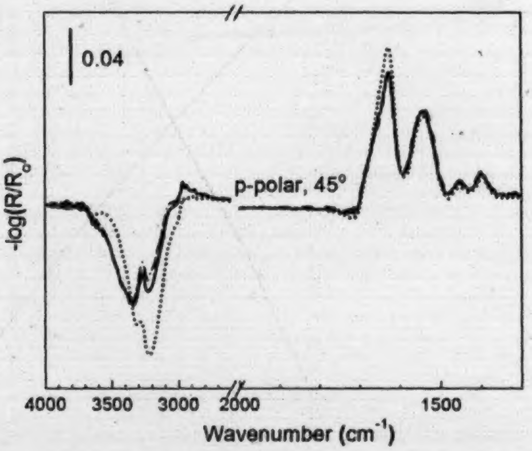

Figure 7.8 *In situ* experimental spectra of Con A after adsorption (21 h at pH 4.8 (2)) (the solid line), after 2 h water washing (the dashed line), 2 h NaCl (1 M) washing (the dotted line) and 20 h water washing (the dash-dot line).

Because of strong attachment of Con A layer on Ge, the adsorbed layer was washed with 0.035 M sodium dodecyl sulphate (SDS) solution, a strong detergent, was applied. The changes in the spectra with time are presented in Figure 7.9. After only 5 min washing the intensity of characteristic amide bands decreased dramatically, indicating that most of Con A was removed from the surface. However, the residual on the surface was observed with the intensity ratio of amide I and II bands reversed from the native state, suggesting that the structure of residual proteins on the surface was destroyed. After another three hours' washing, a further reduction in band intensity was observed. With washing time extended to 20 h, almost all residues were removed. The instant removal of majority of the adsorbed Con A by SDS washing suggests that Con A is physisorbed on Ge surface. The high stability of Con A layer on Ge in water and NaCl solution makes the physisorption to be a simple method for immobilization of Con A molecules at solid surfaces.

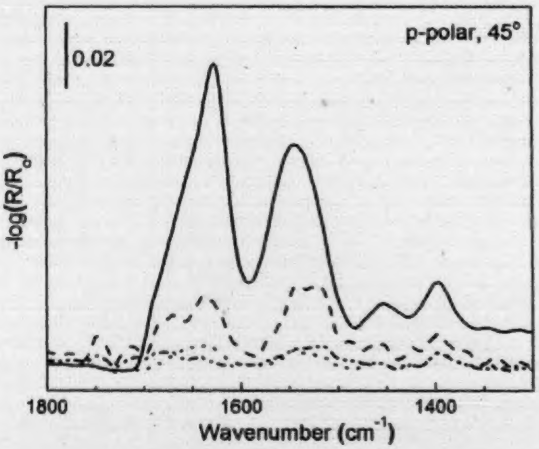

Figure 7.9 *In situ* experimental spectra of Con A after adsorption (21h at pH 4.8(2)) (the solid line) and after SDS washing of the Con A adsorbed layer on Ge for 5min (the dashed line), 3h (the dotted line) and 20h (the dash-dot-dot line).

7.4 Conclusions

The optical effect on modifications of spectra was confirmed by spectral simulation. The comparison of experimental spectra with simulated spectra of hypothetical surface layers with assumed parameters including composition, thickness and structure allowed qualitative and quantitative analysis of the adsorbed protein layers. After a short period of contact at pH 4.8, Con A molecules formed a close-packed dimer monolayer of 3 nm thick on Ge surfaces. Increasing immersion time makes the adsorbed Con A molecules experience an orientation change from flat to more vertical arrangement, increasing the absorbed layer to 5 nm thick after 21h incubation. Further increasing incubation time did not promote any multilayer formation of Con A on Ge at pH 4.8. At pH 7.4, continuous multilayer adsorption of Con A in the form of 6-nm thick tetramer layer on previously absorbed Con A monolayer of dimers was observed. When the pH returns to 4.8, the adsorbed tetramer remained on monolayer of Con A, indicating that the adsorption of Con A is an irreversible process. The protein-protein interaction by hydrogen bonding or hydrophobic interaction appears to dominate the overall adsorption process. Based on the experimental observation and the properties of Con A, the assembling models of Con A on Ge were proposed.

The hydration of adsorbed Con A was analyzed. Matching of simulated spectra with those experimentally measured allowed water contents within Con A to be quantitatively evaluated. The first absorbed layer at pH 4.8 contained around 30% hydration. The second Con A tetramer layer formed at pH 7.4 on the first monolayer of Con A contained 50% water, while the hydration in the first layer remained at 30%, indicating a preferential organization of water molecules in the adsorbed Con A layer.

Con A layers strongly adsorbed on the Ge surface by hydrogen bonding could not be removed by washing with water. Washing with 1 M NaCl solution decreased the hydration of Con A layer, while washing with 0.035 M sodium dodecyl sulphate solution removed the adsorbed layer. These results suggest that the Con A, although stable in water, is physically attached to Ge surface.

References

(1) Horbett, T. A.; Brash, J. L. eds.; Proteins at Interfaces II: Fundamentals and Applications; American Chemical Society: Washington, DC, 1995.

(2) Brash, J. L.; Horbett, T. A. eds.; Proteins at Interfaces: Physicochemical and Biochemical Studies; American Chemical Society: Washington, DC, 1987.

(3) Andrade, J. D.; Hlady, V. Protein adsorption and materials biocompatibility: a tutorial review and suggested hypotheses. Adv. Polym. Sci. 1986, 79, 1-63.

(4) Sandu, C.; Singh, R. K. Energy increase in operation and cleaning due to hear-exchanger fouling in milk. Food Technol. 1991, 45, 84-91.

(5) Hubbell, J. A. Biomaterials in tissue engineering. Bio-Technol. 1995, 13, 565-576.

(6) Ishihara, K.; Oshida, H.; Endo, Y.; Ueda, T.; Watanabe, A.; Nakabayashi, N. Hemocompatibility of human whole blood on polymers with a phospholipid polar group and its mechanism. J. Biomed. Mater. Res. 1992, 26, 1543-1552.

(7) Feng, M.; Morales, A. B.; Beugeling, T.; Bantjes, A.; Vanderwerf, K.; Gosselink, G.; Degrooth, B.; Greve, J. Adsorption of high density lipoproteins (HDL) on solid surfaces. J. Colloid Interface Sci. 1996, 177, 364-371.

(8) Martin, B. D.; Gaber, B. P.; Patterson, C. H.; Turner, D. C. Direct protein microarray fabrication using a hydrogel "stamper". Langmuir 1998, 14, 3971-3975.

(9) Inglis, W.; Sanders, G. H. W.; Williams, P. M.; Davies, M. C.; Roberts, C. J.; Tendler, S. J. B. A simple method for biocompatible polymer based spatially controlled adsorption of blood plasma proteins to a surface. Langmuir 2001, 17, 7402-7405.

(10) Klibanov, A. M. Immobilized enzymes and cells as practical catalysts. Science 1983, 219, 722-727.

(11) Haynes, C. A.; Norde, W. Globular proteins at solid/liquid interfaces. Colloid Surf. B 1994, 2, 517-566.

(12) Ball, A.; Jones, R. A. L. Conformational changes in adsorbed proteins. Langmuir, 1995, 11, 3542-3548.

(13) Ishiguro, R; Yokoyama, Y.; Maeda, H.; Shimamura, A.; Kameyama, K.; Hiramatsu, K., Modes of conformational changes of proteins adsorbed on a planar hydrophobic polymer surface reflecting their adsorption behaviors. J. Colloid Interface Sci. 2005, 290, 91-101.

(14) Sharon, N.; Lis, H. Lectins: Cell-agglutinating and sugar-specific proteins. Science 1972, 177, 949-959.

(15) Fink, A. L.; Calciano, L. J.; Goto, Y.; Kurotsu, T.; Palleros, D. R. Classification of acid denaturation of proteins: intermediates and unfolded states. Biochemistry, 1994, 33, 12504-12511.

(16) Revell, D. J.; Knight, J. R.; Blyth, D. J.; Haines, A. H.; Russell, D. A. Self-assembled carbohydrate monolayers: formation and surface selective molecular recognition. Langmuir 1998, 14 4517-4524.

(17) Gestwicki, J. E.; Strong, L. E.; Cairo, C.W.; Bohem, F. J.; Kiessling, L. L. Cell aggregation by scaffolded receptor clusters. Chem. Biol. 2002, 9, 163-169.

(18) Clark, A.; Denborough, M. The interaction of Concanavalin A with blood-group-substance glycoproteins from human seretions. Biochem. J. 1971, 121, 811-816.

(19) Kornfeld, R.; Ferris, C. Interaction of immunoglobulin glycopeptides with Concanavalin A. J. Biol. Chem. 1975, 250, 2614-2619.

(20) Brattain, M.; Jones, C.; Pittman, J.; Pretlow, T. The purification of carcinoembryonic antigen by glutaraldehyde cross-linked Concanavalin A. Biochem. Biophys. Res. Commun. 1975, 65, 63-67.

(21) Boenisch, T.; Norgaard-Pedersen, B. Carcinoembryonic antigen (CEA) of human tissue extracts: partial characterization of two variants separated by affinity chromatography on Concanavalin A. Clin. Chim. Acta 1975, 60, 25-32.

(22) Harmony, J.; Cordes, E. Interaction of human plasma low density lipoprotein with Concanavalin A and with Ricin. J. Biol. Chem. 1975, 250, 8614-8617.

(23) Picken, R.; Beachman, I. The interaction of Concanavalin A with mutant and wild-type strain of Escherichia coli K12. Biochem. Soc. Trans. 1975, 3, 387-388.

(24) Brunson, K.; Watson, D. Concanavalin A preparation with activities related to bacterial lipopolysaccharide, J. Immunol. 1975, 115, 599-600.

(25) Shoham, J.; Inbar, M.; Sachs, L. Differential toxicity on normal and transformed cells in vitro and inhibition of tumour development in vitro by Concanavalin A. Nature. 1970, 227, 1244-1246.

(26) Inbar, M.; Sachs, L. Structural difference in sites on the surface membrane of normal and transformed cells. Nature 1969, 223, 710-712.

(27) Tsuruo, T.; Yamori, T.; Tsukagoshi, S.; Sakurai, Y. Enhanced cytocidal action of methotrexate by conjugation to Concanavalin A. Int. J. Cancer, 1980, 26, 655-659.

(28) Lebed, K.; Pyka-Fościak, G.; Raczkowska, J.; Lekka, M.; Styczeń, J. Binding activity of patterned Concanavalin A studied by atomic force microscopy. J. Phys.: Condens. Matter. 2005, 17, S1447-S1458.

(29) Heng, Z; Snyder, M. Protein chip technology, Curr. Opin. Chem. Biol. 2003, 7, 55-63.

(30) Mielczarski, J. A.; Dong, J.; Mielczarski, E. Real time qualitative and quantitative evaluations of the adsorption of Concanavalin A on polystyrene. J. Phys. Chem. B, 2008, 112, 5228-5237.

(31) Su, T. J.; Lu, J. R.; Thomas, R. K.; Cui, Z. F.; Penfold, J. The effect of solution pH on the structure of lysozyme layers adsorbed at the silica-water interface studied by neutron reflection. Langmuir 1998, 14, 438-445.

(32) Shoham, M.; Yonath, A.; Sussman, J. L.; Moult, J.; Traub, W.; Kalb, A. J. Crystal structure of demetallized concanavalin A: the metal-binding region. J. Mol. Biol. 1979, 131, 137-155.

(33) McCubbin, W. D.; Kay, C. M. Molecular weight studies on concanavalin A. Biochem. Biophys. Res. Commun. 1971, 44, 101-109.

(34) Bouckaert, J.; Loris, R.; Poortmans, F.; Wyns, L. Crystallographic structure of metal-free concanavalin A at 2.5 Å resolution. Proteins. Struct. Funct. Genet. 1995, 23, 510-524.

(35) Morita, M.; Ohmi, T.; Hasegawa, E.; Kawakami, M.; Ohwada, M. Growth of native oxide on a silicon surface. J. Appl. Phys. 1990, 68, 1272-1281.

(36) Palik, E. D. Handbook of Optical Constants of Solids; Naval Research Laboratory, Academic Press Inc.: Washington, D. C. 1985.

(37) Downing, H. D.; Williams, D. Optical-constants of water in infrared. J. Geophys. Res. 1975, 80, 1656-1661.

(38) Mielczarski, J. A.; Milosevic, M.; Berets, S. L. Optical properties of strongly absorbing media determined by external reflection spectroscopy. Appl. Spectrosc., 1992, 46, 1040-1044.

(39) Hansen, W. N. Electric fields produced by the propagation of plane coherent electromagnetic radiation in a stratified medium. J. Opt. Soc. Am. 1968, 58, 380-390.

(40) Harrick, N. J. Internal Reflection Spectroscopy; Harrick Scientific Corporation, Ossining, New York, 3rd printing 1987.

(41) Mielczarski, J. A.; Yoon, R. H. Fourier transform infrared external reflection study of molecular orientation in spontaneously adsorbed layers on low-absorption substrate. J. Phys. Chem., 1989, 93, 2034-2038.

(42) Mielczarski, J. A.; Yoon, R. H. Spectroscopic studies of the structure of the adsorption layer of thionocarbamate. 2. On cuprous sulfide. Langmuir, 1991, 7,101-108.

(43) Mielczarski, J. A. External reflection infrared spectroscopy at metallic, semiconductor, and nonmetallic substrates. 1. Monolayer films. J. Phys. Chem., 1993, 97, 2649-2643.

(44) Mielczarski, J. A.; Mielczarski, E. Determination of molecular orientation and thickness of self-assembled monolayers of oleate on apatite by FTIR reflection spectroscopy. J. Phys. Chem., 1995, 99, 3206-3217.

(45) Mielczarski, J. A.; Mielczarski, E.; Zachwieja, J.; Cases, J. M. In situ and ex situ infrared studies of nature and structure of thiol monolayers adsorbed on cuprous sulfide at controlled potential. Langmuir, 1995, 11, 2787-2799.

(46) Mielczarski, E.; Mielczarski, J. A.; Cases, J. M. Molecular recognition effect in monolayer formation of oleate on fluorite. Langmuir, 1998, 14, 1739-1747.

(47) Mielczarski, J. A.; Mielczarski, E.; Cases, J. M. Dynamics of fluorite-oleate interactions. Langmuir 1999, 15, 500-508.

(48) Mielczarski, J. A.; Mielczarski, E. Infrared external reflection spectroscopy of adsorbed monolayers in a region of strong absorption of substrate. J. Phys. Chem. B 1999, 103, 5852-5859.

(49) Mielczarski, E.; Duval, Y. B.; Mielczarski, J. A. Spectroscopic characterization of the nature and structure of adsorbed organic monolayers on quartz in the region of very strong absorption of substrate. Reverse surface selection rule. J. Phys. Chem. B 2002, 106, 11985-11992.

(50) Lahiri, J.; Isaacs, L.; Tien, J.; Whitesides, G. M. A strategy for the generation of surfaces presenting ligands for studies of binding based on an active ester as a common

reactive intermediate: a surface plasmon resonance study. Anal. Chem. 1999, 71, 777-790.

(51) Hardman, K. D.; Ainsworth, C. F. Structure of concanavalin A at 2.4-Ang resolution. Biochemistry 1972, 11, 4910-4919.

(52) Einspahr, H.; Parks, E. H.; Suguna, K.; Subramanian, E.; Suddath, F. L. The crystal structure of pea lectin at 3.0-A resolution. J. Biol. Chem. 1986, 261, 16518-16527.

(53) Loris, R.; Hamelryck, T.; Bouckaert, J.; Wyns, L. Legume lectin structure. Biochimica et Biophysica Acta-Protein Structure and Molecular Enzymology 1998, 1383, 9-36.

Chapter 8 General Discussion and Conclusions

Through the study of three related subjects in this thesis, I was introduced into the research field of nanocomposites and biotechnology where surface and interface science plays an important role in the synthesis and applications. The major findings from this study have been described in each chapter. This chapter will summarize the main results presented in this thesis, and emphasize on possible future directions in the related fields.

8.1 Summary of the Obtained Results

Surfactant-templated mesoporous materials have played a prominent role in materials chemistry due to their wide range of potential applications as catalysts, sorbents, chemical/biological sensors, and optical/electronic nanodevices, etc.. Functionalization of the materials of high specific surface area by specific ligands, antibody, enzyme or biological cells to produce inorganic-organic composite can fulfill the requirements to a specific application. Synthesize and application of mesoporous silica coating with thiol functional group on magnetite particles as a sorbent to remove heavy metals from industrial effluents were described in *Chapter 3*. The magnetic core (Fe_3O_4) could solve the problem of practical separation of the spent sorbents from complex multiphases, simply by applying a magnetic field. The chapter elaborated in details on fundamentals of each step in synthesis of the materials, including dense liquid silica coating, molecular templating, sol-gel reaction and calcination, and the application of the sorbent in mercury removal.

Chapters 4 and *5* described the formation and function of silver nanoparticles on the framework of zeolite bound to magnetite for the elemental mercury removal from flue gases of power plants. The simple, yet novel synthesis method, involving the sintering of zeolite with silica coated magnetite, silver ion exchange, thermal reduction, was confirmed by the characterization of XPS, SEM, and TEM etc. The produced multifunctional composites show the great potential as sorbents for the removal of vapour-phase mercury from the flue gas of coal-fired power plants. Complete mercury capture by these novel sorbents is up to 200°C. The sorbents were repeatedly used to capture mercury and thermally release the captured mercury for 10 cycles. No degradation in the performance of the magnetic sorbent was observed. Instead, the capacity of the sorbent was steadily increased with increasing number of recycles. It was found that silver nanoparticles (<20nm) played an important role in the mercury capture with high capacity. The growth of these nanoparticles into hundred nanometers significantly reduced the mercury capture capacity. In-plant test shows the feasibility of the sorbent to capture mercury from flue gases in a full-scale coal-fired power plant.

Chapters 6 and *7* proposed a methodology to study the protein adsorption on solid surfaces. This study was intended to correlate biological activity of proteins with the adsorption conditions, the compositions, and the structure of adsorbed protein layers on different substrate for the biosensor applications. The methodology of comparing in situ FTIR spectra with the spectra of hypothetical multilayer systems simulated with assumed parameters such as composition, thickness and structure, is very effective to obtain fundamental information on the adsorption of protein. In these two chapters, the influence of pH, adsorption time and substrates was studied; the hydration level of the adsorbed layers was evaluated; and the adsorption mechanism was derived. By the methodology, the infrared spectral changes resulted from the chemical and structural changes caused by physicochemical interactions of protein with solid surface could be differentiated from pure optical effects associated with incident beam passing through the multilayer system. XPS was proven to provide valuable support information to this study.

8.2 Contributions to Original Knowledge

1. From factorial design study, it was established the optimal synthesis conditions to mesoporous silica coated magnetic particles of high specific surface area, which was functionalized with thiol group to remove heavy metals from industrial effluents.

2. It was the first time to synthesis magnetic zeolite composites with silver nanoparticles as multi-functional materials for catalysts, disinfectants and sorbents. The novel, yet unique feature of the synthesis process is to use silica coating as a bridge to bind magnetite and zeolite together by sintering. This silica layer also protects magnetite particles from corrosion and oxidation in excessive application environments.

3. The resultant magnetic zeolite composite features both magnetic and molecular sieve properties, which could be easily collected from effluent streams by an external

magnetic field and could introduce silver nanoparticles by ion exchange and controlled thermal reduction to produce recyclable and regenerable magnetic functional materials.

4. The magnetic zeolite composites with silver nanoparticles were primarily tested as sorbents for the elemental mercury removal. It demonstrated powerful adsorption capability, good thermal stability, effective magnetic separation and simple regeneration/recycle.

5. It is the first time to propose a methodology of comparing in situ FTIR spectra with the simulated spectra of hypothetical multilayer systems to study the adsorption of protein on solid surfaces. With this methodology, valuable information about surface composition, thickness, structure and hydration level can be derived, which are closely related to the bio-activity of proteins for the biosensor applications.

6. Characterization techniques, such as AFM, XPS, TEM, SEM, FTIR, Zeta Potential Measurement, TGA, N_2 Adsorption/Desorption Isotherms, AAS, and CVAFS, were extended to the studied systems, providing precise and abundant information about nanocomposites, surface and interface properties.

8.3 Future Directions

The surface science of metal oxides is a field that enjoys a rapidly increasing interest. This is motivated by the desire to contribute to the numerous applications where oxide surfaces play a role. The current trend to synthesize, characterize, and investigate nanomaterials has embraced TiO_2.[1] Titanium dioxide has been attracting the special interests of scientific researchers due to its wide range of applications, in ceramics, in electric devices such as varistors[1], in heterogeneous catalysis, as a photocatalyst,[2, 3, 4, 5, 6] in solar cells for the production of hydrogen and electric energy,[7, 8, 9] as gas sensor,[10, 11] as antibacterial, white pigment in paints and cosmetic products,[12, 13, 14] as a corrosion-protective coating, and as an optical coating.

This material lends itself quite well to building tiny structures in all sorts of sizes and shapes. Such nano-TiO_2 is typically produced in a sol–gel process, where a titanium alkoxide or halide ($TiCl_4$, TiF_4) is hydrolyzed, often in the presence of a template such as nano-spheres, nano-rods or anodic porous alumina,[15, 16] but other techniques, such as hydrodynamic cavitation, lithography, polyelectrolyte complexation, or nanocasting, have been employed as well.[17,18,19,20] The formation of periodic arrangements of nanostructured TiO_2 can also be achieved. For example, zeolite-like mesoporous materials has been formed for TiO_2 and other metal oxides[20]. Such high-surface area materials could be interesting for catalytic applications or in photonics. A hexagonal arrangement of anatase nanocrystals was achieved[21] and rod-like single-crystalline anatase particles could be brought into a regular cubic array.[16] These periodic arrangements are achieved through a balance of electrostatic forces in the solution. They exhibit an extremely regular pore size and a high surface area. Such a structure would allow the influence of surface orientation on the performance of dye-sensitized solar cells or electrochromic devices to be investigated. Interestingly, TiO_2 nanostructures are almost invariably either amorphous or of anatase form—another good motivation for surface scientists to find out more about the surfaces of TiO_2 polymorphs. There is a clear connection between the surface properties, the rational development of improved synthesis routes, and the possible usefulness in applications of nanomaterials.

In the area of biomaterials and biotechnology, the control and modification of surface state is a major challenge. Attachment of proteins and peptides to inorganic surfaces is important for improving biocompatibility or biosensor fabrication.[22,23,24] Reliable, fast, and versatile analytical tools used for medical diagnostics, drug screening, or environmental control are often based on biosensor devices that combine biological recognition with the transduction of a physical response. This can be an electrical signal, a change in mechanical properties, or an optical signal. Thus, the crucial step for developing an array platform is the intimate connection between the transducer surface and the biologically active coating. Adhesion is thus a major issue in all biomaterial applications, and almost always requires the design of the additional treatment of substrates and materials.[25] Biologically active compounds used in biosensor technology (such as nucleic acids, antibodies, and enzymes) work in aqueous solutions while in the living organism. Immobilization of these molecules onto a solid interface imposes a drastic change in their natural environment, which is believed to influence their proper function. The adsorption of proteins at biomaterial surfaces is thus a first step in understanding a series of biochemical and biophysical processes which determine a host's response to artificial organs.[26] Furthermore, the controlled adsorption of biologically active substances can be exploited to "sense" a response in biotechnological devices.[27] Another major area of interest has been the study of cell/surface interactions. The interest in this has been triggered by a broad range of biomaterial applications that rely on cells immobilized on solid surfaces, the most obvious example being the development of new implant materials and tissue regeneration. Cell/surface interactions are very complex and are not completely understood.

The fully-developed characterization techniques for surface and interface provide precise structural information about nanometer-sized systems. These techniques can be classified as scanning probe microscopy techniques, vibrational spectroscopies, electron and ion spectroscopies and diffraction techniques. [28] Scanning probe microscopy techniques, like AFM and Scanning tunneling microscopy (STM), are perhaps the most used characterization tools to determine the surface structural properties. AFM can also be used to measure force-versus-distance curves. [29] Such curves provide valuable information on local material interaction. Vibrational spectroscopies, including Fourier transform infrared (FTIR), sum frequency generation (SFG), high resolution electron energy loss spectroscopy (HREELS) and Raman spectroscopy, have shed much light about the packing density, molecular orientation and the presence of defects in the adsorbed surface monolayers.[30, 31, 32, 33, 34, 35] HREELS also probes molecular state of adsorption sites. Electron-based spectroscopies, such as AES, XPS, UPS(ultraviolet photoemission spectroscopy), and photoemission techniques with synchrotron radiation (EXAFS (extended x-ray absorption fine structure), XANES(x-ray absorption near edge spectroscopy)) have played a major role in investigating the structure and organization of alkanethiols on gold, and in particular, to characterize the S–Au bond, electronic properties of the adsorbed molecules, packing density, the crystalline order, and molecular orientation. [36, 37] Diffraction techniques, such as XRD, LEED (low-energy electron diffraction), atom diffraction, GIXD (grazing incidence x-ray diffraction), etc., were the first to give information about the structure of the S and thiol lattices on Au.[38, 39, 40, 41, 42, 43, 44, 45] They are the best techniques to obtain information on periodic structures. Numerous challenges still remain. The proper characterization techniques will future advance these interdisciplinary researches.

References

[1] U. Diebold *Surf. Sci. Rep.* **48** (2003) 53.

[2] C.N. Satterfield, Heterogeneous Catalysis in Industrial Practice, 2nd ed., McGraw-Hill, New York, 1991.

[3] J. Biener, J. Wang, R.J. Madix *Surf. Sci.* **442** (1999) 47.

[4] Q. Guo, S. Lee, D.W. Goodman *Surf. Sci.* **437** (1999) 38.

[5] M. Sambi, G. Sangiovanni, G. Granozzi, F. Parmigiani *Phys. Rev. B* **54** (1996) 13464.

[6] Z. Zhang, V.E. Henrich *Surf. Sci.* **277** (1992) 263.

[7] A. Fujishima, K. Honda *Nature* **238** (1972) 37.

[8] V.E. Henrich, G. Dresselhaus, H.J. Zeiger *Phys. Rev. Lett.* **36** (1976) 1335.

[9] W.J. Lo, Y.W. Chung, G.A. Somorjai *Surf. Sci.* **71** (1978) 199.

[10] P.K. Dutta, A. Ginwalla, B. Hogg, B.R. Patton, B. Chwieroth, Z. Liang, P. Gouma, M. Mills, S. Akbar *J. Phys. Chem.* **103** (1999) 4412.

[11] Y. Xu, K. Yao, X. Zhou, Q. Cao *Sens. Actuators B* **13–14** (1993) 492.

[12] F.A. Grant *Rev. Mod. Phys.* **31** (1959) 646.

[13] L.G. Phillips, D.M. Barbano *J. Dairy Sci.* **80** (1997) 2726.

[14] J. Hewitt *Cosmet. Toiletries* **114** (1999) 59.

[15] S.M. Liu, L.M. Gan, L.H. Liu, W.D. Zhang, H.C. Zheng *Chem. Mater.* **14** (2002) 1391.

[16] S.D. Burnside, V. Shklover, C. Barbe, P. Comte, F. Arendse, K. Brookes, M. Grätzel *Chem. Mater.* **10** (1998) 2419.

[17] J.E. Sunstrom IV, W.R. Moser, B. Marhik-Guerts *Chem. Mater.* **8** (1996) 2061.

[18] H.A. Bullen, S.J. Garrett *Nano Lett.* **2** (2002) 739.

[19] K. Subramanya Mayya, D.I. Gittins, F. Caruso *Chem. Mater.* **13** (2001) 3833.

[20] F. Schüth *Chem. Mater.* **13** (2001) 3184.

[21] T. Moritz, J. Reiss, K. Diesner, D. Su, A. Chemseddine *J. Phys. Chem. B* **101** (1997) 8052.

[22] A. Pallandre, B. de Lambert, R. Attia, A. M. Jonas, J. L. Viovy *Electrophoresis* **27** (2006) 584.

[23] P. Bataillard, F. Gardies, N. Jaffrezic-Renault, C. Martelet *Anal. Chem.* **60** (1988) 2374.

[24] A.Gebbert, M. Alverez-Icaza, W. Stochlein, R. D. Schmid *Anal. Chem.* **64** (1992) 997.

[25] R. Föch, A. N. Chifen, A. Bousquet, H. L. Khor, M. Jungblut, L.Q. Chu, Z. Zhang, I. Osey-Mensah, E.K. Sinner, W. Knoll, *Chem. Vapor Depos.* **13** (2007) 280.

[26] L. Tang, Y. Wu, R. B. Timmons *J. Biomed. Res*. **28** (1998) 156.

[27] M. Malmsten, B. Lassen, K. Holmberg, V. Thomas, G. Quash *J. Colloid Interf. Sci.* **177** (1996) 70.

[28] C. Vericat, M. E. Vela, G. A.. Benitez, J. A. Martin Gago, X. Torrelles, R. C. Salvarezza *J. Phy.: Condens. Matter* **18** (2006) R867.

[29] H.J. Butt, B. Cappella, M. Kappl *Surf. Sci. Rep.* **59**(2005) 1.

[30] F. Thery-Merland, C. Me'thivier, E. Pasquinet, L. Hairault, C. M. Pradier *Sensors Actuators* B **114** (2006) 223.

[31] X. Ding, K. Moumanis, J. J. Dubowski, L. Tay, N. L. Rowell *J. Appl. Phys.* **99** (2006) 054701.

[32] R. Winter, P. G. Nixon, G. L. Gard, D. J. Graham, D. G. Castner, N. R. Holcomb, D. W. Grainger *Langmuir* **20** (2004) 5776.

[33] A. Kudelski *Vib. Spectrosc.* **39** (2005) 200.

[34] Y. Chen, R. E. Palme, J. P. Wilcoxon *Surf. Sci.* **454–456** (2000) 963.

[35] S. M. Han, W. R. Ashurst, C. Carraro, R. Maboudian *J. Am. Chem. Soc.* **123** (2001) 2422.

[36] P. Feulner, T. Niedermayer, K. Eberle, R. Schneider, D. Menzel, A. Baumer, E. Schmich, A. Shaporenko, Y. Tai, M. Zharnikov *Surf. Sci.* **593** (2005) 252.

[37] D. R. Baer, M. H. Engelhard, A. Lea *Surf. Sci. Spectra* **10** (2003) 47.

[38] P. Fenter, A. Eberhardt, P. Eisenberger *Science* **266** (1994) 1216.

[39] M. G. Samant, C. A. Brown, J. G. II Gordon *Langmuir* **7** (1991) 437

[40] K. Heiser, D. L. Allara, K. Bahnck, S. Frey, M. Zharnikov, M. Grunze *Langmuir* **15** (1999) 5440.

[41] C. M. Whelan, C. J. Barnes, C. G. H. Walker, N. M. D. Brown *Surf. Sci.* **425** (1999) 195

[42] W. Azzam, P. Cyganik, G. Witte, M. Buck, Ch. Wöll *Langmuir* **19** (2003) 8262

[43] R. Gerlach, G. Polansk, H.G. Rubahn *Thin Solid Films* **318** (1998) 270.

[44] F. Balzer, R. Gerlach, G. Polanski, H. G. Rubahn *Chem. Phys. Lett.* **274** (1997) 145.

[45] N. III Camillone, T. Y. B. Leung, P. Schwartz, P. Eisenberger, G. Scoles *Langmuir* **12** (1996) 2737.

Appendix A Characterization Techniques

A.1 Introduction

In this thesis work, many modern techniques have been used for characterization of samples. In most cases, these techniques are not used separately but in combination to provide complementary and confirmative information about surface composition, morphology, orientation and structure, etc..

Theses techniques include atomic force microscopy (AFM), X-ray photoelectron spectroscopy (XPS), scanning electron microscopy (SEM), transmission electron microscopy (TEM), Fourier transform infrared spectroscopy (FTIR), zeta-potential measurement, particle sized measurements, N_2 adsorption-desorption isotherm, magnetization measurement, thermal gravimetric analysis (TGA), atomic absorption spectroscopy (AAS) and cold vapour atomic fluorescence spectroscopy (CVAFS). Some are used during the process of synthesis, while others are applied to the final products. In most cases, a conclusion is drawn from a judicious combination of the analysis by different techniques. A brief discussion of these techniques is presented in this section.

A.2 Atomic Force Microscopy (AFM)

In the field of microscopy, developments in control, manipulation, and measurement on a nanoscopic scale have led to the development of the scanning tunneling microscope by Binnig and Rohrer in 1982[1], the atomic force microscope (AFM)[2] and allied technique[3]. The AFM provides images of a variety of hard periodic surfaces with better than nanometer resolution [4, 5, 6, 7].The AFM images of fragile organic samples, including DNA, proteins, blood cells, Langmuir-Blodgett films, and polymers, have also been reported [8, 9, 10, 11, 12, 13,14, 15, 16]. Molecular and surface forces can also be measured on a near molecular scale. The AFM can be used for both conductive and non-conductive surfaces in air, vacuum or liquid environments at various modes of operations.

A schematic diagram of a typical AFM is shown in Figure A.1. It consists of a piezo scanner, a cantilever substrate, a laser beam system, a photodetector and a feedback control system. The AFM operates by controlling the forces between a tip attached to a cantilever and a sample mounted on a piezoelectric scanner. There are a number of modes to operate the instrument, but in the simplest case of imaging a surface, a sample attached to the piezoelectric scanner is brought into contact with the cantilever. As shown in Figure A.1, a laser beam reflected from the back of the cantilever to a position-sensitive photodiode detection device is used as the sensor to determine the deflection of the cantilever as the sample is rastered underneath the tip. After each scan in X direction, the sample is advanced by one increment in Y direction and the process is repeated. To produce quality images, the AFM must be capable of controlling the tip-sample interaction with great precision. This is accomplished with the use of an electronic feedback loop, which safeguards the tip and sample by keeping forces between them at a user-specified Setpoint level.

Laser beam displacement is monitored over two axes: vertically and horizontally. As the tip traces various surface features, its upward and downward movement shifts the beam between upper and lower photodiode segments, creating voltage differences which are electronically rendered into height information. Lateral displacement of the beam is also monitored, corresponding to the twist of the cantilever caused by frictional phenomena of the tip on the surface. The data of displacements in X and Y directions with corresponding displacement in Z direction, received by the photodiode detector are reported as a three-dimensional image.

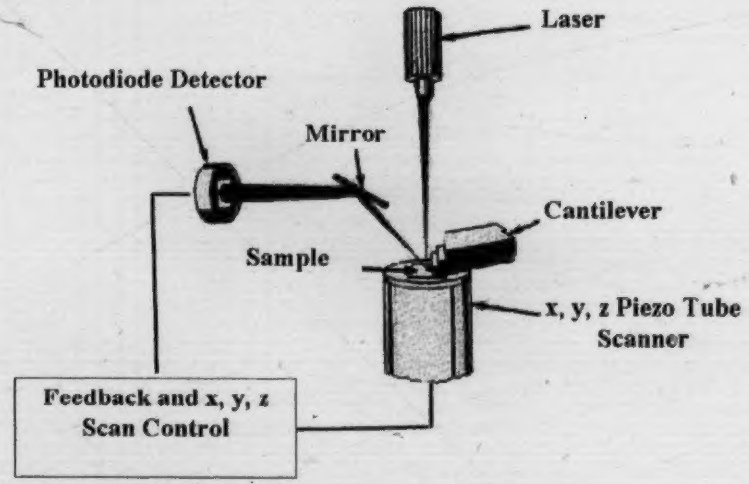

Figure A.1 Schematics of a typical atomic force microscope.

In this work, AFM was used to image the template of micelles and measure the interaction force between an AFM probing tip and a solid sample surface in surfactant solution. William Ducker first provided this method in 1991[17] and it is widely used in research.[18, 19, 20, 21, 22, 23, 24, 25, 26, 27]

A.3 Fourier Transform Infrared Spectroscopy (FTIR)

Infrared spectroscopy is widely used in determining the chemical structure of organic molecules. This technique is based on the absorption of infrared radiation by molecules, which causes the changes in vibrational and rotational energy states of the molecules. For a simple molecule, the amount of energy required to change the vibrational energy level from one state to another is related to the molecular vibrational frequency (υ) by Planck's Law:

$$E = h\upsilon \tag{A.1}$$

where the vibrational frequency is derived from ordinary mechanical model (Simple Harmonic Oscillator Model) and is given by:

$$\upsilon = \frac{1}{2\pi}\sqrt{\frac{K}{\mu}} \tag{A.2}$$

where K is the force constant of the bond between two atoms (N/m); and μ is the reduced mass related to the masses of the individual atoms in the bond by:

$$\mu = \frac{m_1 m_2}{m_1 + m_2} \tag{A.3}$$

in which m_1 and m_2 are the mass of atoms 1 and 2, respectively.

The radiation frequency can also be expressed in wavenumber ($\bar{\upsilon}$) as:

$$\bar{\upsilon} = \frac{1}{2\pi c}\sqrt{\frac{K}{\mu}} = 5.3\times10^{-12}\sqrt{\frac{K}{\mu}} \tag{A.4}$$

where $\bar{\upsilon}$ is the wavenumber of absorption peak (cm^{-1}) and c is the velocity of light in cm/s.

It can be seen from equation (A.4) that higher radiation energy is needed to cause a change in vibrational energy state of the molecules with a bond of greater force constant and/or smaller masses of atoms. Thus, IR bands will appear at higher wavenumbers for stronger bonds and/or a smaller mass of the bonded atoms. For example, IR bonds for C-C, C=C, and C≡C appear at waenumbers of ca. 1429,1667, and 2222 cm^{-1} respectively, because the force constant of a carbon/carbon bond is in the order of single < double < triple. The difference in the absorption of radiation energy for various vibrational modes gives rise to a pattern of IR bands (i.e. spectrum).

Fourier transform infrared (FTIR) spectrometer which has a number of advantages. The most significant advantages are the high sensitivity and fast spectra acquisition in addition to high accuracy and precision in wavelength determination. A few sampling techniques are often used in FTIR spectrometer including transmission, external reflection, internal reflection and diffuse reflection.

A.3.1 Transmission Infrared Spectroscopy

In the transmission mode, the radiation passing through the sample is detected. For powder samples, KBr is often used as the matrix or dilutant in preparing the sample pellets since KBr is transparent in the middle IR range. It should be noted that the possible interactions of chemicals with KBR influence the spectra and it requires dry powder samples. In addition, the low surface sensitivity has limited this technique to the bulk characterization.

A.3.2 External Reflectance Infrared Spectroscopy

In this mode, the single IR beam is directed to a highly reflective sample surface and the reflected IR radiation is detected. External reflectance spectroscopy is particularly useful for studying the structure of thin organic films on the surface that strongly reflects the incident beam. For substrates of relatively low reflectivity, the sensitivity of the technique is reduced. The advantages of external reflectance IR spectroscopy are that the incident beam can be polarized and the incident angle can be controlled to probe the orientation of molecules on the surface as shown in Figure A.2. Two beams, i.e., incident (i) and reflected (r), form a plane called the plane of incidence. The angle θ of incident beam to the normal of the surface is known as the incidence angle. When the electrical field of IR radiation is polarized to have a component parallel to the plane of incidence, p-polarization is obtained (Figure A.2 b). If the electrical field vectors are oriented perpendicular to the plane of incidence, the radiation is s-polarized (Figure A.2 c).

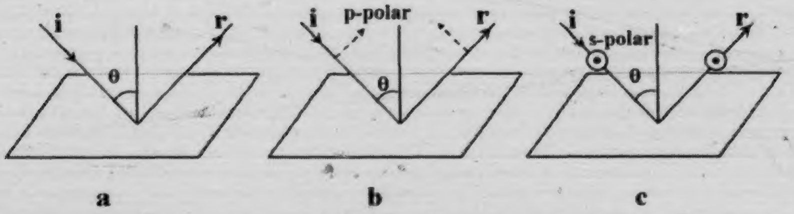

Figure A.2 Optical schematic of an external reflection.

Adsorption and orientation of xanthates and other thiol collectors on copper metal and cuprous sulfide (chalcocite) electrodes, with and without applied potential, have been investigated by Mielczarski and co-workers [28, 29, 30, 31, 32]. The formation of mono and multilayers of surfactants on semiconductors (low adsorption substrate) was detected and the orientation of the individual molecular groups and the nature of chemical bonding between the adsorbed species and surfaces were indentified by using the external reflection spectroscopy at different incident angles with both p- and s- polarized radiation.

A.3.3 Attenuated Total Reflection Infrared Spectroscopy (ATR-IR)

ATR-IR is sometimes referred to as internal reflection infrared spectroscopy. A typical setup for an ATR-IR experiment is shown in Figure A.3. A wire-grid polarizer was placed before the sample and p- or s-polarized light was provided. The ATR crystal can be made of Si, Ge, or ZeSe. The radiation is incident on the crystal in such a manner that total reflection occurs at the crystal-sample interface. ATR is more sensitive than other modes of FTIR, since the multiple reflection paths enhance the signal. Also, it can be modified for in-situ studies. With this technique, large amounts of samples are often required for full coverage of the crystal surface, and the intimate contact between the crystal and samples has to be controlled carefully. When hard materials are analyzed, attention has to be paid to avoid scratching the crystal with the sample.

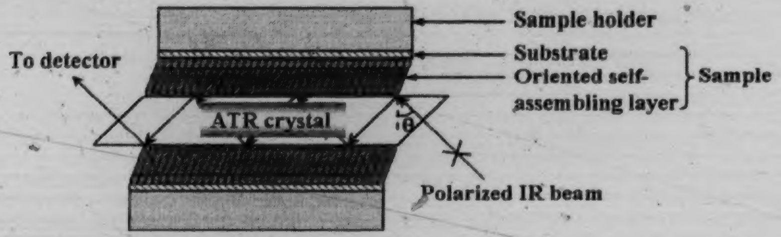

Figure A.3 Typical setup of ATR-IR experiment.

A.3.4 Diffuse Reflectance Infrared Fourier Transform Spectroscopy (DRIFTS)

Diffuse reflection results from the multiple scattering and partial absorption of the light flux impinging on (ideally) a matte-finish surface. Optical configuration of a diffuse reflectance cell is shown in Figure A.4. A small cup, about 10-15 mm in diameter and 3-4 mm deep, is used to hold the sample. Microcups, about 2-3 mm in diameter, may be used whenever there is only a limited amount of sample available. In this technique, the IR beam is focused on the sample by an ellipsoid mirror, and the diffusely reflected beam is collected with a large aperture mirror to direct the beam to the detector. This technique is preferred for fine powder samples and is surface sensitive. Another important feature of DRIFTS is the dependence of the effective penetration depth on the absorption and refractive coefficients of the sample.

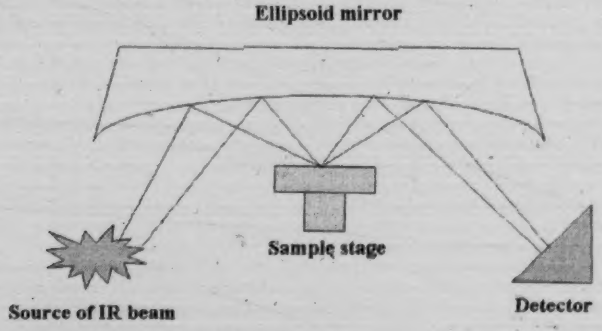

Figure A.4 Optical configuration of a DRIFTS cell.

A.4 Zeta Potential Measurement

In the 1940s Derjaguin, Verway, Landau and Overbeek developed a theory (DVLO) which dealt with colloidal stability. Zeta potential is a very good index of the magnitude of the interaction between colloidal particles and zeta potential measurements are used to assess the stability of colloidal systems.

Most colloidal systems in aqueous medial carry an electric charge. There are many origins of this surface charge depending upon the nature of the particle and its surrounding medium. 1) Dissociation of any acidic/basic groups on a particle surface. The magnitude of the surface charge depends on the acidic or basic strengths of the surface groups and on the pH of the solution. 2) Differential loss of ions from the crystal lattice, like a crystal of AgI, Ag^+ ions dissolve preferentially leaving a negatively charged surface.3) Adsorption of charged species (ions and ionic surfactants). Surfactant ions may be specifically adsorbed on the surface of a particle. Cationic surfactants would bead to a positively charged surface. Anionic surfactants would lead to a negatively charged surface.

The development of a net charge at the particle surface affects the distribution of ions in the surrounding interfacial region, resulting in an increased concentration of counter ions close to the surface. Thus an electrical double layer exists around each particle. The liquid layer surrounding the particle exists as two parts: an inner region (Stern layer) where the ions are strongly bound and an outer (diffuse) region where they are less firmly associated. Within this diffuse layer there is a notional boundary, called the shear plane or the slipping plane, within which the particle acts as a single entity. The potential at this boundary is called zeta potential. The schematic representation of an electrical double layer around a particle is shown in Figure A.5.

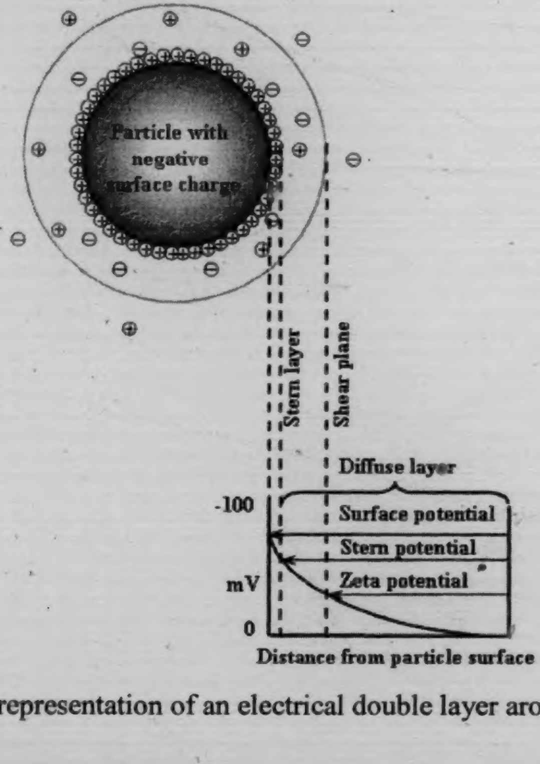
Particle with negative surface charge
Stern layer
Shear plane
Diffuse layer
-100
Surface potential
Stern potential
Zeta potential
mV
0
Distance from particle surface

Figure A.5 Schematic representation of an electrical double layer around a particle.

The magnitude of the zeta potential gives an indication of the potential stability of the colloidal system. If all the particles have a large negative or positive zeta potential they will repel each other and there is dispersion stability. If the particles have low zeta potential values then there is no force to prevent the particles coming together and there is dispersion instability. The most important factor that affects zeta potential is pH. Plot the zeta potential versus pH curve. There may be a point where the plot passes through zero zeta potential. This point is called the isoelectric point (IEP) of colloidal particles, which is very important from a practical consideration. The adsorption density, surface composition and orientation of molecules on a surface can be inferred by measuring the changes of IEP before and after adsorption.

Zetaphoremeter measures the zeta potential of colloidal particles by determining the rate at which these particles move in a known electric field. The technique is referred to as electrophoresis (the movement of a charged particle relative to the liquid which it is suspended in under the influence of an applied electric field). The colloid to be measured is placed in an electrophoresis chamber consisting of two electrode compartments and a connecting chamber (as shown in Figure A.6). A voltage is applied between two electrodes, located in each compartment. The applied voltage produces a uniform electric field in the connecting chamber and the charged particles by moving toward one or the other electrode. Positively charged particles migrate to the cathode (the negative electrode) and conversely, negatively particles migrate toward the anode (the positive electrode).

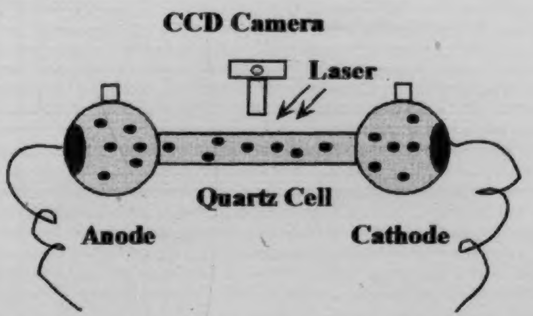

Figure A.6 Schematics of a typical electrophoresis cell of a zetaphoremeter.

Particles are moving under the applied electric field. The speed of the particles is directly proportional to the magnitude of the particle charge or zeta potential. The intensity of the scattered light from moving particles fluctuates with a frequency proportional to the velocity of the particles. The velocity is calculated from the measured frequency and converted to electrophoretic mobility (u_E). u_E is defined as the velocity per unit field strength and is directly proportional to the magnitude of the particle charge or zeta-potential.

One of the methods to relate the electrophoretic mobility (u_E) to zeta-potential (ζ) is by Henry equation

$$u_E = \frac{2\varepsilon\zeta}{3\eta} \cdot f_1(\kappa a) \qquad \text{(A.5)}$$

where ε is dielectric constant, η is viscosity, κ is the reciprocal of the thickness of the double layer and a is the particle diameter, $f_1(\kappa a)$ is Henry's function, a correction factor which takes into account the thickness of the double layer ($1/\kappa$) and particle diameter. In practice an approximation can be made, $f_1(\kappa a)$ approaches 1 for non-polar media and $f_1(\kappa a) = 1.5$ for particle dispersions in polar media.

A.5 X-ray Photoelectron Spectroscopy (XPS)

XPS is an ultrahigh vacuum technique. XPS consists of the application of energy analysis to the electrons (called photoelectrons) emitted from a surface illuminated by X-rays and exhibiting the photoelectric effect. The physical basis of the XPS technique is shown in Figure A.7. The energy carried by an incoming X-ray photon is absorbed by the target atom, raising it into an excited state from which energy is relaxed by the emission of a photoelectron. Photoelectrons are emitted from all energy levels of the target atom and hence the electron energy spectrum is characteristic of the emitting atom type, and may be thought of as its XPS fingerprint. Lines in the spectrum are labeled according to the energy level from which they originate.

The intensities of the various photoelectron lines are important for quantification and depend upon the amount of material present, the cross-section for photoemission at the X-ray energy concerned, and various instrumental and geometrical factors. The energy widths of the peaks are governed by the intrinsic widths of the energy levels involved and their lifetimes in the excited state, coupled with instrumental broadening resulting from the finite energy resolution of the electron energy analyzer and the natural width of the exciting X-ray line. The precise energy and shape of a particular line in an XPS spectrum is a function not only of the emitting element but also of its local environment and chemical state. Any effect that may cause a perturbation of the energy levels of atoms in the surface region of the target will cause a concomitant variation in the XPS spectrum. This gives rise to the chemical shifts in energy that is observed in XPS spectra. These are extremely important for spectral interpretation.

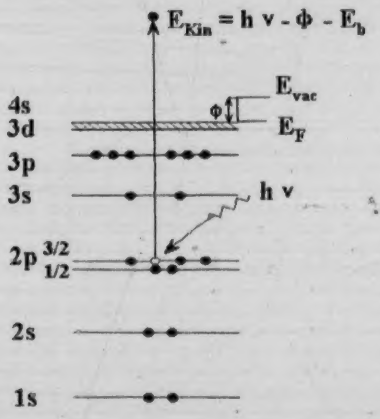

Figure A.7 The electron transition involved in the photoemission of a $2p_{3/2}$ electron from copper.

XPS provides element and chemical state identification for atoms located within the top few atomic layers of the sample under investigation. XPS is an extremely powerful method of surface analysis which is frequently applied to a variety of technological problems, such as in the fields of sorbent, catalysis, polymer and thin film technology. The X-ray beam is less damaging to the specimen surface than the electron beam used in AES (Auger Electron Spectroscopy), therefore XPS is the favoured technique for the analysis of the surface chemistry of radiation sensitive materials. The accumulation of electric charge during the analysis of insulating samples is also less of a problem in XPS than AES, as the positive sample charge formed because of the emission of electrons is readily neutralized by either a low energy electron beam, or by the stray secondary electrons often generated by the X-ray source.

A.6 Scanning Electron Microscopy (SEM)

The SEM is a type of electron microscope that creates various images by focusing a high energy beam of electrons onto the surface of a sample and detecting signals from the interaction of the incident electrons with the sample's surface. The type of signals gathered in a SEM includes secondary electrons, characteristic x-rays, and back scattered electrons. The SEM is capable of producing high-resolution images of a sample surface in its primary use mode, secondary electron imaging. In this manner SEM images have great depth of field yielding a characteristic three-dimensional appearance useful for understanding the surface structure of a sample. Characteristic x-rays are emitted when the primary beam causes the ejection of inner shell electrons from the sample and are used to tell the elemental composition of the sample. The back-scattered electrons emitted from the sample can be used alone to form an image or in conjunction with the characteristic x-rays as atomic number contrast clues to the elemental composition of the sample.

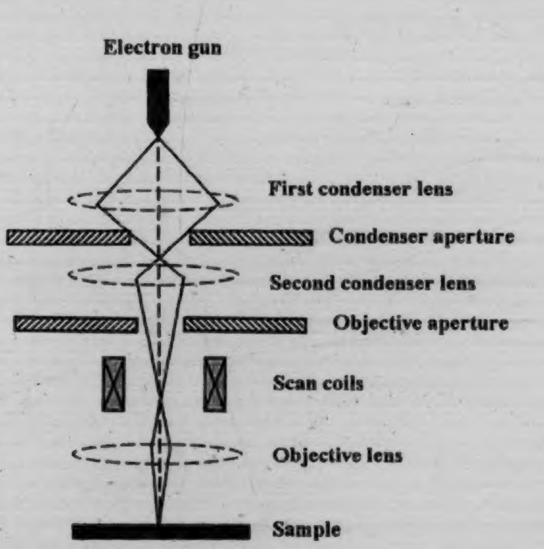

Figure A.8 The structural illustration of SEM.

In a typical SEM, electrons are thermionically emitted from a tungsten or lanthanum hyxaboride (LaB_6) cathode and are accelerated towards an anode; alternatively, electrons can be emitted via field emission (FE), which is the emission of electrons from the surface of a condensed phase into another phase due to the presence of high electric fields. The electron beam generated in the electron gun is attracted through the anode, condensed by a condenser lenses, and focused as very fine focal point on the sample by the objective lens. The beam passes through pairs of scanning coils, where a magnetic field is created which deflects the beam horizontally and vertically so that it scans in a raster fashion over a rectangular area of the sample surface.

When the primary electron beam interacts with the sample, the electrons lose energy by various reactions within a teardrop-shaped interaction volume of the specimen, as shown in Figure A.9, which extends from less than 100 nm to around 5 µm into the surface. The size of the interaction volume depends on the landing energy of electrons, the atomic number of the specimen, the density of specimen and the angle of incidence for the electron beam. The electron specimen interaction and depth profile are summarized in Figure A.9.

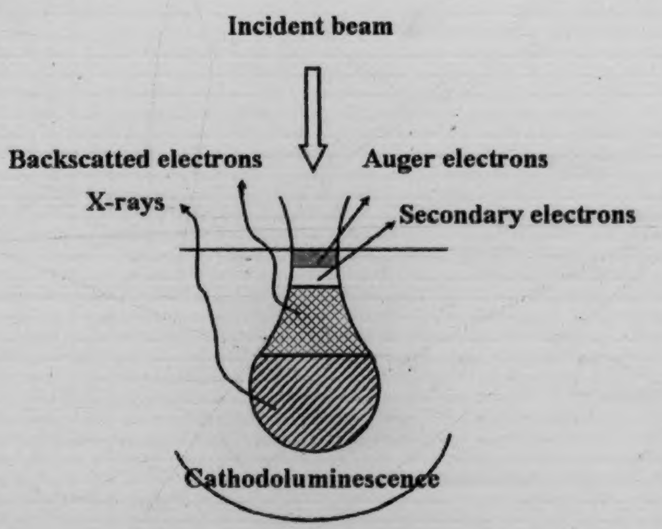

Figure A.9 Electron specimen interaction and depth profile.

The regular SEM requires a conductive sample. Three requirements for preparing samples for a regular SEM are: 1) Remove all water, solvents, or other materials that could vaporize while in the vacuum; 2) Firmly mount all the samples; 3) Non-metallic samples, such as ceramics materials or biological specimen, should be coated with carbon, chrome, or gold etc., so they are electrically conductive. Metallic samples can be placed directly into the SEM. Embedding samples in a resin with further polishing could be beneficial for both materials and biological specimens, especially when imaging in backscattered electrons or X-ray microanalysis are performed.

A.7 Transmission Electron Microscopy (TEM)

The transmission electron microscope (TEM) operates on the same basic principles as the light microscope but uses electrons instead of light. The maximum resolution of a light microscope is limited by the wavelength of light. TEM use electrons as "light source" which have both wave and particle properties and their wave-like property suggest that a beam of electrons can behave like a beam of electromagnetic radiation.

Theoretical resolution (*d*) is mainly based on wavelength of imaging medium,

$$d = 0.61\frac{\lambda}{n\sin\alpha} \qquad \text{(A.6)}$$

where λ is wavelength, n is refractive index of the media around and α is the convergence semi-angle. The wavelength of electrons depends on their speed,

$$\lambda = \frac{h}{mv} \qquad \text{(A.7)}$$

where h is Planck's constant (6.626×10^{-34} J·s), m *is* mass and v is velocity. The speed of electrons is related to their acceleration voltage,

$$\frac{1}{2}mv^2 = eU \qquad \text{(A.8)}$$

$$\text{i.e.} \quad v = \sqrt{\frac{2eU}{m}} \qquad \text{(A.9)}$$

where e is the charge of electron carrier (1.60×10^{-19} C) and U is the acceleration voltage. The much shorter wavelength of electron beam makes it possible to get a resolution a thousand times better than with a light microscope. High resolution transmission electron microscopy (HRTEM) can even observe objects to the order of a few angstrom (10^{-10} m).

A typical TEM works as follows. A stream of monochromatic electrons is generated by thermionic emission or field emission. This stream is focused to a small, thin, coherent beam by the use of condenser lenses. Condenser aperture restricts the beam by knocking out high angle electrons. The beam strikes the specimen and parts of it are transmitted. This transmitted portion is focused by the objective lens into an image. Optional Objective and Selected Area metal apertures can restrict the beam; the Objective aperture enhancing contrast by blocking out high-angle diffracted electrons, the Selected

Area aperture enabling the user to examine the periodic diffraction of electrons by ordered arrangements of atoms in the sample. The image is passed down the column through the intermediate and projector lenses, being enlarged all the way. The image strikes the phosphor image screen and light is generated, allowing the user to see the image. In the bright field imaging mode, the darker areas of the image represent those areas of the sample that fewer electrons were transmitted through (they are thicker or denser). The lighter areas of the image represent those areas of the sample that more electrons were transmitted through (they are thinner or less dense).

A.8 Particle Size Measurement

Particle size measurement is an extremely important parameter across most branches of industry. The stability, chemical reactivity, opacity, flow-ability and material strength of many materials are affected by the size and characteristics of the particles within them. Both Zetasizer and Mastersizer 2000 by Malvern Instruments (Mssachusetts, USA) have been used to measure particle sizes in this work.

A.8.1 Zetasizer

A Zetasizer uses the technique of Photon Correlation Spectroscopy (PCS) to measure submicron particle size of 1nm – 3μm. Particles dispersed in a fluid are in constant random motion, commonly referred to as Brownian motion. Photon Correlation Spectroscopy measures the speed of this motion, calculates the diffusion speed of particles, and relates diffusion coefficient (*D*) to particle size (*r*) using the Srokes-Einstein equation,

$$D = \frac{kT}{6\pi\eta r} \tag{A.10}$$

where *k* is the Boltzmann constant, *T* is the temperature, η is the solvent viscosity and *r* is the equivalent sphere's radius. When Zetasizer works, a mean particle size is calculated as recommended in the ISO 13321 standard.

A.8.2 Mastersizer

Mastersizer measures particle size of powders, dispersions and emulsions within the size range of 0.02-2000 microns. Mie scattering theory was used to fit the measured light signal to a particle size distribution.

The concepts of geometrical optics (refraction by lenses and reflection by mirrors) that are familiar in the macroscopic world do not adequately describe the interactions of particles with light when the particle size is comparable to the wavelength of the light. Mie theory provides rigorous solutions for light scattering by an isotropic sphere embedded in a homogeneous medium. Extensions of Mie theory include solutions for core/shell spheres and gradient-index spheres. Although these theories are restricted to the case of a perfect sphere, the results have provided insight into the scattering and absorption properties for a wide variety of pigment systems, including non-spherical pigments. Like a fingerprint, each size of the particle has its own characteristic scattering pattern and analysis of the overall scattering pattern allows accurate determination of the particle size distribution.

In general, when the light wavelength is similar to the particle diameter, light interacts with the particle over a cross-sectional area larger than the geometric cross section of the particle. The Mie calculation output provides this scattering cross section, C_{sca}. Often this parameter is divided by the geometric cross-sectional area to give a dimensionless scattering efficiency parameter, Q_{sca}.

$$Q_{sca} = \frac{C_{sca}}{\pi r^2} \tag{A.11}$$

However, in pigment applications, the formulation properties and costs depend on particle volume rather than cross-sectional area. Therefore, a more meaningful efficiency parameter is the scattering coefficient per micron, *SCPM*, defined as the scattering cross section divided by particle volume.

$$SCPM = \frac{C_{sca}}{4/3\pi r^3} = \frac{3Q_{sca}}{4r} \tag{A.12}$$

Since the intensity of scattered light varies with the scattering angle, the asymmetry parameter must be considered to give the scattering coefficient, *SC* (μm^{-1}), which is the preferred parameter for correlations with experimental data for systems in which multiple scattering is predominant. The relationship is

$$SC(\mu m^{-1}) = 0.75 \times (1 - \cos\theta) \times SCPM \tag{A.13}$$

where the asymmetry parameter, $\cos\theta$, is the average cosine of the scattering angle, weighted by the intensity of the scattered light as a function of angle.

The Mastersizer measures by using the optical unit to capture the actual scattering patter from a population of particles. Using the theories described above allows calculating the size of particles which created that pattern.

A.9 Thermal Gravimetric Analysis (TGA)

TGA is a technique by which physicochemical properties (moisture, crystalline water, and/ or volatile components) of a substrate and/or surface reaction products can be probed as a function of temperature, whilst the substrate is subjected to a controlled heating rate [33]. The mass of the sample in a controlled atmosphere is recorded continuously as a function of temperature or time during heating. The amount and the rate of weight loss at elevated temperatures are related to the chemical structure and composition of given samples. In general, a higher temperature is required to decompose more stable materials.

In this thesis, thermal gravimetric analysis is used to characterize the removal of surfactants trapped in the mesoporous SiO_2 network on Fe_3O_4. The underlying idea is that most metal oxides decompose at a higher temperature than the thin organic films. Therefore, the net weight loss in the temperature regime in which metal oxides remain stable can be attributed to the decomposition of thin organic films.

A.10 N_2 Adsorption-Desorption Isotherms

Specific surface area and pore size distribution are material properties of solids, which allow a study of chemical-physical characteristics of porous substances. In the present work, the specific surface area and pore size distribution of synthesized porous materials are experimentally measured by nitrogen adsorption-desorption analyses.

A.10.1 BET Specific Surface Area

The specific surface area can be measured by adsorption using the BET isotherm. BET theory is a well-known rule for the physical adsorption of gas molecules on a solid surface proposed by Stephen Brunauer, Paul Hugh Emmett and Edward Teller in 1938 [34]. The BET equation is expressed by Eq. A.14:

$$\frac{1}{V[(P_o/P)-1]}=\frac{C-1}{V_m C}\left(\frac{P}{P_o}\right)+\frac{1}{V_m C} \tag{A.14}$$

P and P_0 are the equilibrium and saturation pressure of adsorbates at the temperature of adsorption, V is the volume the adsorbed gas, V_m is the volume the monolayer adsorbed gas and C is the BET constant.

Equation (A.14) is an adsorption isotherm and can be plotted as a straight line with $1 / V[(P_0/P) - 1]$ on the y-axis and P/P_0 on the x-axis according to experimental results. This plot is called a BET plot. In the range of linear relationship, the value of the slope and the y-intercept of the line are used to calculate the volume of the monolayer adsorbed gas V_m and the BET constant C.

A total surface area S_{total} and a specific surface area S are evaluated by the equations (A.15) and (A.16):

$$S_{total} = \frac{(V_m N s)}{M_V} \tag{A.15}$$

$$S = \frac{S_{total}}{m} \tag{A.16}$$

where N is Avagadro number (6.022×10^{23}); s is the cross section area of adsorbed molecule, such as 16.2×10^{-20} m^2 for nitrogen molecules; M_V is the molar volume of adsorbed gas (22410 cm^3/mol for N_2); m is the weight of sample solid.

A.10.2 Pore Volume and Pore Size Distribution

The most common methods to determine pore volume and pore size distribution are the gas sorption and mercury porosimetry. The two techniques complement each other. Physical adsorption techniques can extend the lower size measurement down to about 2 nm diameter by Barrett-Joyner_Halenda (BJH) method and up to 50 nm; whereas mercury porosimetry is used to obtain porosity information from about 3 nm up about 360 μm diameter which is not attainable by gas sorption.

In the N_2 adsorption/desorption method, the "adsorbed"/ "desorbed" amount is the sum of adsorption/desorption from open pores and condensation in/evaporation from the pores changing their state between being filled-up and containing only adsorbed film. The adsorption process in the pores consists of formation of an adsorbed layer on pore wall; subsequent condensation of the adsorbate in the interior of the pore; the initial relative pressure (P/P_o) close to unity; all pores to be ultimately filled with liquid. The process of desorption is assumed to proceed by capillary evaporation from the interior of the pore followed by a gradual decrease in the thickness of the adsorbed film. The Barrett-Joyner-Halenda (BJH) method for calculating pore size distributions[35] is one of a family of methods[36] based on a model of the adsorbent as a collection of cylindrical pores. The method accounts for capillary condensation in the pores using the classical Kelvin equation (A.17),

$$\ln\frac{P}{P_o}=\frac{2\gamma M_V}{rR_cT} \tag{A.17}$$

where P is the actual vapour pressure, P_o is the saturation vapour pressure, γ is the surface tension, M_V is the molar volume, R_c is the universal gas constant, r is the radius of the droplet.

A.11 Magnetization Measurement

In order to use magnetic separation in industrial applications, it is important to characterize the magnetic properties of the synthesized sorbents. A Quantum Design 9T-PPMS dc magnetometer was used to obtain magnetization curves.

The DC magnetization measurements measure a sample's magnetic moment M in a certain applied magnetic field H at a specific temperature T. It moves the sample through a set of copper coils and analyzes the induced signal with a digital signal processor to determine the sample's magnetic moment.

The samples were placed in a gelcap sample holder and vibrated in the vicinity of a set of pick-up coils. The change of magnetic flux through the coils causes an induction voltage and the voltage profile is proportional to the magnetization of the sample:

$$V(t)=C\frac{df}{dt} \tag{A.18}$$

where $V(t)$ is the induction voltage, $f(t)$ represents the changing flux in the pick-up coils caused by the moving magnetic particles, and C is a constant. The actual sample moment is obtained by numerically integrating the voltage profile and fitting the known waveform for a dipole moving through the detection coils to the resulting data using a regression algorithm.

A.12 Atomic Absorption Spectroscopy (AAS)

AAS uses the absorption of light to measure the concentration of gas-phase atoms. Since samples are usually liquids or solids, the analyte atoms or ions must be vaporized in a flame or graphite furnace. The atoms absorb ultraviolet or visible light and make transitions to higher electronic energy levels. The analyte concentration is determined from the amount of absorption. The schematic illustration of AAS is shown in Figure A.10.

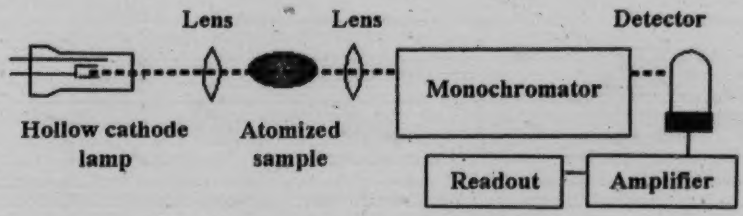

Figure A. 10 Schematic of an atomic-absorption experiment.

The light source is usually a hollow-cathode lamp of the element that is being measured. Since AAS required that the analyte atoms be in the gas phase. Ions or atoms in a sample must undergo desolvation, vaporization and atomization to break the compounds making up the sample into free atoms in a high-temperature source such as a flame (approximately 4500 °C for Nitrous oxide/acetylene flame and 2000 °C for Air/acetylene flame) or graphite furnace. Flame AAS can only analyze solutions, while graphite furnace AAS can accept solutions, slurries, or solid samples. The type of flame used depends on element being analyzed. For refractory elements like Si, Mo, Al, etc., the higher temperature nitrous oxide/acetylene flame is used. For more easily dissociated compounds of elements like Fe, Ni, Zn, Cu, etc., the lower temperature Air/acetylene is used.

The neutral ground state atoms generated in the flame absorb characteristic light emitted from the lamp of the same element being analyzed. The amount of light absorbed by the atoms is generally proportional to the concentration of the element being analyzed. A number of standard solutions are run first on the instrument to obtain the calibration line (absorbance v.s. concentration) and then the samples are analyzed to find the concentration at a certain absorbance on the calibration plot. The concentration range of atomic absorption in solutions is from a few of ppb (part per billion) to ppm (part per million) levels of cations in solution.

In the present work, AAS is used to determine the amount of metal ions loaded on magnetic sorbents, which is calculated from the difference of initial and after-loading equilibrium metal ion concentrations.

A.13 Cold Vapor Atomic Fluorescence Spectroscopy (CVAFS)

Cold vapour atomic fluorescence spectroscopy is a subset of the analytical technique known as atomic fluorescence spectroscopy (AFS). Used in the measurement of trace amounts of volatile heavy metals such as mercury, cold vapour AFS makes use of the unique characteristic of mercury that allows vapor measurement at room temperature. Free mercury atoms in a carrier gas are excited by a collimated ultraviolet light source at 253.7 nm. The excited atoms re-radiate their absorbed energy (fluoresce) at this same wavelength. Unlike the directional excitation source, the fluorescence is omnidirectional and may thus be detected using a photomultiplier tube or UV photodiode. The technique differs from the more conventional atomic absorption (AA) technique in that it is more sensitive, more selective, and is linear over a wide range of concentrations. However, any molecular species present in the carrier gas will quench the fluorescence signal and for this reason, the technique is most commonly used with an inert carrier gas such as argon.

Gold coated traps may be used to collect mercury in ambient air or other media. The traps are then heated, releasing the mercury from the gold while passing argon through the cartridge. This preconcentrates mercury, increasing sensitivity, and also transfers mercury into an inert gas.

A.14 Summary

Several analytical techniques used in this thesis work for characterizing surface and particles properties are briefly reviewed. AFM is suitable for imaging surface topographies and force measurement. FTIR can furnish an insight into the molecular orientation and chemical bonding of surface coatings, while XPS is adapted to determination of surface chemical environments and compositions. Some classical techniques, such as SEM, TEM, TGA and zeta-potential measurement, are also used to provide the direct information on the formation and properties of the resultant products in various synthesis stages very useful. N_2 adsorption-desorption is used for obtaining the specific surface area and pore volume information. The magnetic properties are characterized by DC magnetometer and the particle size is measured by Zetasizer and Mastersizer. Atomic absorption spectroscopy and cold vapour atomic fluorescence spectroscopy is used to assess the applications of the functionalized magnetic sorbents.

References

1 Binnig, G.; Rohrer, H. *Helv. Phys. Acta* 1982, 55, 726-735

2 Binnig, G.; Quate, C.; Gerber, G. *Phys. Rev. Lett.* 1986, 56,930-933

3 Wickramasinghe, H. K. *Sci. Am.* 1989 October, 74-81

4 Marti, **O.;** Drake, B.; Hansma, P. K. Appl. *Phys.* Lett. 1987,51, 484-486

5 Erlandsson, R.; Hadziioannou, G.; Mate, C. M.; McClelland, G. M.; Chiang, S. J. *Chem. Phys. 1*988,89,5190-5193

6 Alexander, S.; Hellemans, L.; Marti, 0.; Schneir, J.; Elings, V.; Hansma, P. K. J. Appl. *Phys.* 1989,65,164-167

7 Friedbacher, G.; Hansma, P. K.; Ramli, E.; Stucky, G. D. Science1991,253,1261-1263

8 Weisenhorn, A. L.; Hansma, P. K.; Albrecht, T. R.; Quate, C.F. *Appl. Phys. Lett.* 1989,54,2651-2653

9 eisenhom.A.L.:Drake.B.:Prater.C.B.:Gould.S.A.C.:Hansma,

P. K:; Ohnesorge,'F.; Egger, hi.; Heyn, S.-P.; Gaub, H. E. *Biophys. J.* 1990,58, 1251-1268

10 Egger, M.; Ohnesorge, F.; Weisenhorn, A. L.; Heyn, S. P.; Drake,B.; Prater, C. B.; Gould, S. A. C.; Hansma, P. K.; Gaub, H. E. *J. Struct.Biol.* 1990, 103, 89-94

11 Butt, H.-J.; Downing, K. H.; Hansma, P. K. *Biophys. J.* 1990,58, 1473-1480

12 Erlandsson, R.; Wigren, R.; Olsson, L. *Microsc. Microanal.Microstruct.* 1990, 1, 471-480

13 Meyer,E.;Howald,L.;Overney,R. M.;Heinzelmann,H.;Frommer, J.; GGntherodt, H.-J.; Wagner, T.; Schier, H.; Roth, S. *Nature (London)*1991,349, 398-400

14 Tsao, Y.-H.; Yang, S. X.;Evans,D. F.; Wennerstrbm,H.*Langmuir*1991, 7,3154-3159

15 Marchant, R. E.; Lea, A. S.; Andrade, J. D.; Bockenstedt, P. *J.Colloid Interface Sci. 1992, 148,261-272*

16 Leung, 0. M.; Goh, M. C. *Science* 1992,255,6446

17 Ducker, W. A.; Senden, T. J.; Pashley, R. M. *Nature* 1991,353, 239-241

18 Ducker, W. A.; Senden, T. J. Pashley, R. M. *Langmuir* 1992, 8, 1831-1836.

19 Wanless, E. J.; Ducker, W. A. *J. Phys. Chem.* 1996, 100, 3207-3214

20 Lachlan M.. Grant, Fredrik Tiberg, and William A. Ducker, *J. Phys. Chem. B* 1998, 102, 4288-4294

21 Ducker, W. A.; Wanless, E. J. *Langmuir* 1999, 15, 160-168

22 Liu, J. F.; Min, G.; Ducker, W. A. *Langmuir* 2001, 17, 4895-4903.

23 Radmacher, M.; Tillmann, R. W.; Fritz, M.; Gaub, H. B. *Science* 1992, 257, 1900-1905.

24 Israelachvili, J.; Wennerstrom H. *Nature* 1996, 379, 219-225.

25 Manne, S.; Gaub, H. E. *Science* 1995, 270, 1480-1482.

26 Takano, H.; Kenseth, J. R.; Wong, S. S. O'Brien, J. C.; Porter, M. D. *Chemical Reviews* 1999, 99, 2845.

27 Noy, A.; Vezenov, D. V.; Lieber, C. M. 1997 *Annual Review of Materials Science* 1997, 27, 381-421.

28 Mielczarski, J. A.; Yoon, R. H., *J. Phys. Chem.* **1989**, *93*, 2034-2038.

29 Mielczarski, J. A. *J. Phys. Chem.* **1993**, *97*, 2649-2663.

30 Mielczarski, J. A.; Mielczarski, E. *J. Phys. Chem.* **1995,** *99*, 3206-3217.

31 Mielczarski, J. A.; Mielczarski, E.; Zachwieja, J.; Cases, J.M. *Langmuir* **1995**, *11*, 2787-2799.

32 Mielczarski, E.; Duval, Y.; Mielczarski, J.A. *J. Phys. Chem. B* **2002,** *106* (46), 11985-11992.

33 Skoog, D.A. and Leary, J.J., 1992, Principles of Instrumental Analysis, Fourth Edition, Harcourt Brace College Publishers, New York, pp 568-571

34 Brunauer, S.; Emmet, H. P.; Teller, E., Adsorption of Gases in Multimolecular Layers, J. Am. Chem. Soc., 1938, 60, 309.

35 Barrett, E. P.; Joyner, L. G.; Halenda, P. P., *J. Am. Chem. Soc.* 1951, 73, 373.

36 Gregg, S. J.; Sing, K. S. W. *Adsorption, Surface Area and Porosity*, 2nd ed.; Academic Press; London, 1982.

Appendix B Continuation of Chapter 2

B.1 Methods for the Preparation of Magnetic Nanocomposites

B.1.1 Molecular Self-assembly (SA)

Molecular self-assembly (SA) is a process of spontaneous formation of a functionalized organic molecular (surfactant) layer on an inorganic substrate in an organic or aqueous solvent [1]. The preparation and characterization of self-assembled (SA) monolayer coatings of various organic surfactants on flat metal or metal oxide surfaces have been reported in a number of publications. These include alkysilane surfactant on hydroxylated surfaces, such as silica and aluminum oxide; alkanethiolates on gold, silver and copper; alcohol and amines on platinum; and carboxylic and hydroxamic acids on aluminum oxide and silver oxide [2, 3, 4, 5, 6, 7, 8, 9, 10, 11]. In more recent publications, bolaamphiphiles with two different reactive head groups at both ends of the molecule are used to manipulate the architecture of organic films on flat metal or metal oxide surfaces such as gold, silica and aluminum oxide [12, 13, 14, 15, 16]. By controlling the relative reactivity of the two functional groups with the surface, one functional group can anchor chemically onto the surface and the other remains reactive to target species. However, most of the fabrications of SA monolayers are limited to flat substrates and few publications have described the preparation and characterization of SA coatings using bolaamphiphiles on metal or metal oxide powders, particularly of magnetic iron oxides which have potential applications in drug delivery, magnetic carrier technology, raw material recovery, biological cell separation, magnetic fluids, magnetic ink, and magnetic memory media [17, 18, 19, 20, 21, 22].

In our laboratory [23], 16-mercaptohexadecanoic acid (MHA) ($HS(CH_2)_{15}COOH$) was assembled onto nanosized magnetic particles (γ-Fe_2O_3) from chloroform. To elucidate the reactivity of polar groups with γ-Fe_2O_3, stearic acid [$CH_3(CH_2)_{16}COOH$], are also self-assembled into monolayer coatings on magnetic particles and characterized by X-ray photon spectroscopy (XPS), diffuse-reflectance infrared Fourier transform spectroscopy (DRIFTS) and film floatation. It is expected that the carboxylic head group (-COOH) of MHA preferentially anchors to the surface of the magnetic particles so that the thiol (-SH) on the other end remains available for different reactions.

The most significant spectral change in the XPS spectra of γ-Fe_2O_3 with and without self assembled layers is the appearance of two C_{1s} bands at 288.3 (COO-) and 284.6 eV (C-C) [24], when the γ-Fe_2O_3 powders were treated by stearic acid and MHA. The ratio of area under the C_{1s} band of higher binding energy to that of lower binding energy was calculated to be ca. 1:17 and 1:15 for γ-Fe_2O_3 self-assembled with stearic acid and MHA, respectively. These values are in excellent agreement with those derived from the molecular structure. For the MHA treated sample, a sulfur band of S_{2p} at 163.3 eV was observed. This band is characteristic of –SH or –S-S- groups without oxidization to sulfate. These spectral changes indicate the presence of self assembled stearic acid and MHA layer on γ-Fe_2O_3.

To determine the orientation of surfactant molecules in the SA monolayers, a surface-sensitive, diffuse-reflectance infrared Fourier transform spectroscopy (DRIFTS) was used, and the spectra are shown in Figure B.1. Over the high wavenumber region, the CH_2 stretching vibration bans at 2924 and 2851 cm^{-1} are observed, suggesting the presence of a hydrocarbon chain as anticipated. The CH_2 bands appeared at the same band positions for bulk MHA and for MHA coated on γ-Fe_2O_3. However, the bands are sharper for the MHA on γ-Fe_2O_3 than for bulk MHA, indicating a more ordered polymethylene chain and confirming the assembly of a densely packed surfactant monolayer. However, over the low wavenumber region, the MHA on γ-Fe_2O_3 resulted in a different spectral feature than bulk MHA. The absence of the carbonyl band at 1703cm^{-1} and the presence of a carboxylate band at 1433 cm^{-1} for the MHA on γ-Fe_2O_3 suggest not only the anchoring of carbonyl groups on γ-Fe_2O_3, transferring a carbonyl to the carboxylate functionality, but also the absence of the second MHA layer, i.e., only a monolayer coverage. Should the second layer be present, a mixed functionality of carboxylate from the first layer (band at 1433 cm^{-1}) and carbonyl from the second layer (band at 1703 cm^{-1}) would be observed.

From film flotation test, the differences of critical surface tensions of MHA-coated γ-Fe_2O_3, stearic acid coated particles and DTDPA (3, 3'-dithiodipropionic acid)-coated particles further confirmed that the terminal group of the MHA coated on γ-Fe_2O_3 is thiol or bisulfide, rather than a carbonyl, sulfate, or sulfonate functionality. It also indicated that long chain hydrocarbon association of amphiphiles is necessary to for a densely packed monolayer, such as MHA on γ-Fe_2O_3.

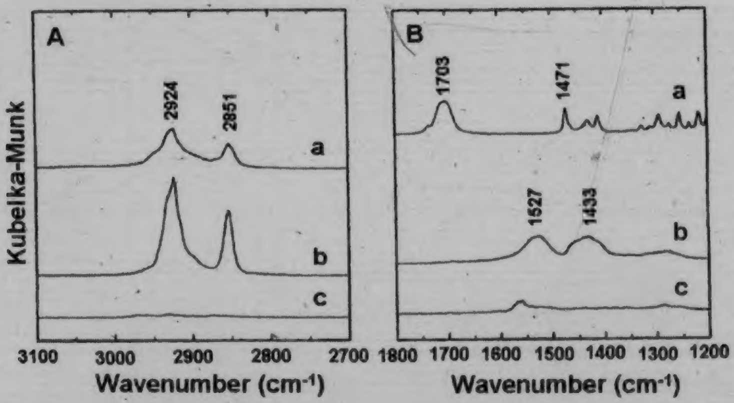

Figure B.1 Infrared spectra in the high (A) and low-frequency (B) regions for (a) MHA in KBr, (b) MHA on γ-Fe_2O_3, and (c) γ-Fe_2O_3.

To examine the nature of the packing of various surfactants on the γ-Fe_2O_3 particle surface and to investigate the stability of self-assembled layers to harsh environments, leaching experiments were conducted by placing the treated particles in acidic (pH = 3) and alkaline (pH = 10) media. These experiments showed that the surface coatings with stearic acid and MHA are stable in aqueous solutions over a pH range from 3 to 10 for a few days. No ferric ions were leached into the solution, indicating that the surface coatings are tightly packed. After the leachate was removed and the powder dried, the same values of critical surface tension were obtained, suggesting that the surfactant layer prepared with stearic acid and MHA remained stable under the test conditions. In contrast, ferric ions were detected (by sodium thiocyanide titration) in leachate of DTDPA-coated γ-Fe_2O_3 exposed to distilled water. These observations confirm the packing information inferred from DRIFTS and film flotation.

It is important to note that a monolayer coating of MHA on γ-Fe_2O_3 only reduced the saturation magnetization (Ms) of magnetic particles marginally (2 emu/g) from 52.7 emu/g of bare γ-Fe_2O_3. The particles remained superparamagnetic after coating.

The magnetic particles fabricated with thio or disulfide groups have potential applications in various areas. It is well-known that thio and disulfide groups have strong affinity with precious metals, such as gold, silver, and copper [25, 26]. The fabricated magnetic particles of large surface area could, therefore, be used to capture gold and silver ions from their leachates. The metal-loaded magnetic particles can then be readily separated from leaching solutions using magnetic separation. In addition, the approach can be readily extended to the fabrication of magnetic particles with other customized functional groups by controlling the reactivity of functional groups of a bolaamphiphile with magnetic particles. The functionalized magnetic particles can be used to recover secondary resources or to remove toxic species from industrial effluents by controlling the reactivity of functional groups with targeted species in the effluents. In addition, the special affinity of thio with antibodies makes fabrication of thio-containing magnetic nanoparticles of special interest in the biological applications.

B.1.2 Direct Silanation

Although self-assembed bolaamphiphile monolayer on magnetic particles is densely packed and stable in acidic and basic environments, the control of the reactivity between the two functional groups and the substrate is crucial in determining the quality of the coatings. The ideal case is that one functional group anchors chemically to the surface while the other is unreactive to the surface. This requirement limits the type of functional groups that can be directly introduced onto the magnetic particles.

A more general approach to fabricating magnetic nanocomposites is direct silanation. Silanation is to use silane coupling agents to tailor surface properties of metal oxides [27]. A typical silane coupling agent has the structure of $Y\text{-}(CH_2)_n\text{-}Si\text{-}X_3$, where X represents the alkoxy or halide groups and Y, the organic functional groups, including amine, thiol, carboxylic, phosphate, vinyl, cyanide, and methacrylate. The $Si\text{-}X_3$ group hydrolyzes readily in the presence of water and catalyst to form silanol groups which couples with surface metal hydroxyl groups, forming Si-O-M bonds upon dehydration. As a result, the organic functional groups (Y) remain reactive on the surface. This unique feature of silane coupling agents has made silanation a widely used method in modifying surface properties. A large volume of literature is available in this area [28, 29, 30, 31, 32, 33].

In the patent of Whitehead et al. [34], they described the procedures of direct silanation of functional groups, including aminophenyl, amino, hydroxyl, sulphydryl, aliphatic and mixed functional groups, on paramagnetic particles and pointed out the potential applications of the resultant magnetic particles. However, no fundamental characterizations of the silanized films are available, in particular the stability of the coatings and possible leaching of iron from the substrate.

It should be noted that coating of silane coupling agents by silanation is a multi-step process. A triangular relationship among substrate, silane, and solvent, along with the parameters that need to be considered, is shown in Figure B.2 [35]. Evidently, hydrolysis is necessary but must be controlled to avoid intramolecular condensation of silane coupling molecules. It is also important to hydrolyze surface metal species to obtain the maximum density of bindings between coupling agent and surface. The interactions and competition between the solvent-solute, solvent-substrate and solute-substrate dictate both coverage and quality of the resultant film. The last (but not the least) parameter (not included in Figure B.2) that needs to be considered is the post-curing during which thermal dehydration enhances chemical binding between substrate and coupling molecules and lateral polymerization among the coupling molecules, resulting in a robust film.

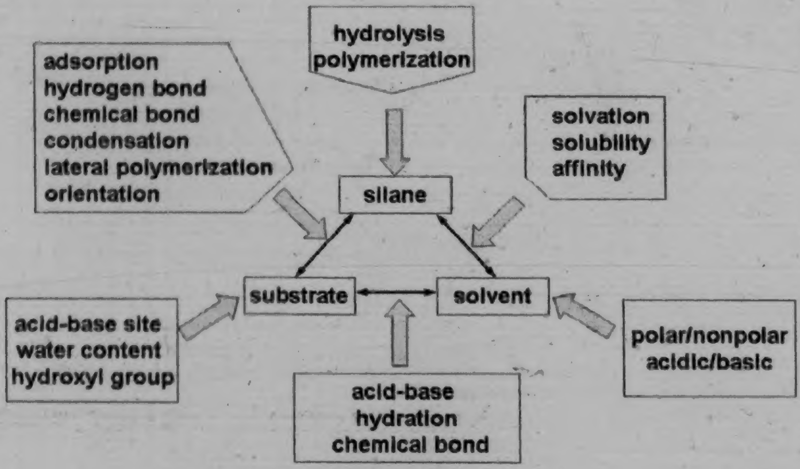
hydrolysis
polymerization
adsorption
hydrogen bond
chemical bond
condensation
lateral polymerization
orientation
solvation
solubility
affinity
silane
substrate
solvent
acid-base site
water content
hydroxyl group
polar/nonpolar
acidic/basic
acid-base
hydration
chemical bond

Figure B.2 Interactions involved in silanation. [6]

In our laboratory, we synthesized and studied the silanation of superparamagnetic (γ-Fe_2O_3) particles with focus on characterization of the coated organic films, such as organo-amine functional groups (3-aminopropyl triethoxysilane (APTES)). The characteristics investigated included the state of the amine groups, the binding of silane on magnetic particles, and the stability of the film [35].

APTES were silanized on γ-Fe_2O_3 from both water and toluene solutions. The presence of N_{1s} and Si_{2p} bands on XPS spectra of synthesized particles suggests that APTES has deposited on γ-Fe_2O_3 from both solutions. The two bands of nitrogen centered at 399.4 and 401.3eV are attributed to the protonated and non-protonated amines, respectively. The fraction of amines protonated is larger in the films silanized from water (26%) than that from toluene (17%), indicating the stronger interaction of amine groups with γ-Fe_2O_3 in water than in toluene. Band-fit analysis revealed that the proportion of oxygen in Si-O environment is higher for the film silanized in water (24%) than in toluene (14%), suggesting a higher degree of hydrolysis of APTES on γ-Fe_2O_3 from water. The XPS analysis also suggests the deposition of APTES as monolayers, and the moderate increase in the number of APTES molecules on γ-Fe_2O_3 from aqueous solutions is attributed to the increased APTES packing density rather than the formation of a three dimentional gelation which involves three dimentional links among APTES molecules.

To determine the degree of hydrolyzation of ethoxy groups and subsequent cross-linking, which have significant impact on the density and stability of the film, DRIFT specctra were therefore collected. In contrast to silanization in water, DRIFTS spectra of the APTES film deposited from toluene solutions showed vibrational bands of methyl group at 2974 and 2887 cm^{-1}, indicating the presence of small fraction of unhydrolyzed ethoxy groups in the film. The unhydrolyzed ethoxy groups on the surface are anticipated to inhibit the lateral polymerization of APTES, thus resulting in a poorer packing density and lower surface coverage films of lower stability than those of the film silanized from water where the hydrolysis is more effective. This observation is consistent with the findings from XPS.

To further confirm the orientation of APTES on γ-Fe_2O_3, the electrokinetics (zeta potentials) of the coated particles were measured. The isoelectric point (IEP), the point where zeta potential is zero, of the particles silanized with APTES from water and toluene was found at about pH 8.5 and 9.2 respectively, in contrast to pH 4.5 for uncoated γ-Fe_2O_3. The similar electrokinetics confirms the condensation of APTES on γ-Fe_2O_3 from both water and toluene with amine groups facing the environment and remaining reactive. The difference in the measured zeta potentials using the particles silanized in water and toluene reflects mainly the variation of APTES orientation on the particles. A slightly lower IEP value observed for the particles silanized in water suggests that more amine groups were hidden inside the film compared to the silanation in toluene. As a result, the contribution from amine groups to the number of positive surface sites decreases while that from silanol groups to the number of negative sites increases. These two effects result in a lower IEP of γ-Fe_2O_3 particles silanized in water than in toluene as experimentally observed. This finding is consistent with XPS analysis, which showed a higher degree of protonation of amine groups considered to bind with the surface.

The stability of the silanized APTES films on γ-Fe_2O_3 was investigated by leaching the particles in pH 2 HCl solutions for 20 h. It was found that the amount of iron leached out reduced form 60 mg/g for unsilanized γ-Fe_2O_3 to 34 mg/g for silanized γ-Fe_2O_3 in water and toluene. Compared to the particles coated with MHA using the SA method, the amount of iron leached out is significant, suggesting that the original particles were not fully protected by APTES, compounded with some degree of detachment of APTES from the surface in acid solutions, for direct silanation from water and toluene.

Detachment of silanized APTES was confirmed by zeta-potential measurements as shown in Figure B.3. After leaching, the zeta potentials shifted back towards the zeta potential values of unsilanized particles. Figure B.3 also shows a much greater shift in IEP by base attack, suggesting that the APTES coating is less stable in basic than in acidic environments. Similar trends in electrokinetics were observed for particles silanized from toluene. In the base environment, an IEP shift from pH 9 to 4.3 was observed. However, in acidic solution, the films formed in toluene were more stable with an IEP shift from pH 9.0 to 8.5 as compared to that from pH 8.5 to 5.5 for the particles silanized in water. This may be related to the lower degree of protonation of amine groups in the films formed from toluene. The protonated amine, attached to the surface through electrostatic attraction, may be detached in acid solution as amine molecules are more soluble at low pH.

Clearly, the direct silanation of APTES from water and toluene solutions on γ-Fe_2O_3 is not suitable for engineering magnetic composite particles for environmental and biological applications. Since silica is more stable in acidic solutions than iron oxide, an alternative approach is to coat the magnetic particles with a thin silica film first, followed by conventional silanation on silica, to improve the film stability and density of surface functionality.

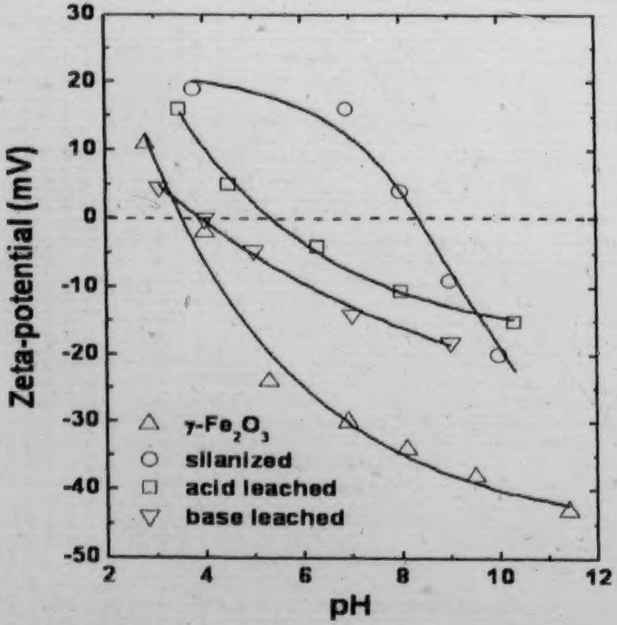

Figure B.3 Zeta-potentials of APTES-silanized magnetic particles from water before and after acid and base leaching.

B.1.3 A Novel Two-Step Silica-Coating

The challenge for the applications of magnetic nanocomposites is to improve the stability of magnetic particles against coagulation and leaching in an acidic environment, with maximized magnetization in an external magnetic field. Ultrathin silica films coated on nanosize magnetic particles are of special interest due to their high stability against aggregation and acid leaching with minimal reduction of magnetization. The silica surfaces are amenable for further functionalization by silanation, using silane coupling agents to produce functional magnetic nanocomposites. This approach remains, therefore, a principal method in engineering magnetic nanocomposites. Two conventional methods suitable for silica coatings on finely dispersed particles are sol-gel and dense-liquid processes.

Sol-Gel Process. The sol-gel process is a commonly used method for coating fine particles. The coating is performed in an organic solvent and the process is based on hydrolysis of precursors, such as tetraethoxy silane (TEOS), in the presence of water and a catalyst, followed by condensation of hydrolyzed TEOS on surface containing metal hydroxyls. With controlled hydrolysis of TEOS, an M-O-Si chemical linkage is established between surface metallic atoms (M) and TEOS, followed by lateral polymerization and finally formation of a three-dimensional network via siloxane bond formation (Si-O-Si) with increasing TEOS concentration and degree of hydrolysis. However, it is well known that silica coatings by the sol-gel process are porous, as schematically shown in Figure B.4 (a). To protect the substrate particles from dissolving in acidic solutions, a thick layer of coatings is required, which reduces the magnetizability significantly and hinders the technological applications of magnetic nanocomposites.

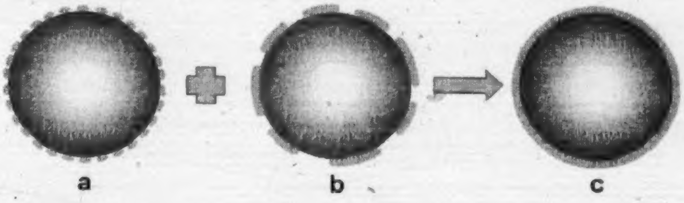

Figure B.4 Schematics of silica-coated magnetic nanocomposites by (a) sol-gel, (b) dense-liquid, and (c) two-step, i.e. (a) followed by (b), processes.

Dense-Liquid Process. This method was first introduced by Iler in 1959 to coat titania with a silica layer from supersaturated silica solutions [36]. Nowadays, the dense-liquid process is widely used to form silica films on surfaces of carbon, steel, alumina, and polymer resins to promote adhesion, to minimize photodegradation, and/or to prevent materials oxidation/corrosion [37, 38, 39]. By controlling the supersaturation level of monosilicic acid (constant reactant addition), silica layers can be formed on surfaces through heterogeneous followed by homogeneous coatings. It has been recognized that surface coating using the dense-liquid process is a complex physicochemical process. At least three competitive processes are present simultaneously: (i) heterogeneous coatings (on a substrate of different chemical compositions; e.g., SiO_2 on γ-Fe_2O_3); (ii) homogeneous coatings (on a substrate of the same chemical compositions; e.g., SiO_2 on

SiO_2); and (iii) homogeneous nucleation (e.g., formation of SiO2 nuclei) followed by homogeneous coatings. In general, the lowest supersaturation level is required for homogeneous coatings, followed by heterogeneous coatings, and finally homogeneous nucleation, which requires an excess energy, as predicted by the Kelvin equation, to account for extremely high curvatures of nuclei [40 , 41]. Although in general, homogeneous nucleation can be avoided by careful control of (silica) supersaturation level just above the critical concentration of heterogeneous coatings (on maghemite), the homogeneous surface coating often presents a challenge to uniform surface coatings. It is evident that, as soon as the substrate is coated with silica even at the submonolayer level, the growth of the coated area (a process similar to homogeneous coating) prevails because it requires a lower supersaturation level. As a result, a nonuniform, patchwise (island) coating, as schematically shown in Figure B.4 (b), is often obtained. With the dense-liquid-coating process, it is therefore inevitable to expose substrate cores to the environment and poison the system by the released species, unless a thick coating layer is applied.

Two-Step Coating. It is clear that neither the sol gel nor the dense-liquid process could meet the requirement of making magnetic nanocomposites of certain technological applications. To coat magnetic particles with a thin protective silica layer and minimize reduction of saturation magnetization, a novel two-step coating process (the sol-gel followed by the dense liquid coating) has been developed in our laboratory [42]. This approach is based on the idea that the sol-gel process can coat a surface uniformly, although the film is often porous, as shown in Figure B.4 (a). In the second step, using the dense-liquid process, the residual ethoxy groups in nano- or microsize pores of the silica film prepared using the sol-gel process are further hydrolyzed, and the pores are anticipated to be closed by and filled with silica under low supersaturation conditions. It is clear that the two-step silica-coating process integrates the advantages of uniform coatings by the sol-gel process and a low supersaturation level required for homogeneous coating by the dense-liquid process. As a result, a uniform thin silica layer, as shown in Figure B.4 (c), can be coated on maghemite or any other magnetic nanoparticles to protect the particles with minimal reduction in saturation magnetization (a key feature of magnetic nanocomposite sorbent) and to provide a surface for further functionalization. It is important to note that the objective of the two-step coating is not to coat more silica on the particles but rather to protect the substrate particles with the thinnest silica coatings possible to maximize the magnetic property of the coated particles.

For comparison, the silica was coated on γ-Fe_2O_3 at the 11 wt% silica level using these three methods. The presence of a silicon band at 103.4 eV and an additional oxygen band at 532.8 eV on the XPS spectra of coated particles confirms the coating of silica on γ-Fe_2O_3. By the analysis of XPS narrow-scan spectra, semi-quantitative analysis showed an area ratio of silica to iron band (Si/Fe) of 0.7, 4.1 and 4.1 for particles coated using the dense liquid, sol gel and two step processes, respectively. A higher Si/Fe ratio indicates a high degree of silica coating. It is evident that the silica coating efficiency is comparable for the sol-gel and two-step processes, higher than that of the dense liquid process.

The formation of silaxone bonds was confirmed for all the coatings by diffuse-reflectance infrared Fourier transform spectroscopy (DRIFTS) [43]. In contrast to the dense liquid or two-step coating process, unhydrolyzed ethoxy was detected for particles coated using only the sol-gel process. The presence of Si-OEt terminal groups is partially responsible for the porous nature of the coated films by the sol-gel process.

To further study the surface properties of the magnetic nanocomposite particles, the electrokinetics of the particles was measured, and the obtained isoelectric points (IEP) for maghemite particles coated with different methods are summarized in Table B.1. As shown, the IEP of pH 3 for maghemite coated using the dense-liquid process is significantly lower than that for uncoated maghemite particles ($pH_{IEP} = 4.5$). However, this value is higher than the IEP of fused silica ($pH_{IEP} = 2.1$), suggesting that silica was coated on maghemite, but only partially (probably in the form of islands) by the dense-liquid process, as illustrated schematically in Figure B.4 (b). When the sol-gel process was used, an IEP of pH 2.4 was obtained, showing an improved coating compared with the dense-liquid process. This value, however, remains slightly higher than the IEP of fused silica, indicating that the surface coating is either incomplete or porous, as confirmed later by leaching tests (Table B.1). When the two-step process was used, an identical electrokinetic behavior between the coated particles and fused silica was observed over the pH range studied, indicating the same surface properties between the two and confirming a full coverage of particles with silica. It is important to note that silica-like electrokinetics of silica coated maghemite with the two-step process ensures its dispersion, as required in many of its technological applications.

Table B.1 Characteristics and stability of silica-coated γ-Fe_2O_3 by dense liquid, sol-gel, and two-step coating processes

Sample and methods	IEP (pH)	Fe leached in 0.01 M HCl (mg/g)	Ms(emu/g)
γ-Fe_2O_3	4.5	60.3	52.0
DL coating	3.0	2.8	48.5
Sol-gel	2.4	1.1	43.2
Two-step	2.2	nil	42.5

Leaching tests were conducted to further examine the state of silica film on γ-Fe_2O_3. The results also are summarized in Table B.1 along with the saturation magnetization of coated particles. It is evident that the amount of iron leached out was below the detection limits for the particles coated with the two-step process in contrast to the single-step, either sol-gel or dense liquid process where 1.1 or 2.8 mg of Fe per gram of particles was detected respectively. Moreover, the saturation magnetization is comparable for particles coated with silica using the sol-gel and two step processes, suggesting that the amount of silica on the surface is virtually the same and confirming the important role of the film structure in protecting the matrix component of magnetic sorbents for biological and environmental applications. It is evident that the two-step silica coating process is successful in making base materials that can be further functionalized by the conventional silanation process to produce magnetic sorbents of a desired functionality.

B.1.4 Mesoporous Silica Coating

Despite the advantage of easy separation from complex multiphase systems by using magnetic composite sorbents, the limited specific surface area of existing magnetic sorbents presents a major challenge to these applications of many technological importances. Even for very fine maghemite (γ-Fe_2O_3) particles (~30 nm), for instance, a specific surface area of only ca. 40 m^2/g is reported [43]. A further decrease in particle size to increase specific surface area is not desirable, because the magnetic forces exerted on these tiny magnetic particles are extremely weak for any substantial migration of the particles to a desired location for separation. Since the specific surface area for a given surface functionality determines separation capacity, there is an urgent need for an innovative approach to increase the surface area of magnetic sorbents.

Surfactant-templated mesostructure materials have played a prominent role in materials chemistry during the last decade. The excitement began with the discovery of hexagonally ordered mesoporous silicate structure by Mobil Corp. (M41S materials) [44, 45, 46] and by Kuroda, Inagaki and co-worker (FSM-16 materials) [47, 48]. Having extremely high surface areas, these materials are easily accessible and of uniform nanopore structures and specific pore volume. Most importantly, the pore sizes exceeded those attainable in zeolites and they could be tuned in the nanometer scale by choosing an appropriate surfactant templating system, sometimes with a co-solvent or swelling agent [49, 50, 51, 52, 53, 54]. As a result, the applications of mesoporous materials in a wide range, such as adsorption, separation, catalysis, biological sensing, medical diagnosis and treatment, molecular engineering and nanotechnology, were envisioned [55, 56, 57, 58, 59, 60, 61, 62].

However, the use of bulk mesoporous siliceous materials in many science and technological applications has inherent limitations, especially for adsorption and separation of targets or contaminants from multiphase industrial effluents of complex nature. One noticeable challenge is to separate the loaded fine particles from industrial effluents for safe disposal or recovery of the adsorbed valuables and recycle of the sorbents.

The above application limitations inherent in mesoporous materials and magnetic sorbents led us to develop a mesoporous material-based magnetic composite sorbent. It is anticipated that incorporating mesoporous coatings on a magnetic core could increase the specific surface area of the resultant magnetic particles drastically without sacrificing magnetization characteristics. Mesoporous magnetic nanocomposite particles of sufficiently high specific surface area formed in this way could be easily separated from a multiphase complex system by magnetic separation and effectively recycles or reused.

The Synthesis Process of Mesoporous Silica Coated Magnetic Particles

The concept of template-based synthesis of mesoporous magnetic nanocomposite particles is illustrated in Figure B.5. In this synthesis, a thin silica layer is deposited on the surface of magnetite particles of desired sized (I). The purpose of silica layer is to protect the magnetic core from being leached into the mother system under severe industrial conditions. The resultant silica surface also facilitates the assembly of structured surfactant templates. With a negatively charged silica surface, cationic surfactant micelles self-assemble on the negatively charged silica layer (II), forming the desired structure. This step is highly dependent on micelle solution concentration and solvent quality [63]. The mesoporous silica network on the magnetic core (III) is formed by filling the spaces among the assembled micelle templates using the conventional sol-gel process [44, 64]. During sol-gel reaction, the positive nature of molecular templates promotes the formation of silica precipitates within the voids among the templates, resulting in a three dimensional continuous silica network. After calcinations at desired temperatures to remove the surfactant templates from the formed silica network, pores are left on the surface (IV). The silica surface of the so-formed mesoporous magnetic nanocomposite particles allows a variety of surface functionalities to be obtained by versatile silanation chemistry (V), which enables "molecular recognition" in numerous applications [35, 65, 66].

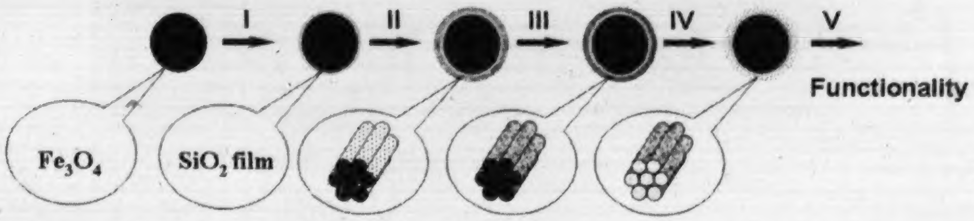

Figure B.5 Illustration of the proposed synthesis process for the preparation of mesoporous magnetic nanocomposite particles: dense-liquid-silica coating (I), molecular templating (II), sol-gel process (III), calcination (IV), and functionalization (V). [76]

The prepared mesoporous magnetic nanocomposite particles have the following important attributes: Strong magnetization for efficient magnetic separation; large specific surface area for high loading capacity; well sealed silica coatings to prevent the substrate materials from leaching into the mother system, as these could otherwise potentially contaminate or interfere with the normal functions of the system; robust and specific functional groups on the surface to recognize and capture desire targets effectively.

Characterization of the Synthesis Process

Templating Study by AFM

Since the formation of mesoporous silica is built on the templates of surfactant molecular suprastructure, studies on the interactions of micelles with silica wafer, which is used to represent the silica coated surface on magnetic particles, were performed first.

Figure B.6 (solid squares) shows the interaction forces between a cantilever tip and bare silica wafer in pure ethanol. There is a measurable attraction between the two at the separation distance below 10 nm. This attractive force is attributed to van der Waals forces. After replacing the ethanol by 5 mmol/L CTAC (cetyl-trimethyl-ammonium chloride) in ethanol solution and incubation for one hour, a repulsive force between the tip and the sample starting at 20 nm during approaching is evident, as shown in Figure B.6 by open squares. This long-range repulsion is attributed to overlap of electric double layers around two positively charged surfaces. It appears that the cationic CTAC surfactant adsorbs on both AFM tip and silica surfaces, rending them both positively charged. At a separation distance around 9 nm, a maximum repulsive force barrier is observed and the tip jumps inward by a distance of 5.7 nm. After this jump-in, a continuous increase in repulsive force is observed as the sample pushed upward against the AFM tip by about 4 nm. This type of force profiles over such a short separation distance suggests a surface of compressible nature, in great contrast to the case measured in pure ethanol, indicating a soft silica surface in CTAC ethanol solutions. Considering all the details in this force profile, we can interpret the observed jump-in being the removal of a single layer of micelles from the gap between the tip and sample under the applied force of AFM tip. It is therefore reasonable to conclude that the silica surface is covered by CTAC micelles, and the size (diameter) of micelles or thickness of single layer micelles on silica is around 5.7 nm.

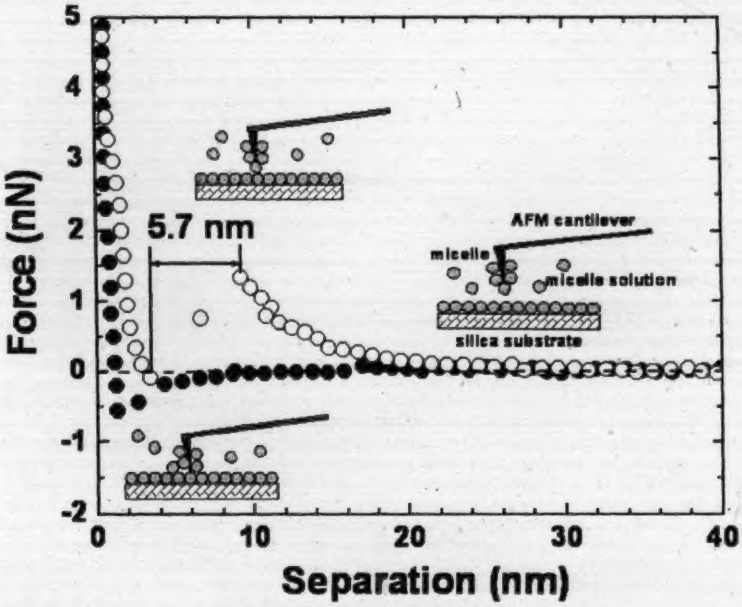

Figure B.6 Interaction forces between a bare silica wafer and AFM tip in ethanol (solid circles) and CTAC ethanol solutions (open circles).

The AFM images of silica in ethanol and 5 mmol/L CTAC ethanol solution are shown in Figure B.7 a) and b), respectively. The silica wafer in ethanol exhibits a smooth, featureless topography (Figure B.7 a). The image of silica wafer obtained in CTAC ethanol solution (Figure B.7b), on the contrary, shows well defined features. It is interesting to note that the size of high spots is of 6 nm range, a value very close to the jump-in distance observed on the force profile. It appears that CTAC at 5 mmol/L concentration in ethanol forms pseudo-spherical micelles. These micelles are assembled on silica surface with well-defined voids of 10-nm diameter. For better view, a higher magnification image of the marked area is shown on the left corner with circles to highlight the voids. By filling in these voids with desired materials and removing the micelles, one can obtain mesoporous surfaces of desired materials. Clearly these assembled micelles can serve as templates for synthesis of mesoporous silica coatings on silica coated magnetic particles.

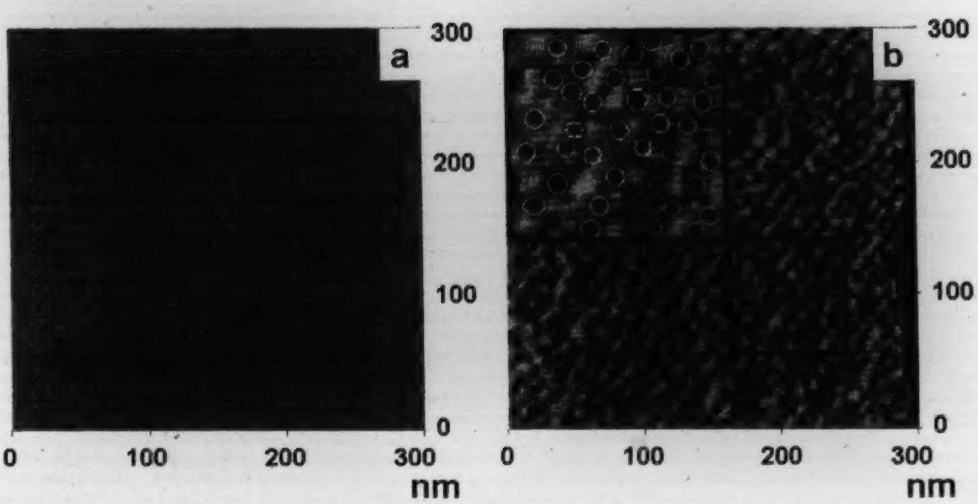

Figure B.7 Silica wafer in ethanol a) and CTAC solutions b) (circles represent voids to be filled by silica using sol-gel method).

Structural properties of surfactants and micellar solutions are crucial when preparing mesoporous structures. Surfactants in solution assemble into structures whose geometry can be described by the surfactant packing parameter [67,68]. This packing parameter is defined as $g = \nu / al$, where ν is the volume of the surfactant tail, *a* is the effective head group area and *l* is the length of the extended surfactant tail. An increase in the packing parameter represents a reduction in curvature of surfactant aggregates. Such change may be achieved by altering the surfactant chain length, introducing twin chains, adding electrolytes, or by addition of polar and non-polar organic additives. Addition of short-chain alcohols as co-surfactants can also be used to alter the packing parameter, resulting in elongated micelles. Furthermore, addition of short-chain amine co-surfactants can decrease the pore size of the inorganic structures. By controlling the packing parameter of different surfactants, mesoporous materials of different structures have been synthesized [69, 70, 71, 72, 73]. Detailed descriptions of reaction variables are available in many monographs [63, 64, 74, 75].

Synthesis Process Monitored by Zeta-potential Measurement

To confirm the role of each step in the proposed synthesis process, the zeta potential distributions of bare magnetite (Fe_3O_4) (step I in Figure B.5 previous), dense liquid silica (DLS) coated magnetite (step II in Figure B.5 previous), templated DLS magnetite (step III), sol-gel coated particles with templates (step IV), and the particles after calcination (step V) were measured over a wide pH range and the results are shown in Figure B.8.

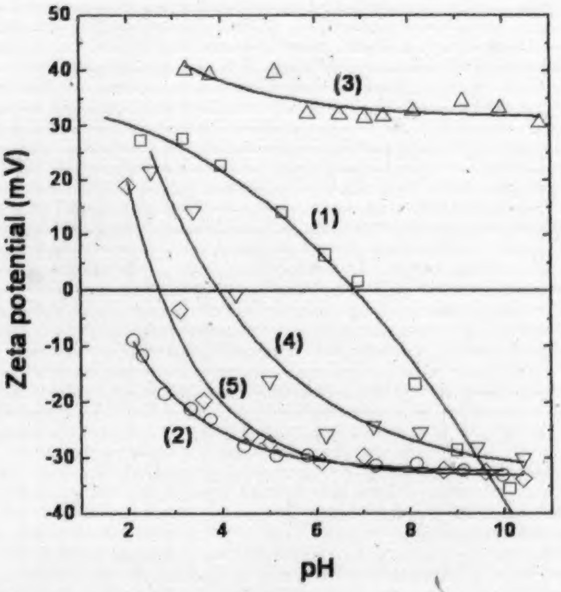

Figure B.8 Zeta potentials of different particles: (1) bare magnetite particles; (2) DLS coated magnetite particles; (3) templated DLS magnetite (4) sol-gel coated particles with templates; and (5) particles after calcination.

The isoelectric point (IEP) of the bare magnetite is at pH 6.8, which is close to the value of mineral magnetite. After DLS coating, the IEP of the coated particles was found at pH=2.0, which is same as the IEP for mineral or fused silica. This silica coating acts as a protective layer to avoid direct contact of the magnetite core with the liquid to be treated. The negative charge of the silica-coated surface, on the other hand, facilitates the assembly of cation surfactant micelles arisen from electrostatic attraction. After molecular templating, the zeta potentials of the resultant particles were positive over a wide pH range. This resembles the zeta potential variation of an oil droplet or air bubble with pH in CTAC aqueous solutions. After sol-gel reaction to fill the voids observed in the AFM images (Figure B.7b), the particles become negatively charged again. The measured IEP of the collected particles is at pH = 4.0, which is different from that for a silica surface. This observation suggests that the trapped CTAC template partially balances the negative charge of silica in the templates voids. After calcination, the surfactant was removed, leaving behind the silica network on the magnetite surface, which has the IEP at pH=2.6, identical to the IEP value for silica. This finding confirms a full coverage of magnetite by silica, making the coated surface silica-like. To further confirm the protection of magnetite particles by the two steps silica coatings, the coated particles were immersed in a 1 M acid solution. The results showed a negligible amount of iron being leached out after a 12 h immersion, indicating good protection of magnetite by silica coatings.

To further verify the necessity and success of each step described in Figure B.5, the samples collected at various stages of the synthesis are characterized by DRIFT and XPS. The results can be found in our related publications [76].

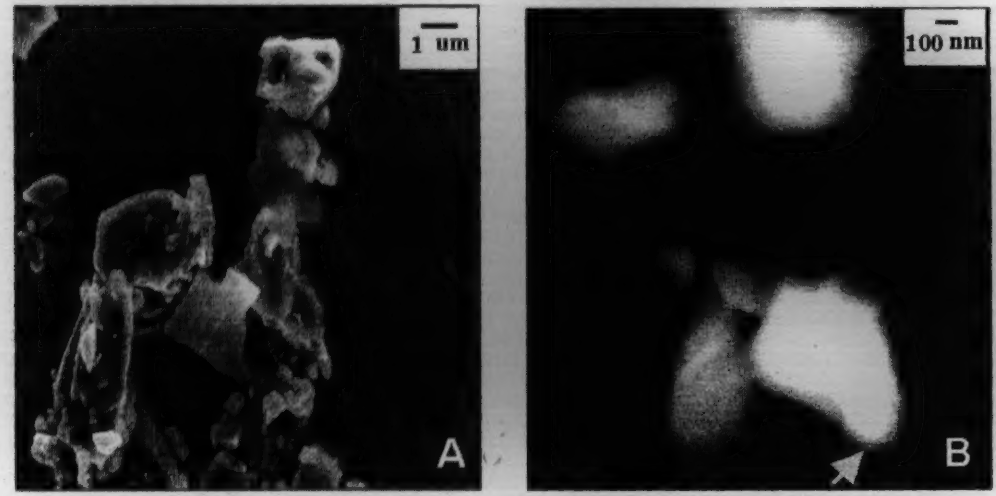

Figure B.9 TEM images of untreated Fe_3O_4 particles (A) and Fe_3O_4 particles with template-assisted silica coatings (B). Micrograph (B) is a dark-field mage, obtained with tilt illumination.

The morphology of Fe_3O_4 and mesoporous silica coated Fe_3O_4 is observed by TEM. Figure 11 shows that bare Fe_3O_4 has a well-defined crystalline feature with sharp edges and corners. In contrast, the TEM image of mesoporous silica coated Fe_3O_4 shows diffuse edges. Combined with the evidence from XPS analysis, these edges can be confidently considered as a homogeneous silica shell around the Fe_3O_4 cores. Figure 11

(b) also shows that no more than one spherical core is included in each composite particle, suggesting that the aggregation of primary particles during synthesis is minimal.

Other Properties

To determine the porous nature of template-assisted silica coatings on the magnetite particles, standard nitrogen adsorption-desorption tests were performed. A large hysteresis existing between the adsorption and desorption branches, which is characteristic of highly porous materials, confirms the formation of mesopores on the magnetite particles. The detailed analysis of the results using the Brunauer-Emmett-Teller (BET) adsorption equation resulted in an increase in specific surface area form 0.07 to 52.3 m^2/g of total material by the deposition of a mesoporous silica film on magnetite cores [76].

To obtain a uniform and well covered mesoporous silica layer on magnetic particles of high specific surface areas, the control of sol gel conditions is extremely important. Many synthesis conditions, such as reaction time, reaction temperature, reactant concentration, type and amount of catalyst and the quality of solvent, could affect the properties of the resultant silica coatings. Thus, optimizing sol-gel conditions by factorial design to minimize the numbers of synthesis while analyzing synergetic effects among different factors were studied [77]. The specific surface area of produced mesoporous silica coated Fe_3O_4 was improved from 52.3 m^2/g to 150 m^2/g, which provides three times more chances of the prevalence of functional groups, so the efficiency of the synthesized magnetic sorbent will be increased.

The magnetization characteristics of synthesized particles is a major concern for potential industrial applications. A strong magnetization is required for the collection by magnet from a complex, multiphase system. As shown in Figure B.10 the room temperature saturation magnetization of bare magnetite is 85.5 emu/g, which reflects the properties of Fe_3O_4 without any oxidation. For the final mesoporous magnetic nanocomposite particles the saturation magnetization remains strong at 73.0 emu/g. The observed decrease of 15% in saturation magnetization is attributed to the coating of diamagnetic silica. Such a reduction does not hinder the subsequent magnetic separation after the resultant mesoporous magnetic particles are loaded with heavy metal ions. More importantly, magnetite particles coated with mesoporous silica remain fairly paramagnetic as shown by minimal coercivity and hysteresis on the magnetization curves (insert of Figure B.10). This magnetization characteristic ensures that the magnetite particles do not become permanently magnetized after exposure to an external magnetic field, which in turn permits the particles to be re-dispersed without significant aggregation when the external magnetic field is removed.

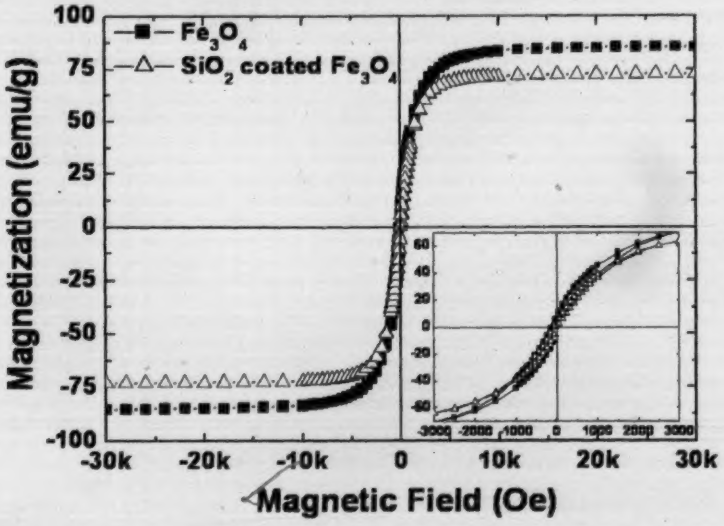

Figure B.10 Room temperature magnetization of bare magnetite and mesoporous magnetic nanocomposite particles.

Our study above clearly shows that with the concept outlined in Figure B.5, mesoporous magnetic nanocomposite particles can be successfully synthesized. The synthesized particles possess the necessary attributes of strong magnetization and high specific surface area for their applications as magnetic sorbents. The dense liquid method followed by the template-assisted sol-gel process resulted in the formation of a uniform, mesoporous thin silica coating on magneitite particles. The resultant particles are well protected for iron leaching from cores, while providing surface amenable for functionalization via well-defined silane-coupling reactions. The functionalized particles have potential applications in a variety of science and engineering disciplines.

B.1.5 Silanation on Mesoporous Silica Coated Magnetic Particles

As mentioned earlier, the synthesized mesoporous magnetic particles exhibited the necessary attributes of strong magnetization, high specific surface area and good protection of magnetic cores for applications as magnetic sorbents. Based on previous success of functionalizing silica surfaces using APTES to obtain reactive amino groups of high affinity for metals [35, 66], APTES was the common choice as silane coupling agent. Furthermore, use of this short-chain alkane amine minimized blockage of pore channels.

The self-assembly of silane coupling agents by silanation is a multistep process. In addition to complex interactions among the substrate, silane and solvent, many other parameters need to be considered. According to Feng et al. [66], the number of surface silanol groups and the amount of adsorbed water molecules on mesoporous materials are two key parameters in determining the density and quality of the functionalized monolayers. As can be seen from the silane-coupling reaction schematically illustrated in Figure B.2, surface silanols are essential because they are the active centers for silane condensation and anchoring on the particle surfaces through siloxane chemical bonds. Adsorbed surface water is necessary for the hydrolysis of APTES in toluene, which initializes the condensation reaction process. However, the presence of excess free water is deleterious to the formation of a clean monolayer, as APTES is known to polymerize into white solid precipitates in the presence of water. The precipitates can potentially block the pores and hence reduce the effective surface area of the functionalized sorbents. For these reasons, a proper amount of water for the hydrolysis of APTES needs to be employed to obtain a monolayer of silanized APTES on the pore surfaces only.

Calcination at 540°C to remove surfactant templates and obtain mesoporous particles (section B.1.4) dehydrates the mesoporous silica-coated magnetite surface and depletes most of the silanol groups. Such a dehydrated surface would result in a poor surface coverage of functional groups if silanized directly. In this study, to optimize the reaction conditions for depositing alkoxysilane monolayers on mesoporous silica-coated Fe_3O_4 surfaces, the particles were rehydrated carefully by steaming the samples. The amount of surface-adsorbed water was controlled by drying. High-purity toluene was used through out the synthesis since toluene was reported in literature to be excellent for removing excess water and forming organic monolayers.

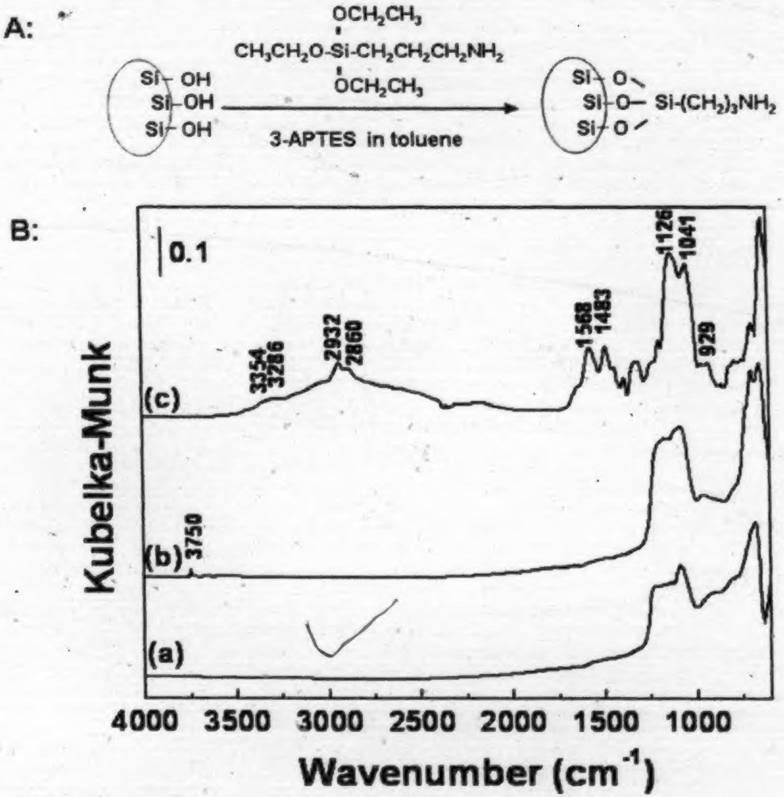

Figure B.11 (A) Schematic diagram for the synthesis of mesoporous-Fe_3O_4 silanized by 3-APTES. (B) DRIFTS spectra of mesoporous-Fe_3O_4 magnetic particles; after (a) calcination, (b) rehydroxylation, and (c) silanation by 3-APTES from toluene.

As shown in DRIFTS spectrum b of Figure B.11 (B), obtained with the steamed and dried samples, the presence of a sharp H-O vibrational band at 3750 cm^{-1} confirms the successful hydrolysis of siloxane bonds by steaming. DRIFTS spectrum c of the silanized mesoporous-Fe_3O_4 in Figure B.11 (B) exhibits the characteristic bands of APTES. A pair of weak broad bands at 3400-3250 cm^{-1} is evident in the spectrum. These two bands are assigned to free amino asymmetric and symmetric stretching vibrations. A strong band at 1568 cm^{-1} is assigned to the deformation bending vibrations of free amine groups on the surface. In addition, two bands at 2932 and 2860 cm^{-1} assigned to asymmetric and symmetric stretching vibrations of CH_2 in alkyl chains, along with a band at 1483 cm^{-1} assigned to CH_2 bending vibrations, are evident. These spectral features confirm the silanation of APTES on the particle surfaces. It is interesting to note that the characteristic bands of Si-O-C at 1167, 1105, 1083, and 959 cm^{-1} almost disappeared after silanation. This finding suggests that most of the ethoxy groups in APTES were hydrolyzed. Two strong bands at 1126 and 1041 cm^{-1} (characteristic of siloxane Si-O-Si stretching vibrations) remained after silanation, indicating that the surface binding of APTES was not by silanols but rather by siloxane bonds. The presence of siloxane binding was further supported by the disappearance of IR bands at 3745 cm^{-1}, assigned to the stretching vibrations of surface silanols in the spectra of silica-coated magnetic particles before calcination and steamed particles (spectrum b in Figure B.11 (B)).

B.2 Practical Applications of MCS

Utilizing the magnetic composites particles to selectively remove heavy metals from industrial effluents or contaminated municipal water or to be used in biological cell separation and biological sensing, the most important thing is to functionlize the surface with specific ligands having specific interaction with targets (heavy metals or bio-molecules), endowing the surface a strong and specific affinity for targeted metal ions. There are two ways to reach this goal, one is direct molecular self-assembling and the other one is by silanation of specific function groups, which allows more versatile groups to be used. The silanation is a promising avenue for introducing specific surface functional groups on mesoporous silica surfaces [66, 78, 79, 80, 81, 82, 83].

B.2.1 SA Monolayer

Cu^{2+} and Ag^{+} Removal

The MHA coated γ-Fe_2O_3 particles (section B.1.1) prepared by the SA method contain reactive thiol and/or disulfide groups that are known to have strong affinity to various metal ions such as gold, silver, and copper. This application is illustrated in our loading tests of Cu^{2+} and Ag^{+} on MHA-coated γ-Fe_2O_3 particles from 10 mmol/L $CuSO_4$ or $AgNO_3$ solutions. The narrow-scan XPS spectra of the loaded particles separated from the liquid/suspension with a hand magnet are shown in Figure B.12. The load of Cu^{2+} and Ag^{+} u on the MHA-coated particles is evident from the presence of Cu_{2p} (934 and 954 eV) and Ag_{3d} (368 and 374 eV) XPS bands on spectra respectively. The area ratio of the copper satellite band to its $2p_{3/2}$ band is lower than expected, suggesting that some of the copper ions are in the cuprous state. It appears that some of cupric ions were reduced to cuprous ions, accompanied by the oxidation of thiol to disulfide, which accounts for the presence of an additional sulfur band of higher binding energy but lower intensity. The surface metal-to-sulfur atomic ratio was found to be 0.6 and 0.8 for copper and silver, respectively. These results suggest a 1:2 (metal-to-sulfur) binding for divalent copper and 1:1 binding for monovalent silver. It is clear that the metal loading efficiency is sufficient for the MHA-coated magnetic sorbents to be used in the removal or recovery of Cu^{2+} and Ag^{+} from industrial effluents.

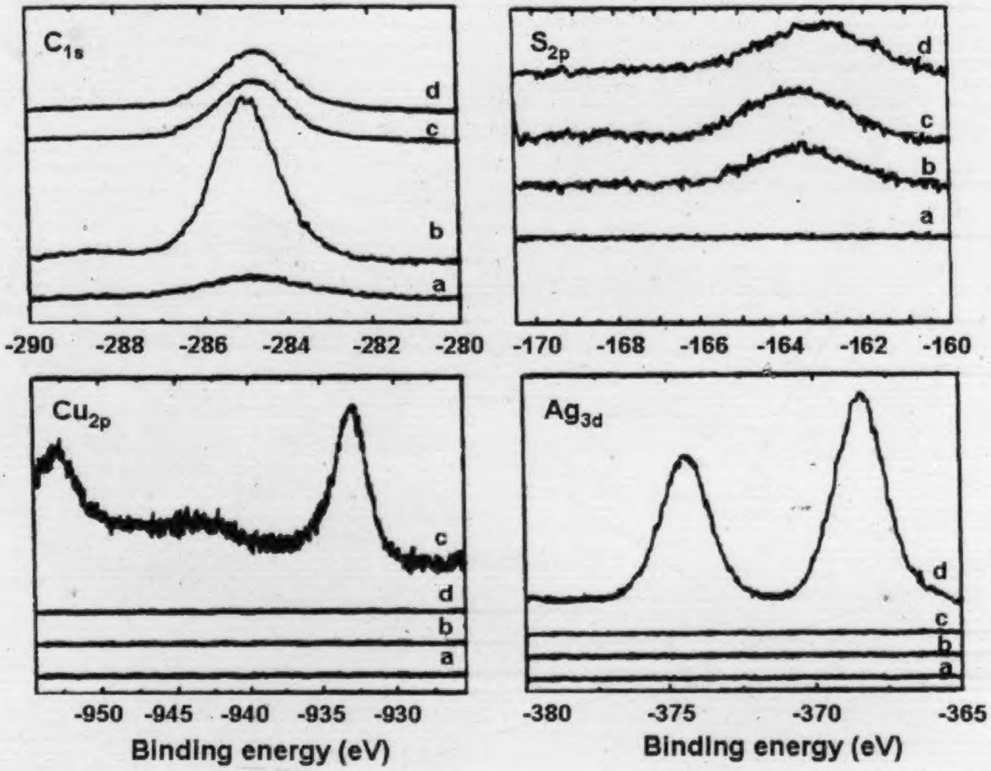

Figure B.12 XPS spectra of narrow scans for the interested elements (a) γ-Fe_2O_3; (b) thiol-type magnetic sorbents; (c) after copper loading; and (d) after silver loading.

B.2.2 Silanized Monolayers on Two-step Silica-coated γ-Fe_2O_3

Cu^{2+} and Zn^{2+} Removal

The silanized magnetic particles with reactive amine groups are found to confer specific adsorption for heavy metal ions, including divalent mercury, lead, copper, zinc, manganese, and monovalent silver in contaminated aqueous and nonaqueous solutions [84].

It was shown (section B.1.2) that APTES films directly silanized onto γ-Fe_2O_3 were unstable in alkaline solutions, although the films silanized from toluene were relatively stable in acidic solutions. An idea to coat γ-Fe_2O_3 with a thin silica layer before silanation was proposed in order to obtain a stable silanized film. In section B.1.3, it was shown that dense thin silica films were successfully coated onto γ-Fe_2O_3 using the sol-gel process followed by dense liquid silica coating. The purpose of silica coating is to make the surface more amenable for silanation. It has been well documented that silanized films on silica are relatively stable compared to those directly silanized on other metal oxides [85]. The silanation of silica coated magnetic particles using APTES in toluene is performed. Toluene is used as a solvent simply due to the fact that the films formed on the magnetic particles are relatively stable compared to those formed from water as shown in section B.1.2. The silanized films on silica coated magnetic particles was characterized by XPS, DRIFTS, zeta-potential measurements, leaching test and thermal gravimetric analysis (TGA) as well documented in literature [43]. It is found that the silanized films on silica coated magnetic particles were more stable in acid solution than on bare magnetic particles, but both unstable in alkaline solutions.

Copper loading on the silanized silica coated magnetic particles of reactive amine groups is shown in Figure B.13. For comparison, copper loading on silica-coated magnetic particles is also shown in this figure. It is evident that at a given pH (5.3), copper can be removed effectively from low concentration solutions (e.g., 100% removal from a 12 ppm solution). With increasing initial copper ion concentrations, the copper removal efficiency decreases as copper loading approaches the capacity limit of about 0.18 mmol of Cu per gram of particles. In contrast, the copper loading on the silica-coated magnetic particles is significantly lower than that on the silanized particles, suggesting the important role of reactive amine groups in this application. It should be noted that the metal ion loading is pH-dependent. The protonation of amino groups and detachment of silane coupling agents are both influenced by pH, thus they will affect metal ion adsorption. In addition, various metal ions such as copper and zinc showed different loading performance, leading to selective adsorption and removal/recovery of various metals. This is demonstrated in our previous publication [43].

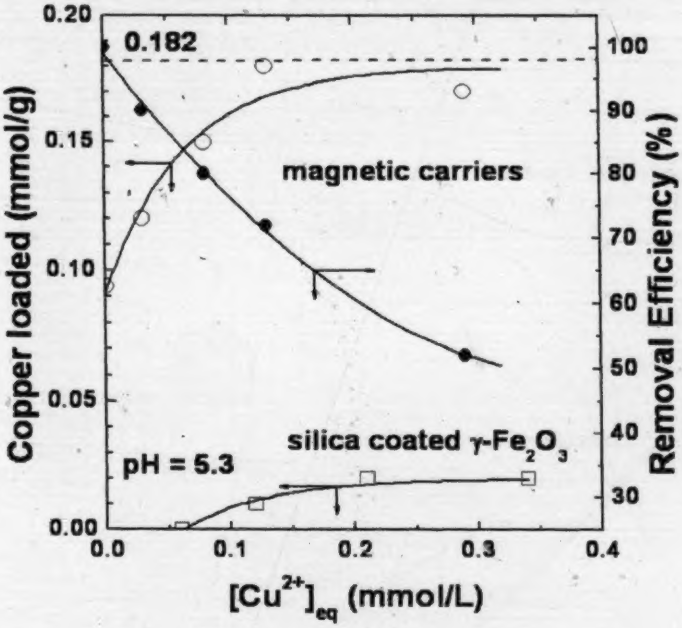

Figure B.13 Copper loading on and removal from APTES silanized on silica-coated γ-Fe_2O_3 particles, in comparison to silica-coated γ-Fe_2O_3 particles at loading pH 5.3.

Stripping of Metal ions and Recycling of Magnetic Sorbents

Stripping of metal ions from loaded magnetic particles is a major step for the subsequent recovery of metals by electrowinning, while the recycling of magnetic particles is a necessary step to offset the high price of magnetic sorbents by lowering the cost in industrial applications. Many methods such as acid washing, EDTA (ethylenediamine tetraacetate) extraction, and electrowinning can be used to strip off metal ions from loaded magnetic sorbents. An ideal method would detach metal ions effectively while maintaining maximum reactivity of magnetic sorbents.

The results of the stripping tests using nitric acid (0.01 M) are shown in Figure B.14. The amount of copper detached vs. the amount of copper loaded exhibits a linear relation with the line passing through the origin of the coordinate and a slope of 1, indicating the complete detaching of loaded copper ions. The mechanism of copper detachment by acid washing seems similar to that in the regeneration of exhausted ion-exchange resins often used in wastewater management. The detachment is most likely accomplished by ion exchange due to the high chemical potential of hydrogen ions in acidic solutions, which compete with copper ions for amino groups on magnetic sorbents.

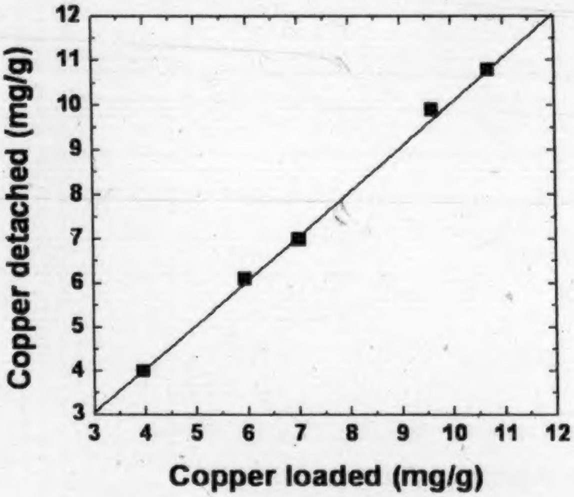

Figure B.14 The amount of copper detached vs. the amount of copper loaded.

After stripping off metal ions, the recycled magnetic carriers were characterized by XPS, DRIFTS, zeta-potential measurements and the copper loading test to determine the density and reactivity of silanized films remained on magnetic sorbents. The results from the analysis all indicate a partial detachment of immobilized silanes from the surface after acid stripping. Moreover, in DRIFTS the band at 1580 cm^{-1} for amino groups on magnetic sorbents shifted to 1615 cm^{-1} after copper loading, indicating the amino groups reacted with copper ions. However, after detachment a new band at 1711 cm^{-1} appeared, which is attributed to oxidization of amines, possibly imides which have little affinity to copper [86], thus reducing the reactivity of magnetic sorbents with copper in the following reloading test.

Considering that amino groups are susceptible to oxidation [87], using EDTA to extract loaded copper from magnetic sorbents may be beneficial. The minimal breakage of siloxane bonds, and hence the detachment of APTES films from the magnetic sorbents are anticipated. Therefore, using EDTA or similar complexing reagent to detach metal ions from loaded magnetic sorbents is worth exploring.

B.2.3 Poly(1-vinylimidazole)-grafting on Magnetic Nanoparticles

Grafting of silane-terminated polymers on silica via chemical siloxane bonds has been reported in a number of studies [88, 89, 90]. In this study [91], a newly synthesized poly(1-vinylimidazole) with trimethoxysilyl terminal groups is chemically anchored (grafted) on nanosize maghemite particles. Poly(1-vinylimidazole) is chosen to graft on nanosize magnetic particles, as the resultant organic-inorganic hybrid magnetic materials are anticipated to expand the sorbent-based separation technology to a multiphase complex system, ranging from biological cell sorting to industrial effluent detoxification and recovery of valuables. Poly(1-vinylimidazole can form complexes with such metal ions as Cu-(II) [92], Zn(II) [93], Cd(II) [94], Ag(I) [95], and Hg(II) [96].

Figure B.15 shows schematically the preparation procedure and the resulting configuration of grafted polymers (thick lines) with bond metals (M). Compared with the polymer-coating method, the polymer-grafting (direct silanation) method offers a number of distinct advantages. First, particle size shows little effect on polymer immobilization. Polymer chains immobilized on magnetic particles would remain flexible. Polymer-grafted magnetic particles can be used in good solvents of the polymer. Finally, the method is applicable to many kinds of polymers.

Poly(1-vinylimidazole) with a terminal trimethoxysilyl group (Im_n) was prepared by telomerization of 1-vinylimidazole with 3-mercaptopropyltrimethoxysilane. The average degree of polymerization, *n*, is 18, as determined by 1H NMR. The DRIFTS measurement combined with elemental and thermal gravimetric analysis showed that immobilization of the synthesized polymer onto magnetic nanoparticles through siloxane bonds ($Mag\text{-}Im_{18}$) was successful. The $Mag\text{-}Im_{18}$ was well-dispersed in water and in organic solvents such as methanol, ethanol, and chloroform. TEM micrograph confirms that the original size and shape of the particles were retained after Im_{18}-grafting. The grafted polymer is stable over a wide solution pH range from 3.5 to 10.0, so $Mag\text{-}Im_{18}$ can be used in a wide range of aqueous environments.

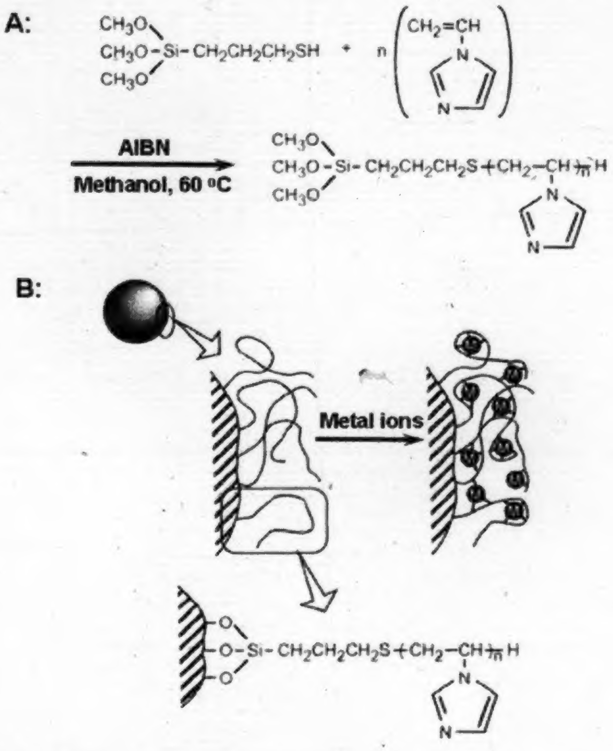

Figure B.15 Synthesis of poly(1-vinylimidazole) (A) and schematic illustration of polymer-grafted magnetic particles (B).

The removal of various metal ions from aqueous solutions is possible by using the Mag-Im$_{18}$ as a collector. Figure B.16 shows the removal efficiency of Cu^{2+}, Ni^{2+}, and Co^{2+} from their bulk solutions. The order of removal efficiency of the metal ions by Mag-Im$_{18}$ was found to be $Cu^{2+} \gg Ni^{2+} > Co^{2+}$. A loading capacity of 0.11 mmol/g at pH 5.3 was determined for copper. This capacity corresponds to a one-quarter amount of imidazolyl groups on the particles (0.44 mmol/g). This observation suggests a preferred coordination number of 4 for Cu^{2+} to complex with imidazolyl groups and confirms that the imidazolyl groups on the flexible polymer chain are effective at capturing copper ions.

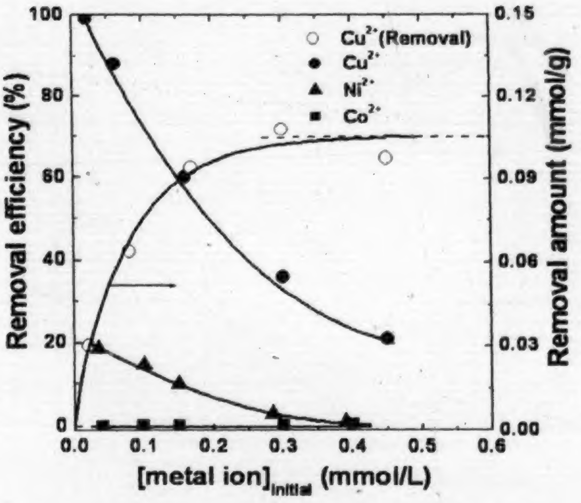

Figure B.16 Removal efficiency of Cu^{2+}, Ni^{2+} and Co^{2+} by, and loading capacity of Cu^{2+} on Mag-Im_{18}. Metal ion solution/Mag-Im_{18} = 10 mL/10 mg at initial solution pH 5.3.

Selective removal of metal ions from aqueous solutions was evaluated by loading tests from a mixture of Cu^{2+}/Co^{2+} solutions. In this set of experiments, the initial concentration of Cu^{2+} and Co^{2+} was fixed at 0.157 mmol/L (10 ppm) and 0.170 mmol/L (10 ppm), respectively. As shown in Figure B.17, the removal efficiency for Cu^{2+} increased with increasing solution pH. The adsorption of copper ions on Mag-Im_{18} is not significant below pH 3. The competitive adsorption of hydrogen ions with metal ions for imidazolyl groups at low pH values accounts for the observed low removal efficiency. Since the imidazolyl groups are most likely protonated at a low pH, the magnetic particles are positively charged, resulting in a strong electrostatic repulsive force between the poly(1-vinylimidazole) on the magnetic particles and positively charged metal ions. This long-range repulsive force also contributes to the observed low copper removal efficiency at solution pH below 3. On the other hand, Co^{2+} cannot be removed by Mag-Im_{18} over the entire pH range studied. The Mag-Im_{18} showed an effective and selective separation of Cu^{2+} from a mixture of Cu^{2+} and Co^{2+} solution. Given the wide selection of polymer functionality, polymer-grafted magnetic particles can provide vast potential applications.

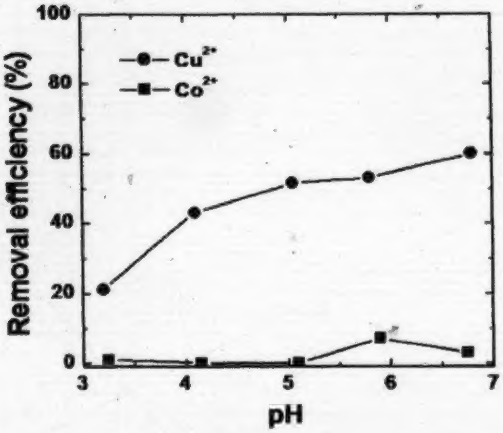

Figure B.17 Removal efficiencies of Cu^{2+} and Co^{2+} by MagIm$_{18}$ from a mixture of Cu^{2+}/Co^{2+} solution. Metal ion solution/Mag-Im$_{18}$ = 10 mL/10 mg at initial $[Cu^{2+}]$ and $[Co^{2+}]$ concentration of 0.157 mmol/L and 0.170 mmol/L, respectively.

B.2.4 Functionalized Mesoporous Silica Coated Magnetic Particles

Separation of Transition Metals

Cupric ion adsorption tests were performed on magnetic composite particles with varying surface treatments. To illustrate the role of molecular templating in synthesis of the silica coating and subsequent capture of target species, the results obtained with the micrometer-sized magnetite coated with silica under the identical conditions but without templating are included for comparison.

From the results shown in Figure B.18, the following general conclusions can be made: (1) The capability of the particles to capture copper ions increased when mesoporous films were formed on the magnetite particles to produce a higher specific surface area (curves (b) and (d) are higher than curves (a) and (c), respectively). (2) Surface functionalization with amine groups by silanation increased the capability of the particles to capture metal ions, arisen from a stronger chemical affinity of the immobilized amine groups for copper ions (curves (c) and (d) are higher than curves (a) and (b), respectively). (3) The functionalized mesoporous surfaces showed the highest loading capacity for copper ions (curve (d)), suitable for detoxification or recovery of copper ions from industrial effluents.

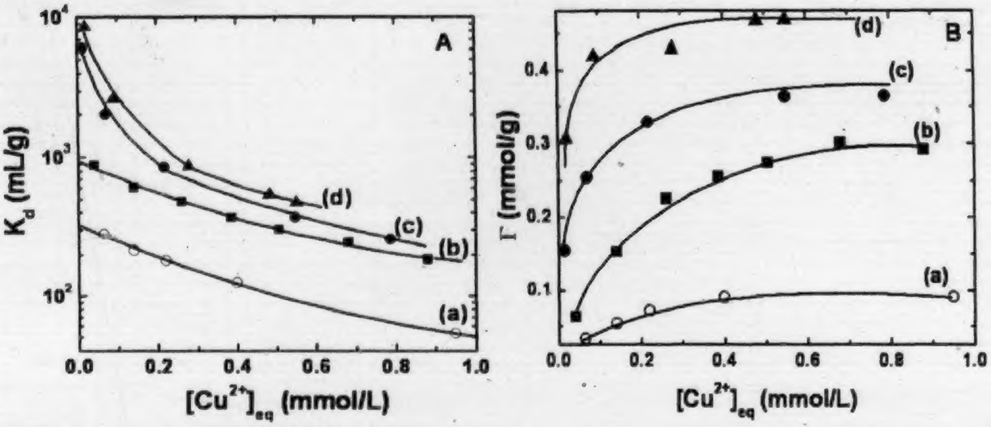

Figure B.18 (A) Distribution and (B) adsorption isotherms of copper ions on different magnetic particles as a function of copper concentration: (a) Fe_3O_4 coated with silica without templating, (b) mesoporous-Fe_3O_4, (c) Fe_3O_4 coated with silica without templating but silanized by 3-APTES, and (d) mesoporous-Fe_3O_4 silanized with 3-APTES.

Mesoporous magnetic particles functionalized with APTES were tested to determine the loadings of other soluble heavy metals. The extractability of soluble metals was examined by adding 50 mg of particles to 25-mL samples of aqueous solutions, each containing 0.5 mmol/L Cu^{2+}, Zn^{2+}, and/or Ni^{2+} ions. In this set of tests, the solution pH varied from 2 to 6. The upper pH limit was set at 6 to avoid precipitation of metal hydroxides, which would complicate the interpretation of results.

Figure B.19(A) shows the loading distribution coefficients, K_d, of different metal ions from the corresponding single element solutions as a function of the equilibrium solution pH. The extractability obtained at pH < 6 was found to be in the order $Cu^{2+} > Ni^{2+} > Zn^{2+}$. The distribution coefficient for each metal is relatively low for pH < 2. At such a low pH, excess H^+ ions compete with metal ions for binding with surface amino groups, resulting in a low metal ion loading capacity [43]. From the results in this figure, a selective loading of copper ions over nickel and zinc is anticipated. The selective loading was confirmed with loading tests in a solution containing all three of these types of heavy metal ions. The distribution coefficient (K_d) obtained as a function of pH in Figure B.19 (B) shows that the extractability of the metal ions from a mixture follows the same order as seen in the single-metal systems, i.e., $Cu^{2+} > Ni^{2+} > Zn^{2+}$. Metal ion loading increases with increasing pH above 2 up to the limiting pH of 5.2 for copper and zinc, but not for nickel.

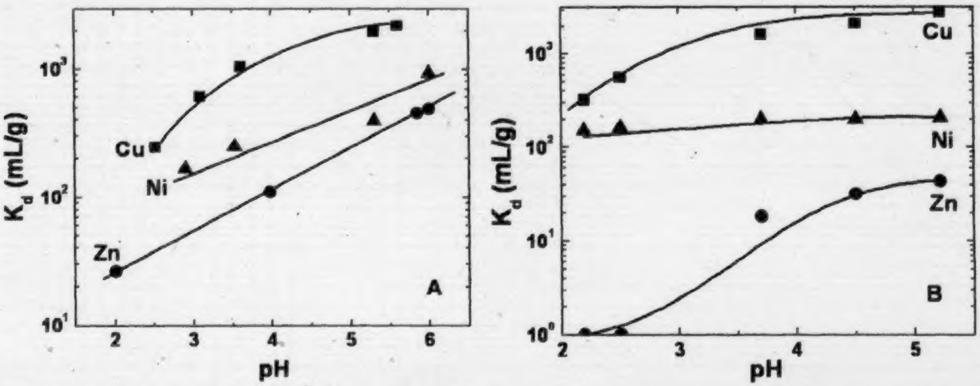

Figure B.19 Loadings of transition metal ions on the amine-terminated mesoporous magnetic particles as a function of solution pH from (A) single-element solutions; and (B) a solution containing copper, nickel, and zinc, each at 0.5 mmol/L concentration.

Stripping and Recycling.

The adsorbed metals were successfully desorbed with 1 M aqueous HCl solutions. The mechanism of copper detachment from silanized mesoporous-Fe_3O_4 particles by acid washing is similar to that explained before [43]. In the reloading test, there is a decrease in the loading capacity of the recycled sorbents by 17%. The reasons for the observed decrease in the loading capacity of the APTES-silanized mesoporous-Fe_3O_4 particles after acid stripping of the loaded copper remain to be investigated. A similar observation was reported by Liu for the loading of copper using amine-terminated nano-Fe_2O_3 particles [43]. His work led to the conclusion that both the protonation/oxidation of amino groups and some degree of detachment of the silanized APTES films during acid stripping contributed to the reduced copper reloading efficiency. We believe that these effects also account for the observations made in the current study. Since long chain alkyl coupling agent will block the pore, it is not good to be used in the functionalization of mesoporous surface. We are continuing to explore other applications of the functionalized mesoporous magnetic particles and are studying the relevant mechanisms.

The above fundamental study demonstrates the feasibility of using APTES-silanized mesoporous-Fe_3O_4 particles in metal recovery and/or removal. The metal ions loaded on the functionalized mesoporous-Fe_3O_4 particles can be detached completely by acid washing. Although the loading capacity of copper on the recycled mesoporous-Fe_3O_4 particles is reduced, improving the stability of the silanized film is anticipated to make the recycling of silanized mesoporous-Fe_3O_4 particles feasible in practice. The concept of using mesoporous-Fe_3O_4 particles functionalized with reactive amine terminal groups for the effective recovery or selective removal of metal ions has thus been demonstrated.

Other Examples of Heavy Metal Removal

It should be noted that other functional groups can be attached onto mesoporous-Fe_3O_4 particles by a similar scheme. For example, carboxylic acid-terminated mesoporous magnetic sorbents can be readily synthesized following the same procedures as used for silanation of APTES [97]. Organic functional groups other than amines are suited to different applications. The surface tailoring method reported here is foreseen to enable diverse design of surface properties of mesoporous-Fe_3O_4 mesoporous materials and could lead to the synthesis of more advanced nanocomposite particles for industrial and environmental applications.

Taking functionalization with mercapto-propyl-trimethoxy-silane (MPTS) through silanation reaction, as an example, the mesoporous magnetic sorbents showed a strong affinity for mercury in aqueous solutions [98]. The isotherm curve in Figure B.20 (A) confirms monolayer adsorption, indicating a chemisorption mechanism of mercury on functionalized mesoporous magnetite surfaces. The maximum loading of mercury at pH 2 is 14 mg/g. The distribution coefficient as a measure of the affinity of an ion exchanger for a particular ion is a sensitive indicator of the selectivity of the ion exchanger to the particular ion in the presence of a complex matrix of interfering ions. For a successful separation, K_d must have a value > 100 mL/g. The result in Figure B.20 (B) shows that the distribution coefficient at pH 2 is well above 100, which confirms the applicability of this kind of mesoporous magnetic particles for mercury removal from industrial effluents.

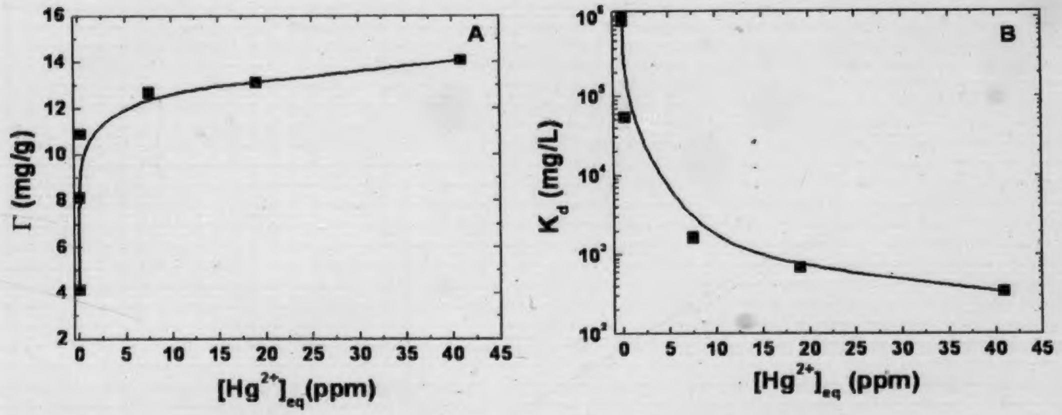

Figure B.20 Mercury adsorption by functionalized magnetic sorbents at pH 2: A) isotherm; and B) distribution.

B.3 Further Directions

In our group, research and development of novel sorbents are taking directions for mercury removal from flue gases of coal-fired power plant. Large mercury adsorption capacity, effective capture, regenerability and recyclability area a few features to be considered to reduce mercury emission, control cost and recover mercury from coal-burning processes. The preliminary results showed promising research direction of zeolite based magnetic sorbents. The research results will be published separately.

The mesoporous silica coating on magnetic particles has a well-characterized surface morphology and can be modified to a wide range of functionality owing to the presence of active hydroxyl groups. For example, the surface can be tuned to strongly acidic or alkaline by grafting different functional groups. Thus it can promise for a wide range of surface catalytic systems with various types of chemical reactions for industrial, biological and pharmacological processes. The industrial processes like flotation, flocculation and ceramic processing, etc., which chiefly depend on the nature of the interface, can be controlled by manipulating surface characteristics. The surface charge and wettability of the silica-coated magnetite surfaces can also be tuned by the adsorption of surfactants, which can be beneficial for controlling dispersion and flocculation in various industrial processes. Silica surface can act as a template for the synthesis of high molecular weight polymers and biomolecules of medical importance. Using this template drug delivery technique can be developed whereby specific drugs can be applied directly to localized area thus resulting in an enhanced remedy without affecting other parts of the body. Photosensitive compounds adsorbed on silica surface can be subjected to external irradiations and their reaction mechanisms can be studied in great detail with better profoundness. Such study can be utilized in developing photo-sensitized chemical machines which can replace electronic chips and can produce pollution-free micro machineries [99]. With magnetic property, the difficulties in recovery and recycling for some applications can be overcome.

In addition, co-condensation reactions, introduction of organic moieties within the silicate framework may increase the flexibility of mesoporous silica coating. The flexibility in choosing organic, inorganic or hybrid building blocks, and combinations of templates allows one to control the materials' properties and to optimize them for each desired application. Periodic mesoporous organosilicas (PMOS) were independently initiated by three groups (Inagaki, group [100], Ozin group [101], and Stein group [102]) in 1999. This category of materials is synthesized using organic monlecules having multiple alkoxysilane groups such as bis(triethoxysilyl)ethane and bis(triethoxysilyl)benzene [103]. Unlike in organic functionalized mesoporous silica phases obtained via grafting or co-condensation procedures the organic groups in PMOS are direct parts of the 3D framework structure, thus giving raise to enormous possibilities to turn their chemical and physical properties in designated ways by varying the structure of the precursors [104]. It is worth to integrate PMOS with magnetic nanoparticles.

B.4 Conclusions

Magnetic nanocomposites were successfully synthesized by molecular self-assembly. By controlling the reactivity of functional groups with surface, 16-ercaptohexadecanoic acid (MHA) was anchored onto γ-Fe_2O_3 surface through chemical bonding between the carboxylic head group of surfactant and iron on the surface, leaving the thiol or disulfide groups reactive. The molecular orientation of MHA self-assembled on γ-Fe_2O_3 was inferred from XPS, DRIFTS and film flotation. This SA film is resistant to acid and base attack.

3-Aminopropyl triethoxy silane (APTES) can be directly silanized onto magnetic particles from water or toluene solutions and the process is characterized by XPS, IR and zeta-potential measurements. APTES films formed on bare magnetic particles from toluene are relatively stable in acid solution compared to the films formed from water. Both films are unstable in alkaline solution.

Silica coatings on magnetic particles were achieved by both sol-gel and dense liquid silica process. A uniform but porous silica layer was coated on magnetic particles by sol-gel process. At low supersaturation level, non-uniform silica coatings were formed by dense liquid silica process. A dense thin silica layer was coated on magnetic particles by a novel two-step process, i.e., sol-gel followed by dense liquid silica coating. The chemical stability of the two-step silica-coated magnetic particles was increased.

Mesoporous silica coating by a combination of dense liquid silica coating and the sol-gel process with molecular templating on magnetic particles can dramatically increase the surface area of the final composites. The templating mechanism and the mesoporous silica coated magnetic particles were studied by AFM, DRIFTS, TEM, zeta-potential measurement and leaching tests. The resultant particles show paramagnetic property with strong saturation magnetization, and the silica surface is amenable for various functionalizations.

The magnetic nanocomposite particles functionalized by silanation with different reactive functional groups, such as –SH, $-NH_2$, and –COOH, have been proven to be effective for removal or recovery of heavy metal ions such as Cu^{2+}, Zn^{2+}, Ni^{2+}, Ag^{+} and Hg^{2+} from aqueous solutions. Selective separation of different metal ions can be achieved by controlling the solution pH. Loaded metal ions on the magnetic particles can be stripped off by acid washing. Magnetic nanocomposites particles with tailored functional groups have potential applications in many scientific and technological applications of different disciplines.

References

[1] Ulman, A. (1991) An Introduction to Ultrathin Organic Films and Langmuir-Blodgett to Self-Assembly, Academic, San Diego.

[2] Pomerantz, M.; Segmuller, A.; Netzer, L.; Sagiv, J. (1986) *Thin Solid Films* 132, 153.

[3] Netzer, L.; Iscovici, R.; Sagiv, J. (1983) *Thin Solid Films* 99, 235.

[4] Allara, D. L.; Nuzzo, R. G. (1985) *Langmuir* 1, 52.

[5] Schlotter, N. E.; Porter, M. D.; Bright, T. B.; Allara, D. L. (1986) *Chem. Phys. Lett.* 132, 93.

[6] Laibinis, P. E.; Hickman, J. J.; Wrighton, M. S.; Whitesides, G. M. (1989) *Science* 245. 845.

[7] Bain, C. D.; Troughton, E. B.; Tao, Yu-Tai; Evall, J.; Whitesides, G. M.; Nuzzo, R. G. (1989) *J. Am. Chem. Soc.* 111, 321.

[8] Walczak, M. M.; Chung, C.; Stole, S. M.; Widrig, C. A.: Porter, M.D. (1991) *J. Am. Chem. Soc.* 113, 2370.

[9] Parikh, A. N.; Allara, D. L.; Azouz, I. B.; Rondelez, F. (1994) *J. Phys.Chem.* 98, 7577.

[10] Yoon, R.-H.; Flinn, D. H.; Guzonas; D. A. (1994) *Colloids Surf.* 87, 163.

[11] Folkers, J. P.; Gorman, L. B.; Laibinis, P. E.; Buchholz, S.; Whitesides, G. M.; Nuzzo, R. G. (1996) *Langmuir* 11, 813.

[12] Allara, D. L.; Hebard, A. F.; Padden, F. J.; Nuzzo, R. G.; Falcone, D. R. (1983) *J. Vac. Sci. Technol.* AI (2), 376.

[13] Ihs, A.; Liedberg, B. (1991) *J. Colloid Interface Sci.* 144, 283.

[14] Uvdal, K.; Bodo, P.; Liedberg, B. (1992) *J. Colloid Interface Sci.* 149, 163.

[15] Goss, C. A.; Charych; D. H.; Majda, M. (1991) *Anal. Chem.* 63, 85.

[16] Smith, E. L.; Alves, L. A.; Andergg, J. W.; Porter, M. D.; Siperko, L. M. (1992) *Langmuir* 8, 2707.

[17] Rozenfeld, O.; Koltypin,Y.; Bamnoker, H.; Margel, S.; Gedanken, A. (1994) *Langmuir* 10, 3919.

[18] Liu, Q.; Friedlaender, F. (1994) *J. Min. Eng.* 7 (4), 449.

[19] Molday, R. S.; Mackenzie, D. (1982) *J. Immunological Methods* 52, 353.

[20] Saito, S. (Ed.) (1988) Fine Ceramics, Elsevier: Amsterdam.

[21] Goldman, P. (1988) In Electronic Ceramics: Properties, Deuices, and Applications; Levinson, L. M., Ed.; Dekker: New York.

[22] Sonti, *S.* V.; Bose, A. (1995) *J. Colloid Interface Sci.* 170, 575.

[23] Liu, Q.; Xu, Z. (1995) *Langmuir* 11, 4617-4622.

[24] Moulder, J. F.; Stickle, W. F.; Sobol, P. E.; Bomben, K. D. (1992) Handbook of X-ray Photoelectron Spectroscopy; Perkin-Elmer Corp.; Eden Prairie, MN.

[25] Wood, R.; Kim, D. S.; Basilid, C. I.; Yoon, R.-H. (1995) *Colloids Surf.* 94, 67.

[26] Zhong, C. H.; Poter, M. D. (1994) *J. Am. Chem. Soc.*116,11616.

[27] Plueddemann, E. P. (1985) In silane, surfaces, and interface,(Ed.), Leyden, D. E., Gordon and Breach Science Publisher, New York, 1-23.

[28] Marquez, M.; Grady, B. P.; Robb, I. (2005) *Colloid Surf. A*, 266, 18.

[29] Nalaskowski, J.; Drelich, J.; Hupka, J.; Miller, J. D. (2003) *Langmuir* 19, 5311.

[30] Ding, W. P.; Meitzner, G. D.; Iglesia, E. (2002) *J. Catal.* 206, 14.

[31] Evans, J.; Zaki, A. B.; El-Sheikh, M. Y.; El-Safty, S. A. (2000) *J. Phys. Chem. B* 104, 10271.

[32] Brunel, D. (1999) *Microporous Mesoporous Mater.* 27, 329.

[33] Lee, S. Y.; Harris, M. T. (2006) *J. Colloid Interface Sci.* 293, 401.

[34] Chagnon, M. S.; Groman, E. V.; Josephson, L.; Whitehead, R. A. (1987) U.S. Patent 4,695,393.

[35] Xu, Z.; Liu, A.; Finch, J. A. (1997) *Appl. Surf. Sci.* 120, 269.

[36] Iler, R. K. (1973) *Surf. Colloid Sci.* 6, 1-100.

[37] Maure, R. E. (1986) *J. Vac. Sci.Technol. A*, 4, 3002.

[38] Niwa, M.; Katada, N.; Murakami, Y. (1990) *J. Phys. Chem.* 94, 6441.

[39] Atik, M.; Zarzycki, J. (1994) *J. Mater. Sc. Lett.* 13, 1301.

[40] Adamson, A. W. (1990) Physical Chemistry of Surfaces, 5th Ed., John Wiley, New York, 297.

[41] Stokes, R. J.; Evans, D. F. (1996) Fundamentals of Interfacial Engineering, John Wiley, New York, 65.

[42] Liu, Q.; Xu, Z.; Finch, J. A.; Egerton, R. (1998) *Chem. Mater.* 10, 3936-3940.

[43] Liu, Q. (1996) An innovative approach in magnetic carrier technology, PhD. Thesis, McGill University, Montreal.

[44] Kresge, C. T.; Leonowicz, M. E.; Roth, W. J.; Vartuli, J. C.; Beck, J. S. (1992). *Nature* 359, 710.

[45] Beck, J. S.; Vartuli, J. C.; Roth, W. J.; Leonowicz, M. E.; Kresge, C. T.; Schmitt, K. D.; Chu, C. T.-W.; Olson, D. H.; Sheppard, E. W.; McCullen, S. B.; Higgins, J. B.; Schlenker, J. L. (1992) *J. Am. Chem. Soc.* 114, 10834.

[46] Kresge, C.T.; Leonowicz, M. E.; Roth, W. J.; Vartuli, J. C. (1992) U. S. Patent 5,098,684.

[47] Yanagisawa, T.; Shimizu, T.; Kuroda, K.; Kato, C. (1990) *Bull. Chem. Soc. Jpn.* 63, 988.

[48] Inagaki, S.; Fukushima, Y.; Kuroda, K. J. (1993) *Chem. Soc., Chem. Commum.* 8, 680.

[49] Stein, A.; Melde, B. J.; Schroden, R. C. (2000) *Adv. Mater.* 12, 1403.

[50] Berggren, A.; Palmqvist, A. E. C.; Holmberg, K. (2005) *Soft Matter* 1, 219.

[51] Hoffmann, F.; Cornelius, M. Morell, J.; Froba, M. (2006) *J. of Nanosci. Nanotechno.* 6, 265.

[52] Ford, D. M.; Simanek, E. E.; Shantz, D. F. (2005) *Nanotechnology* 16, S458.

[53] Hartmann, M. (2005) Chem. Mater. 17, 4577.

[54] Tsang, S. C.; Yu, C. H.; Gao, X.; Tam, K. (2006) *J. Phys. Chem. B* 110, 16914.

[55] Ariga, K.; Nanosci. J. (2004) *Nanotech.* 4, 23.

[56] Shi, J. L.;. Hua, Z. L; Zhang, L. X. (2004) *J. Mater. Chem.* 14, 795

[57] Stein, A. (2003) *Adv. Mate.* 15, 763

[58] Sanchez, C.; Lebeau, B.; Chaput, F.; Boilot, J. P. (2003) *Adv. Mater.* 15, 1969.

[59] Davis, M. E. (2002) *Nature* 417, 813

[60] de Vos, D. E.; Dams, M.; Sels, B. E.; Jacobs, P. A. (2002) *Chem. Rev.* 102, 3615

[61] Schüth, F.; Schmidt, W. (2002) *Adv. Mater.* 14, 629.

[62] Cardin, D. J. (2002) *Adv. Mater.* 14, 553.

[63] Beck, J. S.; Vartali, J. C. (1996) *Curr. Opin. Solid State Mater. Sci.* 1, 76.

[64] Huo, Q.; Margolese, D.; Ciesla, U.; Feng, P. Y.; Gier, T. E.; Sieger, P.; Leao, R.; Petroff, P. M.; Schuth, F.; Stucky, G. D. (1994) *Nature* 368, 321.

[65] Jones, C. M.; Tsuji, K.; Davis, M. (1998) *Nature* 393, 52.

[66] Feng, X.; Fryxell, G. E.; Wang, L.-Q.; Kim, A.Y.; Liu, J.; Kemner, K. M. (1997) *Science* 276, 923.

[67] Israelachvili, J. N.; Mitchell, D. J.; Ninham, B. W. (1976) *J. Chem. Soc., Faraday Trans* 72, 525.

[68] Israelachvili, J. N. (1992) Intermolecular and surface forces. 2nd Edition. Academic Press.

[69] Huo, Q.; Margolese, D. I.; Stucky, G. D. (1996) *Chem. Mater.* 8, 1147.

[70] Øye, G.; Sjöblom, J.; Stöcker, M. (1999) *Microporous Mesoporous Mater.* 27, 171.

[71] Kleitz, F.; Blanchard, J.; Zibrowius, B.; Schueth, F.; Aagren, P.; Linden, M. (2002) *Langmuir* 18, 4963.

[72] Aagren, P.; Linden, M.; Rosenholm, J. B.; Blanchard, J.; Schueth, F.; Amenitsch, H. (2000) *Langmuir* 16, 8809.

[73] Di Renzo, F. ; Testa, F.; Chen, J. D.; Cambon, H.; Galarneau, A.; Plee, D.; Fajula, F. (1999) *Microporous Mesoporous Mater.* 28, 437.

[74] Yang, H.; Coombs, N.; Sokolov, I.; Ozin, G. A. (1996) *Nature* 381, 589.

[75] Wang, L. Z.; Yu, J.; Shi, J. L.; Yan, D. S. (1999) *J. Mater. Sci. Lett.* 18, 1171.

[76] Wu, P.; Zhu, J. ; Xu, Z. (2004) *Adv. Func. Mater.* 14, 345.

[77] Dong, J. ; Xu, Z. (2006) *in:* Kellar, J.J. (Ed.), Functional Fillers and Nanoscale Minerals, by SME, Inc., Littleton, CO, 241-252.

[78] Mercier, L.; Pinnavaia, T. J. (1998) *Microporous Mesoporous Mat.* 20, 101.

[79] Mercier, L.; Pinnavaia, T. J. (1998) *Environ. Sci. Technol.* 32, 2749.

[80] Lim, M. H.; Blanford, C.F.; Stein, A. (1998) *Chem. Mater.* 10, 467.

[81] Brown, J.; Mercier, L.; Pinnavaia, T. J. (1999) *Chem. Commun.* 1, 69-70.

[82] Brown, J. ; Richer, R.; Mercier, L. (2000) *Microporous Mesoporous Mat.* 37, 41.

[83] Antochshuk, V. ; Jaroniec, M. (2002) *Chem. Commun.* 3, 258.

[84] Leyden, D. E.; Luttrell, G. H. (1975) *Anal. Chem.* 47, 1612.

[85] Arkels, B. (1992) Silane coupling agent chemistry, in silicon compounds, register and review, petrarch system catalogue, 59.

[86] Goelzhauser, A.; Panov, S.; Mast, M.; Schertel, A.; Grunze, M.; Woell, Ch. (1995) *Surf. Sci.* 334, 235.

[87] Lund, H.; Baizer, M. M. (1991) Organic Electrochemistry, Marcel Dekker, Inc. New York, 581.

[88] Ihara, H.; Okazaki, S.; Ohmori, K.; Uemura, S.; Hirayama, C.; Nagaoka, S. (1998) *Anal. Sci.* 14, 349.

[89] Kanazawa, H.; Kashiwase, Y.; Yamamoto, K.; Matsushima, Y. (1997) *Anal. Chem.* 69, 823.

[90] Takafuji, M.; Dong, W.; Goto, Y.; Sakurai, T.; Nagaoka, S.; Ihara, H. (2002) *Polym. J.* 34, 437.

[91] Takafuji, M.; Ide, S.; Ihara, H.; Xu, Z. (2004) *Chem. Mater.* 16, 1977.

[92] Gold, D. H.; Gregor, H. P. (1960) *J. Phys. Chem. 64*, 1464

[93] Liu, K. J.; Gregor, H. P. (1965) *J. Phys. Chem. 69*, 1252

[94] Tanford, C.; Wagner, M. L. (1953) *J. Am. Chem. Soc. 75*, 434.

[95] Gold, D. H.; Gregor, H. P. (1960) *J. Phys. Chem. 64*, 1461.

[96] Molina, M. J.; Gomez-Anton, M. R.; Rivas, B. L.; Maturana, H. A.; Pierola, I. F. (2001) *J. Appl. Polym. Sci. 79*, 1467

[97] Shiraishi, Y.; Nishimura, G.; Hirai, T.; Komasawa, I. (2002) *Ind. Eng. Chem. Res.* 41, 5065.

[98] Dong, J.; Xu, Z.; Wang, F. (2008) *App. Surf. Sci.* 254, 3522.

[99] Parida, S. K.; Dash, S.; Patel, S.; Mishra, B. K. (2006) *Adv. Colloid Interface Sci.* 121, 77.

[100] Inagaki, S.; Guan, S.; Fukushima, Y.; Ohsuna, T.; Terasaki, O. (1999) *J. Am. Chem. Soc.* 121, 9611.

[101] Asefa, T.; MacLachlan, M. J.; Coombs, N.; Ozin, G. A. (1999) *Nature* 402, 867.

[102] Melde, B. J.; Holland, B. T.; Blanford, C. F.; Stein, A. (1999) *Chem. Mater.* 11, 3302.

[103] Vinu, A.; Hossain, K. Z.; Ariga, K. (2005) *J. of Nanosci. Nanotechno.* 5/3, 347.

[104] Hoffmann, F.; Cornelius, M.; Morell, J.; Froba, M. (2006) *J. of Nanosci. Nanotechno.* 6, 265.

Appendix C. Factorial Design to Study the Sol-gel Reaction in the Synthesis of Mesoporous Silica Coated Magnetite Particles

To obtain a uniform and well covered mesoporous silica layer on magnetic particles of high specific surface areas, the control of synthesis conditions is extremely important. Many synthesis conditions, such as reaction time, reaction temperature, reactant concentration, type and amount of catalyst, quality of solvent, could affect the properties of the resultant silica coatings. A classical approach to optimize these reaction parameters is to use so called "one-variable-at-a-time" strategy[1]. In this approach, only one variable is varied and optimized each time. Although frequently applied, this classical methodology may not be efficient in determining the true optimal conditions, because it neglects synergetic effect of the variables. To minimize the number of synthesis while considering variable interactions, factorial design of statistical nature is often used to study major trends and determine a promising direction for further experimentation (optimization). The basic idea of the factorial design approach is to devise a small set of experiments, in which all pertinent factors are changed systematically using standard factorial design tables. Subsequent analysis of the experimental results allows factors of major influence and synergetic effect to be identified. Applying the information derived above to a statistical model, one can effectively search for optimal synthesis conditions. The main applications of this methodology have been to the development of new products or processes and to optimization of existing product and manufacturing processes in industrial practices[2].

Since the sol-gel reaction in the synthesis of mesoporous silica coated magnetite particles was identified to be affected by many factors, with the amount of catalyst and TEOS, and reaction time being the major process variables, these three factors were selected as variables to be optimized in synthesis. A standard 2^3 (two levels three variables) factorial design was applied to study relative significance of these parameters in the synthesis of mesoporous silica coatings. The levels for each variables and designs of these experiments are given in Tables C.1 and C.2, respectively. The specific surface area of the synthesized composite particles was used as the response variable. The composition of base solutions in volume ratio of absolute ethanol: DI water: 25% CTAC was set at 180: 13.5: 18. The addition of catalyst and TEOS was adjusted to reflect various levels in Table C.1.

Table C.1 Conditions for 2^3 Factorial Design

	Catalyst ($NH_3 \cdot H_2O$)/mL (A)	Sol-gel reaction time/h (B)	TEOS/mL (C)
+	13.5	15	0.9
-	9	10	0.45

Table C.2 Complete 2^3 Factorial Design: Factors and Levels

No.	Catalyst (A)	Time (B)	TEOS (C)
1	-	-	-
2	+	-	-
3	-	+	-
4	+	+	-
5	-	-	+
6	+	-	+
7	-	+	+
8	+	+	+

The results of the 2^3 factorial design are shown in Table C.3. The specific surface area was measured twice for each sample (β_j', β_j'') and β_j is the average of the two values. One of the most important outcomes using factorial design is the analysis of relative importance of variables, individually and collectively. A quick method to analyze the effects is to use a table of contrast coefficients (Table C.3). For example, the mean is calculated from the first column,

$$\frac{+91.6+65.0+72.2+70.1+76.1+96.5+150.9+68.1}{8}=86.3$$

and the A × C interaction is from the sixth column,

$$\frac{+91.6-65.0+72.2-70.1-76.1+96.5-150.9+68.1}{4}=-8.4$$

Table C.3 Results of the 2^3 Factorial Design Experiments

No.	mean	Catalyst (A)	Time (B)	TEOS (C)	AB	AC	BC	ABC	β_j (m^2/g)	β_j' (m^2/g)	β_j'' (m^2/g)	S_j^2
1	+	-	-	-	+	+	+	-	91.6	92.0	91.2	0.32
2	+	+	-	-	-	-	+	+	65.0	65.6	64.4	0.72
3	+	-	+	-	-	+	-	+	72.2	71.2	73.2	2.00
4	+	+	+	-	+	-	-	-	70.1	70.3	70	0.05
5	+	-	-	+	+	-	-	+	76.1	76.6	75.6	0.50
6	+	+	-	+	-	+	-	-	96.5	96.7	96.3	0.08
7	+	-	+	+	-	-	+	-	150.9	151.1	150.7	0.08
8	+	+	+	+	+	+	+	+	68.1	67.0	69.1	2.20
Divisor	8	4	4	4	4	4	4	4				
Effect	86.3	-22.8	8.0	23.2	-19.7	-8.5	15.2	-31.9				

The remaining effects are obtained in a similar way and summarized in Table C.3. To compare and emphasize the main effects of the synthesis process, it was necessary to calculate the standard error of the effects. Since the adopted experimental design was constituted by eight experiments, the error (σ) was calculated as a linear combination of the eight average values obtained in the respective duplicates.

$$\sigma = [(\frac{1}{8}+\frac{1}{8})\times(\Sigma\frac{s_j^2}{8})]^{\frac{1}{2}}$$

in which s_j is the j th experimental variance.

The analyzed results are summarized in Table C.4. As shown in Table C.4, the main effects of the amount of catalyst and TEOS are more significant than that of the reaction time, reflected by larger surface area changes in response to their variations. Although the results indicate the main effect to be significant, the interactive effects such as A×B and B×C (-19.7 and 15.2) can not be neglected. However, the overall interactive effect of A×B×C (-31.9) turns out to be the most dominant effect for this system.

Table C.4 Summaries of Effects and Standard Errors for the 2^3 Factorial Design

Effect	Estimate ± standard error
Average	86.3±0.22
Main effect	
Catalyst (A)	-22.8±0.43
Time (B)	8.0±0.43
TEOS (C)	23.2±0.43
Two-factor interaction	
A×B	-19.7±0.43
A×C	-8.5±0.43
B×C	15.2±0.43
Three-factor interaction	
A×B ×C	-31.9±0.43

The existence of a significant interaction among the variables for the sol-gel process suggests that the main effects must not be interpreted individually when optimizing synthesis conditions. The interactive effects can be visualized by the diagram shown in Figure C.1. The shadowed face represents the optimum results for specific surface areas. When interpreting this diagram, the three-factor effect is verified to be dominating. The above analysis clearly shows that it would be impossible to carry out a complete analysis of the situation by a univariate study. The factorial design method would suggest optimal conditions for the sol-gel reaction at low catalyst concentration, long reaction time and high TEOS dosage. When the time is fixed at high level (+), reducing the amount of catalyst can increase specific surface area, especially at high level of TEOS.

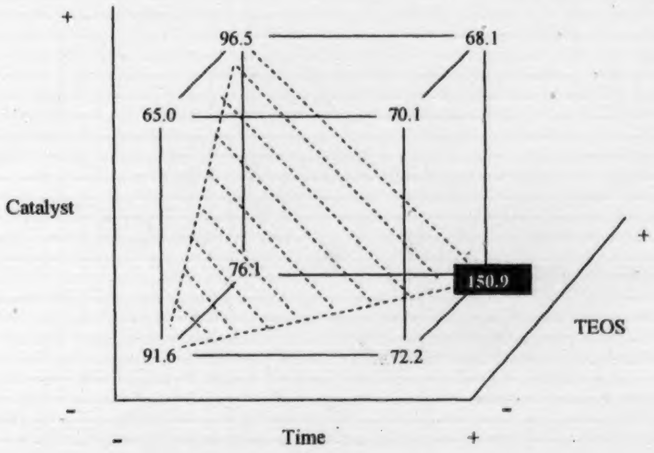

Figure C.1 Factorial Design Diagram for the Surface Area of the Sorbents

Table C.5 Optimization of the Experiment

No.	Catalyst (mL)	Time (h)	TEOS (mL)	BET (m^2/g)
(7)*	9	15	0.9	150.9
(9)	6.8	15	1.125	104.3
(10)	5.6	15	1.350	121.6
(11)	3.4	15	1.575	149.2
(12)	2.2	15	1.800	123.4

Note: (7)* is the No.7 sample of 2^3 factorial design.

From the 2^3 factorial design experiments, it can be concluded that the interaction effects are dominant. Compared with the other two variables, the effect of reaction time is relatively minor and will be kept constant (15 hours) in the following experiments. The other reaction conditions with the corresponding results are given in Table C.5. The surface areas for the tests coded as No.11 (149.2 m^2/g) and No. 7 (150.9 m^2/g) are similar. It appears that a specific surface area of about 150 m^2/g is the optimum for coating mesoporous silica layers on micron-sized magnetite particles.

References

[1] Goupy, J.L., Methods for Experimental Design-principles and applications for physicists and chemists, Data Handling in Science and Technology, Vol. 12, pp 1-8, Elsevier, Amsterdam,1993

[2] Steinberg, D. M. and W. G. Hunter, Experimental Design: Review and Comment, Technometrics, **26**, 71-97 (1984)

Appendix D. Sol-gel Reaction and Silanation

Sol-gel Reaction

The sol-gel process is characterized by hydrolysis of silicon alkoxide precusors such as tetraethoxy silane (TEOS), in the presence of water and catalyst, followed by polycondensation with formation of an oxide gel, which can be converted to an oxide by removal of all liquid components. The following equations represent the reaction sequences,

Hydrolysis:

$$\equiv Si\text{-}OR + H_2O \rightarrow \equiv Si\text{-}OH + ROH \qquad (1)$$

Water condensation:

$$\equiv Si\text{-}OH + \equiv Si\text{-}OH \rightarrow \equiv Si\text{-}O\text{-}Si \equiv + H_2O \qquad (2)$$

Alcohol condensation:

$$\equiv Si\text{-}OR + \equiv Si\text{-}OH \rightarrow \equiv Si\text{-}O\text{-}Si \equiv + ROH \qquad (3)$$

where R is an alkyl group C_xH_{2x+1}.

Silanation

A typical silane coupling agent has the structure of $Y\text{-}(CH_2)_n\text{-}Si\text{-}X_3$, where X represents the alkoxy or halide groups and Y is an organic functional group. Mercapto-propyl-trimethoxy-silane (MPTS) was selected to form the functionalized monolayer because of the high affinity of –SH group to Hg^{2+}. Furthermore, the short-chain alkane, $(CH_2)_3$, will minimize blocking the pore channels.

The density and quality of the functionalized monolayer on the mesoporous materials are greatly affected by two factors: the population of silano groups and the number of adsorbed water molecules on the mesoporous surface[1]. The surface silanols (hydroxyl groups attached to a silicon atom) anchor the organic functional molecules to the particle surface. A sufficient amount of water to form a monolayer on the pore surface will lead to a high concentration of organics in the product (Figure D.1). Excess free water is detrimental, because uncontrolled polymerization of the silane coupling agent may take place within the channels or external to the mesoporous materials.

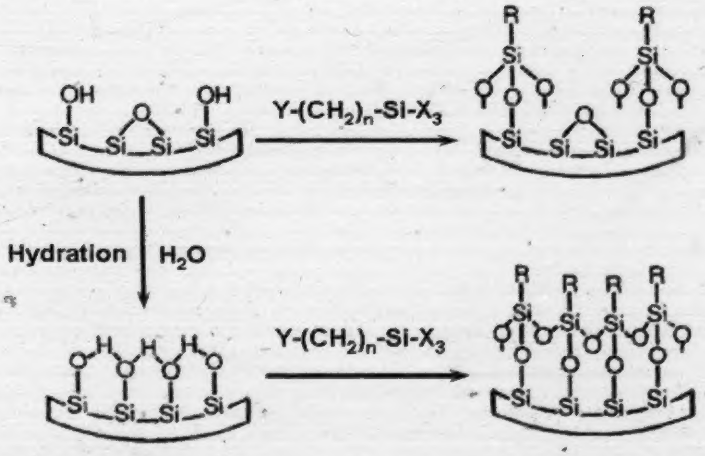
OH
OH
Si
Si
Si
Si
O
Y-(CH2)n-Si-X3
R
Si
Hydration
H2O
H
O

Figure D.1 Hydration and silanation process. (X: alkoxy or halide groups; Y: an organic functional group)

Reference

[1] Feng, X.; Fryxell, G. E.; Wang, L. Q.; Kim, A. Y.; Liu, J.; Kemner, K. M. *Science*, **1997**, *276*, 923-926,.

Appendix E. Theory of the Infrared Spectra Simulation[1,2]

For a multi-layer system, as shown in Figure E. 1, an incident infrared radiation beam is directed towards the surface at a given angle (φ), propagating through the stratified medium. Part of the energy is reflected after interacting with the medium. The reflected electric field of a given polarization is related to the electric field of polarized incident beam by the Jones matrix [*M*], which is characteristic of the stratified medium.

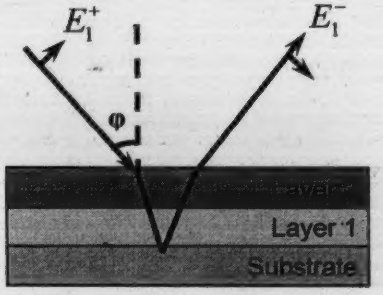

Figure E. 1 Schematic illustration of the interaction between infrared radiation and adsorbed layer.

$$\begin{bmatrix} \dfrac{E_1^-}{H_1^-} \end{bmatrix} = [M] \begin{bmatrix} \dfrac{E_{N-1}{}^+}{H_{N-1}{}^+} \end{bmatrix} \qquad \text{(E.1)}$$

where *E* and *H* are the magnitudes of tangential components of electrical and magnetic fields, respectively, the subscript identifies the phase boundary; and the superscripts – and + represent incident and reflected beam. In the above equation,

$$[M] = [M_2] \cdot [M_3] \cdot \ldots \cdot [M_{N-1}]$$

where $[M_j]$ is a 2 by 2 matrix whose elements are determined by the complex optical constants $\hat{n} = n_j + i \cdot k_j$ (n_j is the reflective index, k_j is the extinction coefficient), the film thickness (d_j) of the j^{th} phase, and the incident angle (φ). It should be noted that Eq. (E.1) is valid for planarly polarized radiation only.

For a parallel polarized (p-polarization) incident beam, the Jones matrix for phase j is given by:

$$[M] = \prod_{j=2}^{N-1} \begin{bmatrix} con\beta_j & \dfrac{-i}{q_j}\sin\beta_j \\ -iq_j\sin\beta_j & con\beta_j \end{bmatrix} = \begin{bmatrix} m_{11} & m_{12} \\ m_{21} & m_{22} \end{bmatrix} \qquad (2)$$

in which $q_j = \xi_j / \hat{n}_j^2$ and $\beta_j = 2\pi(d_j / \lambda)\xi_j$. λ is the wavelength in vacuum and $\xi_j = n_j \cos\varphi = (n_j^2 - n_1^2 \sin^2\varphi)^{1/2}$. The matrix elements of each phase in a stratified medium can be readily calculated if the optical constants and film thickness are known.

The Fresnel reflection coefficient r is defined as the amplitude ratio for reflected and incident electric fields. For p-polar is given by:

$$r = \frac{(m_{11} + m_{12}q_N)q_1 - (m_{21} + m_{22}q_N)}{(m_{11} + m_{12}q_N)q_1 + (m_{21} + m_{22}q_N)} \qquad (3)$$

where m_{ij} is the elements of overall matrix $[M]$.

The reflectance of the stratified medium is therefore given by the magnitude of the reflectance coefficient, i.e. $R = \left|E_1^+\right|^2 / \left|E_1^-\right|^2 = |r|^2$. The absorbance used in spectral representation is then calculated by

$$A = -\log\frac{R}{R_o} \qquad (4)$$

where R and R_o are the reflectance of the stratified medium in the presence and absence of adsorbed layers, respectively. The calculation is limited to parallel polarization, but can be readily extended to perpendicular polarization, simply replacing q_j by p_j $(p_j = \xi_j = \hat{n}_j \cos\varphi = (n_j^2 - n_1^2 \sin^2\varphi)^{1/2})$.

In the text about spectra simulation, R and R_o are specified by listing the stratified components in parenthesis, for example, $A = -\log\dfrac{R(Ge/16nmPS/H_2O)}{R_o(Ge/H_2O)}$.

Reference

[1] Zhenghe Xu, External Reflection Infrared Spectroscopy of Collector Monolayers on Mineral Surfaces: A Computer Simulation Approach, CAMI'95: 3rd Canadian Conference on Computer Applications in the Mineral Industry, Montreal, Quebec, October 22-25, 1995, Canada

[2] Valeri P. Tolstoy, Irina V. Chernyshova, Valeri A. Skryshevsky, Handbook of Infrared Spectroscopy of Ultrathin Films, Wiley-Interscience, A John Wiley & Sons, Inc.

Appendix F: Supporting Information to Chapter 6

F.1 Experimental

Materials. Polystyrene (PS) with average molecular weight 250,000 g/mol was purchased from ACROS. Concanavalin A (ConA) was purchased from Sigma-Aldrich (C2010, carbohydrate and salt are essentially free) and used directly without further purification. Bovine serum albumin (BSA) (fraction V, lyophilized, purity 95%) was supplied by Odczynniki Chemiczne, Poland and used as a blocking agent. Phosphate buffered saline (PBS) buffer solution was prepared from KH_2PO_4 (1.47 mM), Na_2HPO_4 (6.46 mM), KCl (2.68 mM) and NaCl (0.137 M). NaOH and HCl were used to adjust the pH. All solutions were prepared freshly before adsorption experiments. ConA concentration was determined by UV/Vis spectroscopy before and after filtration using 0.2 filter. No agglomeration of ConA in solution was detected. All reagents used were of analytical grade. Ultrapure water from the Millipore (Milli-Q system) was used throughout the experiments.

Infrared (FTIR) Spectroscopy. FTIR spectrometer (Bruker IFS55) equipped with an MCT detector and an attenuated total reflection (ATR) attachment was used to record the ATR spectra. A wire-grid polarizer was placed before the sample and p- or s-polarized light was provided. These accessories were from Harrick Scientific Co. The reflection spectra of the adsorption layers were obtained by the use of polarized light at incidence angle of 45°. The spectrometer was purged with dry air (Balston filter) to minimize the disturbance of water vapor and carbon dioxide to the recorded spectra. The unit of intensity was defined as $-\log(\frac{R}{R_0})$, where R and R_0 are the reflectivities of the system with and without the investigated adsorption layer, respectively. 200 scans were collected for samples and references spectra. The resolution was 4 cm^{-1} (zero-filled = 2) with Blackman–Harris, three-term apodization.

X-ray Photoelectron Spectroscopy (XPS). AXIS NOVA photoelectron spectrometer (Kratos Analytical, Manchester, UK) equipped with monochromatic AlK ($h\nu$=1486.6 eV) anode was used in the studies. The kinetic energy of the photoelectrons was determined with the hemispheric analyser set to the pass energy of 160 eV for wide scan spectra and 20eV for high resolution spectra. Electrostatic charge effect of sample was overcompensated by means θof the low-energy electron source working in combination with magnetic immersion lens. The carbon C1s line with position at 284.6 eV was used as a reference to correct the charging effect. Quantitative elemental compositions were determined from peak areas using experimentally determined sensitivity factors and spectrometer transmission function. Spectrum background was subtracted according to Shirley. The high resolution spectra were analyzed by means of spectra deconvolution software (Vision 2, Kratos Analytical, UK).

In order to study the molecular structure of the top surface layers, i.e. a film of a few nanometers thickness, angle resolved XPS was applied and spectra were recorded for the three take-off angles of = 0°, 60°, and 75°. The take-off angle is defined as the angle between the normal to the surface of the sample and the electron optical axis of the spectrometer. The effective information depth, varies according to $d = d_0 \cos\theta$, where d_o is the maximum information depth (d_o ~10 nm for the C1s line by employing an AlK source). This technique helps to determine structure (molecular distribution) of the adsorbed ConA layer.

F.2 Preparation of Thin film of Polystyrene for ConA Adsorption.

The measurements of ConA adsorption were done by attenuated total reflection (ATR) infrared method, therefore, the thin film of PS was deposited on germanium ATR reflection element with dimension of 50×20×3 mm^3 (16 reflections) and an angle of reflection of 45°. The assembled liquid cell with reflection element is illustrated schematically in Figure F.1 (A).

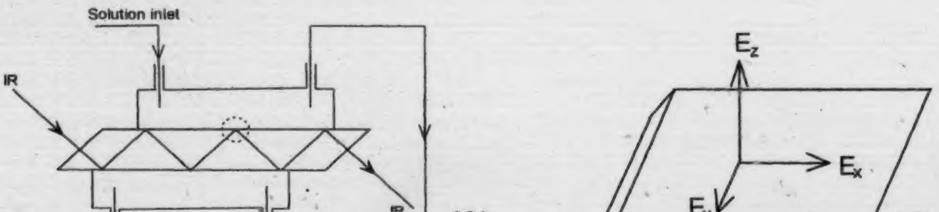

Figure F.1 (A) Schematic illustration of the assembled Teflon liquid cell with Ge reflection element for *in situ* adsorption studies by ATR-IR, (B) Directions of electric field components at Ge interface.

The reflection crystal was polished with alumina powder (<0.05 μm) washed with water and finally with toluene. PS was deposited on both sides of germanium crystal by dip coating from PS toluene solution with concentration of 10 mg/ml solution. The retracing speed of the coating device was equivalent to 18 mm/min. The produced PS film was characterized by XPS, SEM and infrared spectroscopy. The film was pure PS (with only trace amount of oxygen), the layer was continuous, the surface of PS was smooth (SEM results, not shown) and the thickness of the film, determined by infrared technique combined with spectral simulation (for details see Optical Consideration section), was around 16 nm. Reproducibility of the prepared PS films was 16±1 nm.

F.3 Determination of Number of the Active Internal Reflections

Number of the active internal reflections of *in situ* monitoring of protein adsorption could be estimated from geometrical dimensions of liquid cell and reflection element (Figure F.1). However more accurate result can be obtained from the recorded experimental reflection spectra of water in liquid cell.

Two experimental spectra recorded for s- and p-polarizations with germanium reflection element held in liquid cell with and without water allow measurement of water absorbance according to the following expression:

$$Abs = -\log\left(\frac{R(Ge/H_2O)}{R_o(Ge/air)}\right)$$

The water absorbance for one reflection can be simulated based on optical constants of reflection element and water for two polarizations at 45°. By simple fitting of the experimental spectra of water in liquid cell with simulated spectra for two polarizations the number of active reflections of *in situ* measurement was calculated. The number obtained was equal to 12.2 reflections.

F.4 Determination of Thickness and Structure of the Deposited PS Layer

Polystyrene is an excellent substrate used in the study of protein adsorption because of its smooth surface, negligible solubility in water and invariable surface characteristics[1,2]. A lot of work has been done concerning the orientation of PS itself by sum frequency generation (SFG)[2, 3], angle-resolved ultraviolet photoelectron spectroscopy (ARUPS)[4] or near-edge X-ray absorption fine structure (NEXAFS)[5,6], small-angle neutron scattering (SANS)[7]. The above mentioned experimental studies reported that the phenyl groups on the PS surface are orientated closely to the surface normal with a narrow angle distribution. Most recently, by molecular dynamics simulation, it was found[8] that the phenyl rings point outwards at the PS/air or vacuum interface, but rings in the bulk show no preferred orientation. In contrast with the phenyl rings, the bisectors for the methylene groups show little tendency for orientation, even when the methylene groups are close to the surface. In the present work at first approximation it was assumed that PS layer is isotropic.

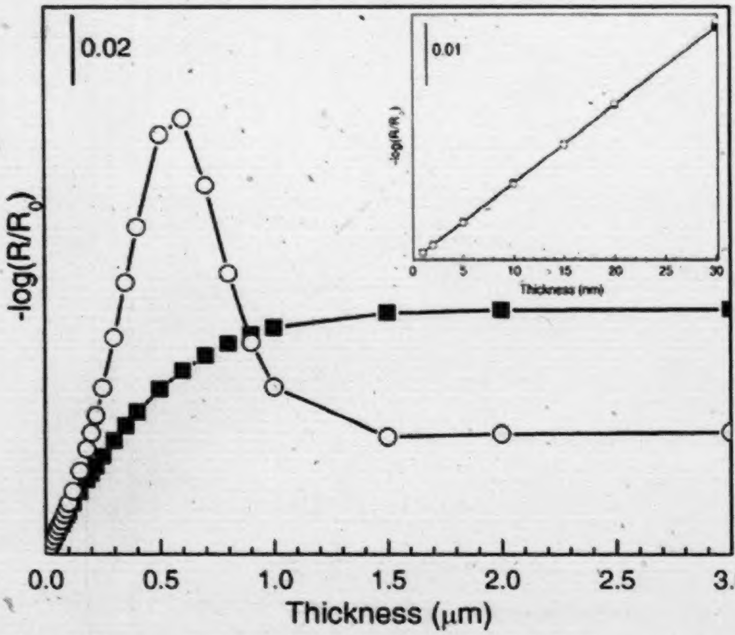

Figure F.2 Simulated absorbance intensity of characteristic PS absorbance band at 1494 cm^{-1} versus thickness of hypothetical PS isotropic layer for p- (filled square line) and s- (open circle line) polarizations. Simulation was performed for system of R(Ge/PS/air) and R_0(Ge/air).

Results of the intensity simulation of the characteristic PS absorbance band at 1494 cm^{-1} versus thickness of the deposited layer (Figure F.2) clearly indicate that for isotropic PS layer with thickness up to 20 nm the reflection spectra recorded for p- and s-polarizations should be identical. Above this thickness other optical effects take place and the intensity of p-polarized and s-polarized spectra vary significantly with thickness up to 1.5 μm (Figure F.2). It should be noted that at thickness above of 1.5 μm constant values are observed for both polarizations with absorbance ratio equal to 2:1, which is characteristic for ATR spectrum of massive sample.

In the case of p-polarization at the Ge/PS interface there are two electric field components (Figure F.1 (B)): the first one vertical to interface in the z direction, E_Z, and the second one parallel to interface in the x direction, E_X. For s-polarization there is only electric field component parallel to interface in the y direction, E_Y. Hence if the PS layer is anisotropic the recorded spectra for both polarizations should be different. Since the ATR experimental spectra of the PS layers recorded in air and in water

$$Abs = -\log \frac{R(Ge/PS/air)}{R_o(Ge/air)} \qquad Abs = -\log \frac{R(Ge/PS/H_2O)}{R_o(Ge/H_2O)}$$

are almost identical for both polarizations (Figure F.3) it implies that PS layer could be considered as an isotropic phase, which simplifies the carried out optical considerations.

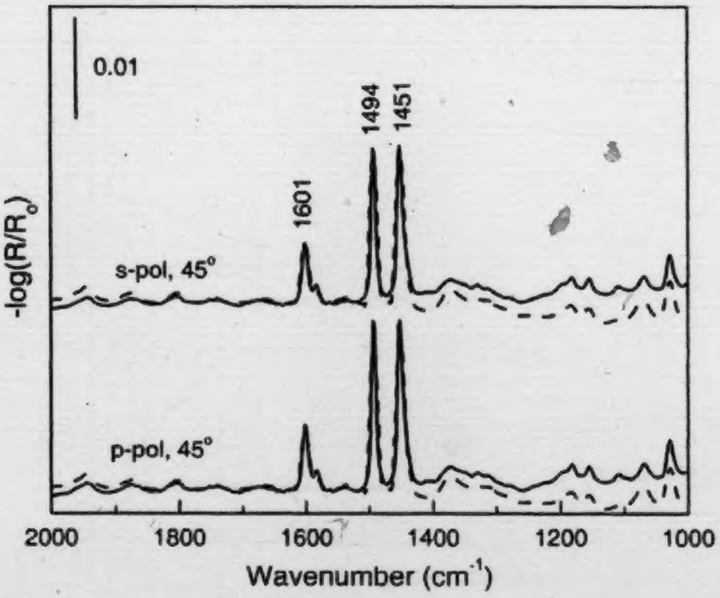

Figure F.3 Experimental spectra (dashed lines) of deposited PS layer on Ge reflection element compared with simulated spectra (solid lines) of 16nm hypothetical isotropic PS layer for both polarizations.

The best fitting of the experimental spectra recorded in air is presented in Figure F.3, which was achieved with assumption of 16 nm thick PS layer. It is possible to obtain the PS layers on Ge crystal by dip coating with precision 16 ± 1 nm.

References

[1] Edward D. P. *"Handbook of Optical Constants of Solids"*, Naval Research Laboratory, Washington, D. C., Academic Press Inc. **1985**.

[2] Chen, C.; Wang, J.; Woodcock, S. E.; Chen, Z. *Langmuir* **2002**, *18*, 1302-1309.

[3] Gautam, K. S.; Schwab, A. D.; Dhinojwala, A.; Zhang, D.; Dougal, S. M.; Yeganeh, M. S. *Phys. Rev. Lett.* **2000**, *85(18)*, 3854-3857

[4] Ueno, N.; Azuma, Y.; Tsutsi, M.; Okudaira, K.; Harada, Y. *Jpn. J. Appl. Phys.* **1998**, *37*, 4979-4982.

[5] Stöhr, J.; Samat, M. G. *J. Elec. Spectroc. Relat. Phenom.* **1999**, *98-99*, 189-207.

[6] Fischer, D. A.; Mitchell, G. E.; Yeh, T. A.; Gland, J. L. *Appl. Surf.Sci.* **1998**, *133*, 58-64.

[7] Jones, R. L.; Kumar, S. K.; Ho, D. L.; Briber, R. M.; Russell, T. *Nature* **1999**, *400*, 146-149.

[8] Clancy, T.; Jang, J.;H.; Dhinojwala, A. and Mattice, W. *J. Phys. Chem. B* **2001**, *105*, 11483-11497.